PHOTOPHYSICAL AND PHOTOCHEMICAL PROPERTIES OF N, C-CHELATE ORGANOBORON COMPOUNDS AND THEIR Pt(II) COMPLEXES

by

Ying-Li Rao

A thesis submitted to the Department of Chemistry

In conformity with the requirements for

the degree of Master of Science

Queen's University

Kingston, Ontario, Canada

(September, 2009)

Canada

Abstract

The impact of two constitutional isomers, 2-(4-BMes$_2$-Ph)-pyridine (p-B-ppy) and 5-BMes$_2$-2-ph-pyridine (p-ppy-B), as N,C-chelate ligands on the structures, stabilities, electronic and photophysical properties, and Lewis acidities of Pt(II) complexes has been investigated. Six Pt(II) complexes, Pt(p-B-ppy)Ph(DMSO), Pt(p-B-ppy)Ph(Py), [Pt(p-B-ppy)Ph]$_2$(4,4'-bipy), Pt(p-ppy-B)Ph(DMSO), Pt(p-ppy-B)Ph(Py), and [Pt(p-ppy-B)Ph]$_2$(4,4'-bipy), have been synthesized and fully characterized. The Lewis acidity of the complexes was examined by fluoride titration experiments using UV-Vis, phosphorescence, and NMR spectroscopic methods, establishing that the p-ppy-B complexes have stronger binding constants while the p-B-ppy complexes have a much lower affinity toward F$^-$.

A diboron compound with both 3-coordinate boron and 4-coordinate boron centers, (5-BMes$_2$-2-Ph-Py)BMes$_2$ (B2ppy) has been synthesized, which is luminescent but have a high sensitivity toward light. UV and ambient light cause this compound to isomerize via the formation of a C−C bond between a mesityl and the phenyl group, accompanied by a drastic color change from yellow to dark olive green. The structure of the dark color species was established by 2D NMR experiments and geometry optimization by DFT calculations. The dark color species can thermally reverse back to (5-BMes$_2$-2-Ph-Py)BMes$_2$ via the breaking of a C−C bond. The N, C-chelate ligand was found to play a key role in promoting this unusual and reversible photo–thermal isomerization process on a tetrahedral boron center.

The impact of Pt(II) on the photoisomeration of four-coordinate boron center was also studied. The free ligand four-coordinate organoboron derivative B-ppy-ppy behaved

in the same way as B2ppy. The photoisomeration process in the corresponding Pt(II) coupled complex (B-ppy-ppy)PtPh(t-Bu-Py) is nearly completely deactivated, which may be attributed to either the low-lying ^{3}MLCT excited state through which the excess energy in excited state was dissipated as phosphorescence or the greater π conjugation which can stabilize the excited state.

Table of Contents

List of Figures

List of Tables

List of Symbols and Abbreviations

A	ampere, absorbance
Å	angstrom
Anal	analysis
B3LYP	Becke 3-Parameter Exchange, Lee, Yang and Parr
bipy	bipyridine
c	concentration
calcd	calculated
cm	centimetres
CH_3CN	acetonitrile
CH_2Cl_2	dichloromethane
COSY	Correlation Spectroscopy
CV	cyclic voltametry
d	doublet
DCM	dichloromethane
dd	doublet of doublets
DFT	density functional theory
DMF	dimethylformamide
DMSO	dimethylsulfoxide
EL	electroluminescent
EML	emitting layer
ETM	electron transport material
eV	electron volt

Hz	hertz
HMBC	Heteronuclear Multiple Bond Correlation
HOMO	highest occupied molecular orbital
HRMS	high resolution mass spectrometry
HSQC	Heteronuclear Single Quantum Coherence
HTM	hole transport material
ISC	intersystem crossing
J	coupling constant
K	Kelvin
l	path length
L	liter, luminance
LC	ligand centered
LLCT	ligand to ligand charge transfer
LMCT	ligand to metal charge transfer
LUMO	lowest unoccupied molecular orbital
m	meter, multiplet
M	molar
mA	milliampere
MC	metal centred
mes	mesityl
mg	milligram
MHz	megahertz
mL	millilitre

MLCT	metal to ligand charge transfer
^{3}MLCT	triplet metal to ligand charge transfer
mmol	millimole
MO	molecular orbital
mol	mole
m. p.	melting point
nm	nanometers
NMR	nuclear magnetic resonance
NOESY	Nuclear Overhauser Effect Spectroscopy
OLED	organic light emitting diode
ph	phenyl
ppy	2-phenylpyridine
py	pyridine
r.t	temperature
s	seconds
S_0	singlet ground state
S_1	singlet excited state
t	triplet
TBAF	tetra-n-butylammonium fluoride
td	triplet of doublets
THF	tetrahydrofuran
TLC	thin layer chromatography
UV	ultraviolet

UV-Vis	ultraviolet-visible
δ	chemical shift
μs	microsecond
λ	wavelength
Φ	quantum yield
τ	lifetime

Chapter 1

Introduction

Organic materials with optoelectronic properties have gained extensive research interest in recent years, due to their potential applications in luminescent materials,[1,2] sensors,[3, 4, 5] solar cells,[6] optical data storage,[7] molecular device,[8] etc. Compared to the traditional inorganic semiconductors, organic counterparts have several advantages. On the one hand organic materials are more flexible in display architecture, which can be processed in solution or doped in polymer as film; on the other hand, the photophysical properties of organic materials can be easily and precisely tuned through modern organic synthetic strategy.

Among numerous organic materials with optoelectronic properties, conjugated organoboron compounds are unique and have superior properties. This chapter will start with general introduction of luminescence, photochemistry and organoboron compounds. Literature reviews on different modifications of photophysical properties of triarylboron compounds constitute the major parts of this chapter, especially metal ion modified triarylboron compounds. As the photochemical property is the result of competition among different fundamental photophysical processes,[9] the photochemistry of organoboron compounds and photochrome-coupled metal complexes will also be reviewed. The final part of this chapter is the motivation and scope of the dissertation.

1.1 Luminescence and photochemistry

When electrons in a molecular excited state go back to ground state, the excess energy can be released as a photon (fluorescence) dissipated non-radioactively, or convert to triplet excited state through intersystem crossing. In organic molecules, the latter event is relatively rare but still can result in emission of a photon, known as phosphorescence. The luminescence can be divided into different categories based on how the electrons are excited. Here we mainly focus on photoluminescence and electroluminescence.

1.1.1 Photoluminescence

Light is the most convenient external energy source to promote molecules into excited state. Moreover, light at a given wavelength with a specific energy can be used to precisely control the level of the excited state to reach. Upon irradiation with light, electrons in the molecular ground state jump to the excited state. Due to the rapid decay of excited electrons to the lowest vibrational energy level of the excited state, the re-emitted light has lower energy than the absorbed one. The wavelength difference between positions of the band maxima in absorption and emission spectra is known as the Stokes shift.

As illustrated in the Jablonski diagram (Figure 1.1), fluorescence and phosphorescence are two pathways of photoluminescence. The lifetime of fluorescence is in the range of 10^{-9} s, much shorter than that of phosphorescence (10^{-6} s), due to the forbidden transition from the triplet excited state to the singlet ground state.[10]

2

Excited Singlet States

S_2 Vibrational Energy States

S_1 Intersystem Crossing

Fluorescence

Excited Triplet States T_1

Phosphorescence

S_0 Radiationless Decay

Ground States
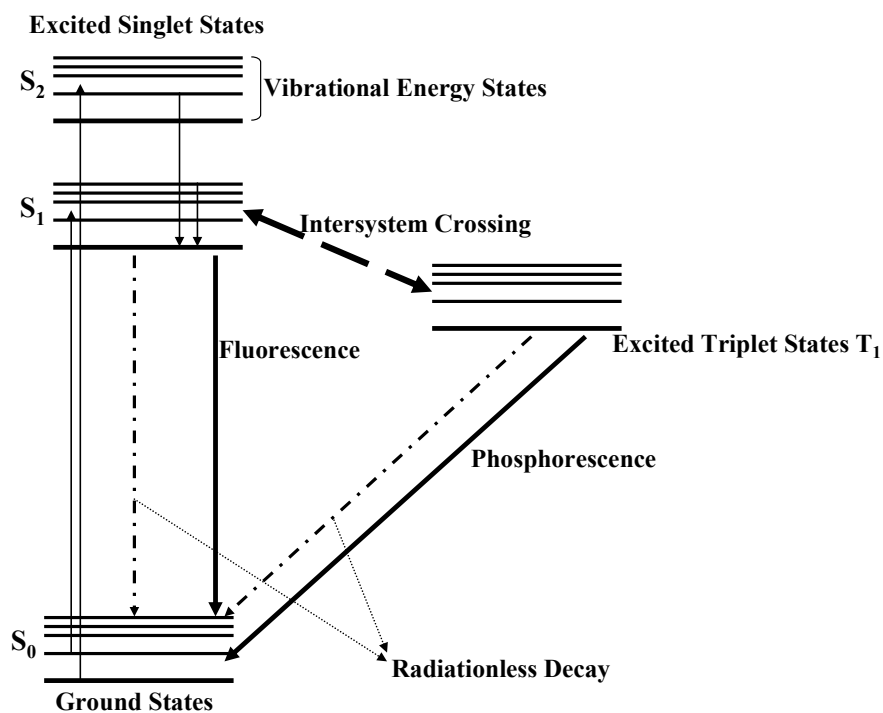
Figure 1.1 Jablonski Energy Diagram.

Fluorescent quantum efficiency is defined as the ratio of the number of photons emitted to the number of photons absorbed. The maximum fluorescent quantum efficiency is 1.0. Determination of quantum efficiency can be achieved through a calibrated integrating sphere system or the use of accurate luminescence standard sample whose emission spectral property closely matches the unknown one.[11] In the latter way, the quantum efficiency of an unknown is related to that of a standard by equation (1):

$$\Phi_u = [(A_s\, F_u\, n_u^2)/(A_u\, F_s\, n_s^2)]\, \Phi_s \qquad\qquad (1)$$

3

in which, the subscript u stands for unknown, s for standard, and Φ is quantum efficiency, A is absorbance at the excitation wavelength, F is the integrated emission intensity, n is refraction index of the solvent used. Generally, the absorbance chosen for excitation should be similar and small (around 0.1) for both unknown and standard sample.

The **fluorescence lifetime** is defined as the average time the molecule stays in its excited state before the radioactive decay. Generally, the longer the excited state lifetime, the higher probability is to undergo photochemical reactions.

1.1.2 Electroluminescence

The commercially available and well-developed OLEDs and LED display are based on electroluminescence.[12] Figure 1.2 shows the OLEDs device structure. The organic emitting layer is between the electron transporting layer and the hole transporting layer. When the electrons and holes from electrodes were injected into and recombined in the organic emitting layer, the excited state of organic emitting layer was generated. The luminescence originated from this excited state is electroluminescence. It is critical for ideal organic emitting layer to be charge-transporting and highly fluorescent.

Different from photoexcitation directly generates singlet excited states, excited states generated in OLEDs originate in electron and hole from opposite electrodes with triplet and singlet excited state in the ratio of 3 : 1. This phenomenon is due to that a triplet excited state with total spin of S=1 has a multiplicity of three, while a singlet excited state with total spin of S=0 has only one multiplicity, which implies during

excitation, only one singlet excited state is created while three triplet excited states should be generated. For most organic materials, owing to the forbidden triplet excited state to singlet ground state transition, 75% of the input energy is wasted while up to 25% of the input energy can be harvested as fluorescence.
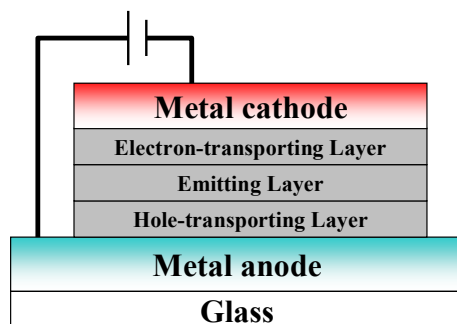
Figure 1.2 Structure of OLEDs.

1.1.3 Photochemistry

Photochemistry concerns the phenomenon of the interactions of light with molecules that leads to structural change or chemical reactions. Photochromism is a subject of photochemistry, which refers to molecules that are interconvertible between two structural forms with different color with at least one reaction irradiated by light.[13] The two interconverting species are isomers, and the color difference indicates different electron arrangements in the excited/ground state of the molecules. As shown in Figure 1.3, upon photon excitation, molecule A can be converted to isomer B, which can go

5

back to A on overcoming an energy barrier thermally. If the photoproduct B is kinetically inert, conversion of B back to A can only be realized by a second light stimuli.
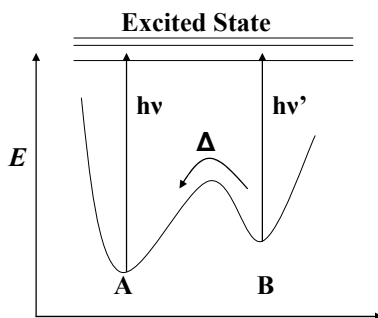
Figure 1.3 Energy profile of a photochromic system.

Some well-known photochromic molecules include spiropyrans,[14] diarylethenes,[15] and azobenzenes.[16] The extensive research interest in photochromism arises from its applications in supramolecular chemistry, data storage device, and even sunglasses in daily life.

1.2 Photophysical properties of organoboron compounds

Organoboron compounds have raised extensive research interest due to their interesting photophysical properties. They have been successfully used as electron-transport materials in OLEDs, high-efficient fluorescent emitters[17-19] and anion sensors.[20-21] There are two classes of organoboron compounds, three-coordinate and four-coordinate ones.

The geometry of the boron center is trigonal planar in three-coordinate organoboron compounds while tetrahedral in four-coordinate organoboron compounds.

As shown in Figure 1.4, the boron center in three-coordinate organoboron compounds adopts a classical sp^2-hybridization with a vacant p_π orbital. The boron center is inherently electron deficient. To prevent the vacant p_π orbital being attacked by donors such as water or oxygen, bulky substituents like the mesityl group, which can impose steric hindrance around the vacant P_π orbital, have been used to obtain many air-stable organoboron compounds. The electron-deficient triarylboron group is able to directly evolve in the photophysical process such as light emission and electron transport. Triarylboron based conjugated systems distinguished themselves as very effective and promising materials as fluorescent emitter in OLEDs, electron-transporting layer and anion sensors.

Attracts e⁻ or :L
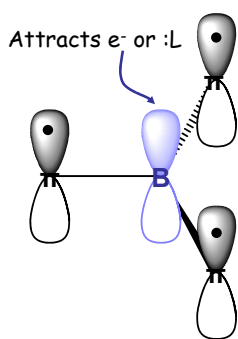
Figure 1.4 sp^2 Hybridization of boron.

The four-coordinate boron center has an extra donor compared to three-coordinate boron center. The hybridization of boron center in four-coordinate organoboron compound changes from sp^2 to sp^3 and adopts a tetrahedral geometry. The boron center in tetrahedral boron systems usually plays a structural role to constrain the chelating molecule in a planar fashion. Based on the chelate chromphore, there are mainly three types of chelation: N, N-, or N, O-, or N, C-chelate. The representative examples are shown in Figure 1.5. Molecules **1.1**, based on 8-hydroxyquinoline,[22] and **1.2**[23] are excellent candidates as emitting and electron-transporting materials in OLEDs. Boron-dipyrromethene (BODIPY) 1.3 and its analogs[24] are a class of fluorescent dyes with wide applications in imaging area. Recently reported boryl-substituted thienylthiazoles **1.4** have superior performance as electron-transporting material.[25]

R=Et, 2-Naphthy, Ph

1.1

1.2

1.3

1.4
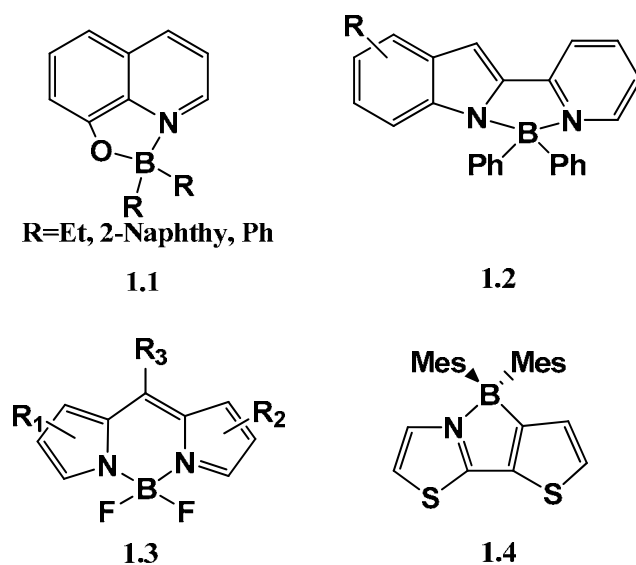
Figure 1.5 Examples of four-coordinate organoboron compounds**.**

1.2.1 Luminescent and electron-transporting triarylboron compounds

Compared to traditional luminescent organic materials, organoboron compounds have higher luminescent efficiency, which can be attributed to the intramolecular charge transfer process with a large Stokes shift that can decrease the intramolecular fluorescence self-quenching. Moreover, the bulky mesityl protecting group not only protects the boron center from moisture, but also prevents intermolecular stacking and interaction in the solid state, leading to intense solid-state emission.[26, 27] The electron-accepting nature of boron center renders the possibilities of triaryboron compounds serving as electron-transporting materials.[17]

In order to achieve high luminescent quantum efficiency, electron-rich groups such as thiophenyl or triarylamine groups are incorporated into the π conjugated system, which can induce phenomenal intramolecular charge transfer to the electron-deficient boron center. The emission color of triarylboron compounds may be easily tuned by varying the π conjugated system or Lewis acidity of the boron center.

The design of triarylboron compounds can be roughly classified into the following three categories: incorporation of boryl group into (A) at the main chain; (B) at terminal position; (C) at the side positions of the π conjugated system.[28]
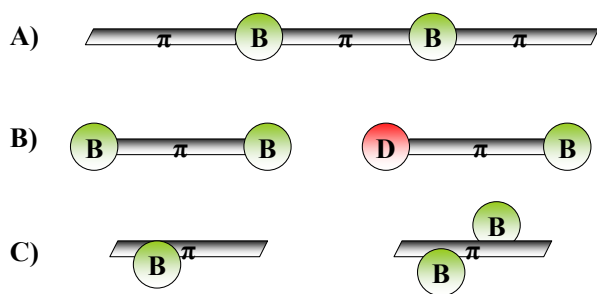
Figure 1.6 Schematic presentations of conjugation in organoboron compounds (with B representive of boron moiety, D representive of electron donating group).

Type A design is mostly found in polymer chain, with two valencies of boron center occupied in the molecular backbone.[29]

In type B, electron-deficient boryl groups are put in the terminal of π conjugated system and can extend the π conjugation. Molecules **1.5a** and **1.5b**, designed by Shirota, are excellent candidate as electron-transport materials.[17]
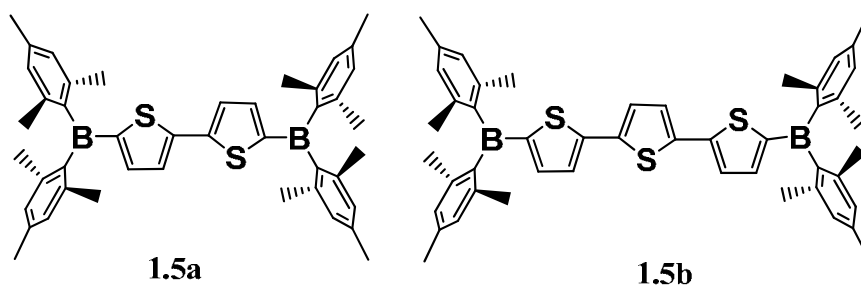
Figure 1.7 Molecules with boryl group at the terminal π conjugated system.

A donor group at the other end of the conjugated chain can induce a phenomenal intramolecular charge transfer process from an electon-donating group to a boron center. The HOMO is localized on the electron-donating moiety, while the LUMO is localized on the electron-deficient boron center. The excited state is highly polarized and can be proved by the solvent-dependent emission. The excited state can be stabilized by polar solvent, resulted in a red-shift emission relative to that in less-polar solvent.

Incorporation of a bulky boryl group at the lateral position not only extends the p_π - π^* conjugation through the short axis, but also increases the steric congestion of the aromatic main chain. 3-borylbithiophene and derivatives from the Yamaguchi group are presented in Figure 1.8, which exhibit an unusually large Stokes shift and intense solid state emission. Through the modification of the terminal π conjugated system, full color emission was achieved when an oligothiophene was employed as the electron-donating skeleton.[30]
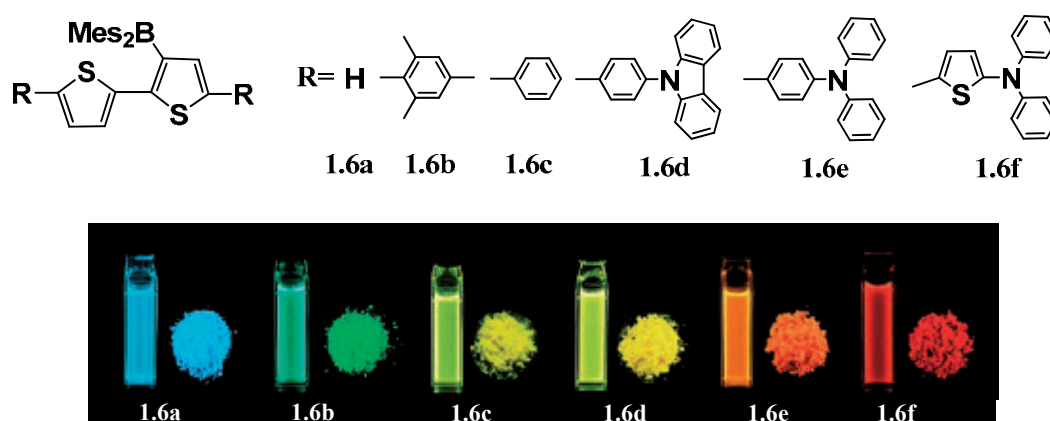
Figure 1.8 Fluorescence in solid state and THF solution of 3-borylbithiophene derivatives.

11

1.2.2 Triarylboron compounds as fluoride sensors

1.2.2.1 Background

The selective recognition of anions has raised much research attention due to its potential applications in anion separation technologies and in sensors. In particular, recognition of fluoride is of great current interest.

Fluoride is widely used for water fluoridation and in many health products, like toothpastes, associated with the prevention of tooth decay and the treatment of osteoporosis. Sodium fluoride is the most commonly used addictive in water. However, excess fluoride can cause bone and tooth damage as a result of fluorosis.[31, 32] Fluoride is also a component in nerve agents. Therefore, monitoring fluoride in water and the environment is very important.

To date, recognition of fluoride through biologically inspired systems, by virtue of hydrogen bonding or electrostatic interaction between the anionic guest (fluoride) and the receptor, has been successfully implemented mostly in organic solvents.[33] Considering that fluoride is a Lewis base, facile utilization of the interaction between Lewis acid (three-coordinate boron center) and Lewis base (fluoride) is also an attractive strategy for detection of fluoride. The Lewis acidity of three-coordinate boron is caused by the vacant p orbital of boron center which is susceptible for nucleophilic attack from anions and other donors, such as water.

For sterically protected triaryboron, Lewis bases such as Cl⁻, Br⁻, I⁻ have no interaction with boron center, due to their size and the bond strength in the order of B-F >

B-Cl > B-Br > B-I. Triarylboron compounds with bulky protecting groups around boron center have a high selectivity toward fluoride owing to steric congestion. Because of these, organoboron compounds have received extensive research interest as alternative fluoride sensors.

1.2.2.2 Design of triarylboranes as fluoride sensors

The interaction between fluoride and three-coordinate boron center results in a four-coordinate adduct which could be characterized explicitly by multinuclear ^{1}H, ^{11}B, and ^{19}F NMR spectrometry. The F-B binding events could be monitored by electrochemical fluorescence or absorption spectroscopic methods. After the fluoride complexation, the vacant P_π orbital no longer exists, leading to the disruption of $P_\pi - \pi^*$ orbital conjugation. The diminishment of the π to p_π - π^* transition band would be observed from the UV-Vis absorption spectra. In addition, the intramolecular p_π to π^* down to acceptor charge transfer process would also be disrupted causing a fluorescent intensity change.

Based on the absorption and fluorescence change, triayrlboron fluoride sensors can be classified into the following three categories: (A) Colorimetric change sensors; (B) Fluorescence turn-off sensors; (C) Fluorescence turn-on sensors.

Tris(9-anthryl)borane **1.7**, designed by Yamaguchi's group,[34] can capture fluoride in THF with a high binding constant $(2.8 \pm 0.3) \times 10^5$ M^{-1}, in comparison to smaller binding constants, ~10^3 M^{-1}, to AcO$^-$ and OH$^-$, and does not bind to Cl$^-$, Br$^-$, I$^-$ at all. As shown in Figure 1.9, the addition of fluoride caused a naked-eye distinguishable color change, from yellow to colorless, of the solution, owing to that the characteristic π to p_π

(B) band disappearing and new bands assigned to an anthyl π to π^* transition at a higher energy appearing.
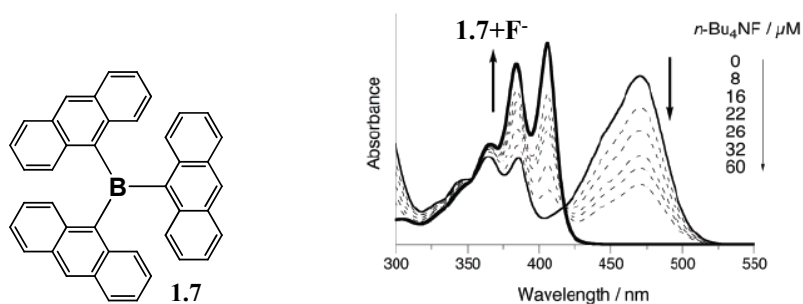
Figure 1.9 UV-Vis absorption spectral change of **1.7** (4.0×10^{-5} M) in THF upon addition of TBAF.

Since the intramolecular charge transfer originating from p_π to π^* conjugation was turned off after fluoride binding in organoboron compounds, fluorescence changes depend on the nature of the resulting LUMO. If the new LUMO still localizes over the π framework as a normal π conjugated system with a much more efficient π to π^* transition compared to the previous charge transfer transition, the fluorescence change would be expected as turn-on, which has a higher fluorescence intensity than before. Otherwise, the intramolecular charge-transfer fluorescence would be quenched after the addition of fluoride, behaving as turn-off sensors.[35, 36]

One example of "turn-on" sensors for F⁻ was reported by Yamaguchi and co-workers.[37] The system is based on functionalized dibenzoborole derivatives, which showed a dramatic fluorescence intensity increase and fluorescence color change in the

14

visible region upon the addition of F⁻. The original LUMO dominated by p_π-π^* conjugation is turned off with fluoride binding to the boron center. The quantum efficiency of triarylboron molecule **1.8** in Figure 1.10 increased from 0.02 to 0.42 after fluoride binding, along with color change from red to blue.
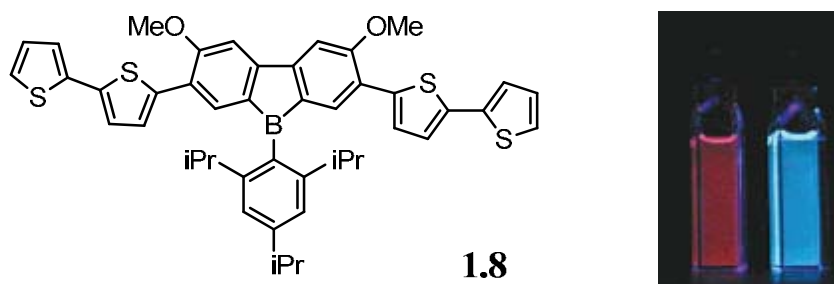
Figure 1.10 Left: molecule **1.8**; Right: Fluorescence change upon addition of TBAF in THF (left: before addition of TBAF; right: after addition of TBAF).

The previous triaryboron compounds all showed a high selectivity for fluoride in organic solvents; however, they failed to capture fluoride in aqueous media, which is more practically useful. The main challenge for detection of fluoride in water is the high hydration enthalpy ($\Delta H° = -504$ kJ/mol), which can be attributed to the small size and hydrogen bonds with water. To conquer this problem, the key factor is to enhance the Lewis acidity of the boron center. Even though it is well-known that B(C₆F₅)₃ ($E_{1/2}^{red} = \sim$ -1.17 V vs FeCp₂$^{+/0}$)[5a] possesses the strongest Lewis acidity, it is unstable toward air and moisture. For practical use as stable fluoride sensor, the incorporation of bulky groups such as the mesityl is inevitable. The only drawback is the electron-donating nature of the

mesityl moiety that diminishes the Lewis acidity of the boron center. Other ways to enhance the Lewis acidity of boron center include incorporation of electron-withdrawing groups like pyridine as the π-conjugated skeleton, chelation of two Lewis acidity center, and utilizing Columbic effects through cationic boranes.

Some examples from Gabbai and co-workers that demonstrate the different strategies to capture F⁻ are shown in Figure 1.7.[38-40] Compared **1.9a**, with the chelation of two Lewis acidity centers, can greatly enhance the binding constant to 5×10^9 M^{-1} in THF and the fluoride adducts are fairly stable toward water. The Lewis acidity of **1.9b** is enhanced by the cationic phosphonium moiety. Synergetic effect from chelation, cationic boranes, and hydrogen bonding can further enhance the Lewis acidity of boron center. Compared **1.9d** is a cationic Lewis acidic borane which also possesses C-H··F-B hydrogen bonding. Among these four molecules, **1.9d** is the only one that can capture fluoride in water under biphasic conditions.
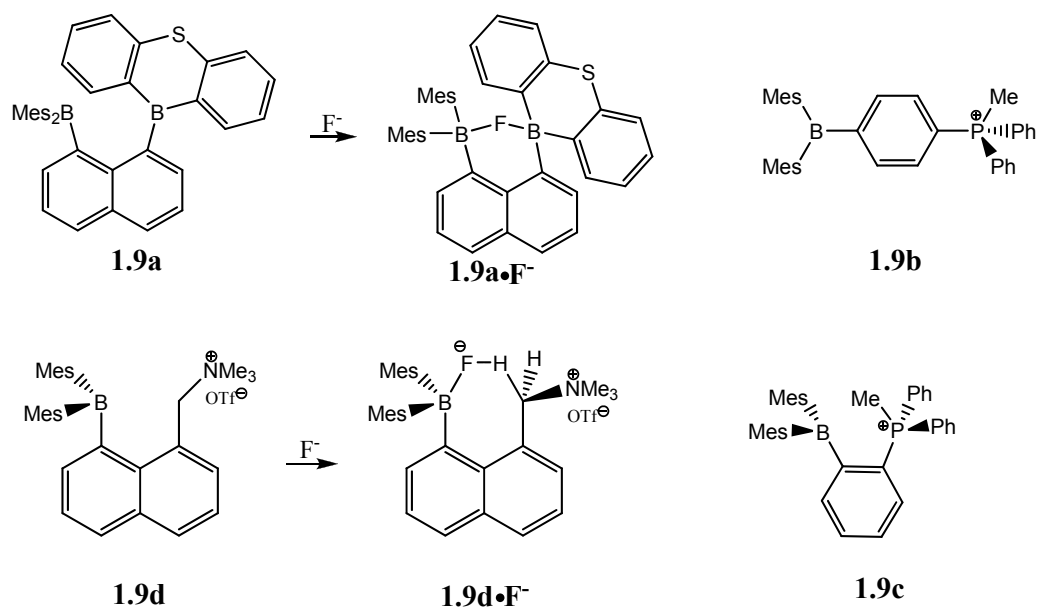
Figure 1.11 Examples organoboron compounds as fluoride sensor.

1.3 Photophysical properties of metal-modified triarylboron compounds

The previously discussed luminescent properties of organoboron compounds and their application as fluoride sensor originate from the p_π, π electronic state. To further modify the photophysical properties of organoboron compounds, one possible approach is to combine an organoboron system with an other electronic system in one molecule. Transition metal complexes with tunable redox properties and spectroscopic characteristics are especially attractive.[41, 42] Based on the binding modes, the majority of metal-containing triarylboron compounds reported to date belong to two categories: σ complexes and π complexes. The former has a metal center bound to a σ donor such as cyclopentadienyl anion that is functionalized by a triarylboron center while the latter

contains a metal ion that is bound to a π donor such as 2,2'-bipy with a conjugated triarylboron group.

Molecular systems which integrate transition metal complexes and a triarylboron moiety together have new photophysical properties, which are primarily reflected in the following aspects: the luminescence nature changes from fluorescence to phosphorescence, an increase of electroluminescence efficiency, and the enhancement of the Lewis acidity of the boron center.

Heavy metal atoms can induce efficient intersystem crossing through strong spin-orbit coupling to facilitate the harvesting of phosphorescence, which can achieve 100% electroluminescent quantum efficiency theoretically. Hence, incorporation of heavy metal atoms into organoboron compounds can greatly improve the electroluminescent efficiency.[12, 43]

On the other hand, the metal chelation to a conjugate triarylboron ligand can enhance the electron accepting ability of the boron center.[5] The great enhancement of the electron accepting ability of the boron center can be attributed to the triarylboron containing ligand σ donation to the metal center that reduces the electron density of the ligand itself, and the increased π-conjugation also effectively lowers the $\pi*$ level. Compared to the traditional fluorescent sensor, the major advantage of a phosphorescent sensor is that the phosphorescent sensor can achieve signal purification by excluding the background emissions through time-gated acquisition, due to the longer life time of phosphorescence.

Overall, different metal ions and different auxiliary ligands of the metal center have been found to have a significant impact on the photophysical and electrochemical properties of organboron systems. Examples of different types of organoboron containing metal complexes with their photophysical properties are presented briefly below.

1.3.1 Ir(III) complexes

Ir(III) complexes have been studied extensively due to their applications in the photonic area. The $5d^6$ Ir(III) complex adopts an octahedral geometry. The $5d^6$ metal ion can facilitate the mixing of singlet and triplet excited states, leading to the removal of the spin-forbidden nature of radiative relaxation from triplet excited state back to ground state. As a consequence, Ir(III) complexes show intense phosphorescence at room temperature. In particular, cyclometalated Ir(III) complexes have excellent performance as phosphors in OLEDs.[44] The cyclometalated ligands are monoanionic and can form charge-neutral and air-stable tris-ligand complexes.

To better understand the emission pathway, the phenylpyridine (ppy) cyclometalated complex Ir(ppy)$_3$ (Figure 1.12) is chosen as the illustration.
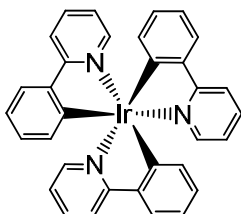
Figure 1.12 Molecular structure of Ir(ppy)$_3$.

The luminescence of Ir(ppy)$_3$ origins from the MLCT (Metal-to-Ligand-Charge-Transfer) and $^3\pi$-π^* LC (ligand-centered) electronic transition states.[45] The HOMO is principally composed of a negative-charged phenyl ring and the d orbital of metal center, while the LUMO is dominated by the pyridyl ring. In general, the emission band is blue-shifted with electron-withdrawing group on the phenyl ring, or electron-donating group on the pyridyl ring, according to the decrease of HOMO energy level or the increase of LUMO energy level. An alternative approach to tune the emission color involves the incorporation of ancillary ligands. From theoretical calculations of the molecular orbital energy and experimental results, the ancillary ligand acetylacetone (acac) has a superior performance, due to its high triplet energy level, which can suppress the non-radioactive relaxation and allow efficient phosphorescence from $^3\pi$-π^* LC and MLCT state.[46, 47]

A number of cyclometalated Ir(III) complexes functionlized by a BMes$_2$ group have been shown recently to have potential applications as phosphorescent emitters in OLEDs and fluoride sensors.

Different from the inductively electron withdrawing group (such as F), the B(Mes)$_2$ group is a strong π acceptor and also inductively donating. The electrochemical and photophysical properties of an Ir(III) complex can be changed in a unique way through modification by B(Mes)$_2$ groups. As demonstrated by Marder et al,[48] the new Ir(III) complex [Ir(ppy-X)$_2$](acac) (Figure 1.13), with an electron-deficient moiety X=B(Mes)$_2$, shows a similar $E_{1/2}^{ox}$ (0.36 V) to those of an electron donating moiety [X=N (0.31 V); X=O (0.42 V), X=S (0.41 V)]. In contrast, the Ir-B complex shows a much less negative $E_{1/2}^{red}$ value (-2.41 V) than those of Ir-N, Ir-O, Ir-S (-2.7 to -2.9 V). In the Ir-B

complex, the LUMO level is no longer dominated by the pyridyl ring but also spread over to the electron-deficient boron center and phenyl ring, while the HOMO is still dominated by the π orbital of phenyl ring and the metal d orbital. As a result, the presence of an electron-deficient boron moiety on the phenyl ring can greatly stabilize the MLCT state, which leads to the large red-shift in MLCT absorption band and emission spectra (maxima: 605 nm), relative to the un-substituted Ir(ppy)$_2$(acac) complex (520 nm). The quantum efficiency Φ of the Ir-B complex is 0.18, which was shown to be an effective phosphorescent emitter in OLEDs.
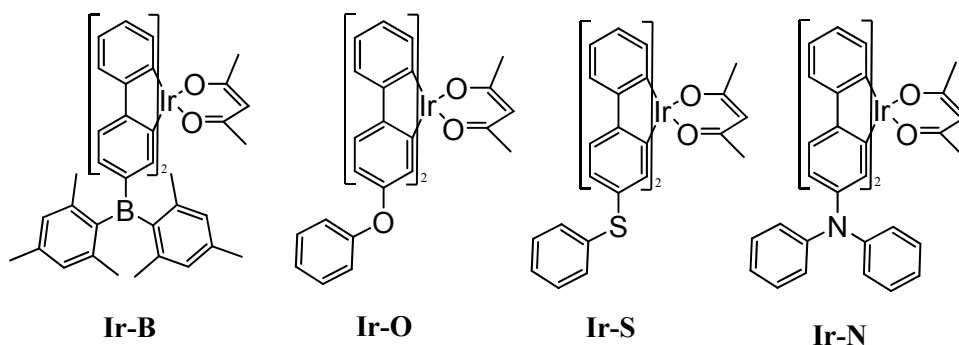
Figure 1.13 Different Ir(III) complexes Ir(ppy-X)$_2$acac (X=B, O, S, N).

Soo Young Park et al also synthesized a cyclometalated Ir(III) complex **1.10** (Figure 1.14) with the incorporation of a bulky B(Mes)$_2$ group into the ligand, which can serve as colorimetric and ratiometric fluoride ion sensor.[49] This complex and its fluoride adduct both displayed intense room temperature phosphorescence (Φ=0.57, λ_{max}=512 nm for the complex, and Φ=0.38, λ_{max}=567 nm for the complex fluoride adduct). The

phosphorescent quantum efficiency Φ maintained at 0.09 (Φ=0.06 for fluoride adduct) after equilibrium with air.
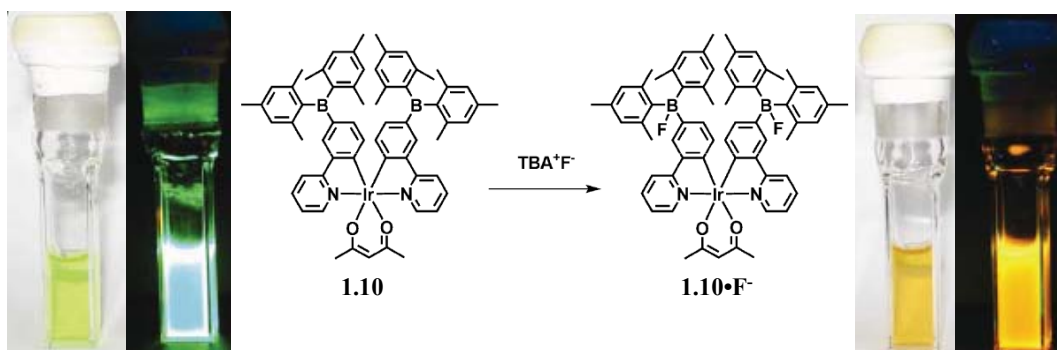
Figure 1.14 The absorption and phosphorescence change in THF of 1.10, left: before addition of TBAF, right: after addition of TBAF.

1.3.2 Pt(II) complexes

Square planar $5d^8$ Pt(II) complexes also have interesting luminescent properties as a result of the strong spin-orbital coupling, which can serve as chemosensor and vaporchromic materials and emissive dopants in OLEDs.[50-52]

In general, luminescent Pt(II) complexes contain either polypyridine ligands or cyclometalated ligands.[53, 54] The emission of Pt(II) polypyridine complexes usually originates from a MLCT transition [dπ(Pt) to π* (py)] mixed with ^{3}LC (ligand centered) transitions. The emission of cyclometalated Pt(II) complexes with ligands such as 2-phenylpyridine or 2-(2'-thienyl)pyridine, is mainly attributed to a ^{3}LC excited state with a small portion of ^{1}MLCT character.[55] The HOMO involves a mixture of phenyl (or

thienyl), Pt and electron-donating ancillary ligands, while the LUMO involves predominately the cyclometalating ligand.

Unlike octahedral Ir(III) complexes, due to its square-planar geometry Pt(II) complexes can be stacked together, which allows for d^8–d^8 metal-metal interactions as well as π-π interactions between the coordinated ligands. The d^8–d^8 metal-metal interactions can result in MMLCT (Metal-Metal-to-Ligand-Charge-Transfer) emission. When the distance between $5d^8$ Pt(II) ions is close enough, a filled Pt-Pt antibonding orbital (σ^*) forms. As shown in Figure 1.15, the electronic transition between the σ^* orbital and ligand-based π^* orbital is the origin of the MMLCT transition.[56]
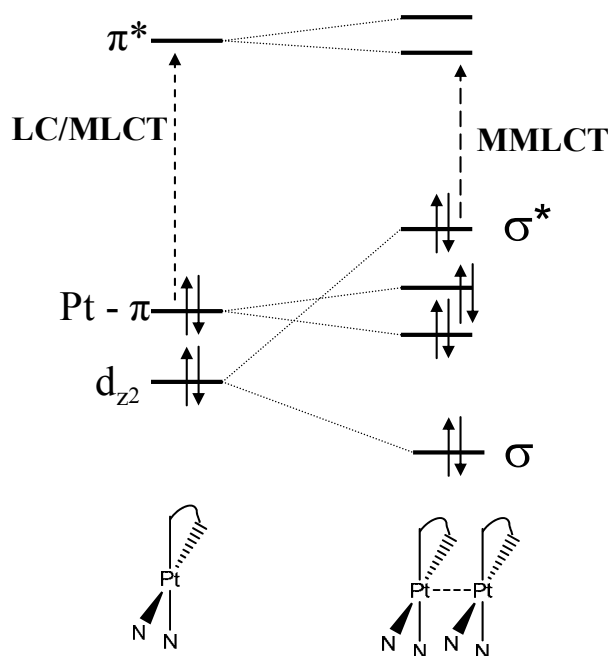
Figure 1.15 Qualitative MO schemes for mononuclear and dinuclear N, N-chelate Pt(II) complexes.[56]

The B(Mes)$_2$ functionalized Pt(II) complexes can greatly enhance the MLCT transition. One possible explanation is that the synergetic effects of Pt(II)-to-Ligand MLCT and π(aryl)-p(B) CT interactions can stabilize the MLCT state and lower the energy level of MLCT state below that of non-emissive excited d-d triplet state, leading to strong emission. In Figure 1.16, a Pt(II) complex with a N, N-chelate ligand (*N*-2-(5-BMes$_2$)pyridyl)-7-azaindole, **1.11**) from the Wang group has a much brighter emission (λ_{max} = 543 nm, τ = 25.0 μs, Φ = 0.01 in CH$_2$Cl$_2$, under N$_2$) than that of the complex with no-B(Mes)$_2$-functionalized NPA ligand.[57] N. Kitamura et al also reported the [Pt(BMes$_2$-ph-tpy)Cl]$^+$ complex **1.12a** shows room temperature emission at λ_{max}=550 nm with a quantum yield Φ=0.011, while the no-B(Mes)$_2$-functionalized [Pt(ph-tpy)Cl]$^+$ showing emission at λ_{max}=535 nm, Φ=0.0021. The quantum yield of **1.12a** is larger than the relevant value of [Pt(ph-tpy)Cl]$^+$ by a factor of 5. The more sterically congested complex **1.12b** [Pt(BMes$_2$-duryl-tpy)Cl]$^+$ with less conjugation between π(aryl)-p(B) is not emissive at all.[58]

| 1.11 | 1.12a | 1.12b |
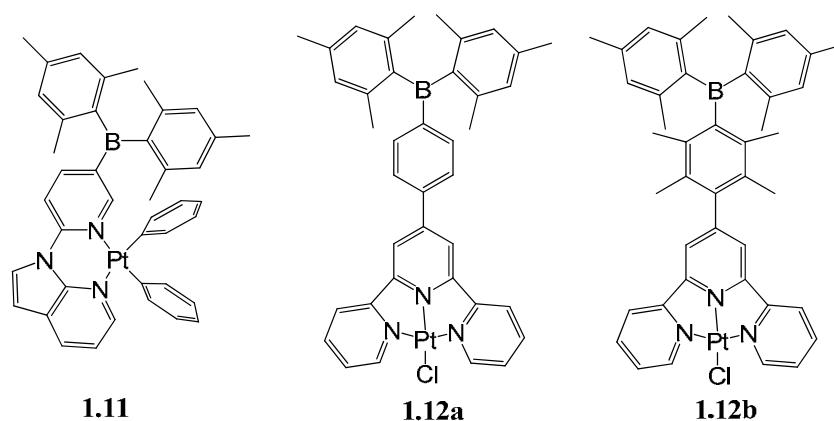
Figure 1.16 Representative structures of Pt(II) ion modified triarylboron compounds.

Fluoride sensing based on a B(Mes)$_2$ functionalized Pt(II) complex can also be visualized by either a colorimetric change or a phosphorescent change. The distinct MLCT absorption bands of Pt(II) complexes in the visible region can be quenched by the addition of fluoride ions.

Wang et al has demonstrated that the reduction peak of **1.13** [Pt(B$_2$bipy)Ph$_2$] ($E_{1/2}^{red1}$ = -1.69 V) is much more positive than that of B$_2$bipy ($E_{1/2}^{red1}$ = -1.34 V), which proved that Pt(II) chelation to the organoboron system can greatly enhance the Lewis acidity of boron center. As shown in Figure 1.17, upon addition of fluoride to **1.13** in DCM, the low-energy MLCT band was quenched, with the color changing from red to orange with 1 eq of fluoride (1F: 1complex adduct), and then yellow to colorless with more addition of fluoride (2F:1complex adduct). The complex adduct with 1 eq of fluoride is stable toward water, supporting the strong electron-accepting ability of the metal complex.[59]

1.13
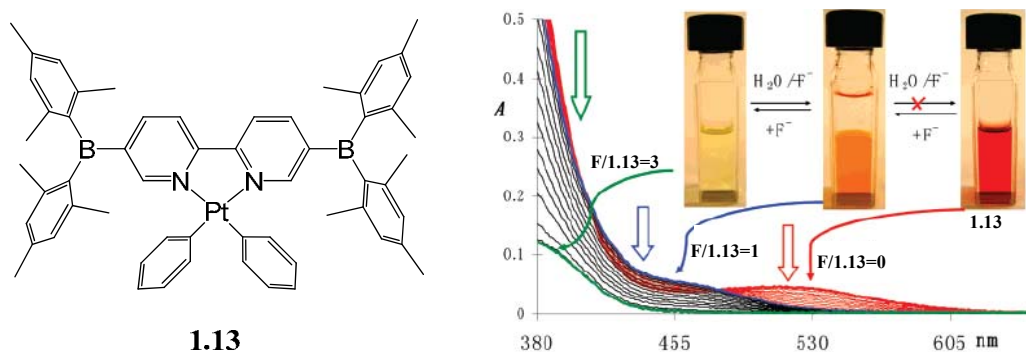
Figure 1.17 The MLCT region of the UV-Vis titration and the visual color change of **1.13** [Pt(B$_2$bipy)Ph$_2$] by TBAF in CH$_2$Cl$_2$.

1.3.3 Ferrocene-derivatised triarylboron compounds

Ferrocene is well-known for its redox activity and substituents on the cyclopentadienyl ligands alter the oxidation/reduction potential in an expected way with electron donating groups shifting the oxidative potential in the anodic direction. Boron-containing Lewis acids based around a ferrocene backbone (Figure 1.18) can be exploited for the recognition of the fluoride anion, depending on the shift of redox potential of the ferrocene moiety.[60-62]
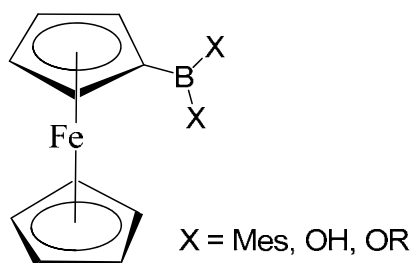
Figure 1.18 Structure of ferrocene-derivatised organboron compounds.

1.4 Photochemistry of organoboron compounds

Organoboron compounds also possess interesting photochemical properties, even though photochemistry based on organoboron moiety is not as well-developed as organic molecules, which can be attributed to that the light absorbance part is mainly localized in organic moiety of organoboron compounds.[63]

Nevertheless, there are many well-documented examples about the photochemistry of organoboron compounds. For example, Hancock and co-workers have studied the

photochemistry of some aminoboranes and anilinoboranes with a B=N double bond, which is isoelectronic with the C=C bond. Figure 1.19 shows an example of photocyclisation of anilinodimestiylboranes in the presence of iodine.[64]

R = H, Me
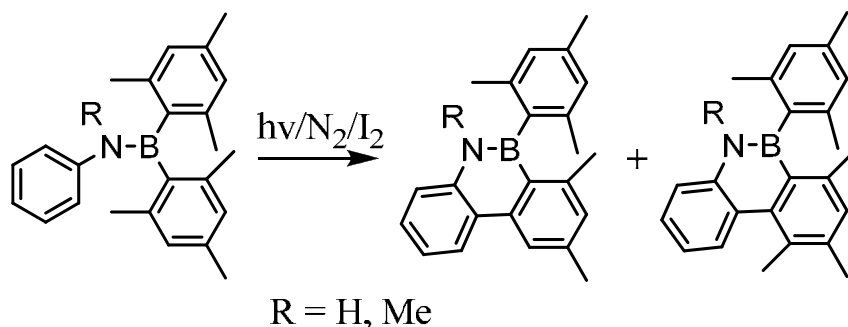
Figure 1.19 Photocyclisation of anilinodimestiylboranes in the presence of iodine.

The photolysis of tetramethylammonium (4-diphenyl)triphenylborane in oxygen-free acetonitrile resulted in a boratanorcaradiene anion, 2,5,7,7-tetraphenyl-7-boratabicyclo[4.1.0] hepta-2,4-diene, which was confirmed by X-ray crystallography.[65] The study showed new B-C, C-C bond were formed intramolecularly as presented in Figure 1.20.
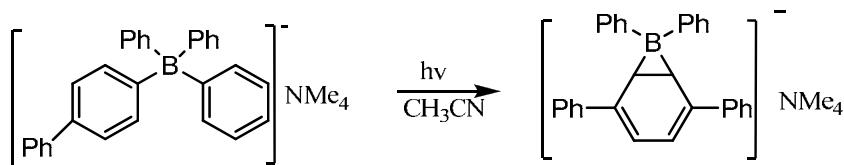
Figure 1.20 Photocylisation of tetramethylammonium(4-diphenylyl)triphenylborane in oxygen-free acetonitrile.

1.5 Metal complexes containing photochromic ligands

Generally speaking, the coupling of photochromes and metal complexes can induce electronic communications between each other, or trigger molecular self-assembly/disassembly due to the large conformational rearrangement or charge redistribution of coordinated photochromes.[66-68] Applications that will benefit from such integrated system include optical data storage, molecular machines and photoresponsive materials. Transition metals with tunable redox properties, efficient intersystem crossing between excited singlet and triplet states have a profound impact on the photochromic moiety.

Systems that promote electronic communications between photochromes and metal complexes are presented here. With an appropriate linker, the energy transfer between the ^{3}MLCT excited state involving the metal ion and the localized intraligand state on photochromes may be accomplished. Platinum-dithienylethene (DTE) complex which united two components (the Pt-terpyridyl and photochrome dithienylethene) through an acetylide linker (Figure 1.21) from Wolf's group demonstrated this type of energy transfer from the metal moiety to the DTE photochrome.[69] Ring closing of the photochrome DTE can be achieved by irradiation at a wavelength (λ_{max} = 465 nm) belonging to the MLCT band of the Pt-(trpy) component, without direct irradiation with UV light (302 nm) where the DTE moiety absorbs.
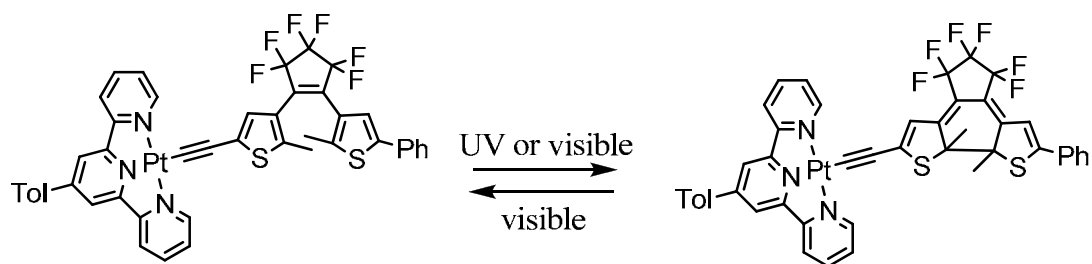
Figure 1.21 Photochromism of Platinum-DTE complex.

De Cola and co-workers have reported a dinulear complex containing dithienylethene as the spacer (Figure 1.22).[70] The ring closing behavior of dithienylethene in the ruthenium complex has a better quantum efficiency than that of the osmium complex. This difference can be attributed to the fact that the lowest excited state in the ruthenium complex is ^{3}LC, which is involved in the photo-isomerization pathway, while in the osmium complex, the lowest excited state is ^{3}MLCT, where the energy dissipated as phosphorescence.
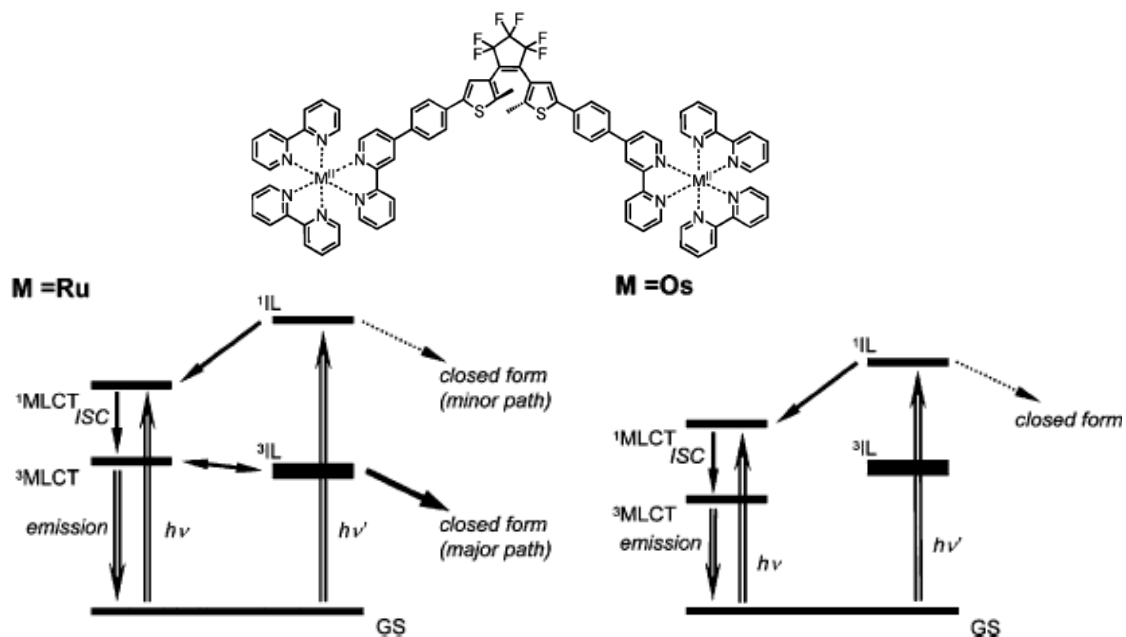
Figure 1.22 Energy diagram of Ru and Os dinuclear complex linked with dithienylethene.[70]

1.6 Scope of the thesis

From the above discussions it is evident that organoboron compounds and metal complexes have intriguing photophysical and photochemical properties. The aim of this thesis is to explore the photophycial and photochemical properties of triarylboron and tetrahedral boron compounds and their metal complexes. Bulky triarylborane group modified phenylpyridine (ppy) and Pt (II) were chosen as the molecular skeleton and metal center individually, based on the following considerations: (1) Pt(II) complexes with ppy ligands impose interesting luminescent properties; (2) intramolecular C-H bond

activation on a Pt(II) center allows easy chelation of Pt(II) to ppy at ambient temperature; (3) the N, C-chelation site of ppy is also open for modification with another four-coordinate boryl group.

In Chapter 2, two constitutional isomers of (BMes$_2$)phenylpyridine, one with BMes$_2$ group on phenyl ring while the other one with that on pyridine ring were designed and synthesized. Their impacts on Pt(II) complexes were studied. The Pt(II) complexes with different ancillary ligands were also studied. In Chapter 3, the synthesis of a new hybrid diboron molecule (5-BMes$_2$-py-2-phenyl)BMes$_2$ which contains both 3-coordinate and 4-coordinate triarylboron groups is described. Such design leads to our discovery of unusual photochromic properties of 4-coordinate organoboron compounds, which were investigated in detail. In Chapter 4, the photochromic behavior of N, C-chelate 4-coordinate organoboron-coupled Pt(II) complex was studied. In the final Chapter 5, a general summary of the work in this thesis with key conclusions and proposed future work is presented.

1.7 References

(1) Kalinowski, J. *Opt. Mater.* **2008**, *30*, 792.

(2) Ermakov, O. N.; Kaplunov, M. G.; Efimov, O. N.; Stakharny, S. A. *Proc. of SPIE* **2007**, *6636*, 1.

(3) Domaille, D. W.; Que, E. L.; Chang, C. L. *Nat. Chem. Biol.* **2008**, *4*, 168.

(4) Burnworth, M.; Rowan, S. J.; Weder, C. *Chem. Eur. J.* **2007**, *13*, 7828.

(5) Knapton, D.; Burnworth, M.; Rowan, S. J.; Weder, C. *Angew. Chem. Int. Ed.* **2006**, *45*, 5825.

(6) Aberle, A. G (Ed.), Special Issue "Recent Advances in Solar Cells", *Advances in OptoElectronics*, vol. *2007*, Hindawi Publishing Corp., Egypt, **2007**.

(7) Mockus, N. V.; Rabinovich, D.; Petersen, J. L.; Rack, J. J. *Angew.Chem., Int. Ed.* **2008**, *47*, 1458–1461.

(8) Yam, V. W.-W.; Ko, C.-C.; Zhu, N. *J. Am. Chem. Soc.* **2004**, *126*, 12734–12735.

(9) Anslyn, E. V.; Dougherty, D. A. In *Mordern Physical Organic Chemistry*.

(10) Balzani, V.; Bergamini, G.; Campagna, S.; Puntoriero, F. *Top. Curr. Chem.* **2007**, *280*, 1.

(11) L. Pavia, D.; M. Lampman, G.; S. Kriz, G. In *Introduction To Spectroscopy*; Brooks/Cole: Washington, 2001.

(12) Yersin, H., Ed. In *Highly Efficient OLEDs with Phosphorescent Materials;* Wiley-VCH: Weinheim, Germany, 2008.

(13) Balzani, V.; Credi, A.; Venturi, M. In *Molecular Devices and Machines*; Wiley-vch: Weinheim, 2003.

(14) Berkovic, G.; Krongauz, V.; Weiss, V. *Chem. Rev.*, **2000**, *100*, 1741.

(15) Bouas-Laurent, H.; Durr, H. *Pure Appl. Chem.*, **2001**, *73*, 639.

(16) Shinkai, S. In *Molecular Switches (Ed.: B.L. Feringa)*, Wiley-VCH, 2001, p. 309.

(17) Noda, T.; Shirota, Y.; *J. Am. Chem. Soc.* **1998**, *120*, 9714.

(18) Doi, H.; Kinoshita, M.; Okumoto, K.; Shirota, Y. *Chem. Mater*. **2003**, *15*, 1080.

(19) Jia, W. L.; Bai, D. R.; McCormick, T.; Liu, Q. D.; Motala, M.; Wang, R.; Seward, C.; Tao, Y.; Wang, S. *Chem. Eur. J*. **2004**, *10*, 994.

(20) Yamguchi, S.; Shirasaka, T.; Akiyama, S.; Tamao, K. *J. Am. Chem. Soc*. **2002**, *124*, 8816.

(21) Hudnall, T. W.; Chiu, C. W.; Gabbai, F. P. *Acc. Chem. Res*. **2009**, *42*, 388.

(22) Wu, Q.; Esteghamatian, M.; Hu, N. X.; Popovic, Z.; Enright, G.; Tao, Y.; D'Iorio, M.; Wang, S. *Chem. Mater*. **2000**, *12*, 79.

(23) Liu, Q.; Mudadu, M. S.; Schmider, H.; Thummel, R.; Tao, Y.; Wang, S. *Organometallics*. **2002**, *21*, 4743.

(24) Speiser, S. *Chem. Rev.* **1996**, *96*, 1953.

(25) Wakamiy, A.; Taniguchi. T.; Yamaguchi, S. *Angew. Chem. Int. Ed*. **2006**, *45*, 3170.

(26) Zhao, C. H.; Wakamiya, A.; Lnukai, Y.; Yamaguchi, S. *J. Am. Chem. Soc*. **2006**, *128*, 15934.

(27) Li, H.; Sundararaman, A.; Venkatasubbaiah, K.; Jakle, F. *J. Am. Chem. Soc*. **2007**, *129*, 5792.

(28) Elbing, M.; Bazan, G. C. *Angew. Chem. Int. Ed*. **2008**, *47*, 834.

(29) Zhao, C. H.; Wakamiya, A.; Yamaguchi, S. *Macromolecules*. **2007**, *40*, 3898.

(30) Wakamiya, A.; Mori, K.; Yamaguchi, S. *Angew. Chem. Int. Ed*. **2007**, *46*, 4273.

(31) Matsuo, S.; Kiyomiya, K.; Kurebe, M. *Arch. Toxicol*. **1998**, *72*, 798.

(32) Briancon, D. *ReV. Rheum.* **1997**, *64*, 78.

(33) Gale, P. A. *Coord. Chem. ReV*. **2001**, *213*, 79.

(34) Yamaguchi, S.; Akiyama, S.; Tamao, K. *J. Am. Chem. Soc*. **2001**, *123*, 11373.

(35) Bai, D. R.; Liu, X. Y.; Wang, S. *Chem. Eur. J*. **2007**, *13*, 5713.

(36) Liu, X. Y.; Bai, D. R.; Wang, S. *Angew. Chem. Int. Ed*. **2006**, *45*, 5475.

(37) Yamaguchi, S.; Shirasaka, T.; Akiyama, S.; Tamao, K. *J. Am. Chem. Soc*. **2002**, *124*, 8816.

(38) Hudnall, T. W.; Melaimi, M.; Gabbai, F. P. *Organic Letters*. **2006**, *8*, 2747.

(39) Chase, P. A.; Henderson, L. D.; Piers, W. E.; Parvez, M.; Clegg, W.; Elsegood, M. R. J. *Organometallics*. **2006**, *25*, 349.

(40) Sole, S.; Gabbai, F. P. *Chem. Commun.* **2004**, *11*, 1284.

(41) Michalec, J. F.; Bejune, S. A.; MaMillin, D. R. *Inorg. Chem*. **2000**, *39*, 2708.

(42) Bebby, A.; Bettington, S.; Samuel, I. D.W.; Wang, Z. *J. Mater. Chem*. **2003**, *13*, 80.

(43) Yersin, H. *Top. Curr. Chem*. **2004**, *241*, 1.

(44) Lamansky, S.; Djurovich, P.; Murphy, D.; Adbel-Razzaq, F.; Lee, H. E.; Adachi, C.; Burrows, P. E.; Forrest, S. R.; Thompson, M. E. *J. Am. Chem. Soc*. **2001**, *123*, 4304.

(45) Sajoto, T.; Djuorvich, P.; Tamayo, A.; Yousufuddin, M.; Bau, R.; Tompson, M. E. *Inorg. Chem*. **2005**, *44*, 7992.

(46) Liu, Z.; Bian, Z.; Li, Z.; Nie, D.; Huang, C. *Inorg. Chem*. **2008**, *47*, 7849.

(47) Zhao, Q.; Li, L.; Li, F.; Yu, M.; Liu, Z.; Huang, C. *Chem. Commun*. **2008**, 685.

(48) Zhou, G.; Ho, C. L.; Wong, W. Y.; Wang, Q.; Ma, D.; Wang, L.; Lin, Z.; Marder, T. B.; Beeby, A. *Adv. Funct. Mater*. **2008**, *18*, 499.

(49) You, Y.; Park, S. Y. *Adv. Mater*. **2008**, *20*, 3820.

(50) Kui, S. C. F.; Chui, S. S. Y.; Che, C. M.; Zhu, N. *J. Am. Chem. Soc.* **2006**, *128*, 8297.

(51) Kunugi, Y.; Mann, K. R.; Miller, L. L.; Exstrom, C. L. *J. Am. Chem. Soc.* **1998**, *120*, 589.

(52) Yam, V. W.; Chan, K, H.; Wong, K. M.; Chu, B. W. *Angew. Chem. Int. Ed*. **2006**, *45*, 6169.

(53) McGarrah, J. E.; Eisenberg. R. *Inorg. Chem*. **2003**, *42*, 4355.

(54) N. Kozhenvnikov, D.; N. Kozhevnikov, V.; M. Ustinova, M.; Santoro, A.; W. Bruce, D.; Koenig, B.; Czerwieniec, R.; Fischer, T.; Zabel, M.; Yersin, H. *Inorg. Chem*. **2009**, *48*, 4179.

(55) Brooks, J.; Babayan, Y.; Lamansky, S.; Djurovich, P.; Tsyba, I.; Bau, R.; Tompson, M. E. *Inorg. Chem*. **2002**, 41, 3055.

(56) Ma, B; Li, J.; Djurovich, P. I.; Yousufuddin, M.; Bau, R.; Tompson, M. E. *J. Am. Chem. Soc.* **2005**, *127*, 28.

(57) Zhao, S. B.; McCormick, T.; Wang, S. *Inorg. Chem.* **2007**, 46, 10965.

(58) Sakuda, E.; Funahashi, A.; Kitamura, N. *Inorg. Chem.* **2006**, 45, 10670.

(59) Sun, Y.; Ross, N.; Zhao, S. B.; Huszarik, K.; Jia, W. L.; Wang, R. Y.; Wang, S., *J. Am. Chem. Soc.* **2007**, 129, 7510.

(60) Broomsgrove, A. E. J.; Addy, D. A.; Bresner, C.; Fallis, I. A.; Thompson, A. L.; Aldridge, S. *Chem. Eur. J*. **2008**, 14, 7525.

(61) Day, J. K.; Bresner, C.; Fallis, I. A.; Doi, L. L.; Watkin, D. J.; Coles, S. J.; Male, L.; Hursthouse, M. B.; Aldridge, S. *Dalton. Trans*. **2007**, 3486.

(62) Aldridge, S.; Bresner, C.; Fallis, I. A.; Coles, S. J.; Hursthouse, M. B. *Chem. Commn*. **2002**, 740.

(63) Pelter, A.; Pardasani, R. T.; Pardasani, P. *Tetrahedron*. **2000**, *56*, 7339.

(64) Hancock, K. G.; Kramer, J. D. *J. Am. Chem. Soc.* **1973**, *95*, 3425.

(65) Wilkey, J. D.; Schuster, G. B. *J. Org. Chem*. **1987**, *52*, 2117.

(66) Kurihara, M.; Nishihara, H. *Coord. Chem. Rev.*, **2002**, *226*, 125.

(67) Nishihara, N. in *Inorganic Photochromism*, ed. Fukuda, Y.; Kodansha, Springer, 2007, pp. 239–257;

(68) Kume, S.; Nishihara, H. *Struct. Bonding*, **2007**, *123*, 79.

(69) Robert, M. N.; Nagle, J. K.; Finden, J. G.; Branda, N. R.; Wolf, M. O. *Inorg. Chem.* **2009**, 48, 19.

(70) Jukes, R. T. F.; Adamo,V.; Hartle, F.; Belser, P.; De Cola, L. *Inorg.Chem.*, **2004**, *43*, 2779.

Chapter 2

Impact of Constitutional Isomers of (BMes$_2$)phenylpyridine on Structure, Stability, Phosphorescence, and Lewis Acidity of Mononuclear and Dinuclear Pt(II) Complexes

2.1 Introduction

Conjugated triarylboron compounds are known to display unique photophysical properties due to the p_π to π^* conjugation through the vacant p orbital on the boron center. Incorporation of a metal ion in the triarylboron compounds can lead to ambient temperature phosphorescence, high Lewis acidity and visual, electrochemical and phosphorescent sensors for anions.

Among the transition metal complexes, luminescent square-planar Pt (II) complexes are quite interesting, due to their potential applications as vapochromic materials, and photochemical devices for converting light to chemical energy and emissive dopants in OLEDs. In addition to *N,N*-chelate ligands,[1] *N,C*-chelate Pt(II) complexes based on phenylpyridine (ppy)[2] or *N*-(2-py)-7-azaindole (NPA)[3] functionalized by a BMes$_2$ group have been reported.

The ppy chelate chromophore and its derivatives are most effective in producing highly emissive Ir(III) phosphorescent compounds.[4] Several Ir(III) complexes based on BMes$_2$ functionalized ppy (*p*-B-ppy, *m*-B-ppy) and the closely related pq (*p*-B-pq) molecule (Figure 2.1) have been reported recently and used successfully either as a phosphorescent emitter in OLEDs and a sensor for fluoride ions.[2] Notably, these

previously reported ppy derivatives all have the BMes$_2$ group at the phenyl ring, instead of the pyridyl or quinoline ring, perhaps due to the relative easy functionalization of the phenyl ring, compared to the pyridyl or quinoline ring. Our group have reported recently that the direct attachment of a BMes$_2$ group to a pyridyl ring (e.g. 2,2-bipy) can greatly enhance its Lewis acidity.[1c, 1d] Hence, the B-ppy constitutional isomers with a BMes$_2$ group attached on the pyridyl ring such as *p*-ppy-B, shown in Figure 2.1, are worthy candidates for investigation.
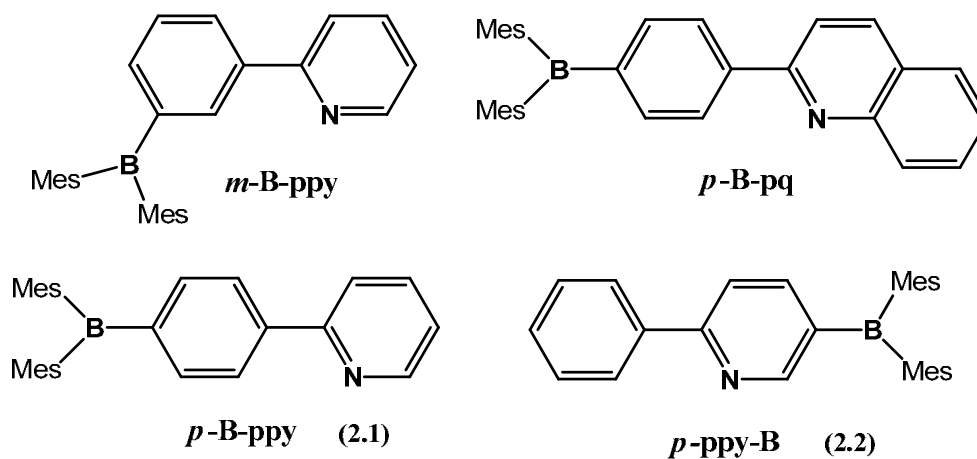
Figure 2.1 Structures of general N, C-chelate Ligands.

Based on these considerations, we have synthesized ligand **2.1** (*p*-ppy-B) and compared its properties to that of ligand **2.2** (*p*-B-ppy) shown in Figure 2.1, and a series of *N, C*-chelate Pt(II) complexes based on these two ligands shown in Figure 2.2. *N, C*-chelate Pt(II) complexes based on ppy and derivative ligands are known to display mostly

[3]LC phosphorescence.[5] The inclusion of the BMes$_2$ group on the ppy ligand would allow the direct observation of its impact on MLCT transitions and the possible enhancement of MLCT phosphorescence. The impact of the isomers of *p*-B-ppy and *p*-ppy-B on the properties of the metal complexes will be examined. To facilitate our investigation, Pt(II) complexes with different ancillary ligands such as DMSO and pyridine were prepared and examined. In addition, to examine the impact of the *p*-B-ppy and *p*-ppy-B ligands on possible electronic communication between two boron centers via a conjugated Pt$_2$ unit, dinuclear Pt(II) complexes with 4,4'-bipyridine as the bridging/ancillary ligand were also prepared and investigated. The anion binding ability of the new Pt(II) complexes was studied through UV-Vis, phosphorescence and NMR spectroscopic methods.

2.1a, L = DMSO   2.2a, L = DMSO
2.1b, L = py   2.2b, L = py

2.1c, R$_1$ = BMes$_2$; R$_2$ = H
2.2c, R$_1$ = H; R$_2$ = BMes$_2$
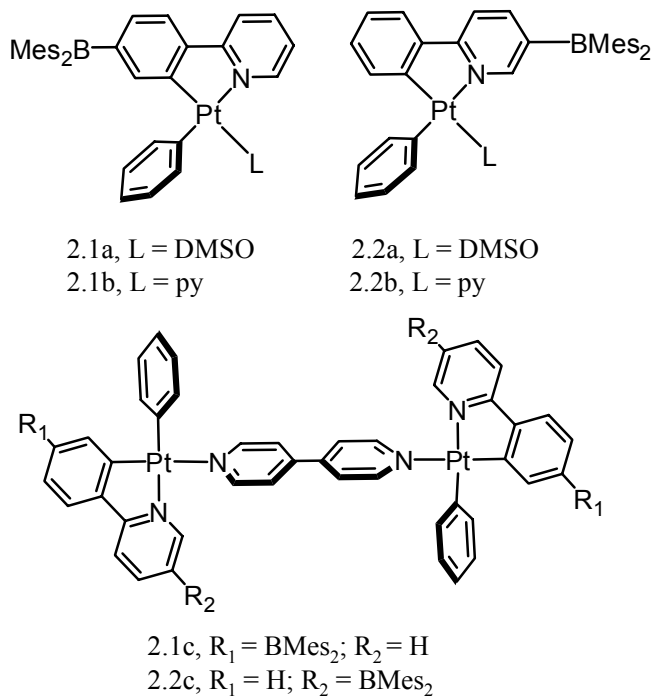
Figure 2.2 Structures of metal complexes, **2.1a**, **2.1b**, **2.1c**, **2.2a**, **2.2b**, **2.2c.**

2.2 Experimental

2.2.1 General considerations

All reactions were performed under N_2 with standard Schlenk techniques unless otherwise noted. All starting materials were purchased from Aldrich Chemical Co. and used without further purification. DMF, THF, Et_2O, and hexanes were purified using an Innovation Technology Co. solvent purification system. CH_2Cl_2 was freshly distilled over P_2O_5 prior to use. Deuterated solvents were purchased from Cambridge Isotopes and were used as received without further drying. NMR spectra were recorded on Bruker Avance 400 or 500 MHz spectrometers. High-resolution mass spectra were obtained from a Waters/Micromass GC-TOF EI-MS spectrometer, which was internally calibrated before use. Cyclic voltammetry was performed using a BAS CV-50W analyzer with a scan rate of 100 mV/s to 1 V/s and a typical concentration of 0.003 M in DMF using 0.10 M tetrabutylammonium hexafluorophosphate (TBAP) as the supporting electrolyte. A conventional three-compartment electrolytic cell consisting of a Pt working electrode, a Pt auxiliary electrode, and a Ag/AgCl reference electrode were employed using the ferrocenium/ferrocene couple as the standard ($E_{1/2}$ = 0.55 V in DMF). UV-Vis spectra were recorded on an Ocean Optics UV-visible spectrometer. Excitation and emission spectra were recorded on a Photon Technologies International QuantaMaster model C-60 spectrometer. Emission lifetimes were measured on a Photon Technologies International Phosphorescent spectrometer (Time-Master C-631F) equipped with an Xenon flash lamp and digital emission photon multiplier tube using a band pathway of 5 nm for excitation

and 2 nm for emission. [PtPh$_2$(DMSO)$_2$] was synthesized according to the previous report.[6]

2.2.2 Synthesis of 2-(4-bromophenyl) pyridine

2-(4-Bromophenyl) pyridine is a previously known compound.[7] The procedure described here for this molecule is different from the previously reported one. To a stirredTHF(30 mL) solution of 1 4-dibromobenzene (4 g, 16.9 mol) at -78 °C was added dropwise an n-BuLi solution (1.6 M; 11.6 mL, 18.6 mol) over 2 min. The resulting solution with white precipitates was stirred for 1 h at -78 °C, and a B(OMe)$_3$ solution (30 mmol, 3.3 mL) was then added. After stirring at -78 °C for 1 h, the resulting transparent solution was warmed to ambient temperature and stirred overnight. A saturated NH$_4$Cl solution (20 mL) was added. After extraction of the aqueous layer with Et$_2$O (2×30 mL), the organic layer was dried with Na$_2$SO$_4$. After removal of the solvent, the residual 4-bromophenylboronic acid was used in next step without further purification. A mixture of toluene (60 mL), ethanol (20 mL), and water (20 mL) was stirred and purged by nitrogen for 1 h. 2-Bromopyridine (1.58 g, 10 mmol), 4-bromophenylboronic acid (2.00 g, 10 mmol), Pd(PPh$_3$)$_4$ (0.31 g, 0.25 mmol), and NaOH (2.5 g, 62.5 mmol) were added to the mixed solvents. The mixture was stirred at room temperature for 2 days. The aqueous layer was separated and extracted with CH$_2$Cl$_2$ (3×30 mL). The combined organic layers were dried over Na$_2$SO$_4$, and the solvents were evaporated under reduced pressure. Purification of the

crude product by column chromatography (CH$_2$Cl$_2$/hexane, 1:1) afforded the product 2-(4-bromophenyl)pyridine as a white solid in 51% yield (0.68 g).

2.2.3 Synthesis of 2-(4-BMes$_2$-Ph)-Pyridine (2.1)

To a stirred THF solution of 2-(4-bromophenyl)pyridine (0.60 g, 2.3 mmol) at -78°C was added dropwise via a syringe an n-BuLi solution (1.60 M) (1.5 mL, 2.4 mmol) over 2 min. The resulting bright yellow solution was stirred for 1h at -78°C, then a solution of dimesitylboron fluoride (0.75 g, 90%, 2.5 mmol) in Et$_2$O was quickly added. The reaction mixture was kept at -78 °C for another 1h and then allowed to reach ambient temperature and stirred overnight. After the removal of the solvent, purification of the crude product by column chromatography (CH$_2$Cl$_2$/hexane, 2/1) afforded the **2.1** as a white solid in 81% yield. ^{1}H NMR (400 MHz, CDCl$_3$, 25°C, δ, ppm): 8.73 (d, J = 6.0 Hz; 1H), 8.99 (d, J = 8.0 Hz; 2H), 7.78 (m; 3H), 7.65 (d; J = 8.4 Hz; 2H), 7.26 (dd; 1H), 6.85 (s; 4H), 2.34 (s, 6H), 2.05 (s, 12H). ^{13}C{^{1}H}NMR (100 MHz, CDCl$_3$, δ, ppm): 157.53, 150.12, 146.78, 142.67, 142.06, 141.19, 139.05, 137.11, 137.05, 128.52, 126.73, 122.78, 121.32, 23.78, 21.55. HRMS: calcd for C$_{29}$H$_{31}$BN [M]$^+$: m/z 404.2549, found 404.2548.

2.2.4 Synthesis of 5-BMes$_2$-2-ph-pyridine (2.2)

3-Bromo-2-phenylpyridine is a previously known molecule.[8] The synthetic method we employed is different from the literature procedure, namely, via Suzuki coupling of phenylboronic acid and 2,5-dibromopyridine at ambient temperature in a similar manner

as described for the synthesis of 2-(4-bromophenyl)pyridine. 5-BMes$_2$-2-Ph-pyridine was obtained by adding dimesitylboron fluoride after lithiation of 3-bromo-2-phenylpyridine in diethyl ether at -78 °C in the same manner as for the synthesis of **2.1**. Purification of the crude product by column chromatography (CH$_2$Cl$_2$/hexane, 1/1) afforded **2.2** as a white solid in 46% yield. ^{1}H NMR (400 MHz, CDCl$_3$, 25°C, δ, ppm): 8.75 (s; 1H), 8.12 (d, J = 7.2 Hz; 2H), 7.84 (dd, J = 8.0 Hz, J = 1.6 Hz; 1H), 7.75 (d; J = 8.0 Hz; 1H), 7.48 (m; 3H), 6.86 (s; 4H), 2.33 (s, 6H), 2.06 (s, 12H). ^{13}C{^{1}H}NMR (100 MHz, CDCl$_3$, δ, ppm): 159.81, 157.51, 144.79, 141.06, 139.46, 139.25, 129.90, 129.10, 128.70, 127.50, 120.07, 116.91, 23.85, 21.53. HRMS: calcd for C$_{29}$H$_{31}$BN [M]$^+$: m/z 404.2549, found 404.2552.

2.2.5 Synthesis of Pt(p-B-ppy)Ph(DMSO) (2.1a)

To a stirred THF (20 mL) solution of [PtPh$_2$(DMSO)$_2$] (96 mg, 0.19 mmol) was added p-B-ppy (80 mg, 0.20 mmol). The mixture was stirred at 50°C for 6 h and the solvent was removed under reduced pressure. Yellow needle crystals of **2.1a** were obtained from hexane/CH$_2$Cl$_2$ (65% yield). ^{1}H NMR (500 MHz, CD$_2$Cl$_2$, 25°C, δ, ppm): 8.69 (d, J = 5.5 Hz; 1H, py), 7.94 (m; 2H, py), 7.60 (d, J = 7.5 Hz; 1H, py), 7.28 (m; 4H, Ph), 6.75 (m; 8H), 2.91 (s; 6H, *Me*-DMSO), 2.34 (s, 6H, *p-Me*-Mes), 1.93 (s, 12H, *o-Me*-Mes). ^{13}C{^{1}H}NMR (100 MHz, CD$_2$Cl$_2$, δ, ppm): 165.16, 151.94, 151.85, 149.44, 146.62, 144.47, 140.56, 139.02, 138.34, 137.31, 133.22, 128.32, 128.08, 123.54, 122.82, 122.62,

119.87, 44.16, 23.43, 21.32. Anal. calcd for $C_{37}H_{40}BNOPtS$: C 59.04, H 5.36, N 1.86; found: C 59.15, H 5.43, N 1.92.

2.2.6 Synthesis of Pt(*p*-ppy-B)Ph(DMSO) (2.2a)

To a stirred THF (20 mL) solution of [PtPh$_2$(DMSO)$_2$] (96 mg, 0.19 mmol) was added 5-BMes$_2$-2-ph-py (80 mg, 0.20 mmol). The mixture was stirred at 50°C for 6 h and the solvent was removed under reduced pressure. Bright yellow needle crystals of **2.2a** were obtained from hexane/CH$_2$Cl$_2$ (60% yield) under nitrogen. ^{1}H NMR (500 MHz, CD$_2$Cl$_2$, 25°C, δ, ppm): 9.57 (s; 1H, py), 7.94 (d, J= 8.0 Hz; 1H, py), 7.86 (d, J = 8.0 Hz; 1H, py), 7.71 (d, J = 7.5 Hz; 1H, *py*-Ph), 7.48 (d, satellite, J = 8.0 Hz, J_{Pt-H} = 66.0 Hz; 2H, *o*-ph), 7.09 (m; 3H, *py*-Ph), 7.01 (m; 2H, Ph), 6.90 (s; 4H, Mes), 6.68 (d, satellite, J = 7.5 Hz, J_{Pt-H} = 65.0 Hz; 1H, Ph), 2.72 (s; 6H, *Me*-DMSO), 2.35 (s; 6H, *o-Me*-Mes), 2.10 (s, 12 H, *p-Me*-Mes). ^{13}C{^{1}H}NMR (100 MHz, CD$_2$Cl$_2$, δ, ppm): 167.63, 159.15, 154.10, 146.34, 146.23, 146.06, 144.21, 139.83, 138.00, 137.84, 130.49, 128.77, 128.36, 125.24, 124.39, 123.19, 118.82, 44.07, 23.78, 21.37. Anal. calcd for $C_{37}H_{40}BNOPtS$: C 59.04, H 5.36, N 1.86; found: C 59.44, H 5.83, N 1.81.

2.2.7 Synthesis of PtPh[5-B(OH)(Mes)-2-Ph-py](DMSO) (2.2a-OH)

To a THF solution (10 mL) of **2.2a** (20 mg, 0.027 mmol) was added 5 mL of toluene. The solution was kept under air and the solvent was allowed to slowly evaporate at ambient temperature. Yellow crystals of **2.2a-OH** were obtained and isolated after ~20 days in

~70% yield. ^{1}H NMR (400 MHz, DMSO-d^6, 25°C, δ, ppm): 10.67 (s; 1H, B-OH), 9.83

(s; 1H, Py), 8.06 (d, J = 8.0 Hz; 1H, Py), 7.95 (d, J = 8.0 Hz; 1H, Py), 7.77 (d, J = 7.5 Hz;

1H, Ph), 7.38 (d, satellites, J = 7.5 Hz, J_{Pt-H} = 65.0 Hz; 2H, Ph), 7.01 (m; 3H, ph, Py-Ph),

6.89(m; 2H, Py-Ph), 6.83 (s; 2H, Mes), 6.50 (d, satellites, J = 8.0 Hz, J_{Pt-H} = 45.0 Hz;

1H, *Py*-ph), 2.53 (s; 6H, Me-DMSO), 2.26 (s; 3H, *o*-Me-Mes), 2.13 (s, 6 H, *p*-Me-Mes).

Anal. calcd for $C_{20}H_{30}BN_2PtS$: C 51.70, H 4.65, N 2.15; found: C 50.87, H 4.47, N 2.08.

2.2.8 Synthesis of Pt(*p*-B-ppy)Ph(Py) (2.1b)

To a CH_2Cl_2 (2 mL) solution of **2.1a** (20 mg, 0.027 mmol) was added pyridine (3 µL,

0.037 mmol). Yellow powders of **2.1b** were obtained after several hours standing of the

solution (90% yield). ^{1}H NMR (500 MHz, CD_2Cl_2, 25°C, δ, ppm): 8.86 (dd, J = 7.2 Hz, J

= 1.6 Hz; 2H, Py), 7.87 (m; 3H, py, *py*-Ph), 7.70 (d, J = 5.2 Hz; 1H, *py*-Ph), 7.56 (d; J =

8.0Hz; 1H, B-*Ph*), 7.46 (td; J = 6.0 Hz, J = 1.2 Hz; 2H, Py), 7.29 (s, satellites, J_{Pt-H} = 45.0

Hz; 1H, B-*Ph*), 7.25 (dd, satellites, J = 8.0Hz, J = 1.2Hz; 2H, Ph), 7.14(dd, J =7.6 Hz, J =

1.2Hz; 1H, B-*Ph*), 7.08 (td, J = 7.6 Hz, J = 1.2 Hz; 1H, B-*Ph*), 6.78 (s; 4H, *H*-Mes), 6.63

(m; 3H, Ph), 2.32 (s; 6H, *p*-*Me*-Mes), 2.00 (s; 12H, *o*-Me-Mes). Anal. calcd. for

$C_{40}H_{39}BN_2Pt$: C 63.75, H 5.22, N 3.72; found: C 64.19, H 5.01, N 3.62.

2.2.9 Synthesis of Pt(*p*-ppy-B)Ph(py) (2.2b)

To a CH_2Cl_2 (2 mL) solution of **2.2a** (20 mg, 0.027 mmol) was added pyridine (3 µL,

0.037 mmol). The mixture was kept standing for several hours. After the removal of

solvent and washing with hexanes, the yellow powder of **2.2b** was obtained in 90% yield.

^{1}H NMR (500 MHz, CD$_2$Cl$_2$, 25°C, δ, ppm): 8.68 (dd, J = 7.5 Hz, J = 1.5 Hz; 2H, Py),

7.91 (dd, J = 8.0 Hz, J = 1.5 Hz; 1H, *Py*-B), 7.84 (d, J = 8.0 Hz; 1H, *Py*-B), 7.67 (d; J =

8.0 Hz; 1H, *Ph*-Py), 7.58 (t, J = 8.0 Hz; 1H, Py), 7.53 (s; 1H, *Py*-B), 7.50 (dd, satellites, J

= 8.0 Hz, J = 1.0 Hz, J_{Pt-H} = 65.0 Hz; 2H, Ph), 7.16 (t, J = 8.0 Hz; 2H, Py), 7.09 (td, J =

8.0 Hz, J = 1.0 Hz; 1H, *Ph*-Py), 7.05 (dd, J = 8.0Hz, J=1.5Hz; 1H, *Ph*-Py), 7.01 (m; 1H,

Ph-Py), 6.95 (t, J = 7.5 Hz; 2H,Ph), 6.86 (t, J = 7.5 Hz; 1H, Ph), 6.81 (s; 4H, *H*-Mes),

2.35 (s; 6, *p-Me*-Mes), 1.99 (s; 12H, *o-Me*-Mes). ^{13}C{^{1}H}NMR (100 MHz, CD$_2$Cl$_2$, δ,

ppm): 154.74, 151.07, 140.74, 139.38, 138.08, 136.88, 128.62, 127.04, 126.03, 124.64,

122.92, 121.94, 120.91, 119.00, 118.41, 23.47, 21.24. Anal. calcd for

C$_{40}$H$_{39}$BN$_2$Pt·DMSO: C 60.65, H 5.45, N 3.37; found: C 60.82, H 5.62, N 3.28.

2.2.10 Synthesis of [Pt(*p*-B-ppy)Ph]$_2$(4,4'-bipy) (2.1c)

To an acetone solution (20 mL) of **2.1a** (20 mg, 0.027 mmol) was slowly added 4,4'-

bipyridine (2.0 mg, 0.013 mmol) in acetone (2 mL). The mixture was kept standing at

ambient temperature and the solution was allowed to evaporate slowly. Orange cluster

crystals of **2.1c** were formed and precipitated out after two days (90% yield). ^{1}H NMR

(500 MHz, CD$_2$Cl$_2$, 25°C, δ, ppm): 9.03 (d, J = 5.0 Hz; 2H, Py), 7.92 (m; 2H, 5, *Py*-Ph),

7.77 (d, J = 5.0 Hz; 1H, *Py*-Ph), 7.72 (dd; J = 5.0Hz, J = 1.5 Hz; 2H, Py), 7.59 (d, J = 8.0

Hz; 1H, B-*Ph*), 7.29 (m, satellites; 3H, ph, B-*Ph*), 7.17 (dd, J = 8.0 Hz, J = 1.0 Hz; 1H,

B-*Ph*), 7.11 (td, J = 7.0 Hz, J = 1.5 Hz; 1H, *Py*-Ph), 6.80 (s; 4H, *H*-Mes), 6.70 (t, J = 7.5

Hz; 2H, Ph), 6.64(t, J = 7.5Hz; 1H, Ph), 2.34(s; 6H, *p-Me*-Mes), 2.01 (s; 12H, *o-Me*-Mes). Anal. calcd for $C_{80}H_{76}B_2N_4Pt_2$: C 63.83, H 5.09, N 3.72; found: C 63.21, H 5.24, N 3.51.

2.2.11 Synthesis of [Pt(*p*-ppy-B)Ph]₂(4,4'-bipy) (2.2c)

To a CH_2Cl_2 solution (10 mL) of **2.2a** (20 mg, 0.027 mmol) was slowly added 4,4'-bipyridine (2.0 mg, 0.013 mmol) in CH_2Cl_2 (2 mL). 5 mL of hexane was layered on top. The mixture was kept standing at ambient temperature. Needle-like yellow crystals of **2.2c** formed and precipitated out overnight (85% yield). ^{1}H NMR (500 MHz, CD_2Cl_2, 25°C, δ, ppm): 8.86 (d, J = 6.5 Hz; 2H, py), 7.92 (dd, J = 8.0 Hz, J = 1.5 Hz; 1H, *Py*-B), 7.87 (d, J = 8.0 Hz; 1H, *Py*-B), 7.80 (s; 1H, *py*-B), 7.70 (d; J = 7.5 Hz; 1H, *Ph*-Py), 7.52 (d, satellites, J = 7.0 Hz, J_{Pt-H} = 65.0 Hz; 2H, Ph), 7.28 (d, J = 6.5 Hz; 2H, Py), 7.17 (d, satellites, J = 7.5 Hz, J_{Pt-H} = 42.0 Hz; 1H, *Ph*-Py), 7.05(m; 2H, 4, 5-*Ph*-Py), 6.99 (t, J = 7.5 Hz; 2H, Ph), 6.87 (t, J = 7.5 Hz; 1H, Ph), 6.69 (s; 4H, *H*-Mes), 1.98 (s; 6H, *p-Me*-Mes), 1.96 (s; 12H, *o-Me*-Mes). Anal. calcd for $C_{80}H_{76}B_2N_4Pt_2·1/3CH_2Cl_2$: C 62.92, H 5.04, N 3.65; found: C 62.84, H 5.27, N 3.45.

2.2.12 Molecular orbital calculations

DFT molecular orbital calculations were performed for ligands **2.1**, **2.2**, and metal complexes **2.1b**, **2.2b**. The geometrical parameters obtained for **2.2**, half molecule of **2.1c**, and **2.2c** from X-ray diffraction experiments were used as the starting point for the

47

geometry optimization of **2.2**, **2.1b**, and **2.2b**. The energy calculations were performed using Gaussian03 package with the B3LYP/6-311++G** basis set for all atoms except Pt, for which LAN2LDZ basis set was used.[9-10]

2.2.13 X-ray crystallographic analysis

Single crystals of *p*-ppy-B (**2**) and complexes **2.1a, 2.2a, 2.1c, 2.2c, 2.2a-OH** were mounted on glass fibers for data collection. Data were collected on a Bruker Apex II single-crystal X-ray diffractometer with graphite-monochromated Mo Kα radiation, operating at 50 kV and 30 mA and at 180 K. Data were processed on a PC with the aid of the Bruker SHELXTL software package (version 5.10)[11] and corrected for absorption effects. No significant decay was observed in all crystals except **2.2c**. The crystals of **2.2c** lose solvent rapidly when removed from solution. We have attempted to seal the crystal along with the mother liquor in a capillary, but without success. The best data set we collected for **2.2c** was obtained by mounting a fresh crystal quickly to a glass fiber cooled to 180 K on the goniometry head. Substantial loss of solvent molecules from the crystal lattice was still evident which is responsible for the poor quality of the data collected for **2.2c** and the low diffraction intensity (only about 30% reflections have intensity greater than 2σ). Nonetheless, we were able to establish the key structural features of molecule **2.2c**. All structures were solved by direct methods. Compound **2.2a** contains 0.5 hexane per complex in the lattice while compound **2.1c** and **2.2a-OH** contain two acetone molecules and two toluene molecules per complex, respectively, which were all modeled

and refined successfully. Most of the non-hydrogen atoms were refined anisotropically. The positions of hydrogen atoms were calculated, and their contributions in structural factor calculations were included. For structure **2.2c**, due to the sever disordering of the structure and the lack of sufficient data, most of the carbon atoms were refined isotropically. The crystal data of the complexes are given in Table 2.1. Important bond lengths and angles for all the compounds are listed in Table 2.2. The solvent composition from the formula in the crystallographic data for **2.2a**, **2.1c**, **2.2c** and **2.2a-OH** are different from the results of elemental analysis. For **2.2a**, **2.1c** and **2.2a-OH**, the difference is due to the different batches of crystal in X-ray crystal structural analysis and elemental analysis. For **2.2c**, the containing solvent molecules in the crystal lattice escaped quickly after the solution becoming dried.

Table 2.1 Crystallographic data for **2.1a**, **2.2a**, **2.1c**, **2.2c**, and **2.2a-OH**.

Compound	2.1a	2.2a	2.1c	2.2c	2.2a-OH
Formula	$C_{37}H_{40}NBOSPt$	$C_{37}H_{40}NBOSPt/0.5C_6H_{14}$	$C_{40}H_{38}N_2BPt/C_3H_6O$	$C_{40}H_{38}N_2BPt$	$C_{28}H_{30}NBO_2SPt/2C_7H_8$
FW	752.66	795.75	810.70	752.62	834.76
Crystal system	Orthorhombic	Monoclinic	Monoclinic	Orthorhombic	Triclinic
Space Group	$P2_12_12_1$	$P2_1/c$	$P2_1/n$	Cmca	P-1
a, Å	8.8185(11)	16.465(3)	17.8308(7)	31.937(5)	11.5949(12)
b, Å	20.861(3)	9.3894(18)	8.5324(3)	11.0495(16)	13.1194(17)
c, Å	35.238(5)	24.111(5)	24.2444(9)	21.821(3)	13.8204(14)
α,°	90	90	90	90	110.618(8)
β,°	90	103.167(2)	105.149(2)	90	102.690(7)
γ,°	90	90	90	90	97.594(8)
V, Å^3	6482.5(14)	3629.6(12)	3560.4(2)	7700(2)	1868.4(4)
Z	8	4	4	8	2
$D_{calc,}$ g·cm^{-3}	1.542	1.456	1.512	1.298	1.484
T, K	180	180	180	180	180
µ, mm^{-1}	4.423	3.954	3.977	3.670	3.847
$2\theta_{max}$, °	54.36	52.00	54.40	54.34	54.60
Reflns measd	72570	33583	32681	36437	14080
Reflns used	14278	7141	7881	4358	14080
Parameters	774	415	441	289	421
R [I>2σ(I)]: $R_1{}^a$ wR$_2{}^b$	0.0448 0.0758	0.0388 0.0845	0.0566 0.0870	0.0729 0.1472	0.0552 0.1276
R (all data): $R_1{}^a$ wR$_2{}^b$	0.0676 0.0828	0.0537 0.0911	0.1525 0.1125	0.2651 0.2201	0.0848 0.1445
GOF on F^2	1.070	1.050	0.962	0.946	1.023

^{a} $R_1 = \Sigma|F_0| - |F_c|/\Sigma|F_0|$
^{b} $wR_2 = [\Sigma w[(F_0{}^2 - F_c{}^2)^2]/\Sigma[w(F_0{}^2)^2]]^{1/2}$, $w = 1/[\sigma^2(F_0{}^2) + (0.075P)^2]$, where $P = $ [Max $(F_0{}^2, 0) + 2F_c{}^2]/3$

Table 2.2 Selected bond lengths (Å) and angles (°) for **2.1a**, **2.2a**, **2.1c**, **2.2c** and **2.2a-OH**.

2.1a		2.2a-OH	
Pt(1A)-C(12A)	2.008(8)	Pt(1)-C(12)	2.023(6)
Pt(1A)-C(1A)	2.038(8)	Pt(1)-C(1)	2.051(6)
Pt(1A)-N(1A)	2.120(6)	Pt(1)-N(1)	2.119(5)
Pt(1A)-S(1A)	2.280(2)	Pt(1)-S(1)	2.2906(15)
Pt(1)-C(1)	2.013(7)	B(1)-O(1)	1.331(9)
Pt(1)-C(12)	2.017(7)	B(1)-C(20)	1.563(9)
Pt(1)-N(1)	2.136(6)	B(1)-C(10)	1.585(9)
Pt(1)-S(1)	2.288(2)	C(12)-Pt(1)-C(1)	92.0(2)
C(12A)-Pt(1A)-C(1A)	92.2(3)	C(12)-Pt(1)-N(1)	171.3(2)
C(12A)-Pt(1A)-N(1A)	171.6(3)	C(1)-Pt(1)-N(1)	79.7(2)
C(1A)-Pt(1A)-N(1A)	79.4(3)	C(12)-Pt(1)-S(1)	88.69(17)
C(12A)-Pt(1A)-S(1A)	89.3(2)	C(1)-Pt(1)-S(1)	177.78(16)
C(1A)-Pt(1A)-S(1A)	175.3(2)	N(1)-Pt(1)-S(1)	99.50(14)
N(1A)-Pt(1A)-S(1A)	99.02(18)	O(1)-B(1)-C(20)	124.0(5)
C(1)-Pt(1)-C(12)	90.1(3)	O(1)-B(1)-C(10)	114.8(6)
C(1)-Pt(1)-N(1)	80.3(3)	C(20)-B(1)-C(10)	121.2(6)
C(12)-Pt(1)-N(1)	170.3(3)		
C(1)-Pt(1)-S(1)	178.71(19)		
C(12)-Pt(1)-S(1)	90.1(2)		
N(1)-Pt(1)-S(1)	99.41(17)		
2.2a		2.1c	
Pt(1)-C(12)	2.010(5)	Pt(1)-C(1)	1.987(8)
Pt(1)-C(1)	2.021(5)	Pt(1)-C(12)	1.997(9)
Pt(1)-N(1)	2.121(4)	Pt(1)-N(2)	2.118(6)
Pt(1)-S(1)	2.2888(14)	Pt(1)-N(1)	2.124(7)
C(12)-Pt(1)-C(1)	91.7(2)	C(1)-Pt(1)-C(12)	93.5(3)
C(12)-Pt(1)-N(1)	171.22(19)	C(1)-Pt(1)-N(2)	177.7(3)
C(1)-Pt(1)-N(1)	80.34(19)	C(12)-Pt(1)-N(2)	88.8(3)
C(12)-Pt(1)-S(1)	88.79(16)	C(1)-Pt(1)-N(1)	80.3(3)

C(1)-Pt(1)-S(1)	175.47(15)	C(12)-Pt(1)-N(1)	173.5(3)
N(1)-Pt(1)-S(1)	99.48(12)	N(2)-Pt(1)-N(1)	97.4(3)
2.2c			
Pt(1)-C(1)	2.12(2)	N(2)-Pt(1)-C(12)	81.6(8)
Pt(1)-C(12)	1.993(18)	N(2)-Pt(1)-N(1)	96.9(7)
Pt(1)-N(1)	2.090(13)	C(12)-Pt(1)-N(1)	176.0(7)
Pt(1)-N(2)	1.990(19)	N(2)-Pt(1)-C(1)	171.2(10)
N(1)-Pt(1)-C(1)	86.8(6)	C(12)-Pt(1)-C(1)	94.2(6)

2.3 Results and discussion

2.3.1 Syntheses

2.3.1.1 Syntheses of ligands 2.1 and 2.2

As shown in Figure 2.3, the synthesis of *p*-B-ppy (**2.1**) was achieved by Suzuki-Miyaura coupling of 4-bromophenylboronic acid with 2-bromopyridine, followed by substitution of the bromo group with $BMes_2$ in THF. This is a different procedure from the previously reported one for compound **2.1** where Stille coupling methods were used.[2a] Compound **2.2**, *p*-ppy-B was achieved by Suzuki coupling of phenylboronic acid and 2,5-diboromopyridine, followed by substitution of the bromo group with $BMes_2$ in diethyl ether.
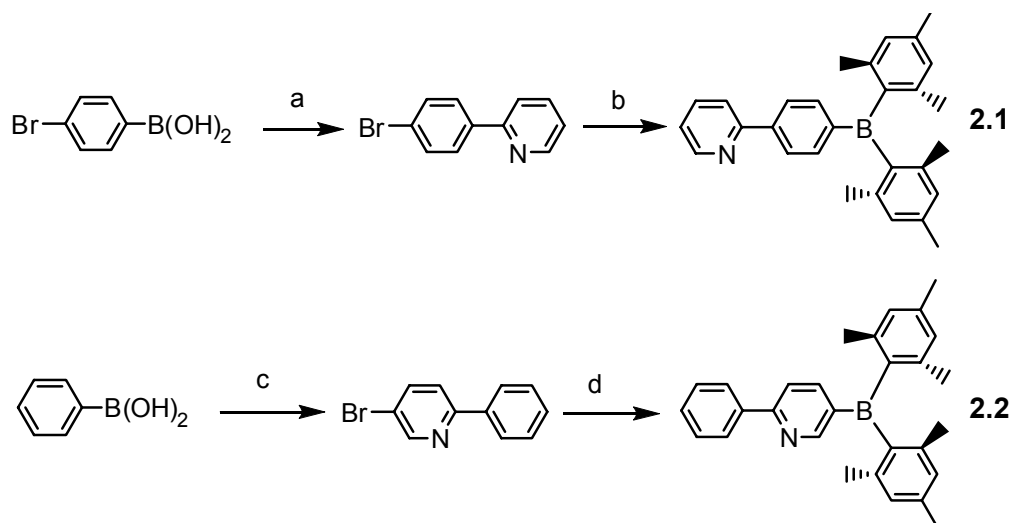
Reagents and conditions: a) 2-bromopyridine, Pd(PPh$_3$)$_4$, and NaOH, toluene, alcohol, and water (3:1:1), rt. 48 h; b) (i) n-BuLi, THF, -78 $^\circ$C; (ii) B(Mes)$_2$F, -78 $^\circ$C to rt, overnight; c) 2, 5-bromopyridine, Pd(PPh$_3$)$_4$, and NaOH, toluene, alcohol, and water (3:1:1), rt. 48 h; d) (i) n-BuLi, Et$_2$O, -78 $^\circ$C; (ii) B(Mes)$_2$F, -78 $^\circ$C to rt, overnight.

Figure 2.3 Synthetic scheme for **2.1** and **2.2.**

2.3.1.2 Syntheses of metal complexes

The DMSO complexes Pt(*p*-B-ppy)Ph(DMSO) (**2.1a**) and Pt(*p*-ppy-B)Ph(DMSO) (**2.2a**) were obtained readily by cyclometalation reactions of [PtPh$_2$(DMSO)$_2$] with ligands **2.1** and **2.2**, respectively, in THF at 50°C. Because DMSO in **2.1a** and **2.2a** is a relatively weak donor, it can be replaced readily by other donor ligands such as pyridine. The pyridine complexes Pt(*p*-B-ppy)Ph(py) (**2.1b**) and Pt(*p*-ppy-B)Ph(py) (**2.2b**) were obtained by the reaction of excess pyridine with **2.1a** and **2.2a**, respectively, through a ligand substitution reaction. Similarly, metal complexes [Pt(*p*-B-ppy)]$_2$(4,4'-bipy) (**2.1c**) and [Pt(*p*-ppy-B)]$_2$(4,4'-bipy) (**2.2c**) were obtained by reacting 0.5 eq 4,4'-bipy with 1 eq.

2.1a and **2.2a** respectively. The synthetic scheme for metal complexes **2.1a**, **2.1b** and

2.1c was shown in Figure 2.4. Metal complexes **2.2a**, **2.2b**, **2.2c** were synthesized in the

similar way. The free ligands and all Pt(II) complexes were fully characterized by NMR,

HRMS or elemental analyses.
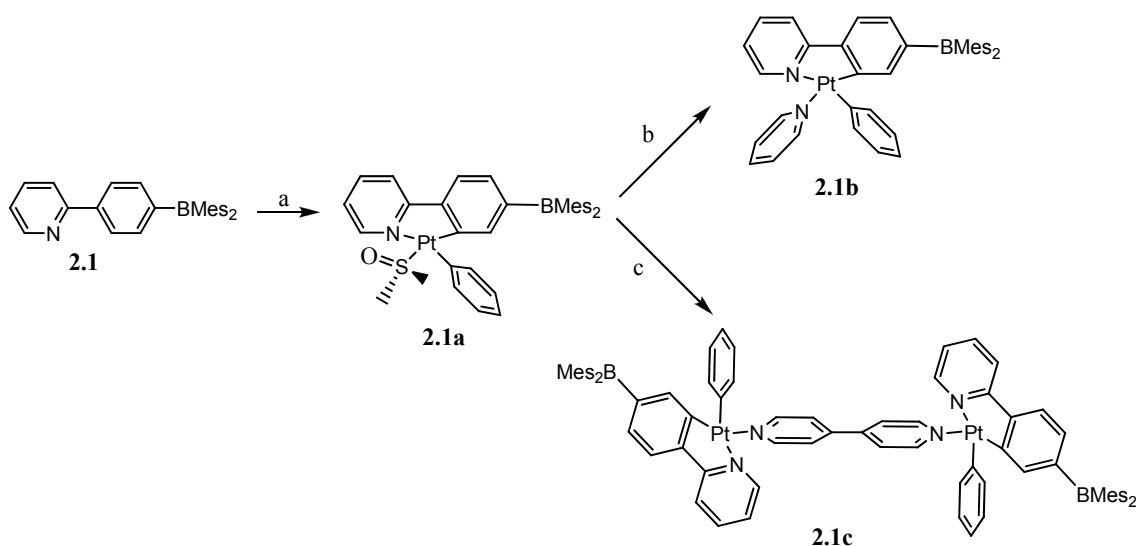
Reagents and conditions: a) 1 eq PtPh$_2$(DMSO)$_2$, THF, 50 °C, 8h; b) 2 eq pyridine, CH$_2$Cl$_2$, 1h;
c) 0.5eq 4, 4-bipyridine, CH$_2$Cl$_2$, 1h

Figure 2.4 Synthetic scheme for **2.1a**, **2.1b** and **2.1c**.

2.3.2 Structures

2.3.2.1 Structure of 2.2 (*p*-ppy-B)

The crystal structure of **2.2** (*p*-ppy-B) was determined by single-crystal X-ray diffraction

analysis and shown in Figure 2.5. The phenyl and the pyridyl planes are off coplanarity

by 23.6°. The three coordinate boron center adopts a trigonal coplanar geometry, with

slight distortion. The C(10)-B(1)-C(1) angle is 122.9(1)°, the C(10)-B(1)-C(20) angel is

117.9(0) °, and the C(1)-B(1)-C(20) angle is 119.1(0) °, The C-B bond distance is around

1.57 Å, with 1.57(3) Å, 1.58(2) Å, 1.56(8) Å for C(10)-B(1), C(20)-B(1), C(1)-B(1)

individualy.
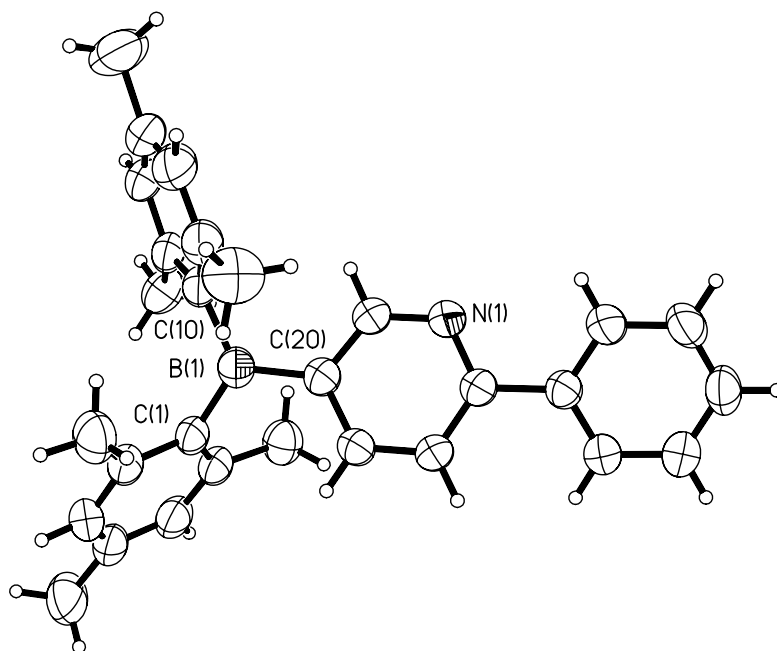
Figure 2.5 The structure of **2.2** (*p*-ppy-B) with 50% thermal ellipsoids**.**

2.3.2.2 Structure of 2.1a and 2.2a

The structures of complexes **2.1a**, **2.2a** were established by single-crystal X-ray

diffraction analyses and shown in Figure 2.6 and Figure 2.7, respectively. The Pt(II)

center in both compounds is four-coordinated, adopting a square planar geometry. With

such constraint, the phenyl and pyridyl planes in Pt(II) complexes are in coplanarity compared to their corresponding free liangds. The Pt-C, Pt-N and Pt-S bond lengths and angles in **2.1a** and **2.2a** are similar. One common feature in the structures of **2.1a** and **2.2a** is that the oxygen atom of the DMSO ligand is oriented toward the *ortho*-H atom of the pyridyl ring with the C(11)···O(1) and H(11)···O(1) separation distances being 2.98 Å to 3.04 Å, and 2.13 Å to 2.19 Å, respectively, consistent with a hydrogen bond.
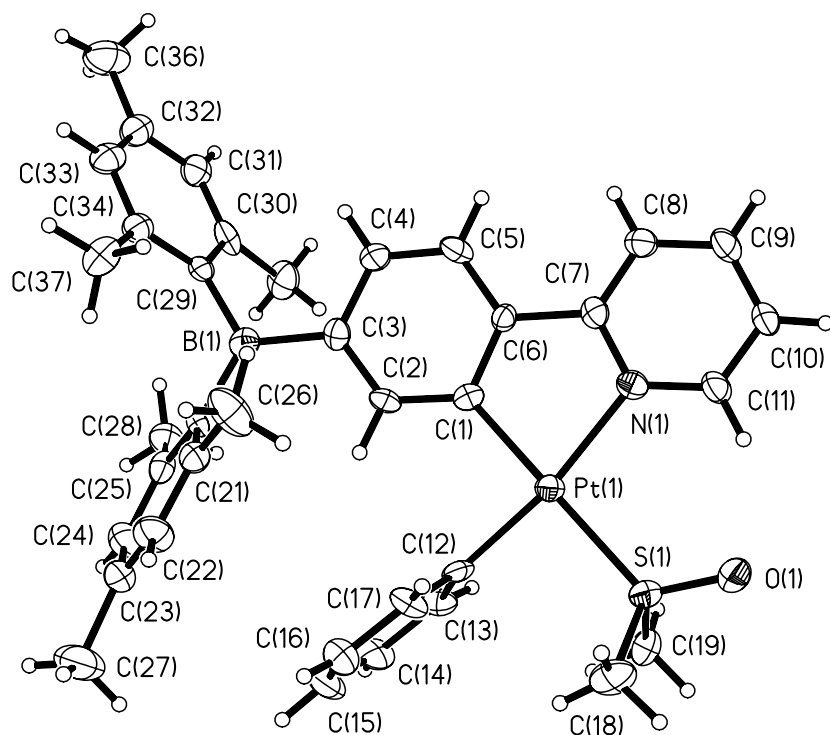
Figure 2.6 The structures of **2.1a** with 50% thermal ellipsoids and labeling schemes.
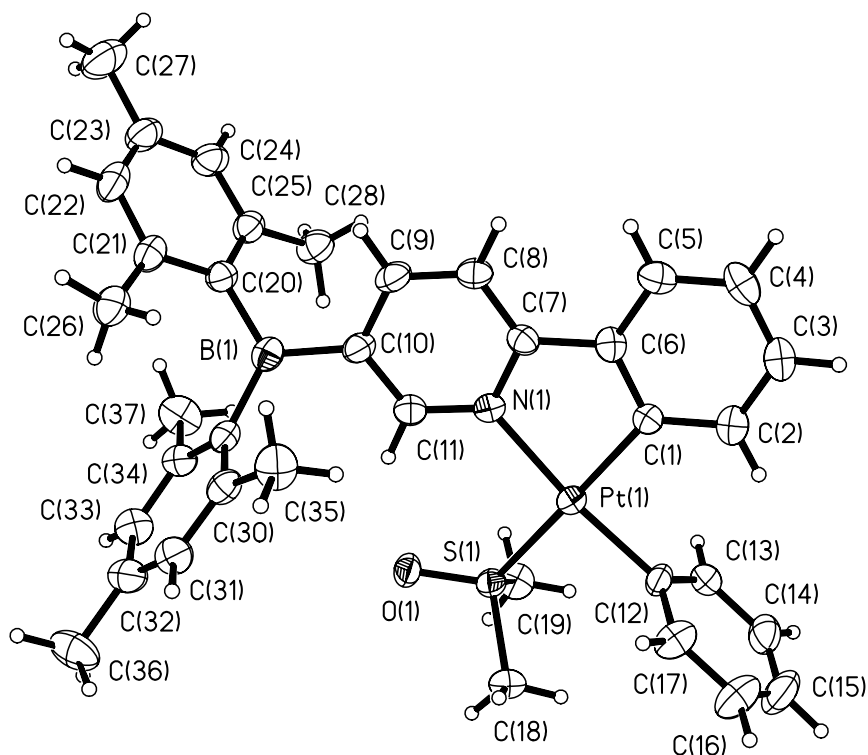
Figure 2.7 The structures of **2.2a** with 50% thermal ellipsoids and labeling schemes.

The key difference between these two structures is that in **2.1a** the DMSO ligand is far away from the BMes$_2$ group while in **2.2a** it is close to the BMes$_2$ group. In fact the separation distance between O(1) and B(1) in **2.2a** is only 4.58(2) Å, O(1) and C(29), 4.07 Å.

The crystal structures shown in Figure 2.6 and Figure 2.7 established unequivocally that the auxiliary ligand DMSO in **2.1a** and **2.2a** is bound to the Pt(II) center *trans* to the phenyl ring not the pyridyl ring of the ppy chelate. NMR spectra confirmed that this "*cis* isomer" (the two phenyl rings being *cis* to each other) is formed

exclusively for both **2.1a** and **2.2a**. This can be explained by the well established intramolecular C-H bond activation mechanism on a Pt(II) center[12] depicted for the formation of complex **2.1a** in Figure 2.8.
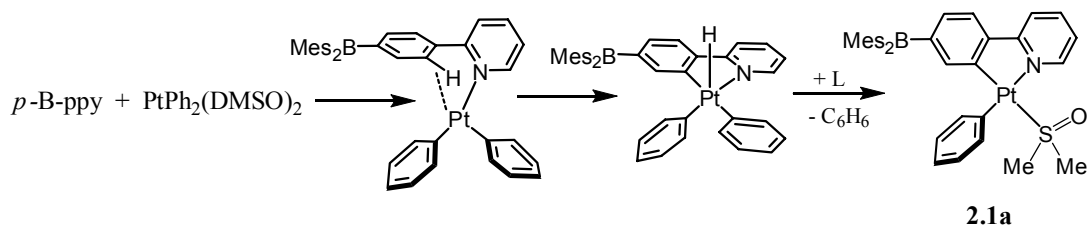
Figure 2.8 Schematic formation of complex **2.1a.**

The greater *trans* effect exerted by the phenyl ring of ppy in the five-coordinate Pt(IV) intermediate leads to the *regio*-selective reductive elimination of the phenyl group *trans* to it along with the H atom from the Pt(IV) center as a benzene molecule. The subsequent DMSO coordination gives rise to complex **2.1a**. Similar regio-selective cyclometalation reactions involving a Pt(II) center have been observed previously.[3b, 12]

In the asymmetric unit of **2.1a**, there are two independent molecules that form a stacked pair with a Pt-Pt separation distance of 4.906(1)Å, as shown in Figure 2.9.
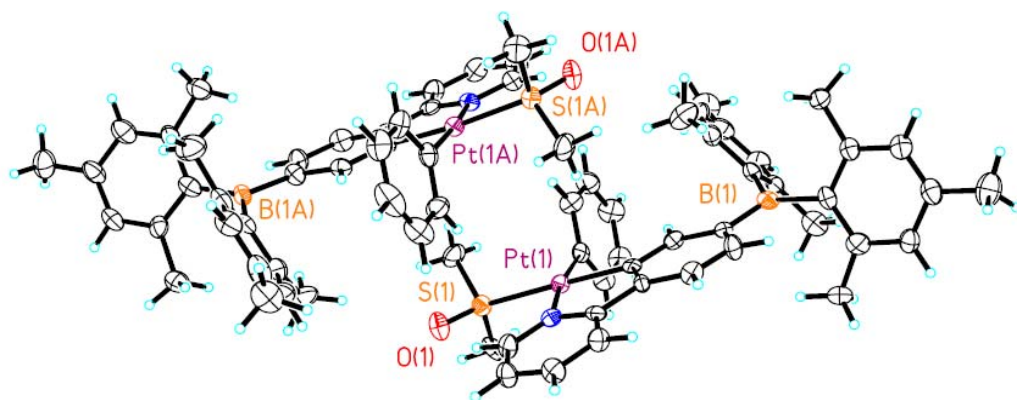
Figure 2.9 Diagrams showing the two neighboring molecules of **2.1a** in the crystal lattice.

2.3.2.3 Structures of 2.1b and 2.2b

Although the structure of **2.1b** and **2.2b** were not determined due to the lack of suitable crystals, the coordination environments around Pt center are believed to be similar to those of **2.1c** and **2.2c** molecules in the following Section 2.3.2.4.

2.3.2.4 Structures of 2.1c and 2.2c

2.3.2.4.1 Structures of 2.1c and 2.2c in the solid state

As shown in Figure 2.10 and Figure 2.11, complexes **2.1c** and **2.2c** display a similar "*cis*" structure as those of **2.1a** and **2.2a** with the two pyridyl rings being *cis* to each other on the same Pt(II) center. Hence, the replacement of the DMSO ligand by 4,4'-bipy does not alter the *cis*-structure of the complexes due to the strong *trans* effect of the phenyl group.
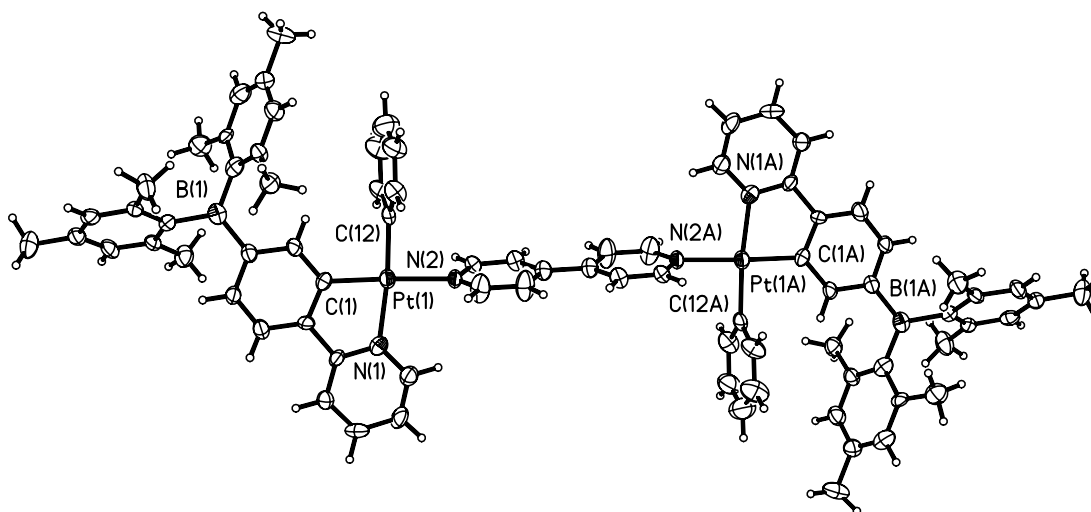
Figure 2.10 The structure of **2.1c** with 50% thermal ellipsoids and labeling schemes.
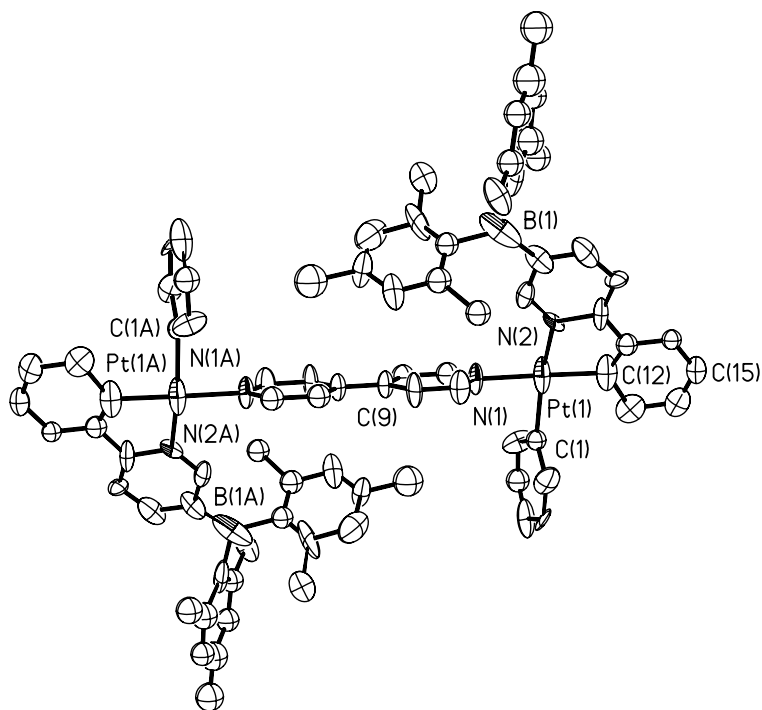
Figure 2.11 The structure of **2.2c** with 50% thermal ellipsoids and labeling schemes. Hydrogen atoms are omitted.

The Pt-C bond lengths in **2.1c** are notably shorter than those of **2.1a** and **2.2a** and the N(1)-Pt(1)-C((12) (173.5(3)°) and N(2)-Pt(1)-C(1) (177.7(3)°) angles are much less distorted from linearity, compared to the corresponding S-Pt-C bond angles in **2.1a** and **2.2a**. This may be attributed to the greater steric interactions imposed by DMSO in **2.1a** and **2.2a**. The intramolecular Pt-Pt separation distance in **2.1c** is 11.375(1) Å, much longer than the shortest intermolecular Pt-Pt distance, 8.532(1) Å. The molecule of **2.1c** has a crystallographically imposed inversion center. The two BMes$_2$ groups have an *anti* configuration with a 22.1 Å separation distance between the two B atoms.

The molecule of **2.2c** has a crystallographically imposed inversion center and a mirror plane symmetry on which the two Pt atoms and the entire bipy linker lie. As a consequence of the mirror plane symmetry, the entire molecule of **2.2c** is disordered over the two sites related by mirror plane reflection, as show in Figure 2.12.
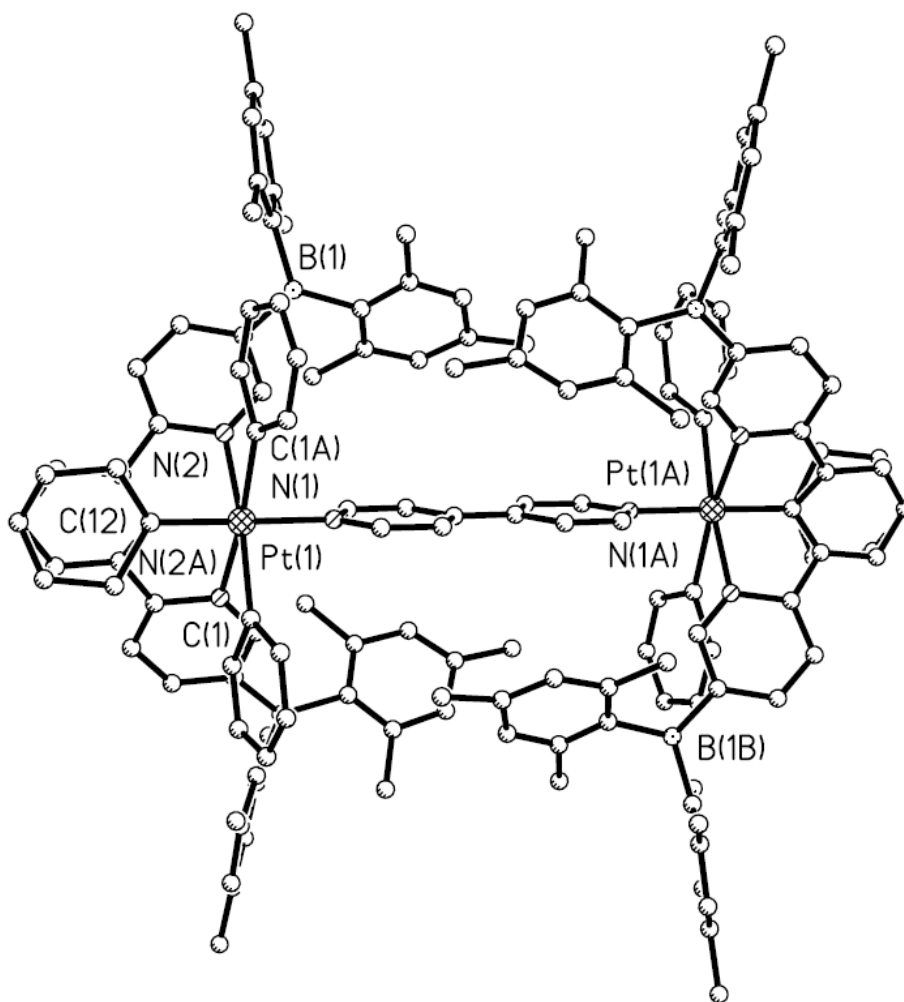
Figure 2.12 A diagram showing the disordering of molecule **2.2c**.

Although we have been able to model the disorder successfully, the quality of the structure data is poor due to both disordering and the poor quality of the diffraction data. Due to the disordering the structure of **2.2c** in the solid state could have either a *syn* or an *anti* configuration (Figure 2.13) with respect to the relative orientation of the two BMes$_2$ groups.
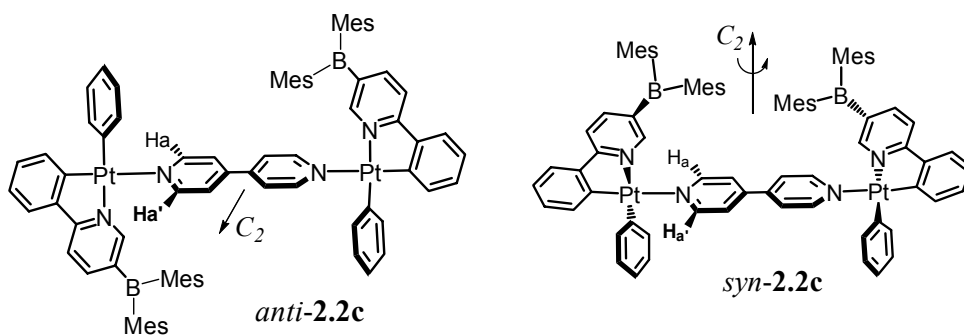
Figure 2.13 Structures of *syn* and *anti* isomers of **2.2c**.

From the space-filling diagram of anti-**2.2c** (Figure 2.14), with the bulky BMes$_2$ group the whole molecule is very crowded. As we can imagine, the BMes$_2$ group in **2.2c** on the same side with the 4,4'-bipy linker imposes a much greater steric interactions between the two BMes$_2$ groups in the *syn* configuration. The *anti* configuration of the two BMes$_2$ group is clearly the favored one for **2.2c** in the solid state. The separation distance of the two B atoms of **2.2c** in the *anti* structure shown in Figure 2.11 is 13.2 Å, much shorter than that of **2.1c**.
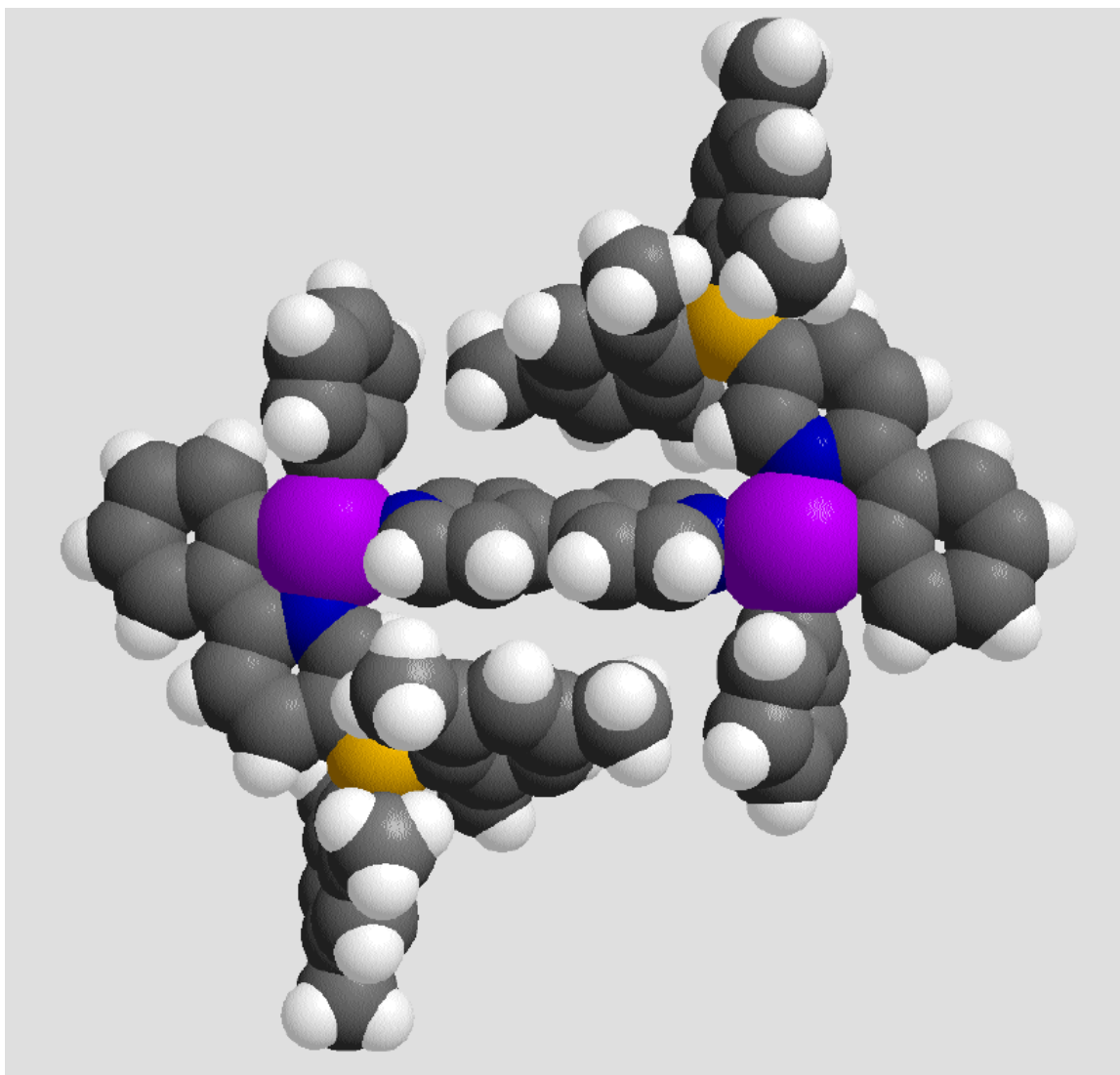
Figure 2.14 A space filling diagram showing the structure of anti-**2.2c**.

2.3.2.4.2 Structure of 2.1c and 2.2c in solution

In solution, due to the free rotation around the Pt-N (bipy) bond or the bridging C-C bond

between 4,4'-bipy, coexistence of *syn* and *anti* isomers of **2.1c** (Figure 2.15) and **2.2c**

(Figure 2.13) are possible. To establish this, we recorded variable temperature ^{1}H NMR spectra for **2.1c** and **2.2c** in CD_2Cl_2.
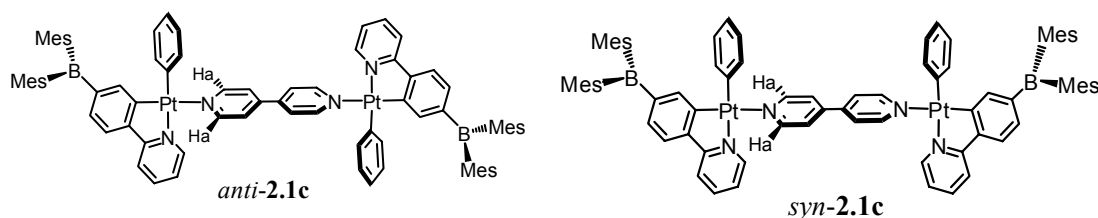
Figure 2.15 Structures of *syn* and *anti* isomers of **2.1c** and **2.2c.**

For **2.1c**, from the ^{1}H NMR spectra at 200 K in CD_2Cl_2 (Figure 2.16), the ortho-H_a peaks became broad, indicating the coexistence of the *syn* and *anti* isomers. Further lowering the temperature to 185 K, the chemical shifts of the H_a were still not fully resolved and the free energy of activation for the rotation barrier between *syn* and *anti* isomers was estimated to be 38 kJ• mol^{-1}. The calculation of activation energy is based on the following equation 3.1:

$$\Delta G = RT_c \, [\, 23 + \ln (T_c / \Delta v) \,] \quad (3.1)$$

Where T_c is coalescence temperature and expressed in Kelvin, Δv is the frequency separation of the initially sharp lines and R is the gas constant. The error limit is +/- 0.1 kJ• mol^{-1}.
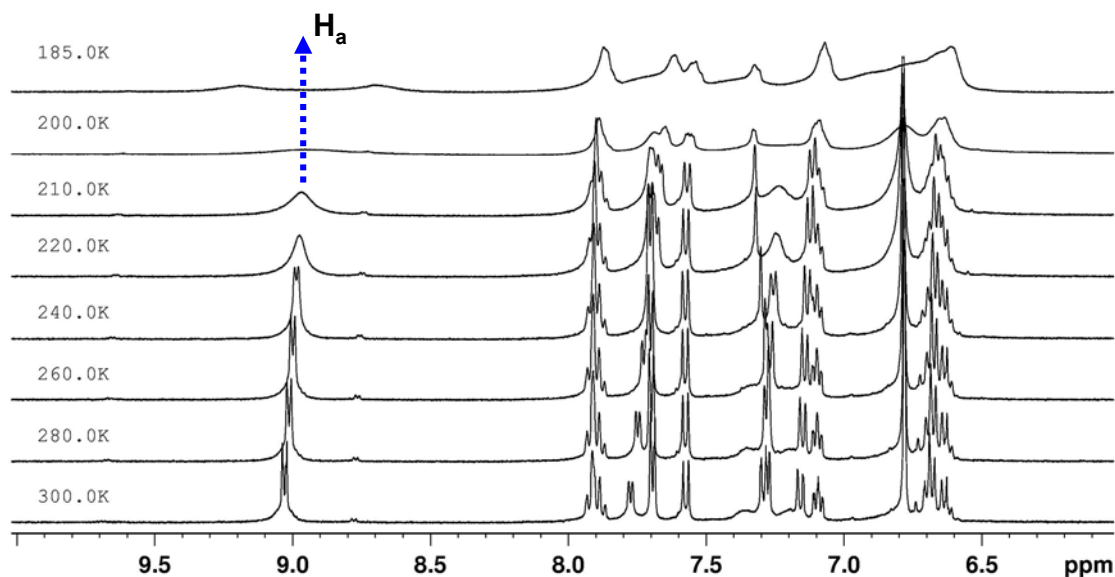
Figure 2.16 Variable-temperature ^{1}H NMR spectra of aromatic region of **2.1c** in CD$_2$Cl$_2$ with field strength 400M.

For **2.2 c**, from the ^{1}H NMR spectra at ~200 K in CD$_2$Cl$_2$ (Figure 2.17), two sets of well resolved *ortho*-H$_a$ peaks from the 4,4'-bipy ligand were observed at 8.6 to 9.0 ppm region which can be attributed to the *syn-* and *anti-*isomer, respectively. Lowering temperature further to 185 K causes the splitting of each peak into two which can be attributed to H$_a$ and H$_{a'}$ protons shown in Figure 2.13. This can be explained by the C_2 symmetry of both isomers and the apparent lack of mirror plane symmetry, due to the strong steric interactions. The activation barrier for the *anti* and *syn* configuration inter-conversion of **2.2c** was estimated to be 41 kJ·mol^{-1} based on the VT NMR data. This larger barrier compared to that of **2.1c** (38 kJ·mol^{-1}) is consistent with the much steric structure of **2.2c**. Hence, we have established that the two constitutional isomers of B-

66

ppy and ppy-B do have a distinct impact on the structure of the Pt(II) complexes in solution and the solid state.
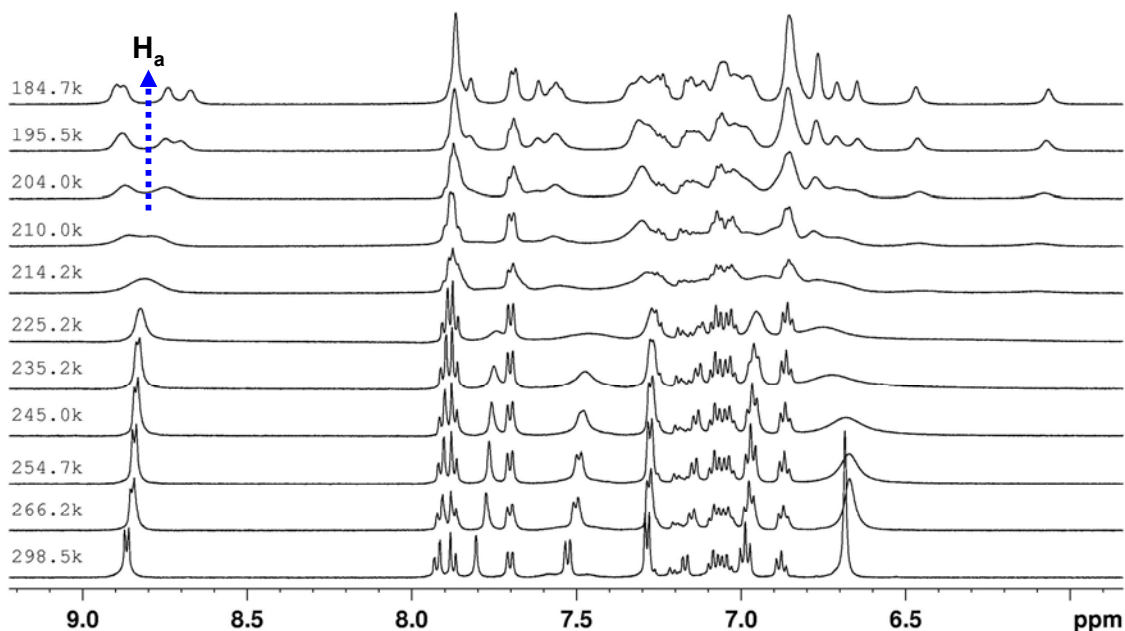
Figure 2.17 Variable-temperature ^{1}H NMR spectra of aromatic region of **2.2c** in CD$_2$Cl$_2$, with field strength 400M.

2.3.3 Stability of Pt(II) complexes and the formation and structure of 2.2a-OH

All Pt complexes are stable toward air and water, except **2.2a**. With same ancillary ligand DMSO, there is also a notable difference in the stability of **2.1a** and **2.2a** toward adventitious H$_2$O molecules in solution. Compound **2.1a** is stable in solution under air for a long period of time while compound **2.2a** undergoes slow decomposition upon long

standing under air with nearly quantitative formation of a new compound Pt[*p*-ppy-BMes(OH)]Ph(DMSO) (**2.2a-OH**). **2.2a-OH** was fully characterized by NMR spectrometry, elemental analysis and single-crystal X-ray diffraction. Its structure is shown in Figure 2.18.
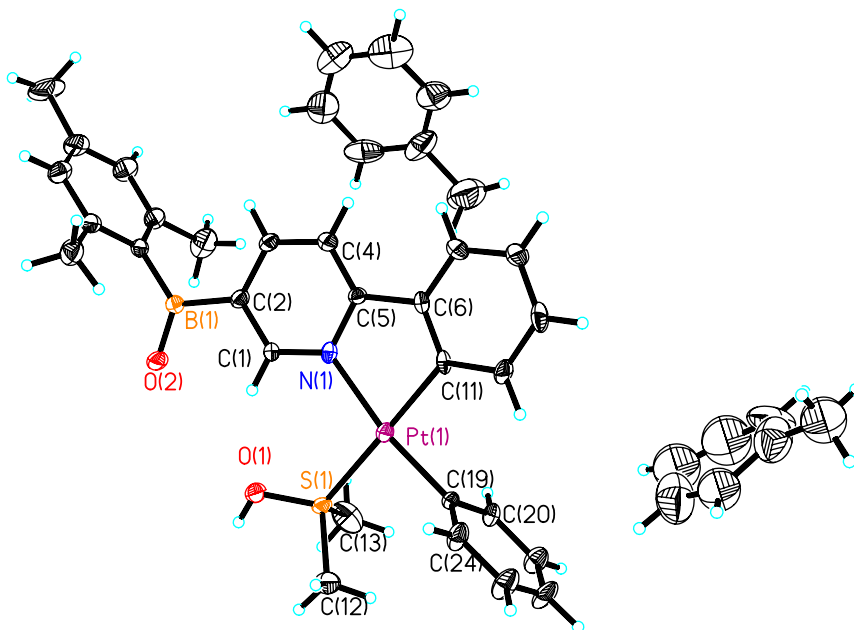
Figure 2.18 A diagram showing the structure of **2.2a-OH** with two solvent toluene molecules in one crystal lattice.

The Pt-ligand bond lengths and angles of **2.2a-OH** are similar to those of **2.1a** and **2.2a**. The B-O bond length of 1.331(9) Å is much shorter than that of a typical B-O single bond (~1.50-1.55 Å, e.g., Ph₂Bq, q = 8-hydroxyquinoline anion and derivatives),[13] and clearly supporting a B=O double bond, due to the donation of the oxygen lone pair electrons to the empty p_π orbital of the B atom. When the water-free solution of **2.2a** is

kept under nitrogen, **2.2a** does not show any sign of decomposition. Hence, we attributed the decomposition of **2.2a** to an internal DMSO facilitated B-C bond hydrolysis process as illustrated in Figure 2.19. The greater Lewis acidity and the close proximity to the DMSO ligand of the BMes$_2$ group in **2.2a**, compared to that in **2.1a** are believed to be responsible for the unusual decomposition of the ppy-B ligand.
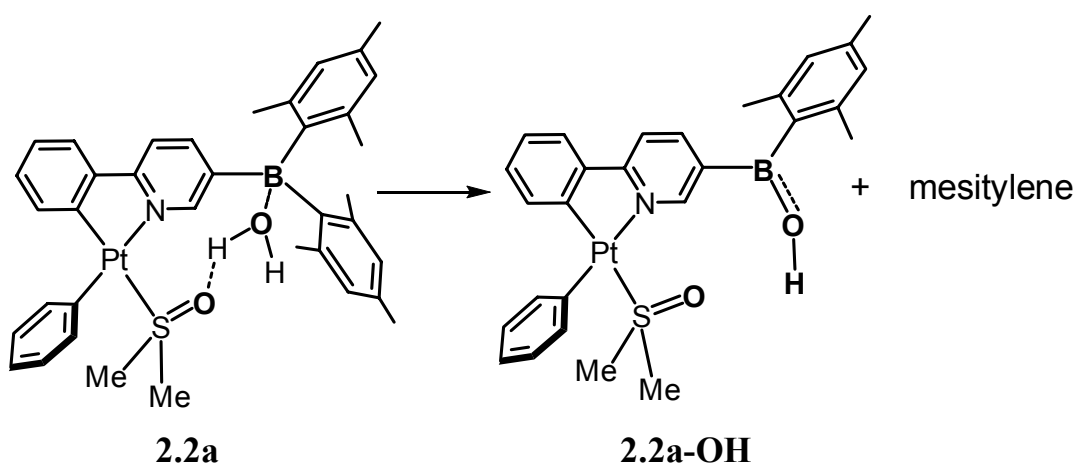
Figure 2.19 Hydrolysis process of **2.2a**.

Interestingly, as shown in Figure 2.20, the molecule of **2.2a-OH** forms a hydrogen-bond linked dimer through the DMSO oxygen atom and the hydroxo group in the crystal lattice. Each of these dimers stacks with a neighboring dimer with a Pt-Pt separation distance of 5.189(1) Å. Furthermore, compound **2.2a-OH** forms a highly porous crystal lattice that hosts two toluene solvent molecules per molecule of **2.2a-OH**, as shown in Figure 2.21.
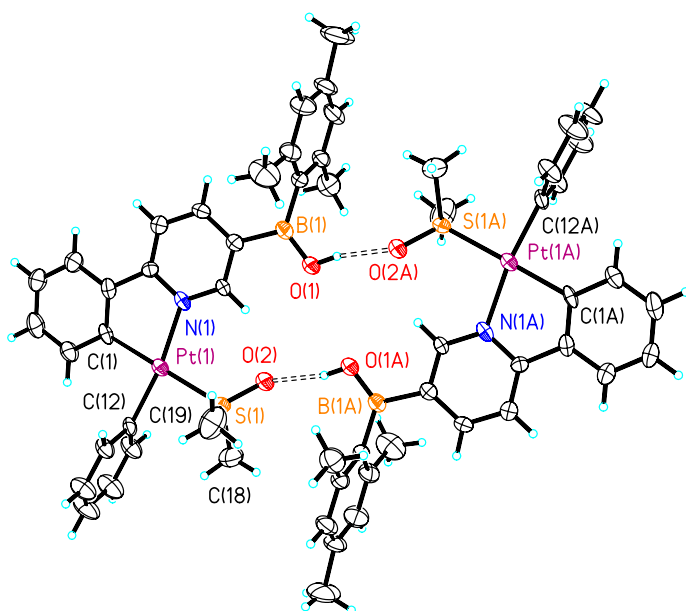
Figure 2.20 A diagram showing the structure of the hydrogen bonded dimer of **2.2a-OH**.
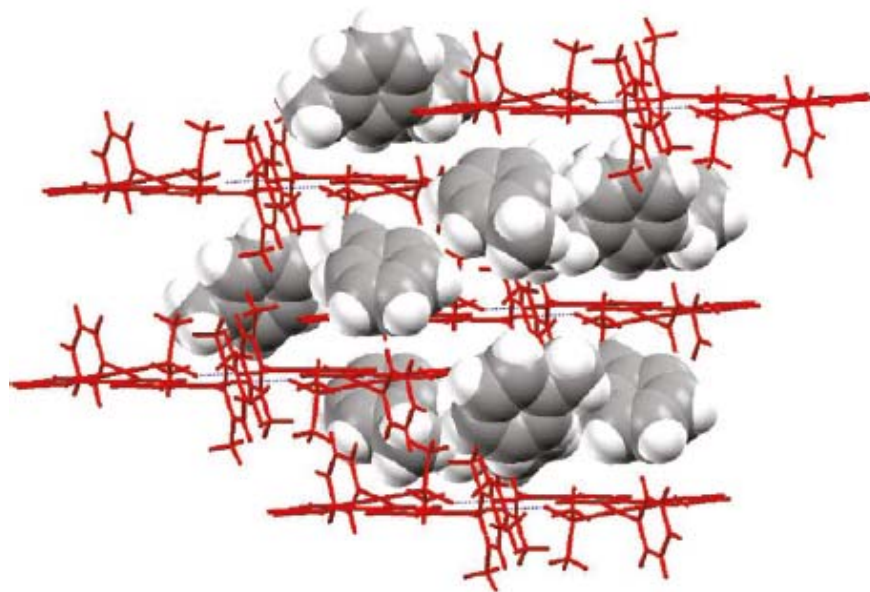
Figure 2.21 Crystal lattice packing diagram of **2.2a-OH** showing the toluene solvent molecules in the lattice.

2.3.4 Electrochemical properties

The reduction potentials of the free ligands and the Pt(II) metal complexes were recorded by cyclic voltammetry (CV: DMF as the solvent, NBu_4PF_6 as the electrolyte).

2.3.4.1 Ligands 2.1 and 2.2

As shown in Table 2.3 and Figure 2.22, **2.2** (*p*-ppy-B) displayed a reversible reduction peak at -2.12 V (vs $FeCp_2^{+/0}$), which can be attributed to the three-coordinate boron center. The reduction potential is more positive than that of **2.1** (*p*-B-ppy), -2.16 V, supporting the fact that the pyridine ring can enhance the electron accepting ability of the boron center much more effectively than the phenyl ring.
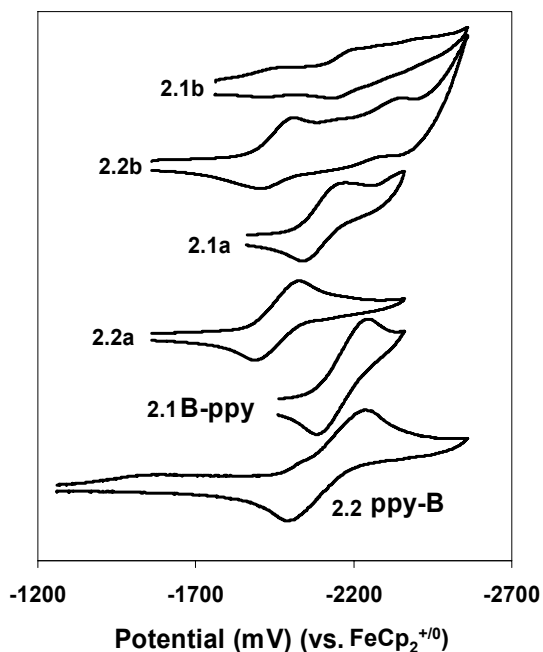
Figure 2.22 The CV diagrams for the ligands **2.1**, **2.2** and Pt(II) complexes recorded in DMF.

71

Table 2.3 Electrochemical data

Compound	2.1	2.1a	2.1b	2.2	2.2a	2.2b
$E_{1/2}^{red1}$ (V)	-2.16	-2.10	-2.17	-2.12	-1.96	-1.96

All potentials are relative to $FeCp_2^{+/0}$, measured in DMF, using NBu_4PF_6 as the electrolyte with scan rates 100 mV to 1000 mV.

2.3.4.2 Metal complexes with Ligands 2.1, 2.2

The ligands **2.1** and **2.2** in the complexes exist as anionic ligands. Thus, in the absence of any metal chelation to stabilize the negative charge, one would predict that the Lewis acidity/electron accepting ability of the boron center should be much reduced, compared to the neutral molecules. Upon chelation by a positively charged metal ions such as Pt(II), the negative charge of the ligand should be greatly reduced and the π conjugation of the ligand should be significantly enhanced, which may lead to an increase of the electron accepting ability of the B-ppy or ppy-B ligand. This was indeed observed in the *p*-ppy-B Pt(II) complexes **2.2a** and **2.2b**, both of which display a reduction potential of -1.96 V, that is 0.16 V more positive than the free ligand.

However, for the *p*-B-ppy Pt(II) complexes **2.1a** and **2.1b**, the impact of Pt(II) chelation to the *p*-B-ppy ligand is either very small or negligible as shown by the

potentials of complexes **2.1a** and **2.1b** (-2.10 V, -2.17 V, respectively), that are 0.06 V more positive or identical to that of the free ligand.

This supports the fact that metal binding to the N,C-chelation ligands is only effective in enhancing the electron accepting ability of the triarylboron if the BMes$_2$ group is on the pyridyl ring. This can be easily understood since when the BMes$_2$ group is on the negatively charged phenyl ring, the boron center will have a more negative charge, compared to that on the pyridyl ring, due to its close proximity to the negatively charged phenyl ring, thus reducing its electron accepting ability. This is also consistent with our earlier reports on Pt(II) chelation enhanced electron accepting ability of 7-azaindolyl derivative N,C-chelate ligands with a BMes$_2$ group on the N-heterocyclic ring.[3a]

2.3.4.3 Metal complexes with different auxiliary ligands

The somewhat more positive reduction potential of **2.1a**, compared to that of **2.1b**, indicates that the auxiliary ligand also has an impact on the LUMO level of the molecule. This may be explained by the fact that a strong σ donor such as pyridine can significantly weaken the ppy σ donation to the Pt(II) center, thus diminishing the effect of metal-chelation, compared to the relatively weaker DMSO σ donor.

Interestingly, the same phenomenon was not observed for **2.2a** and **2.2b**, perhaps due to the fact that the BMes$_2$ group is *cis* to the auxiliary ligand, thus less sensitive to its perturbation. For the pyridine complex **2.2b**, a 2nd reduction peak at -2.34 V is also

observed which can be ascribed to the pyridyl ring reduction.[5] CV data of the dinuclear

Pt(II) complexes **2.1c** and **2.2c** could not be obtained due to their poor solubility in DMF.

2.3.5 Absorption spectra

The electronic properties of ligands and their metal complexes were studied by UV-Vis

absorption spetra. The absorption spectra of the free liand p-B-ppy and p-ppy-B are

shown in Figure 2.23 along with the Pt(II) complexes. The π to π^* absorption band of **2.2**

is slightly red shifted (333 nm) compared to that of **2.1** (329 nm). The Pt(II) complexes of

2.1 and **2.2** display absorption bands similar as the corresponding free ligands and a new

well resolved MLCT band with moderate intensity in the 380 -500 nm region.

Compared to the free ligand, the π to π^* absorption band is red shifted, due to the

fact that the metal chelation enhances the π conjugation, hence decreasing the π-π^* gap.

Hence, the well-resolved MLCT low energy band can be attributed to the $BMes_2$ group

that stabilizes the π^* level and the phenyl auxiliary ligand that enhances Pt(II) d orbital

energy level.

For Pt(II) complexes, with the same auxiliary ligand, the MLCT absorption band of

the p-ppy-B complexes is red shifted relative to that of p-B-ppy complexes, which is in

agreement with the fact that the pyridyl ring in conjugation with the boron center is more

effective in lowering the π^* energy level than the phenyl ring. The extinction coefficients

of the dinuclear complexes **2.1c** and **2.2c** are nearly twice those of the corresponding

mononuclear compounds **2.1b** and **2.2b**. For both p-B-ppy and p-ppy-B series, the MLCT

energy follows the order of DMSO > 4,4'-bipy ~ py, supporting that the electron

donating ability of the ligands to the Pt(II) center follows the order of DMSO < 4,4'-bipy

~ py.
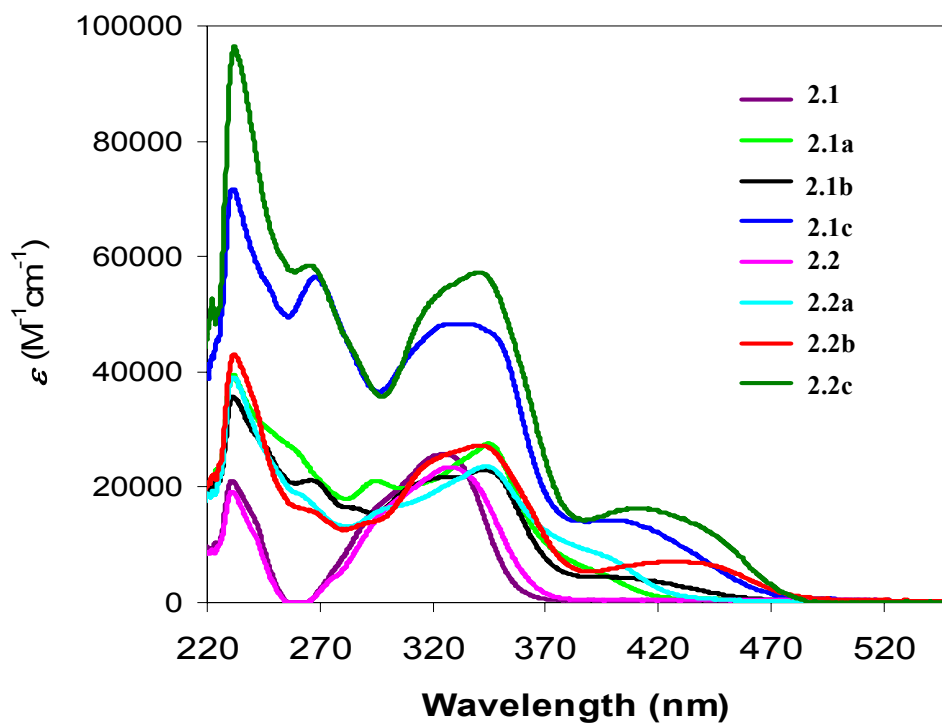
Figure 2.23 UV-Vis absorption spectra of ligands **2.1**, **2.2** and their Pt(II) complexes recorded in CH₂Cl₂.

2.3.6 Luminescence Properties

2.3.6.1 Ligands 2.1 and 2.2

The luminescent properties of the free ligands were examined by fluorescent spectroscopy. Under UV irradiation, **2.1** (*p*-B-ppy) and **2.2** (*p*-ppy-B) both display blue

luminescence in solution (CH_2Cl_2) at ambient temperature with λ_{max} = 409 nm (Φ = 0.16) for **2.1** and 412 nm (Φ = 0.01) for **2.2**. As shown in Figure 2.24, the emission band of **2.1** has a strong dependence on the solvent polarity with λ_{max} shifting from 374 nm in hexane to 425 nm in DMF (λ_{ex} = 344 nm), indicating a polarized excited state and the charge transfer emission. In contrast, the emission of **2.2** (Figure 2.25) is much less solvent-dependent emission, from 409 nm in hexane to 425 nm in DMF (λ_{ex} = 345 nm), indicating a less polarized excited state than that of **2.2**.
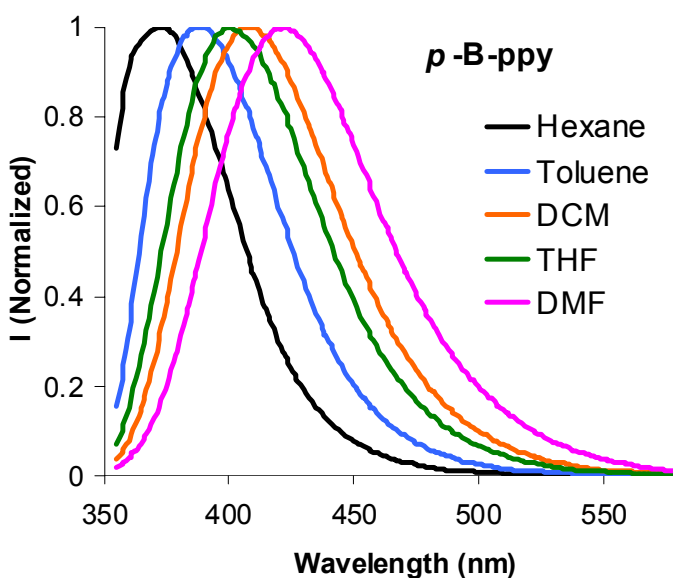
Figure 2.24 The normalized emission spectra of **2.1** in various solvents with λ_{ex} = 345 nm, concentration = ~1.0 x 10^{-5} M.
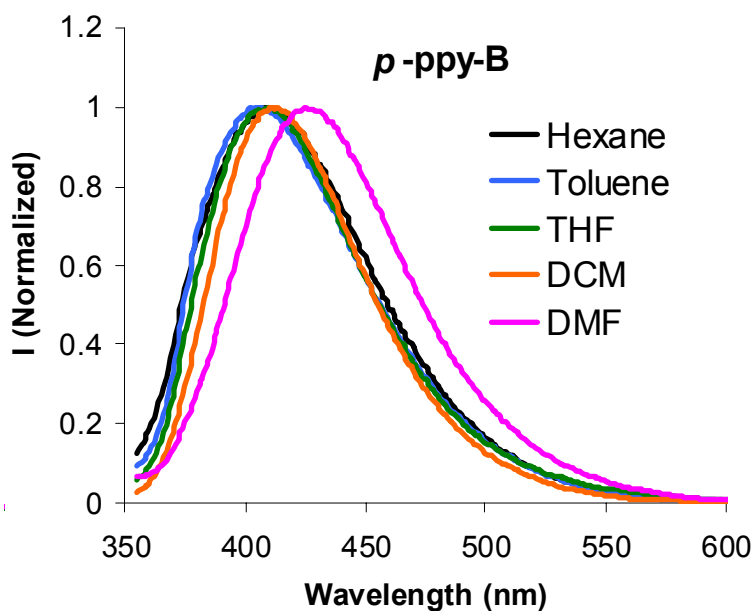
Figure 2.25 The emission spectra of **2.2** in various solvents with λ_{ex} = 345 nm, concentration = ~1.0 x 10^{-5} M.

2.3.6.2 Pt(II) complexes 2.1a, 2.1b, 2.1c, 2.2a, 2.2b, and 2.2c.

In contrast to the free ligands, the emission of the Pt(II) complexes are all dominated by phosphorescence. The luminescence data of the complexes are summarized in Table 2.4. The emission spectra at ambient temperature under nitrogen and at 77K of the complexes are shown Figure 2.26 and Figure 2.27.
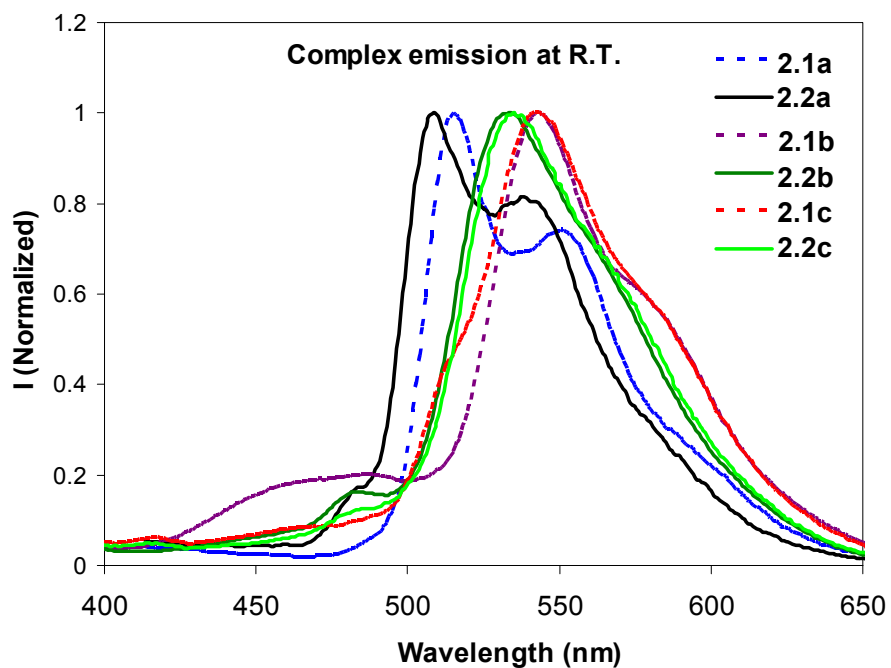
Figure 2.26 Emission spectra of complexes in CH_2Cl_2, 2.0 x 10^{-5} M, under N_2 at 298 K.
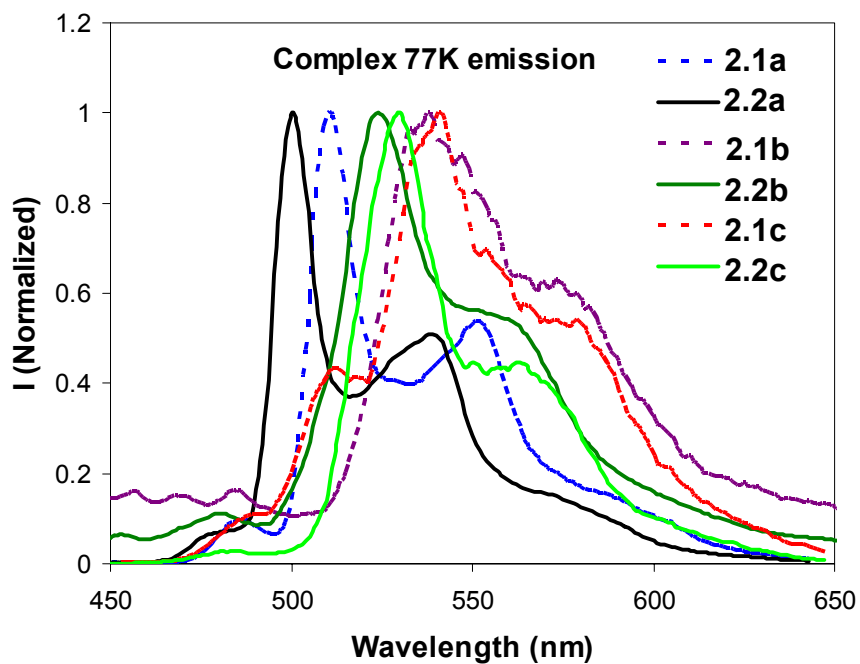
Figure 2.27 Emission spectra of metal complexes in CH_2Cl_2, 2.0 x 10^{-5} M, 77 K.

Table 2.4 Absorption and Luminescence data

Compound	Abs, nm (ε, M^{-1}cm^{-1})	λ_{em}, nm /τ, μs[b] (CH$_2$Cl$_2$, rt)	λ_{em}, nm /τ, μs (CH$_2$Cl$_2$, 77K)	Φ^a (CH$_2$Cl$_2$, rt)
2.1, *p*-B-ppy	326 (2.6 $\times$ 10^4)	409	/	0.16
2.2, *p*-ppy-B	329 (2.3 $\times$ 10^4)	412	/	0.012
2.1a	344 (2.7 $\times$ 10^4) 392 (5.4 $\times$ 10^3)	515 /14.7(1)	511 /28.2(1)	0.004
2.2a	345 (2.5 $\times$ 10^4) 394 (8.3 $\times$ 10^3)	509 /24.1(1)	501 /40.2(1)	0.01
2.1b	343 (2.3 $\times$ 10^4) 411 (4.1 $\times$ 10^3)	543 /7.1(1)	538 /13.4(2)	0.03
2.2b	345 (2.7 $\times$ 10^4) 425 (7.1 $\times$ 10^3)	534 /8.1(1)	525 /14.0(1)	0.03
2.1c	343 (4.7 $\times$ 10^4) 411 (1.3 $\times$ 10^4)	543 /8.8(2)	541/13.1(1)	0.006
2.2c	344 (5.7 $\times$ 10^4) 425 (1.5 $\times$ 10^4)	535 /7.1(1)	530 /12.5(1)	0.003

[a]The quantum efficiency for the free ligands was obtained under air using 9,10-diphenylanthracene as the standard. For the Pt(II) complexes, the quantum efficiency was measured under N$_2$ using Ir(ppy)$_3$ as the standard (Φ = 0.40).[9a]

[b]The decay lifetime at r.t. for the Pt(II) complexes was measured under N$_2$.

For **2.1a** and **2.2a** well-resolved vibronic fine features are observed in the emission spectra at ambient temperature, indicative of ligand-centered emission. For **2.1b**, **2.2b**, **2.1c** and **2.2c**, the ambient temperature emission spectra are broader than those of **2.1a** and **2.2a** and the vibronic fine features are less obvious. However, at 77 K the emission spectra of all Pt(II) complexes (Figure 2.27) have well defined vibrational features, supporting that ^{3}LC (ligand-centered) emission dominates in these complexes. The fact that the emission maxima of the Pt(II) complexes show little change with temperature also supports that the emission is dominated by ^{3}LC excited state since MLCT dominated emission is known to show a greater dependence on temperature.[14] There is a notable shoulder peak in the emission spectrum of **2.1b** at ~485 nm at 298 K which is resolved with fine vibronic features at 77 K. This peak is insensitive to oxygen, thus attributed to ligand based singlet emission.

For a given ancillary ligand, the emission maximum of the *p*-B-ppy complexes is in general red-shifted by a few nanometers, compared to the *p*-ppy-B complexes. This trend is opposite that of the MLCT absorption band in the UV-Vis spectra. Since the luminescence was dominated by the ^{3}LC excited state, the emission red shift of the *p*-B-ppy complexes relative to those of *p*-ppy-B can be attributed to the greater polarized excited state of the former, as revealed by the free ligands.

For either *p*-B-ppy or *p*-ppy-B complexes, the emission maxima of the 4,4'-bipy and py complexes are similar but about 30 nm red shifted, compared to the corresponding DMSO complexes. This trend is consistent with that of the MLCT band observed in the

UV-vis absorption spectra. Hence, some MLCT contributions to the phosphorescent emission band are very likely.

Compared to Pt(ppy)(acac) and its derivatives,[5a] the quantum efficiency of complexes **2.1a**, **2.1b**, **2.2a** and **2.2b** are either much lower or comparable, which may be attributed to their much longer decay lifetimes (~13 to 40 μs), about 10 times greater than those of Pt(ppy)(acac) and its derivatives. Although the diplatinum complexes **2.1c** and **2.2c** have similar absorption and emission spectra as the corresponding monoplatinum complexes **2.1b** and **2.2b**, their emission quantum efficiency is however much lower than the mononuclear complexes, which may be attributed to intramolecular triplet-triplet quenching.

2.3.7 Molecular orbital calculations

To better understand the origin of the electronic transitions in the free ligands and the metal complexes, DFT calculations for ligands **2.1** (*p*-B-ppy) and **2.2** (*p*-ppy-B) and their Pt(II) complexes **2.1b** and **2.2b** were performed.

The HOMO and LUMO diagrams of **2.1** and **2.2** are shown in Figure 2.28. The HOMO of **2.1** consists of contributions nearly exclusively from the mesityls while the LUMO is dominated by the p_π orbital of the boron atom with significant contributions from the pyridyl and phenyl ring. The LUMO level of **2.2** closely resembles that of **2.1**, but the HOMO level has significant contributions from the pyridyl ring, in addition to the mesityls. Hence, although the lowest electronic transition for both **2.1** and **2.2** may be

described as charge transfer from mesityl to the B-ppy or ppy-B unit, but for **2.2**, due to the direct conjugation of the pyridyl ring with the B atom, its excited state is less polarized than **2.1**, thus explaining the greater solvent-dependent emission of **2.1**.

HOMO of B-ppy **(2.1)**   LUMO of B-ppy **(2.1)**

HOMO of ppy-B **(2.2)**   LUMO of ppy-B **(2.2)**
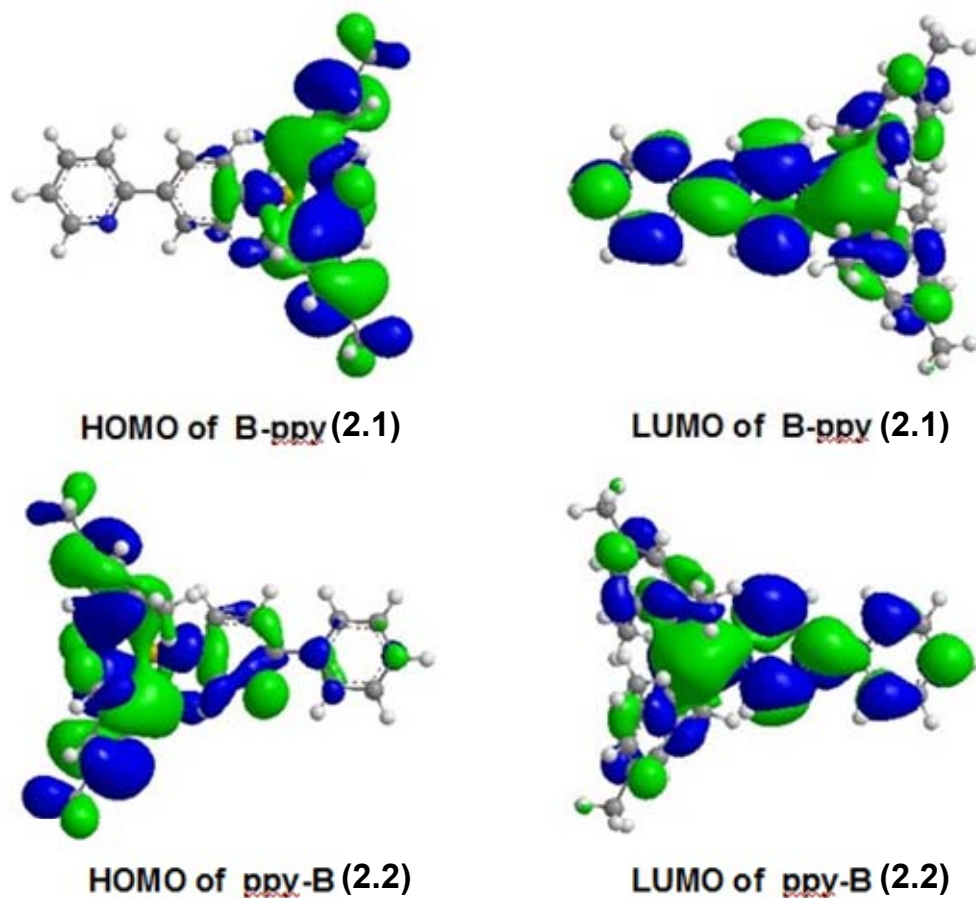
Figure 2.28 HOMO and LUMO orbitals of free ligands **2.1** and **2.2**, plotted with a 0.015 iso-contour value.

For the molecular orbital of metal complexes (Figure 2.29), the HOMO of **2.1b** is dominated by the π orbitals of the phenyl group with some contributions from the Pt(II) *d* orbitals. However, HOMO-1 which is very close in energy to HOMO (0.001 Hartree difference) is a π orbital centered on the phenyl portion of the ppy chelate with significant *d* orbital contributions of the Pt(II) ion. The LUMO of **2.1b** is a π* orbital dominated by the B atom and the ppy chelate with significant contributions from the py ligand. For **2.2b**, HOMO and HOMO-1 are nearly identical in energy (0.0007 Hartree difference) with HOMO being the π orbital localized on the ppy ring and the Pt atom and HOMO-1 being the phenyl π orbital with some Pt *d* orbital contributions. The LUMO of **2.2b** is a π* orbital similar to that of **2.1b** but without significant contributions from the py ligand. Hence, the lowest electronic transitions in **2.1b** and **2.2b** likely involve both π→π* transitions localized on the B-ppy chelate and inter-ligand charge transfer from phenyl to the B-ppy ligand, with MLCT contributions in both transitions. This is in agreement with the UV-Vis and luminescent data.

2.1b   **2.2b**

LUMO

HOMO

HOMO-1
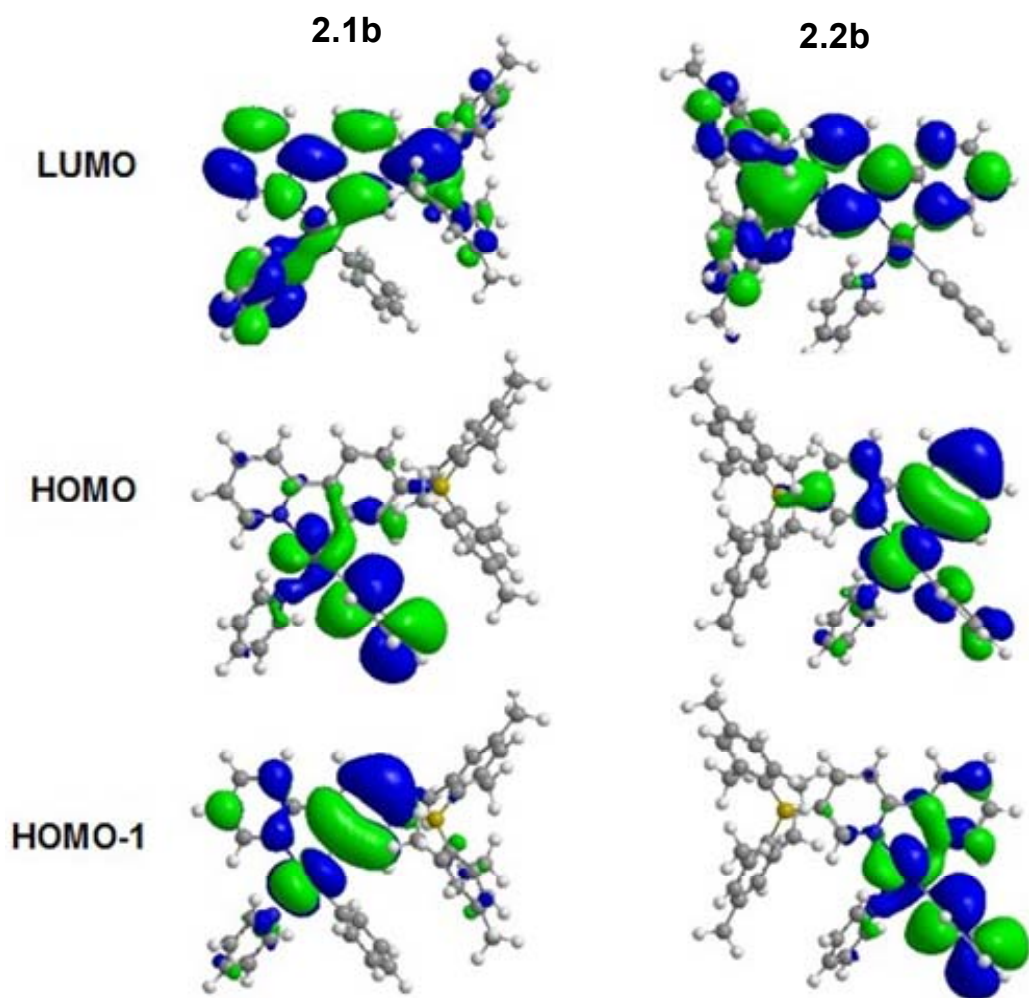
Figure 2.29 HOMO and LUMO orbitals of **2.1b**, **2.2b**, plotted with a 0.015 iso-contour value.

2.3.8 Lewis acidity---response to fluoride ions of ligands 2.1 and 2.2

The interactions of ligands and metal complexes with fluoride ions were examined by UV-Vis absorption spectra titration, fluorescent and phosphorescent titrations and ^{1}H and ^{19}F NMR titrations.

2.3.8.1 UV-Vis absorption spectral titration by fluoride

As shown in Figure 2.30 and Figure 2.31, upon addition of TBAF in CH_2Cl_2, the low energy absorption band belonging to π to p_π-π^* transition at 327 nm and 330 nm, respectively, in the spectra of **2.1** (*p*-B-ppy) and **2.2** (*p*-ppy-B), is quenched and blue-shifted. The saturation point is reached for both compounds with ~0.7 eq. F$^-$ added, an indication that both molecules bind to fluoride fairly strongly. Nonetheless, the Stern-Volmer plot (A/A$_o$ versus the equivalents of F$^-$ added) (Figure 2.32) shows clearly that the **2.2** has a somewhat stronger binding toward F$^-$ than **2.1**, which is consistent with its greater electron accepting ability as established by the CV data. The binding constants of *p*-B-ppy and *p*-ppy-B with fluoride have been found to be 5×10^7 M^{-1}, 6×10^7 M^{-1}, respectively, thus demonstrating that the direct conjugation of a pyridyl ring with the BMes$_2$ group is more efficient in enhancing the Lewis acidity of the boron center than the phenyl group.
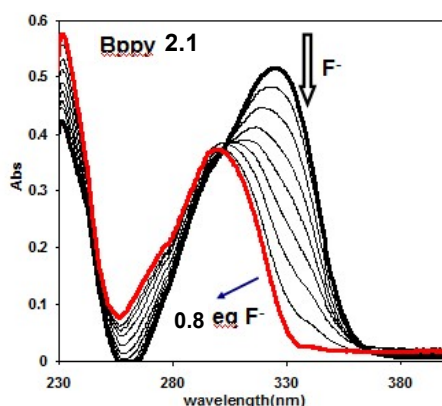
Figure 2.30 UV-Vis spectral change of **2.1** (2.0 x 10^{-5} M) with the addition of NBu$_4$F in CH_2Cl_2.
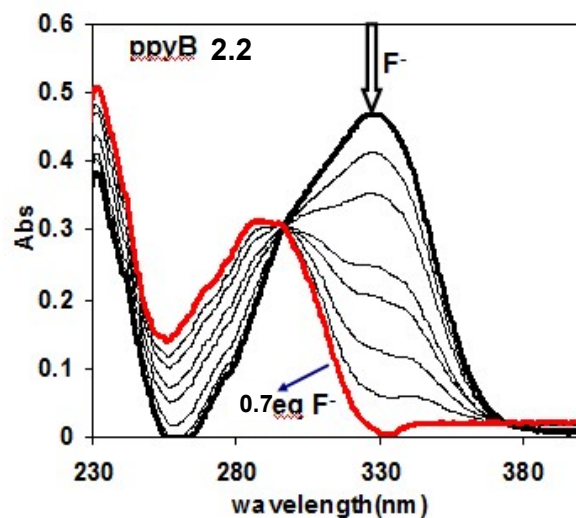
Figure 2.31 UV-Vis spectral change of **2.2** (2.0×10^{-5} M) with the addition of NBu$_4$F in CH$_2$Cl$_2$.
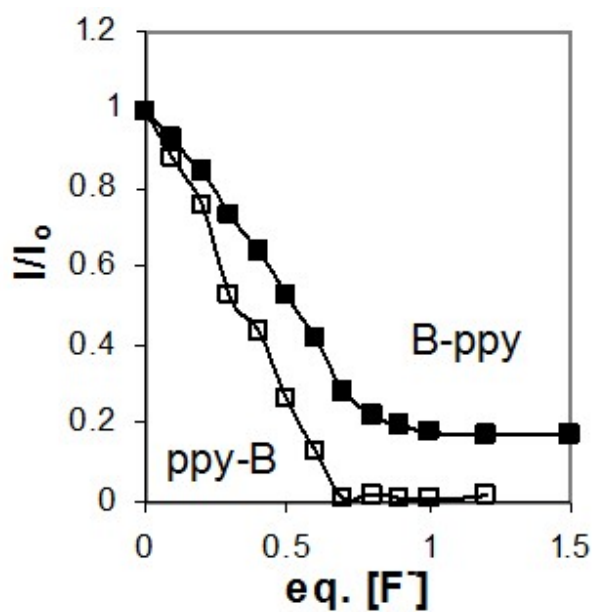
Figure 2.32 Fluoride titration graph of **2.1** and **2.2** from UV-Vis absorption spectra.

2.3.8.2 Fluorescent spectra of titration by fluoride

In the fluorescent spectra (Figure 2.33 and Figure 2.34), the emission band of both **2.1** and **2.2** undergoes similar quenching with the addition of fluoride. The emission quenching is due to that the vacant p_π orbital at boron center is blocked by fluoride, resulted in the dimishment of intramolecular charge transfer emission. Again, **2.2** shows a slightly stronger binding with fluoride than **2.1** does, as demonstrated in the Stern-Volmer plot in Figure 2.35.
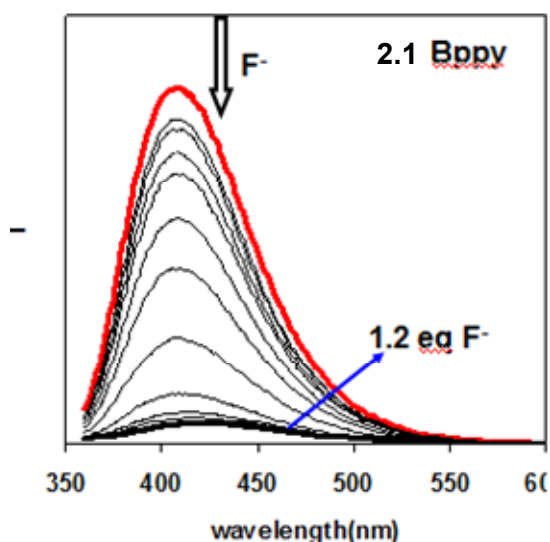
Figure 2.33 Fluorescent spectral change of **2.1** (2.0 x 10^{-5} M) with the addition of NBu$_4$F in CH$_2$Cl$_2$.
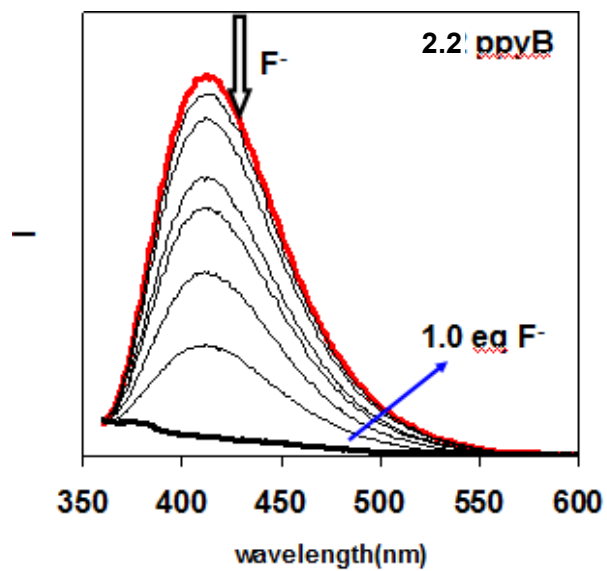
Figure 2.34 Fluorescent spectral change of **2.2** (2.0 x 10^{-5} M) with the addition of NBu$_4$F in CH$_2$Cl$_2$.

Figure 2.35 Stern-Volmer plots at λ_{max} from fluorescent spectra for both **2.1** and **2.2**.

2.3.9 Lewis acidity---response to fluoride ions of metal complex 2.1a, 2.1b, 2.1c, 2.2a, 2.2b, 2.2c

2.3.9.1 UV-Vis absorption spectra of titration by fluoride

Unlike the free ligands, the response of the Pt(II) complexes **2.1a** and **2.2a** toward fluorides is quite different.

(1) Complexes with ligand **2.2** have stronger Lewis acidity than those of ligand **2.1**.

As shown by the UV-vis spectra in Figure 2.36, the addition of excess TBAF (~1.5 eq.) to the solution of **2.1a** causes only 20% decrease of the intense π to $\pi*$ peak at 347 nm and very little change of the MLCT band between 380-450 nm. In contrast, both π to $\pi*$ and MLCT bands in **2.2a** experience about 80% decrease of intensity and reach saturation point with ~1 eq. F⁻. The stronger binding ability of **2.2a** was demonstrated from the Stern-Volmer plot (A/A_o versus the equivalents of F⁻ added) (Figure 2.37).

The same trend was also observed between **2.1b** and **2.2b**, **2.1c** and **2.2c**, as shown by the titration spectra and the Stern-Volmer plots in Figure 2.38, Figure 2.39 and Figure 2.40. The apparent weaker response of the *p*-B-ppy Pt(II) complexes toward fluoride can be attributed to the weaker electron accepting ability of the boron center in the *p*-B-ppy complexes, relative to that of the *p*-ppy-B complexes, as supported by the CV data. The stability constants for the binding of one fluoride ions to **2.1a**, **2.1b**, **2.2a** and **2.2b** hosts in CH_2Cl_2 were determined from the UV-Vis titrations, fitting the absorbance changes at several wavelengths.[17] The binding constants of **2.1a**, **2.1b**, **2.2a** and **2.2b** have been found to be $9\times10^5\,M^{-1}$, $1\times10^5\,M^{-1}$, $7\times10^7\,M^{-1}$, $8\times10^7\,M^{-1}$, respectively.
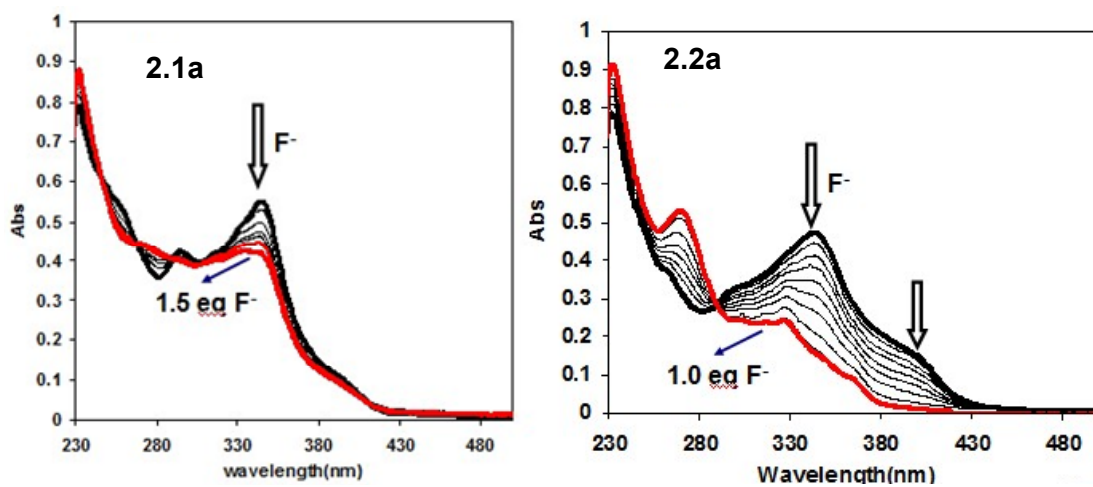
Figure 2.36 The UV-vis spectral change of of **2.1a** (left) and **2.2a** (right) $(2.0 \times 10^{-5}$ M) with the addition of NBu_4F in CH_2Cl_2.
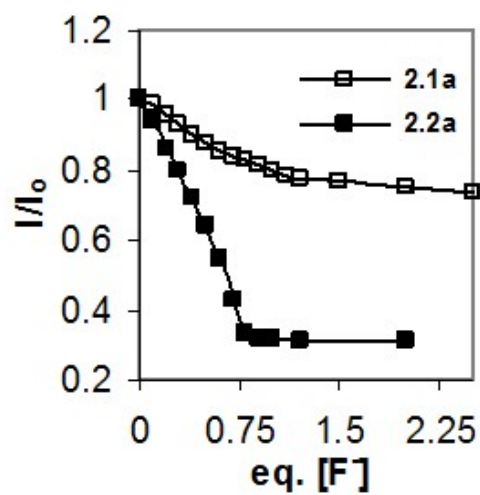
Figure 2.37 Fluoride titration spectrum from UV-Vis absorption spectra for both **2.1a** and **2.2a**.
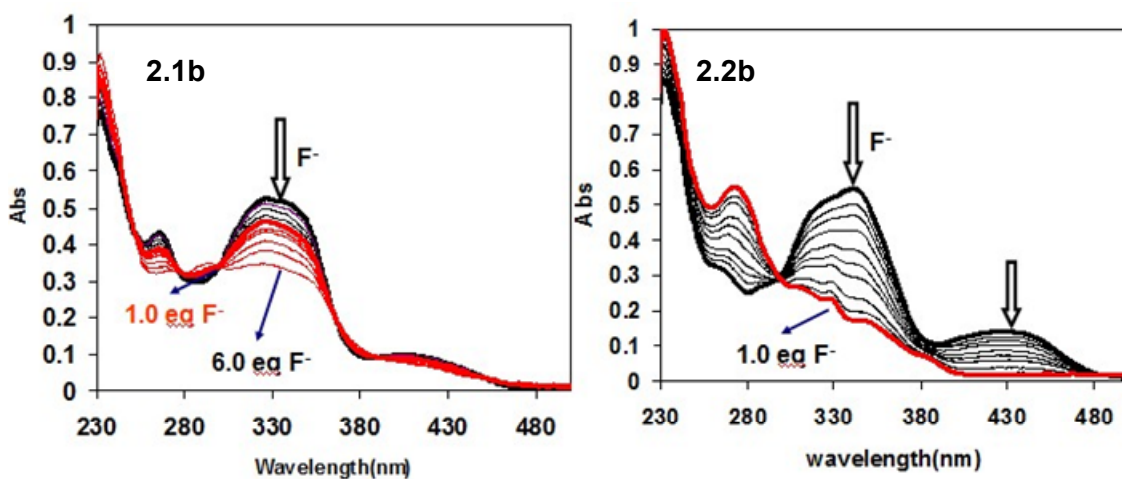
Figure 2.38 The UV-vis spectral change of of **2.1b** (left) and **2.2b** (right) (2.0×10^{-5} M) with the addition of NBu_4F in CH_2Cl_2.
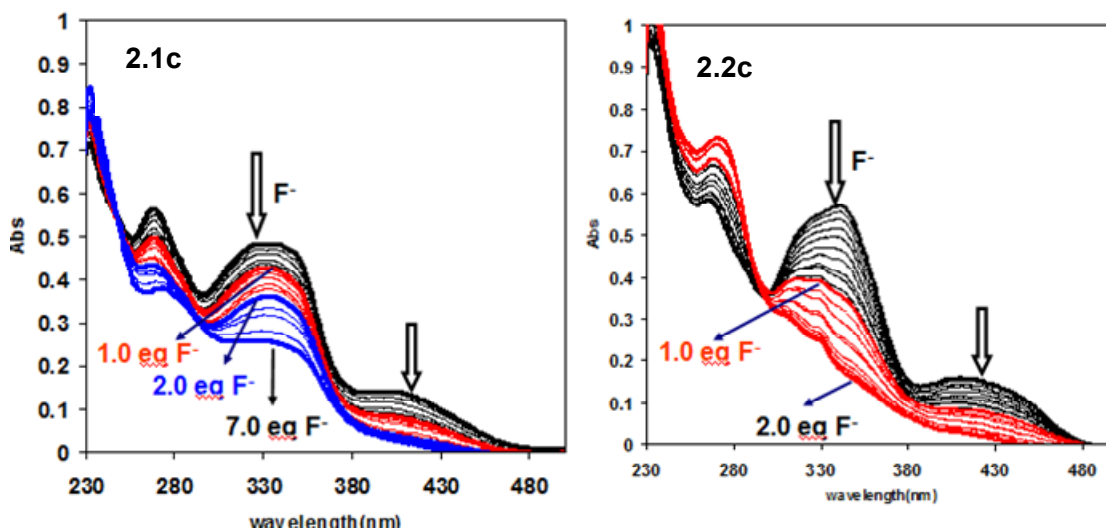
Figure 2.39 The UV-vis spectral change of of **2.1c** (left) and **2.2c** (right) (1.0×10^{-5} M) with the addition of NBu_4F in CH_2Cl_2.
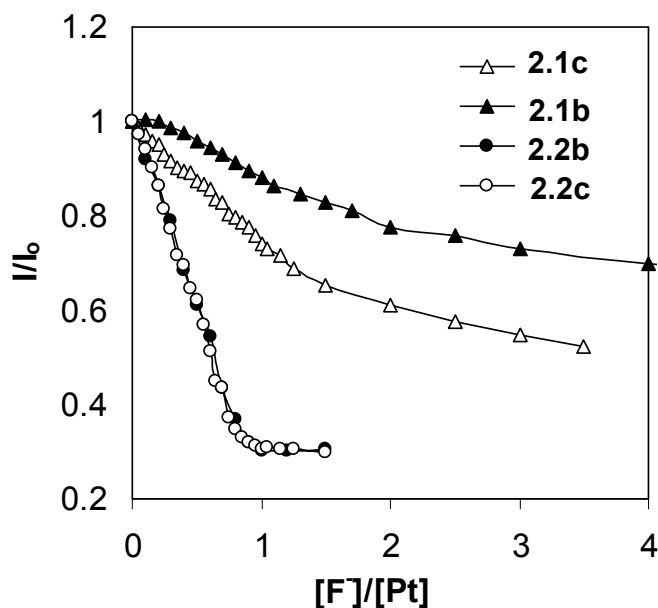
Figure 2.40 Stern-Volmer plots at λ_{max} from UV-Vis absorption spectra for **2.1b**, **2.1c**, **2.2b** and **2.2c**.

(2) Comparison between complexes **2.1a**, **2.1b**, **2.1c** and their free ligand **2.1**.

      However, compared to the free *p*-B-ppy ligand, the response of **2.1a**, **2.1b** and **2.1c** toward fluoride is much weaker. This can be explained by steric factors. The BMes$_2$ group in the complexes is sterically more constrained, compared to that in the free ligand. As a result, if both ligand and the complex show similar reduction potentials, the Lewis acidity of the metal complexes would be lower than the free ligand due to the greater steric interaction imposed by the binding of fluoride in the complex, which is the case for the *p*-B-ppy complexes.

(3) Comparison between mononulclear py and dinuclear bipy Pt(II) complexes .

The difference between the mononuclear Pt(II) complex **2.2b** and the corresponding dinuclear bipy complex **2.2c** is that the amount of F⁻ needed to reach the saturation point for **2.2c** is about twice of that for **2.2b** due to the presence of two boron acceptor centers.

Nonetheless, the Stern-Volmer plots of I/I_o (at 345 nm) against the amount of fluoride ions per Pt atom shown in Figure 2.33 indicate that the two boron centers in **2.2c** respond to fluoride ions as if they were two fully independent boron units with binding strength identical to that of the mononuclear Pt(II) compound **2.2b**, thus supporting that there is little electronic communication between the two boron centers in the dinuclear Pt(II) complexes. This conclusion can also be reached by the essentially identical change of the UV-vis spectra of **2.2b** and **2.2c** with fluoride ions shown in Figure 2.38 and Figure 2.39.

In contrast, the UV-Vis spectral change of **2.1b** and **2.1c** has a notable difference: for **2.1b** several isobestic points are present in the 280-500 nm regions while for **2.1c** they are absent. Furthermore, the Stern-Volmer plots for **2.1b** and **2.1c** shown in Figure 2.40 do not overlap with **2.1c** showing somewhat greater response toward F⁻.

Based on these data, we can conclude that some degree of electronic communication is present between the two boron centers in **2.1c**. The apparent lack of electronic communications between the two Pt(II) units in **2.2c** is likely caused by the strong steric interactions, which is much reduced in **2.1c**, making electronic communications between the two Pt(II) units via the bipy bridge possible in the latter.

93

2.3.9.2 Phosphorescent spectra of titration by fluoride.

Due to the difficulty of carrying out phosphorescent titration in an oxygen-free environment, the phosphorescent titration experiments were performed for the py and the bipy complexes only. The phosphorescent data provide qualitative information concerning the impact of the fluoride ions on luminescence, but they are not accurate in terms of stoichiometry due to the difficulty of controlling concentrations when preparing and transporting the sample for each addition of fluoride in and out of a dry box.

Nonetheless, the titration data shown in Figure 2.41 illustrates that the addition of fluoride shifts the emission peak to a shorter wavelength for both **2.1b** and **2.2b**, with the emission color changing from yellow-green to blue-green. The fluoride adduct emission spectrum (λ_{max} = 489 nm) of **2.2b** is similar to that of Pt(ppy)L$_2$ complexes reported by Thompson and coworkers,[5] and attributable to ppy-centered emission. Thus, the fluoride addition switches the ppy-B ligand based phosphorescence to ppy-based phosphorescence by blocking the boron center. The fluoride adduct spectrum of **2.1b** is more complex with contributions not only from the ppy phosphorescence but also the ligand-based singlet emission band. The general trend of the phosphorescent response of **2.1b** and **2.2b** toward fluoride ions is similar to the N,C-chelate complex[3a] Pt(*N,C*-BNPA)Ph(SMe$_2$), reported recently by us.
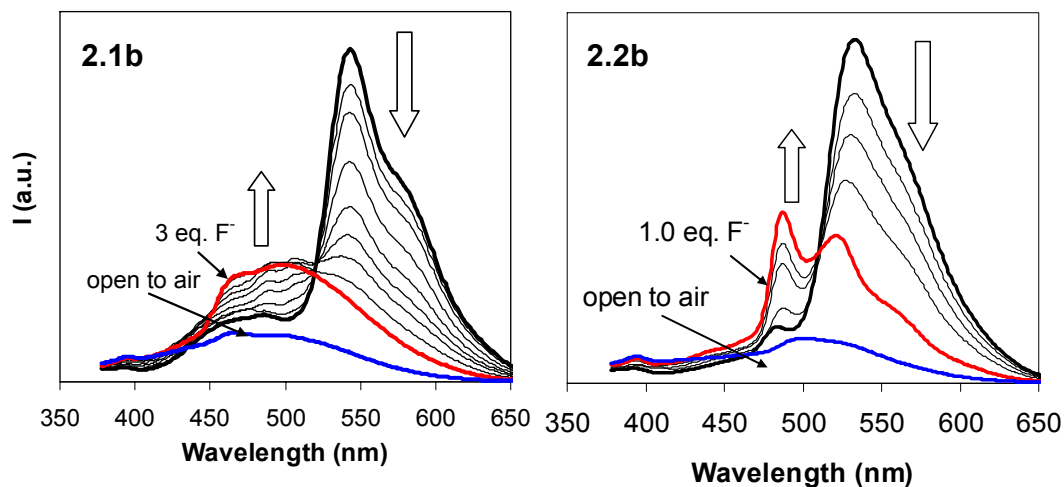
Figure 2.41 Phosphorescent emission spectral change of Pt(II) complexes **2.1b** and **2.2b** with the addition of NBu$_4$F in CH$_2$Cl$_2$ under N$_2$ at ambient temperature.

As shown in Figure 2.42, the phosphorescent titration spectra of the dinuclear complexes **2.1c** and **2.2c** display some unique features that are not observed in **2.1b** and **2.2b**. For **2.1c**, the emission spectrum initially gains intensity greatly with the addition of fluoride. Further addition of fluorides leads to the decrease of emission intensity and the final emission spectrum of the fluoride adduct resembles that of the **2.1b** fluoride adduct, clearly due to the formation of the 2:1 adduct. The high energy emission band with distinct vibrational features in the **2.1c** fluoride adduct is attributed to 4,4'-bipy. The 4,4'-bipy emission spectra is shown in Figure 2.43.

95
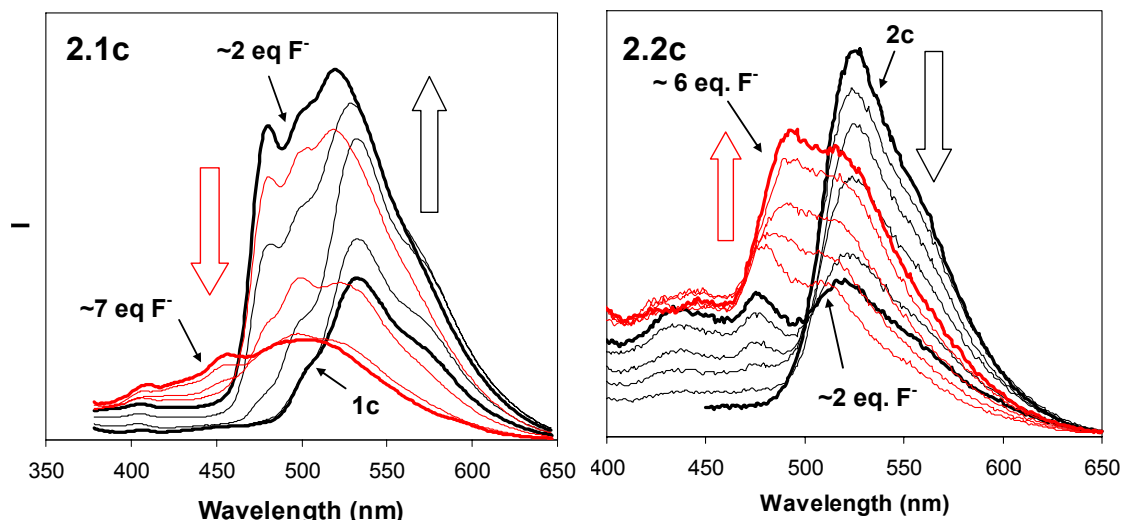
Figure 2.42 Phosphorescent emission spectral changes of Pt(II) complexes **2.1c** and **2.2c** with the addition of NBu$_4$F in CH$_2$Cl$_2$ under N$_2$ at ambient temperature.
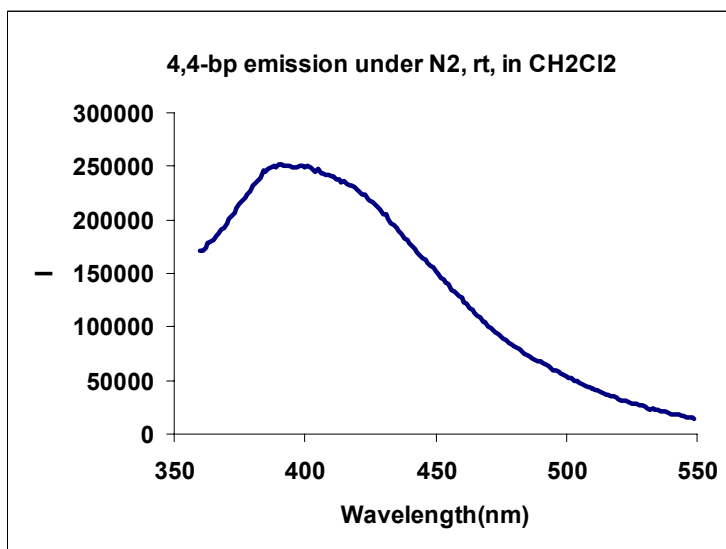
Figure 2.43 Emission spectra of 4,4'-bipyrine in CH$_2$Cl$_2$ under N$_2$ at ambient temperature.

The initial rise of the emission intensity of **2.1c** with F⁻ may be explained by the formation of the 1:1 adduct which, if behaves like **2.1b** should have a much greater emission efficiency than **2.1c**, thus a great enhancement of the emission. The fluoride ions may be therefore described as the "activator" for the emission of the 1:1 complex. This "activation" effect is only possible through electronic communication between the two Pt(II) units in the same molecule. Thus, the phosphorescent response of **2.1c** toward fluoride is consistent with the UV-vis titration data.

2.3.9.3 NMR study of titration by fluoride.

To verify that the fluoride ions are indeed bound to the boron center in the metal complexes, we carried out NMR spectral titration experiments in CD_2Cl_2 for all complexes. With the boron moiety on the pyridine ring, complexes **2.2a**, **2.2b**, **2.2c** reached the saturated point upon less amount of fluoride addition compared to that of **2.1a**, **2.1b** and **2.1c** with boron moiety on the phenyl ring. This is another proof that the Lewis acidity of boron center can be further enhanced with boron moiety directly connected to the pyridine ring. The ¹H NMR spectra of all complexes undergo gradual change with the addition of fluoride and become broad due to the equilibrium between bound and nonbound species (see Figure 2.44 to Figure 2.49).
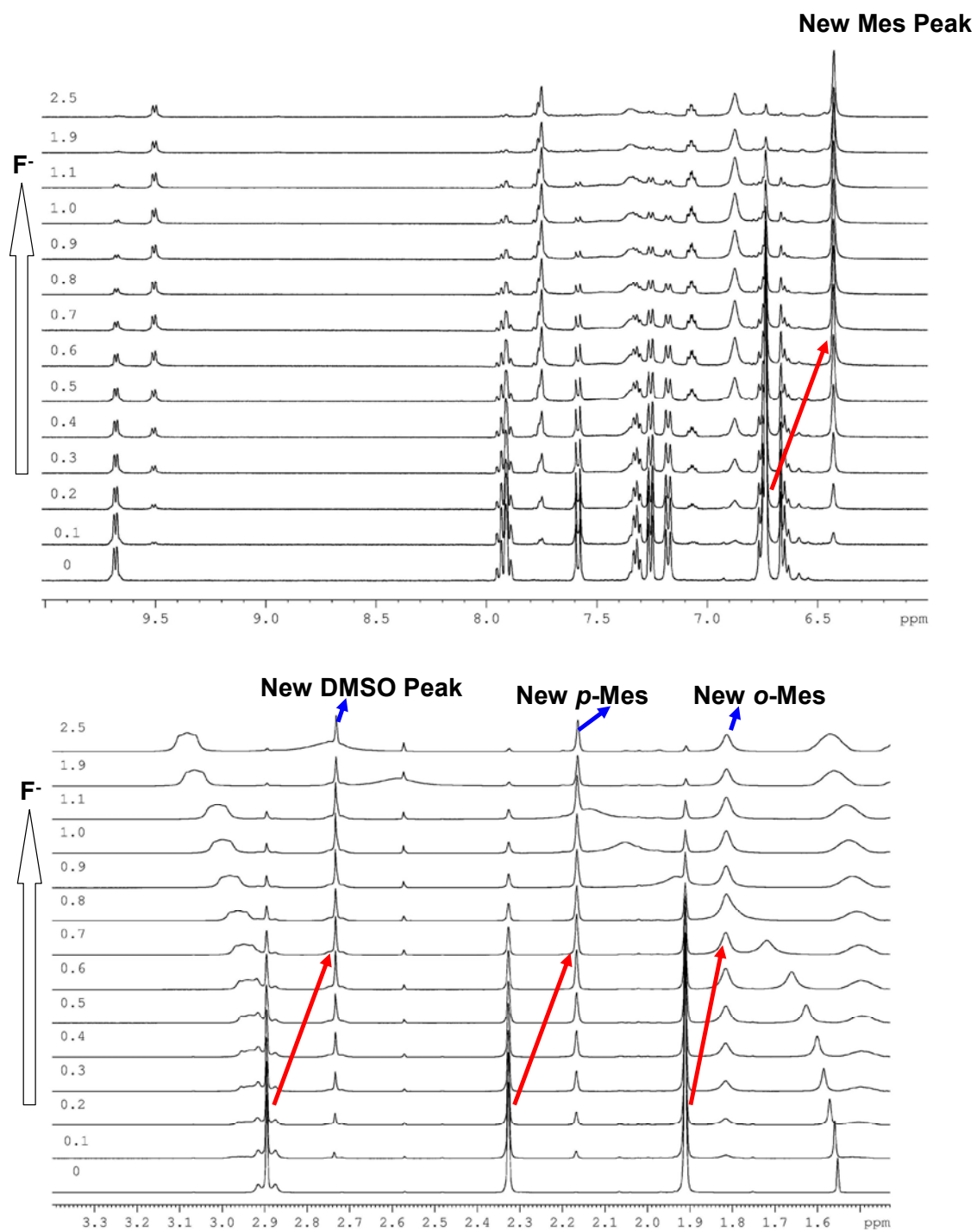
Figure 2.44 The ^{1}H NMR titration spectra of **2.1a** by TBAF in CD_2Cl_2 (Top: aromatic region; Bottom: aliphatic region).

98
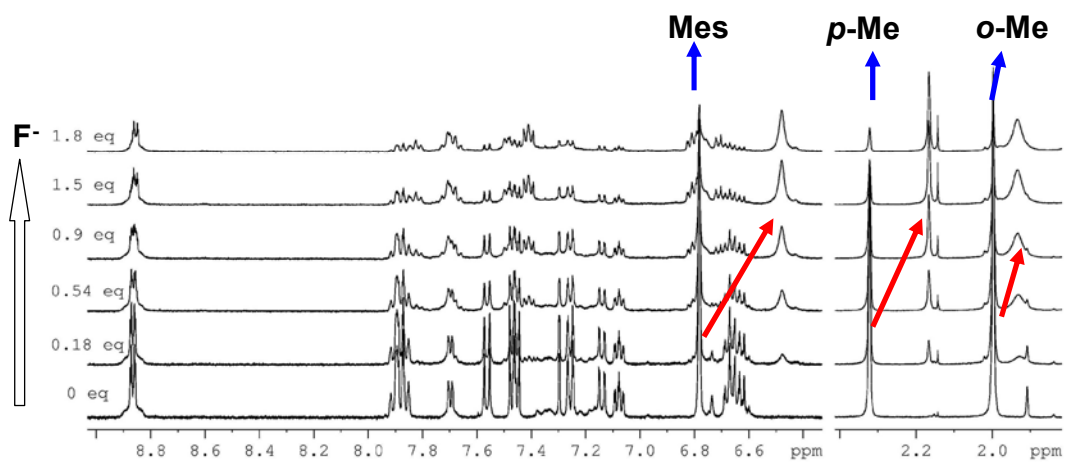
Figure 2.45 The ^{1}H NMR titration spectra of **2.1b** by TBAF in CD$_2$Cl$_2$.
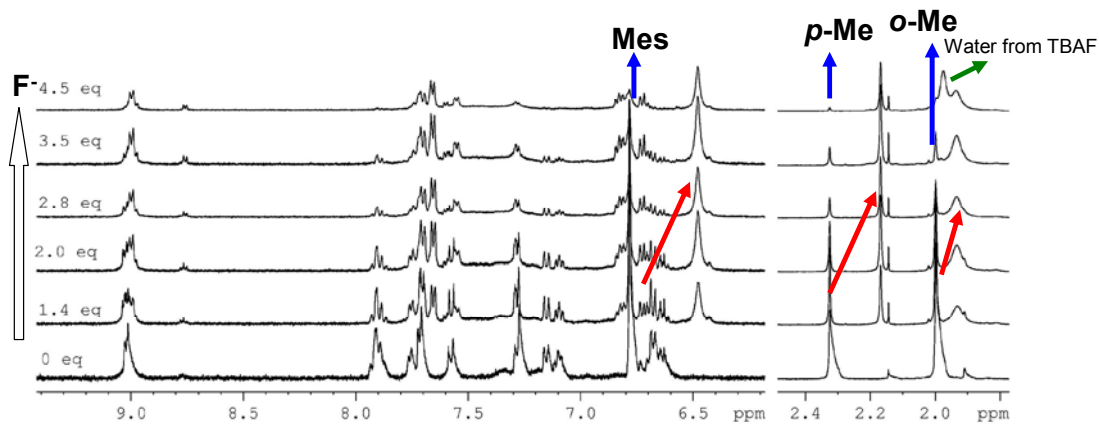
Figure 2.46 The ^{1}H NMR titration spectra of **2.1c** by TBAF in CD$_2$Cl$_2$.
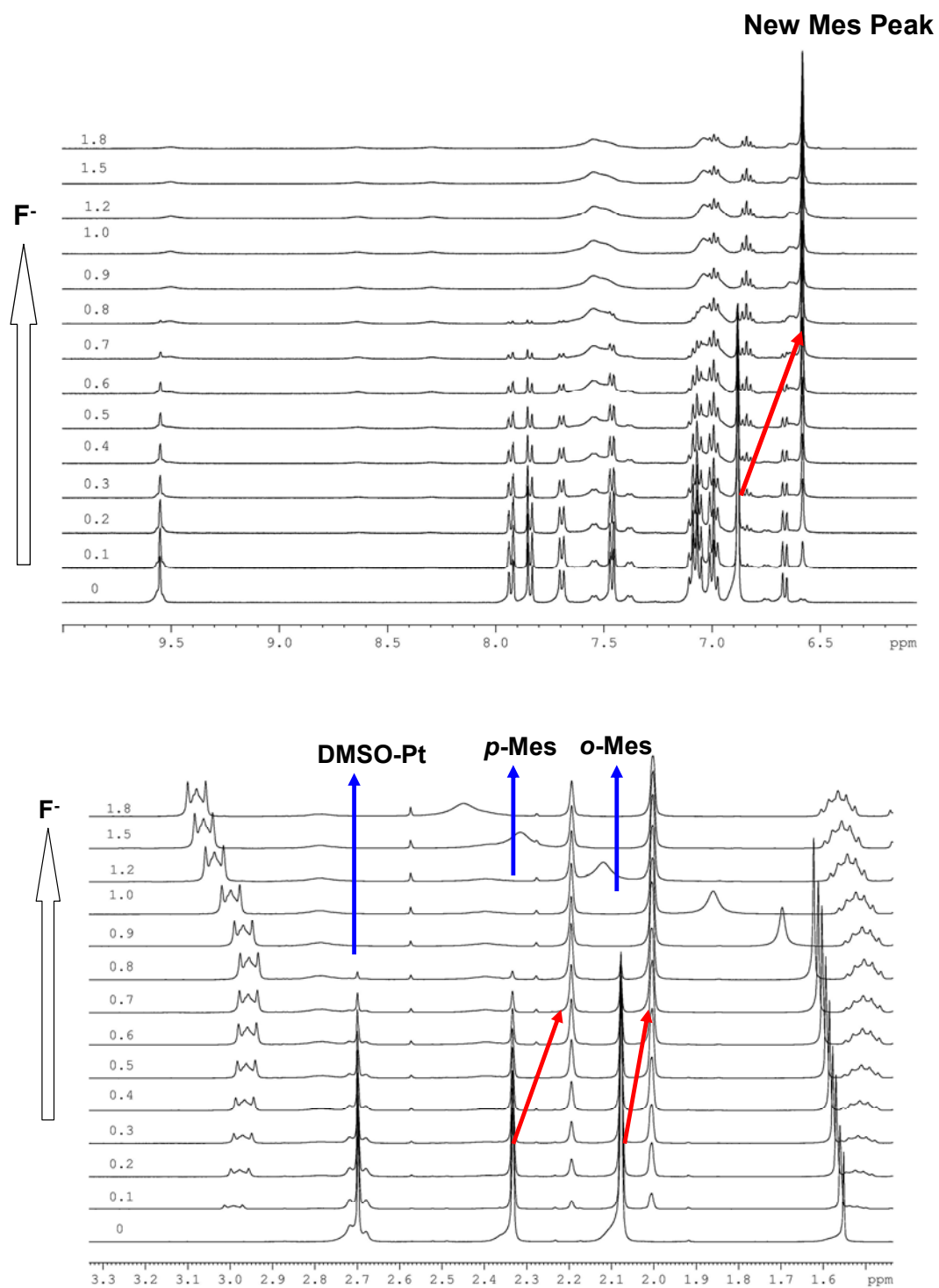
Figure 2.47 The ^1H NMR titration spectra of **2.2a** by TBAF in CD_2Cl_2 (Top: aromatic region; Bottom: aliphatic region).
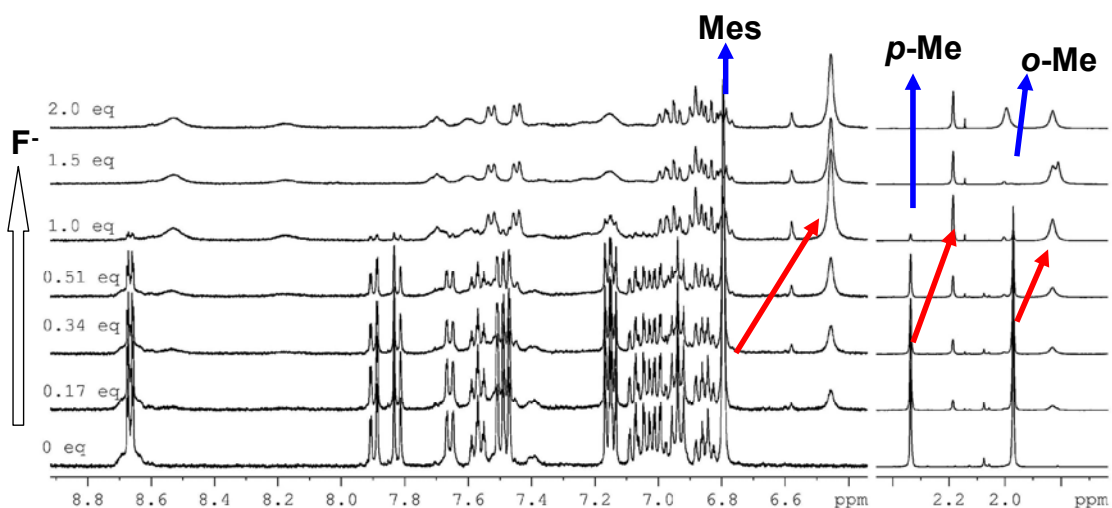
Figure 2.48 The ^{1}H NMR titration spectra of **2.2b** by TBAF in CD$_2$Cl$_2$.
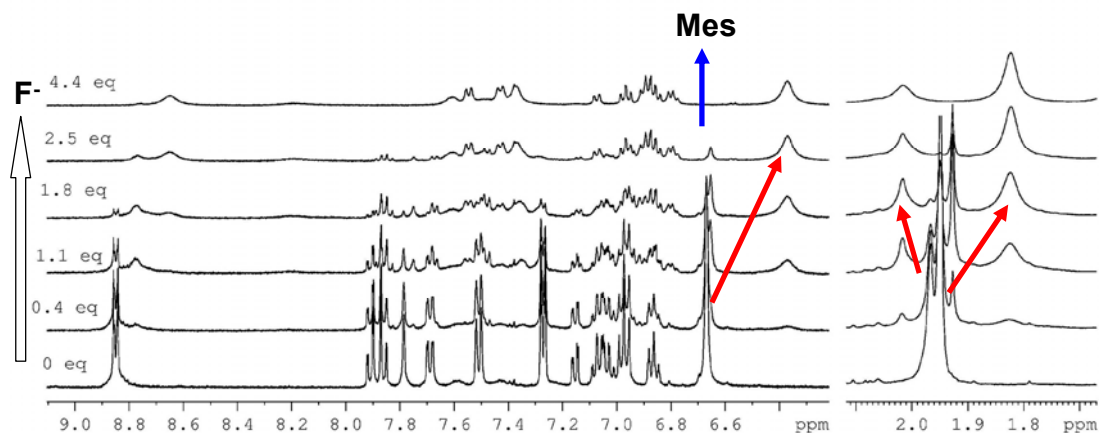
Figure 2.49 The ^{1}H NMR titration spectra of **2.2c** by TBAF in CD$_2$Cl$_2$.

^{19}F NMR data are most informative. Our previous studies have shown that the chemical shift of F$^-$ bound to a B(Ar)Mes$_2$ group appears typically at ~-175 to -180 ppm. The ^{19}F chemical shifts for all complexes upon fluoride binding are summarized in Table 2.1. The ^{19}F NMR data indeed showed that all Pt(II) complexes except **2.2a** display one

characteristic chemical shift at ~ -175 to -178 ppm that grows in intensity with increasing

amount of TBAF added, confirming that the fluoride is indeed bound to the boron center.

The chemical shift for a fluoride bound to a Pt center usually appears in the region of -

230 to -280 ppm, depending on the nature of other ligands and the oxidation state of the

Pt atom, with distinct $^1J_{Pt-F}$ coupling satellites.[15] The absence of any Pt-F signals in ^{19}F

NMR spectra of all Pt(II) complexes further confirmed that the fluoride ion is bound to

the boron center.

Table 2.5 ^{19}F NMR data of the fluoride adducts for all complexes.

Compound	**2.1a**	**2.1b**	**2.1c**	**2.2a**	**2.2b**	**2.2c**
^{19}F, ppm in CD$_2$Cl$_2$	-175.3	-175.8	-176.0	-176.9, -177.7	-177.1	-177.0

For the DMSO complex **2.2a**, two fluoride chemical shifts were observed at -

176.9 ppm and -177.7 ppm with nearly equal intensity in the fluoride adducts, indicating

the possible presence of isomers. Based on the crystal structural data of previously

published fluoride adducts involving a B(Ar)Mes$_2$ group,[16] the two mesityl groups in the

adduct are oriented above and below the B-Ar plane, respectively, to minimize steric

interactions, the F atom lies approximately in the same plane with B-Ar. As a

consequence, if there is sufficient hindered rotation around the B-C(Ar) bond due to the

bulky B(F)Mes$_2$ group, two possible and distinct structures for the fluoride adduct in the

Pt(II) complexes can coexist in solution, as depicted for the *p*-ppy-B complex in Figure

2.50. For **2.2a**, the auxiliary ligand DMSO is on the same side with the B(F)Mes$_2$ group

in the fluoride adduct and is much more sterically demanding than either phenyl or pyridyl, and perhaps as a consequence, both structures **A** and **B** are observed. For *p*-B-ppy complexes the phenyl group is always on the same side with the $BMes_2$ group, which has a steric demand similar to that of py, and as a result, regardless of the nature of the auxiliary ligand L, only one ^{19}F chemical shift is observed. ^{19}F NMR spectra of all complexes are shown here from Figure 2.51 to Figure 2.56.
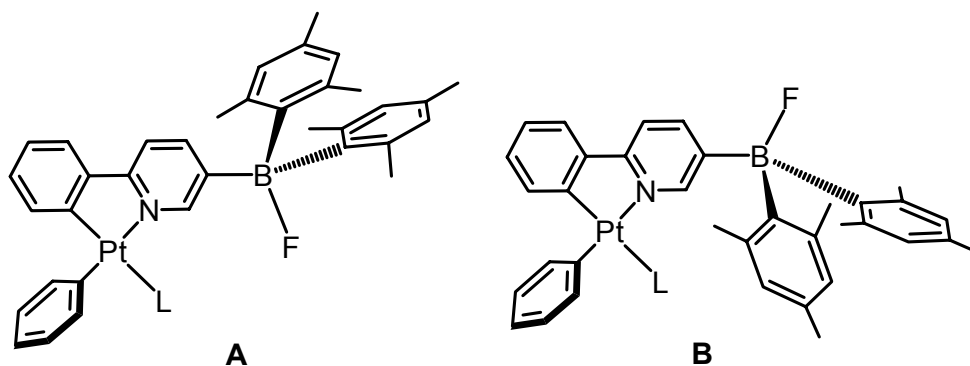
Figure 2.50 Possible structures of **2.2a** upon fluoride binding.
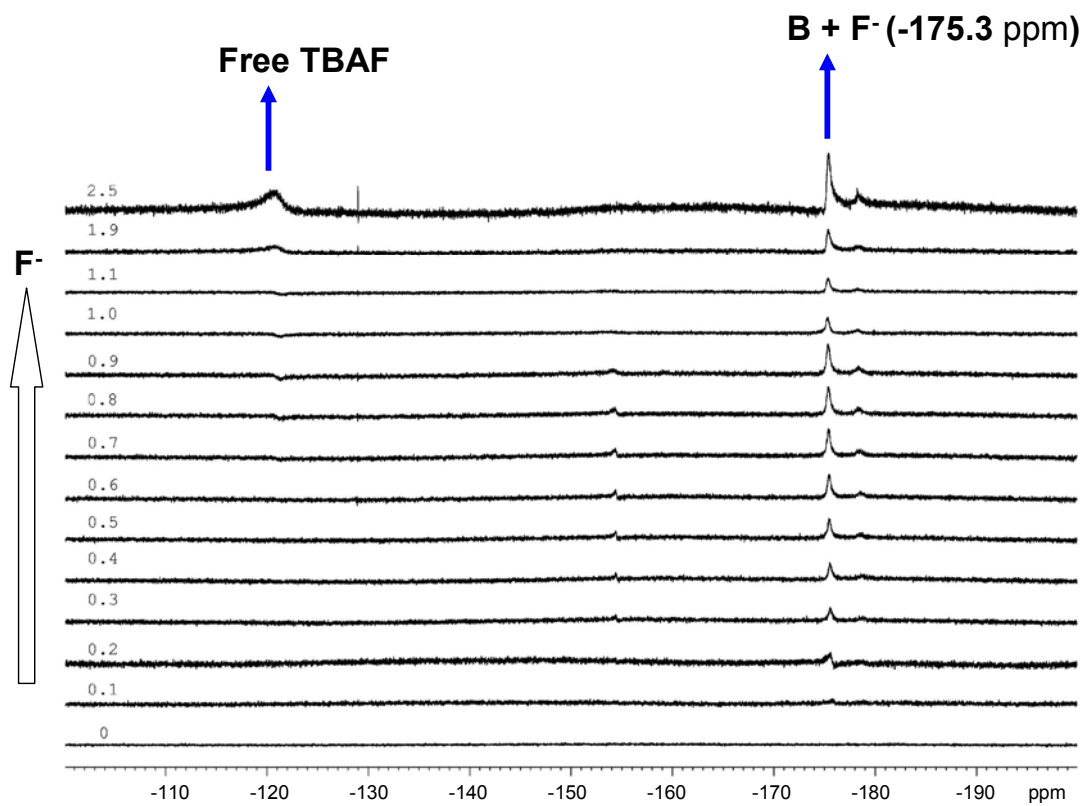
Figure 2.51 The ^{19}F NMR titration spectra of **2.1a** by TBAF in CD$_2$Cl$_2$.
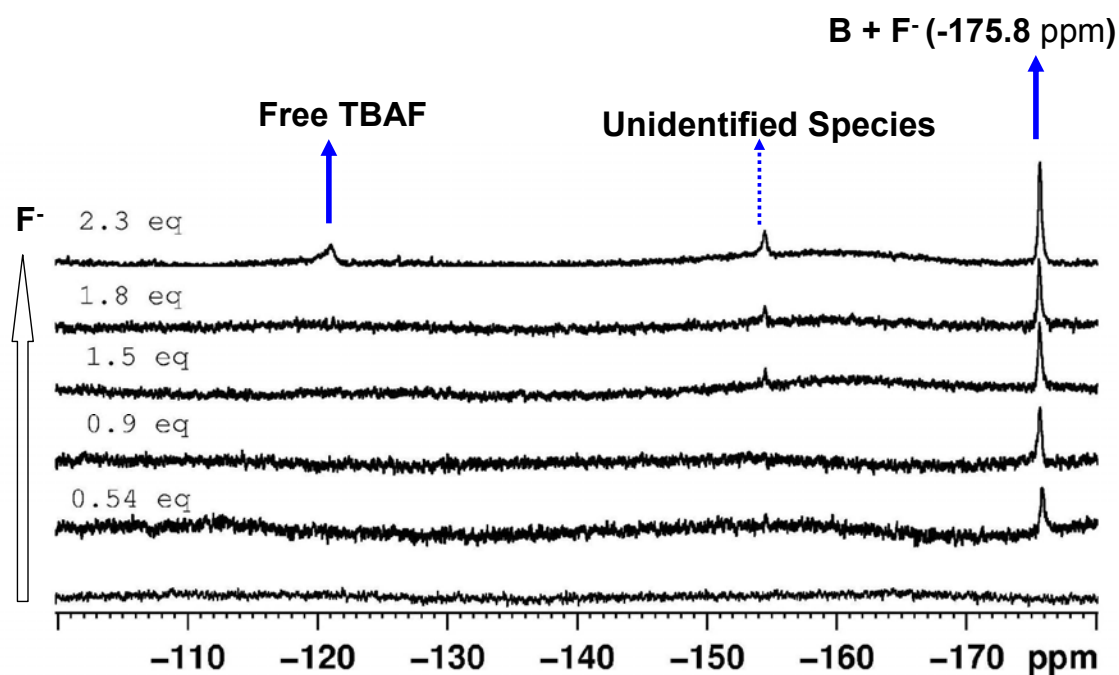
Figure 2.52 The ^{19}F NMR titration spectra of **2.1b** by TBAF in CD_2Cl_2.
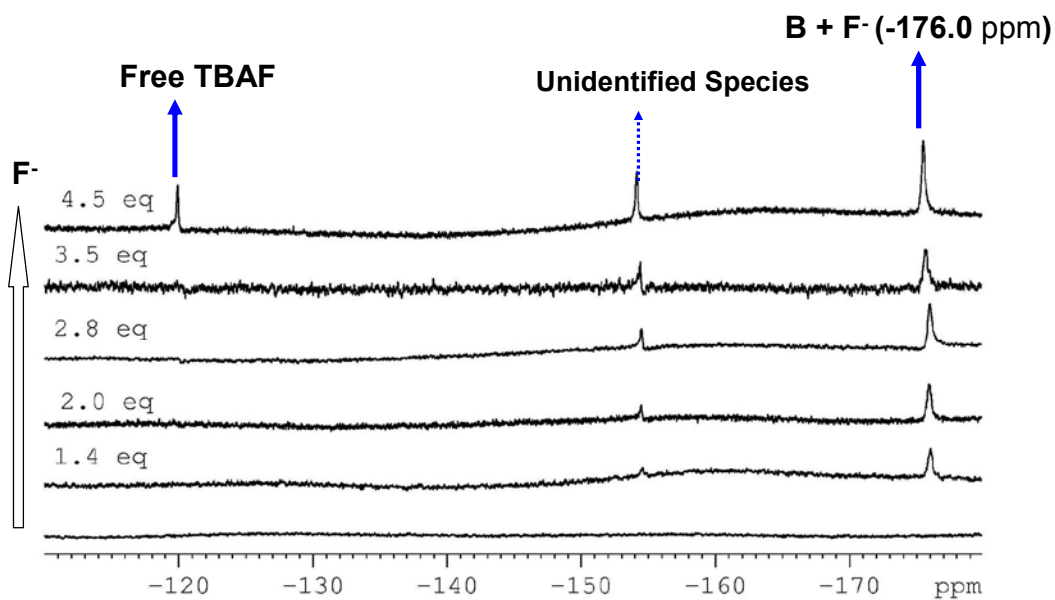
Figure 2.53 The ^{19}F NMR titration spectra of **2.1c** by TBAF in CD_2Cl_2.
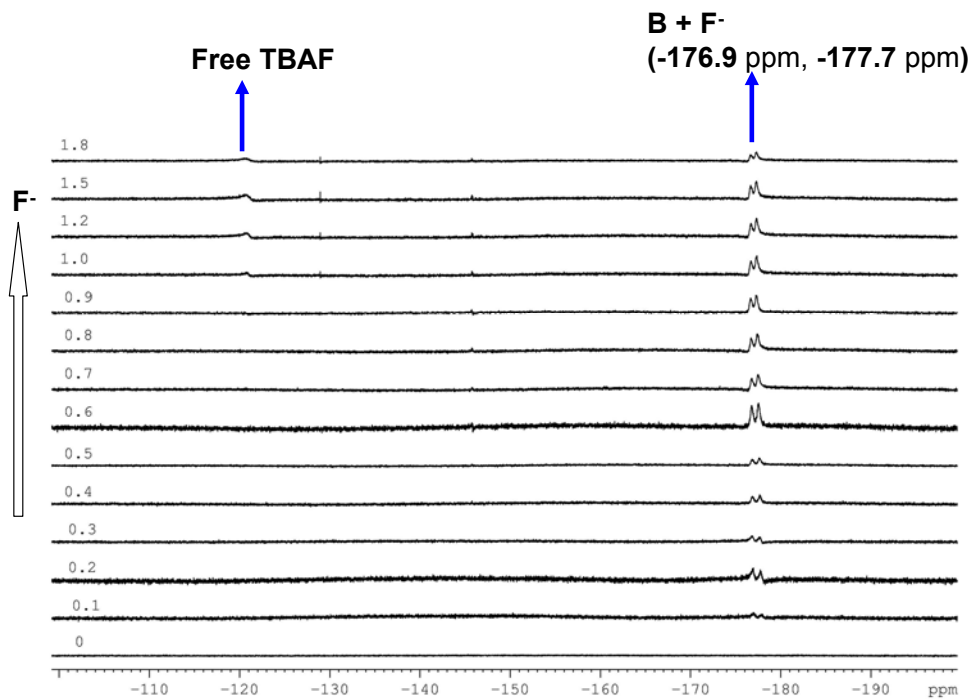
Figure 2.54 The ^{19}F NMR titration spectra of **2.2a** by TBAF in CD_2Cl_2.
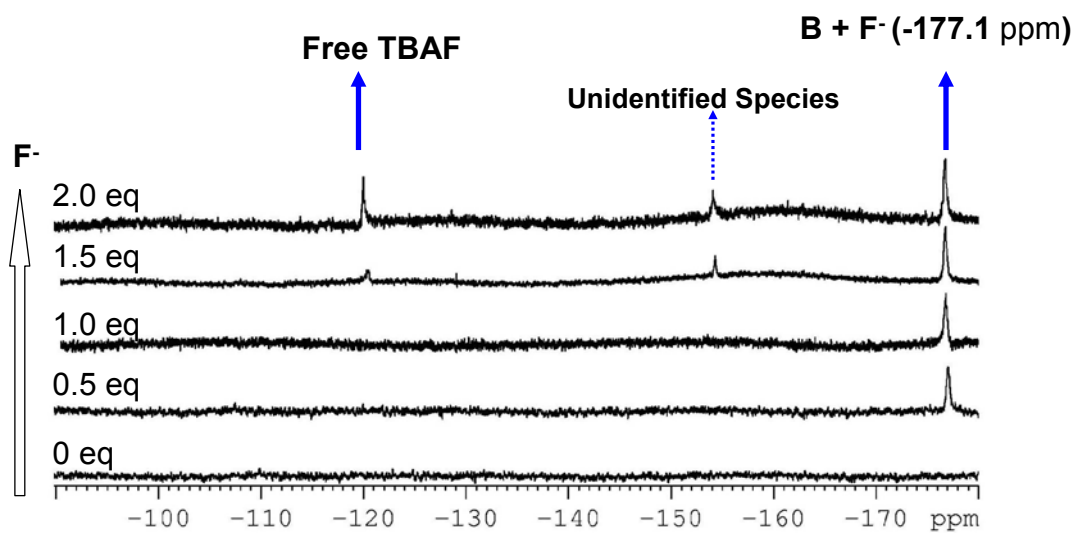
Figure 2.55 The ^{19}F NMR titration spectra of **2.2b** by TBAF in CD_2Cl_2.
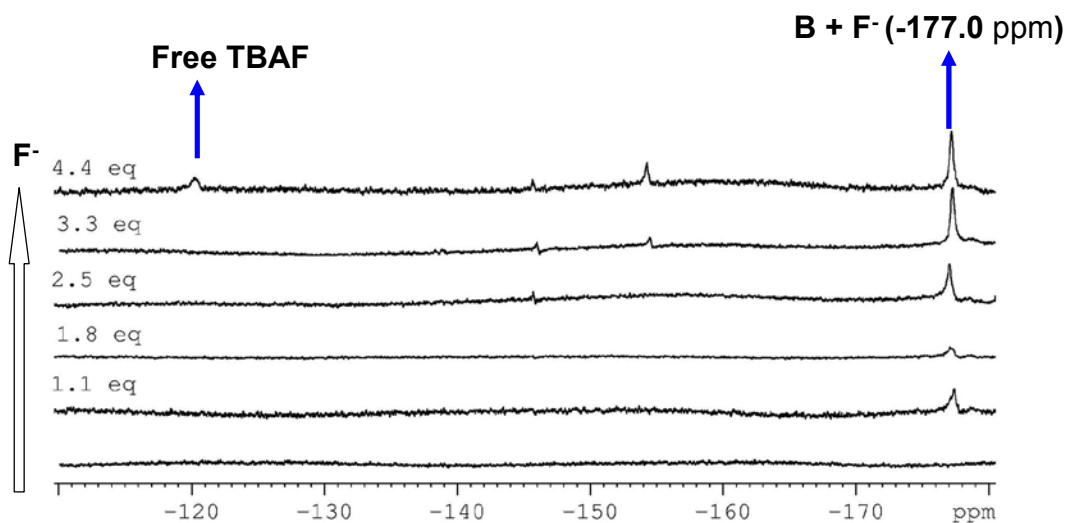
Figure 2.56 The ^{19}F NMR titration spectra of **2.2c** by TBAF in CD_2Cl_2.

2.4 Conclusions

This study has shown that the two constitutional isomers of *p*-B-ppy and *p*-ppy-B have distinct impact on the structure, stability, electronic and photophysical properties of the Pt(II) complexes. For *p*-B-ppy, Pt(II) chelation does not enhance the electron accepting ability of B-ppy due to the change of a neutral *p*-B-ppy molecule to an anionic ligand and the direct conjugation of the B center with the negatively charged phenyl ring. The greater steric constraint in the Pt(II) complexes of *p*-B-ppy also significantly diminishes the Lewis acidity of the B center, as demonstrated by the low binding strength of the Pt(II) complexes with fluorides, relative to the free ligand *p*-B-ppy. For *p*-ppy-B, Pt(II) chelation does enhance its electron accepting ability, but does not significantly change its Lewis acidity with fluoride. Hence, we can conclude that for N,C-chelate ligands, it is most effective with the boron moiety being directly conjugated with the nitrogen

107

heterocycle in order to enhance the electron accepting ability and Lewis acidity. Furthermore, metal chelation often introduces a greater steric constraint on the $BMes_2$ group, thus may have a negative impact on its binding ability with anions such as fluoride. In the dinuclear Pt(II) complexes, electronic communication between the two boron centers is possible in sterically less congested systems such as **2.1c** that allow extended conjugation through the entire molecule. Lastly, the phosphorescent decay lifetimes of the Pt(II) complexes *p*-B-ppy and *p*-ppy-B are all much longer than those of Pt(ppy)(acac) and its derivatives, which may be due to the stabilization of the excited state by the $BMes_2$ group or the influence of the phenyl ligand and the auxiliary ligand. To fully establish the role of the boron center in B-ppy and ppy-B ligands, it is necessary to synthesize Pt(*p*-B-ppy)(acac) and Pt(*p*-ppy-B)(acac) complexes so that direct comparison with Pt(ppy)(acac) can be made.

2.5 References

(1) (a) Jia, W. L.; Bai, D. R.; McCormick, T.; Liu, Q. D.; Motala, M.; Wang, R.; Seward, C.; Tao, Y.; Wang, S. *Chem.Eur. J.* **2004**, 10, 994. (b) Sakuda, E.; Funahashi, A.; Kitamura, N. *Inorg. Chem.* **2006**, 45, 10670. (c) Sun, Y.; Ross, N.; Zhao, S. B.; Huszarik, K.; Jia, W. L.; Wang, R. Y.; Wang, S. *J. Am. Chem. Soc.* **2007**, 129, 7510. (d) Sun, Y.;Wang, S. *Inorg. Chem*. **2009**, 48, 3755.

(2) (a) Zhou, G. J.; Ho, C. L.; Wong, W. Y.; Wang, Q.; Ma, D. G.; Wang, L. X.; Lin, Z. Y.; Marder, T. B.; Beeby, A. *Adv. Funct. Mater*. **2008**, 18, 499. (e)You,Y. M.; Park, S.Y. *Adv. Mater*. **2008**, 20, 3820. (f) Zhao, Q.; Li, F. Y.; Liu, S. J.; Yu,M. X.; Liu, Z. Q.; Yi, T.; Huang, C. H. *Inorg. Chem*. **2008**, 47, 9256.

(3) (a) Zhao, S. B.; McCormick, T.; Wang, S. *Inorg. Chem*. **2007**, 46, 10965. (b) Hudson, Z. M.; Zhao, S. B.; Wang, S. *Chem. Eur. J.* **2009**, 15, 6131 – 6137.

(4) Baldo, M. A.; Brian, D. F. O.; You, Y.; Shoustikov, A.; Sibley, S.; Thompson M. E.; Forrest, S. R. *Nature*. **1998**, 395.

(5) Brooks, J.; Babayan, Y.; Lamansky, S.; Djurovich, P.; Tsyba, I.;Bau, R.; Tompson, M. E. *Inorg. Chem*. **2002**, 41, 3055.

(6) Klein, A.; Schurr, T.; Knodler, A.; Gudat, D.; Klinkhammer, K. W. K.; Jain, V.; Zalis, S.; Kaim, W. *Organometallics*. **2005**, 17, 4125.

(7) Ono, K.; Joho, M. Eur. J. *Inorg. Chem*. **2006**, 3676.

(8) Prokopcova, H.; Kappe, C. O. *J. Org. Chem*. **2007**, 72, 4440.

(9) Gaussian 03, Revision C.02, Frisch, M. J.; Trucks, G. W.; Schlegel, H. B.; Scuseria, G. E.; Robb, M. A.; Cheeseman, J. R.; Montgomery, Jr., J. A.; Vreven, T.; Kudin, K.

N.; Burant, J. C.; Millam, J. M.; Iyengar, S. S.; Tomasi, J.; Barone, V.; Mennucci, B.; Cossi, M.; Scalmani, G.; Rega, N.; Petersson, G. A.; Nakatsuji, H.; Hada, M.; Ehara, M.; Toyota, K.; Fukuda, R.; Hasegawa, J.; Ishida, M.; Nakajima, T.; Honda, Y.; Kitao, O.; Nakai, H.; Klene, M.; Li, X.; Knox, J. E.; Hratchian, H. P.; Cross, J. B.; Bakken, V.; Adamo, C.; Jaramillo, J.; Gomperts, R.; Stratmann, R. E.; Yazyev, O.; Austin, A. J.; Cammi, R.; Pomelli, C.; Ochterski, J. W.; Ayala, P. Y.; Morokuma, K.; Voth, G. A.; Salvador, P.; Dannenberg, J. J.; Zakrzewski, V. G.; Dapprich, S.; Daniels, A. D.; Strain, M. C.; Farkas, O.; Malick, D. K.; Rabuck, A. D.; Raghavachari, K.; Foresman, J. B.; Ortiz, J. V.; Cui, Q.; Baboul, A. G.; Clifford, S.; Cioslowski, J.; Stefanov, B. B.; Liu, G.; Liashenko, A.; Piskorz, P.; Komaromi, I.; Martin, R. L.; Fox, D. J.; Keith, T.; Al-Laham, M. A.; Peng, C. Y.; Nanayakkara, A.; Challacombe, M.; Gill, P. M. W.; Johnson, B.; Chen, W.; Wong, M. W.; Gonzalez, C.; and Pople, J. A.; Gaussian, Inc., Wallingford CT, 2004.

(10) (a)Becke, A. D. *J. Chem. Phys.* **1993**, *98*, 5648. (b) Lee, C.; Yang, W.; Parr, R. G. *Phys. ReV. B* **1988**, *37*, 785. (c) Miehlich, B.; Savin, A.; Stoll, H.; Preuss, H. *Chem. Phys. Lett.* **1989**, *157*, 200. (d)Hariharan, P. C.; Pople, J. A. *Theor. Chim. Acta* **1973**, *28*, 213.

(11) *SHELXTL*, version 6.14; Bruker AXS: Madison, WI, 2003.

(12) (a) Zhao, S. B.; Wang, R. Y.; Wang, S. *J. Am. Chem. Soc*. **2007**, 129, 3092. (b) Yagyu, T.; Ohashi, J. I.; Maeda, M. *Organometallics.* **2007**, 26, 2383.

(13) Cui, Y.; Liu, Q. D.; Bai, D. R.; Jia, W. L.; Tao, Y.; Wang, S. *Inorg. Chem*. **2005**, 44, 601.

(14) Sajoto, T.; Djurovich, P. I.; Tamayo, A.; Yousufuddin, M.; Bau, R.; Tompson. M. E. *Inorg. Chem.* **2005**, 44, 7992.

(15) (a) Cross, R. J.; Haupt, M.; Rycroft, D. S.; Winfield, J. M. *J. Organomet. Chem.* **1999**, 587, 195. (b) Jasim, S. A.; Perutz, R. N. *J. Am. Chem. Soc.* **2000**, 122, 8685. (c) Clark, H. C. S.; Fawcett, J.; Holloway, J. H.; Hope, E. G.; Peck, L. A.; Russell, D. R. *Dalton Trans.* **1998**, 1249.

(16) Zhao, S. B.; Wucher, P.; Hudson, Z. M.; McCormick, T. M.; Liu, X. Y.; Wang, S.; Feng, X. D.; Lu, Z. H. *Organometallics.* **2008**, 27, 6446.

(17) Connors, K. A. Binding Constants: *The Measurement of Molecular Complex Stability Constants*, John Wiley and Sons, **1987**.

Chapter 3

Photo-thermal Isomeration of a Hybrid Three and Four-Coordinate

Boron Compound (5-BMes$_2$-2-ph-py)BMes$_2$

3.1 Introduction

Triarylboron compounds have wide applications in areas such as anion sensing, fluorescent emitter, electron-transporting materials.[1-10] Four-coordinate organoboron compounds also distinguish themselves as excellent candidate for fluorescent dyes and highly-efficient emissive layer in OLEDs.[11-17] Moreover, four-coordinate boron center can constrain the molecule in a planar fashion and enhance molecular electron affinity.[18]

The combination of both trigonal and tetrahedral boron functionalities in the same conjugate system renders the possibility to further optimize the properties of the material, hence its performance in optoelectronic devices. Despite such premise, molecules that contain both a triarylboron center and a four-coordinate diarylboron group are unknown previously. To study the impact of triarylboron center to the four-coordinate boron center, we therefore initiated the synthesis and photophysical property investigation of a hybrid diboron molecule (5-BMes$_2$-py-2-phenyl)BMes$_2$ (**3.1**), as shown in   Figure 3.1. With the boryl group at appropriate position of Lewis base (nitrogen) containing π conjugated framework, which allows intramolecular coordination from the Lewis base to boron atom, the boron center turns out to be four-coordinate.

3.1
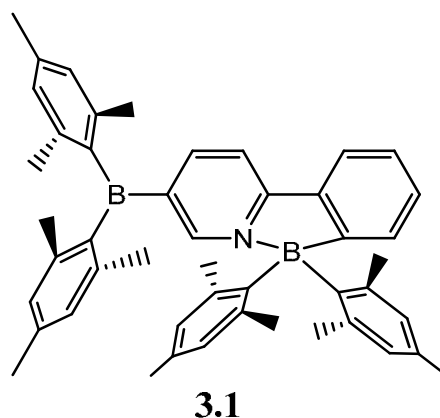
Figure 3.1 Molecular structures of **3.1.**

The investigation on diboron molecule **3.1** also revealed a rare phenomenon − a reversible photo-thermal switching of intramolecular C-C bond formation/breaking process involving a tetrahedral B center.

3.2 Experimental

3.2.1 General considerations

All reactions were performed under N_2 with standard Schlenk techniques unless otherwise noted. All starting materials were purchased from Aldrich Chemical Co. and used without further purification. DMF, THF, Et_2O, and hexanes were purified using an Innovation Technology Co. solvent purification system. CH_2Cl_2 was freshly distilled over P_2O_5 prior to use. Deuterated solvents were purchased from Cambridge Isotopes and were used as received without further drying. NMR spectra were recorded on Bruker

Avance 400 or 500 MHz spectrometers. High-resolution mass spectra were obtained from a Waters/Micromass GC-TOF EI-MS spectrometer, which was internally calibrated before use. Cyclic voltammetry was performed using a BAS CV-50W analyzer with a scan rate of 100 mV/s to 1 V/s and a typical concentration of 0.003 M in DMF using 0.10 M tetrabutylammonium hexafluorophosphate (TBAP) as the supporting electrolyte. A conventional three-compartment electrolytic cell consisting of a Pt working electrode, a Pt auxiliary electrode, and a Ag/AgCl reference electrode were employed using the ferrocene/ferrocenium couple as the standard ($E_{1/2}$ = 0.55 V in DMF). UV-Vis spectra were recorded on an Ocean Optics UV-visible spectrometer. Excitation and emission spectra were recorded on a Photon Technologies International QuantaMaster model C-60 spectrometer. Emission lifetimes were measured on a Photon Technologies International Phosphorescent spectrometer (Time-Master C-631F) equipped with an Xenon flash lamp and digital emission photon multiplier tube using a band pathway of 5 nm for excitation and 2 nm for emission.

3.2.2 Synthesis of 3.1

Synthesis of 2-(2-bromophenyl)-5-bromopyridine. This compound was synthesized using a modified Suzuki coupling procedure.[19] A mixture of toluene (60 mL), ethyl alcohol (20 mL), and water (20 mL) was stirred and purged by nitrogen for 1 h. 2-Bromophenyl boronic acid (0.88 g, 4.39 mmol), 2,5-dibromopyridine (1.04 g, 4.39 mmol), Pd(PPh$_3$)$_4$ (0.14 g, 0.11 mmol), and NaOH (1.20 g, 3.00 mmol) were added to the mixed solvents. The mixture was stirred at room temperature for 2 days. The water layer

was separated and extracted with CH_2Cl_2 (3 x 30 mL). The combined organic layers were dried over Na_2SO_4, and the solvents were evaporated under reduced pressure. Purification of the crude product by column chromatography (CH_2Cl_2/Hexane, 1/1) afforded the product as a white solid in 51% yield (0.68 g).

Synthesis of (5-BMes$_2$-2-ph-py)BMes$_2$ (B$_2$ppy, 3.1). This compound was synthesized using a procedure similar to those of previously reported organoboron compounds.[20] To a stirred diethylether solution of 2-(2-bromophenyl)-5-bromopyridine (0.32 g, 1.00 mmol) at -78°C was added dropwise via a syringe an n-BuLi solution (1.60 M) (1.38 mL, 2.20 mmol) over 5 min. The resulting yellow solution was stirred for 1 h at -78°C, and then a solution of dimesitylboron fluoride (0.72 g, 90%, 2.40 mmol) in Et_2O was quickly added. The reaction mixture was kept at -78°C for another 1 h and then allowed to reach ambient temperature and stirred overnight. After the removal of the solvent, purification of the crude product by column chromatography (CH_2Cl_2/Hexane, 2/1, 1% ethyl acetate) afforded the product as a yellow solid in 41% yield. The resulting yellow solid was recrystallized, avoiding light, from CH_2Cl_2/hexane to give yellow crystals of **3.1**. ^{1}H NMR (500 MHz, C_6D_6, 25°C, δ, ppm): 8.87 (s; 1H), 8.04 (d, J =7.5Hz; 1H), 7.65 (dd, J = 8.0 Hz, J = 1.0 Hz; 1H), 7.55 (d, J = 7.5 Hz; 1H), 7.23 (d, J = 8.0 Hz; 1H), 7.16 (t, J =7.0 Hz; 1H), 7.07 (t, J =7.5 Hz; 1H), 6.73 (s, 8H), 2.23 (s, 6H), 2.20 (s, 6H), 1.88 (s, 24H). ^{13}C{^{1}H}NMR (100 MHz, C_6D_6, δ, ppm): 168.68, 161.04, 155.53, 147.04, 146.09, 140.97, 140.36, 139.87, 137.00, 135.21, 133.702, 132.248, 130.75, 129.24, 128.35, 128.23, 128.10, 127.99, 127.86, 125.73, 122.46, 117.16, 25.53, 23.52, 21.35, 21.07. Anal. Calcd for $C_{47}H_{51}NB_2$: C 86.64, H 7.89, N 2.15. Found: C 85.75, H 8.15, N 1.97. Due to the high

sensitivity of **3.1** toward oxygen under ambient light in both solution and the solid state, it is very difficult to obtain a high purity sample for CHN analysis. The results here represent our best efforts.

3.2.3 General procedure for photo-conversion of 3.1 → 3.1a →3.1b

For NMR under N$_2$ (3.1 → 3.1a): The photoisomerization of **3.1** was carried out by preparing a C$_6$D$_6$ (dried over CaH$_2$) solution (~0.03 M) in a NMR tube inside an inert atmosphere dry box. The solution was placed under a hand-held UV lamp (365 nm) at room temperature and the exposure time was recorded. After each exposure period, the NMR spectrum was recorded. For kinetic data, calibrated integrals by using an internal reference for selected peaks are used.

For NMR under N$_2$ (3.1a → 3.1): The solution of **3.1a** in C$_6$D$_6$ in NMR tube was prepared in the same manner as described above. After the temperature inside the NMR probe was increased to the desired temperature and the ^{1}H NMR spectra showing conversion of **3.1a → 3.1** were recorded with time.

For NMR under O$_2$ (3.1 → 3.1a →3.1b): The solution of **3.1** was prepared in C$_6$D$_6$ in the same manner as for the experiments under N$_2$. The NMR spectrum of the fresh solution under N$_2$ was recorded. Excess O$_2$ (about 10 folds) was introduced to the solution via a syringe. The NMR tube was then exposed to either a hand-held UV lamp at 365 nm or a compact fluorescent lamp from Fisher Scientific (the emission spectrum of the fluorescent lamp is shown in Figure 3.2) at room temperature. The NMR spectra

were then recorded at various light exposure time intervals. For kinetic data, integrals

calibrated by using an internal reference, for selected peaks are used.

For UV-Vis absorption experiments: The solution was prepared in the same manner as

for NMR experiments except that the NMR tube was replaced by a UV cuvette that has a

screw-on cap and the solution concentration is $\sim 1.25 \times 10^{-4}$ M. The solvent used is

toluene, freshly distilled.
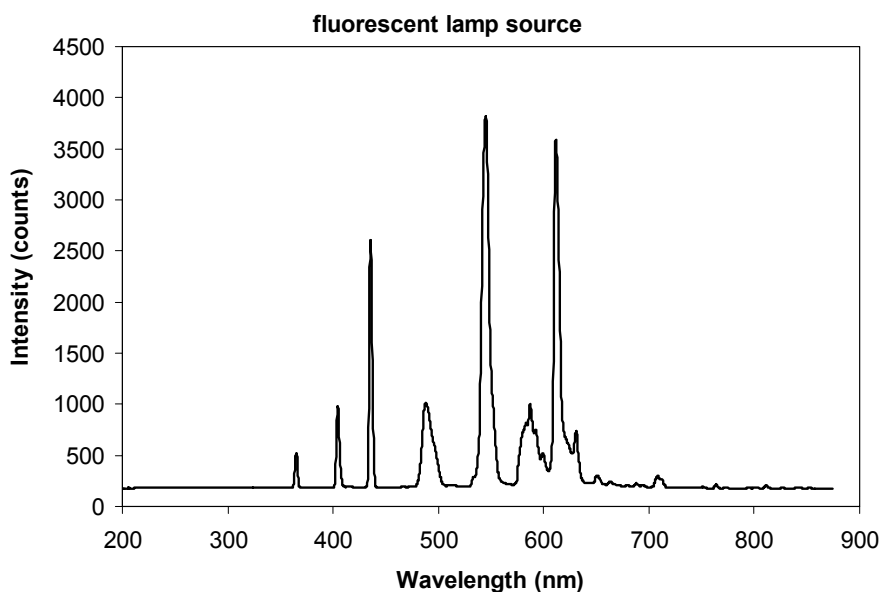
Figure 3.2 Fluorescent lamp source.

3.2.4 Synthesis of 3.1b

(5-BMes$_2$-py-2-phenyl)BMes$_2$ (3.1) (0.03 g, 0.047mmol) in toluene (15 mL) was reacted

at r.t. with oxygen under UV (365nm) light for 3 hrs. After the removal of the solvent,

117

purification of the crude product by preparative TLC plates (CH$_2$Cl$_2$/Hexane, 1/1) afforded the product as a white solid (yield ~92%, based on NMR). ^{1}H NMR (500 MHz, C$_6$D$_6$, 25°C): 9.00 (s; 1H), 8.22 (d; J=7.5Hz; 1H), 7.38 (dd; J = 8.0 Hz, J = 2.0 Hz; 1H), 7.27 (td; J = 7.5Hz, J = 1.5 Hz; 1H), 7.22 (td; J = 7.5 Hz, J = 1.5 Hz; 1H), 7.09 (d; J = 7.5 Hz; 1H), 7.96 (d; J =7.5Hz; 1H), 6.75(s; 2H), 6.73(s, 4H), 2.16(s, 6H), 2.11(s, 3H), 2.01(s, 6H), 1.99 (s, 12H); ^{13}C{1H} NMR (100 MHz, CD$_2$Cl$_2$): 161.46, 156.49, 142.83, 141.26, 140.99, 140.12, 139.84, 139.46, 137.97, 137.46, 136.87, 136.06, 130.87, 130.25, 129.08, 128.56, 128.27, 127.54, 123.33, 23.42, 21.22, 21.02, 20.62 ppm. HRMS, calcd. for C$_{38}$H$_{40}$BN: m/z 522.3332; found: 522.3349.

3.2.5 Characterization of (MesBO)$_3$

The boroxin compound was obtained from the reaction mixture of compound **3.1** with oxygen under UV irradiation. It was identified by ^{1}H NMR and high resolution mass spectra. ^{1}H NMR (δ, ppm): 6.67 (s; 6H; Ar), 2.49 (s; 18H; ortho-Me), 2.14 (s; 9H; para-Me). These values are similar to those reported in the literature reported.[24] HRMS calcd. for C$_{27}$H$_{33}$B$_3$O$_3$: *m/z* 438.2723; found: 438.2715.

3.2.6 Quantum yield measurement

Quantum yields of **3.1** were determined in CH$_2$Cl$_2$ using 9,10-diphenylanthracene as the standard at 298 K (Φ_r = 0.90). The absorbance of all the samples and the standard at the

excitation wavelength is approximately 0.096-0.109. The quantum yields were calculated as described in Chapter 1.

3.2.7 Molecular orbital calculations

DFT molecular orbital calculations were performed for **3.1**. The geometrical parameters obtained for **3.1** from X-ray diffraction experiments were used as the starting point for its geometry optimization. The energy calculations were performed using Gaussian03 package with the B3LYP/6-311G(d) basis set for all atoms.[21,22]

3.2.8 X-ray crystallographic analysis

Single crystals of **3.1, 3.1b** were mounted on glass fibers for data collection. Data were collected on a Bruker Apex II single-crystal X-ray diffractometer with graphite-monochromated M_o K_α radiation, operating at 50 kV and 30 mA and at 180 K. Data were processed on a PC with the aid of the Bruker SHELXTL software package (version 5.10)[23] and corrected for absorption effects.

3.3 Results and discussion

3.3.1 Synthesis

As shown in Figure 3.3, the synthesis of **3.1** was achieved by Suzuki-Miyaura coupling of 4-bromophenylboronic acid with 2, 5-dibromopyridine, followed by substitution of the bromo group with $BMes_2$ in ether. The bromo groups at 2 and 5-position are both reactive

under Suzuki coupling reaction condition. In order to differentiate between them and avoid the disubstituted product, the Suzuki coupling reaction was conducted at r.t, by virtue of the higher reactivity of the bromo group at the 2-position on pyridine.

3.1
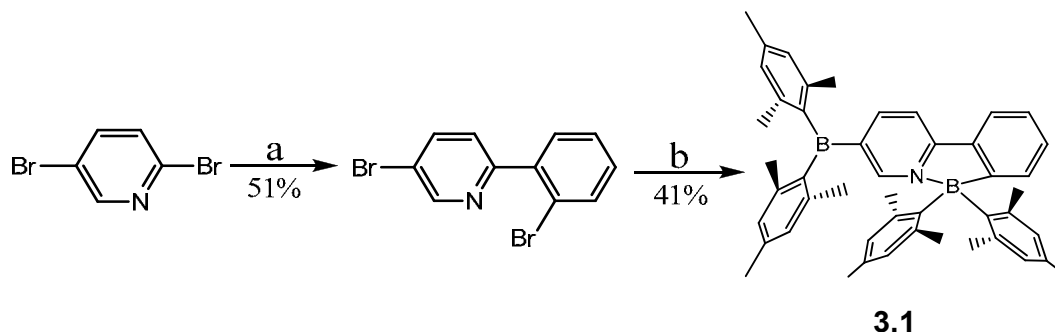
[a]Reagents and conditions: a) (i) toluene, ethanol, and water (3:1:1), 2-bromophenyl boronic acid, $Pd(PPh_3)_4$, and NaOH, r.t, 48 h; b) (i) n-BuLi, Et_2O, -78 °C; (ii) $B(Mes)_2F$, rt, overnight.

Figure 3.3 Synthetic scheme for **3.1.**

3.3.2 Structure of 3.1

The crystal structure of **3.1**, determined by a X-ray diffraction analysis, is shown in Figure 3.4. The three-coordinate boron center adopts a typical trignoal planar geometry. The four-coordinate boron adopts a tetrahedral geometry. With the intramolecular N(1) to B(1) coordination, the phenyl and the pyridyl planes are constrained in coplanarity. The B-C bond lengths around the tetragonal B(1) center (1.628(6) – 1.666(6) Å) are much longer than those around the trigonal B(2) center (1.554(6) – 1.588(6) Å). The B-N bond

120

length in **3.1** (1.636(5) Å) is within the normal B-N bond length range in a tetrahedral environment.[18]
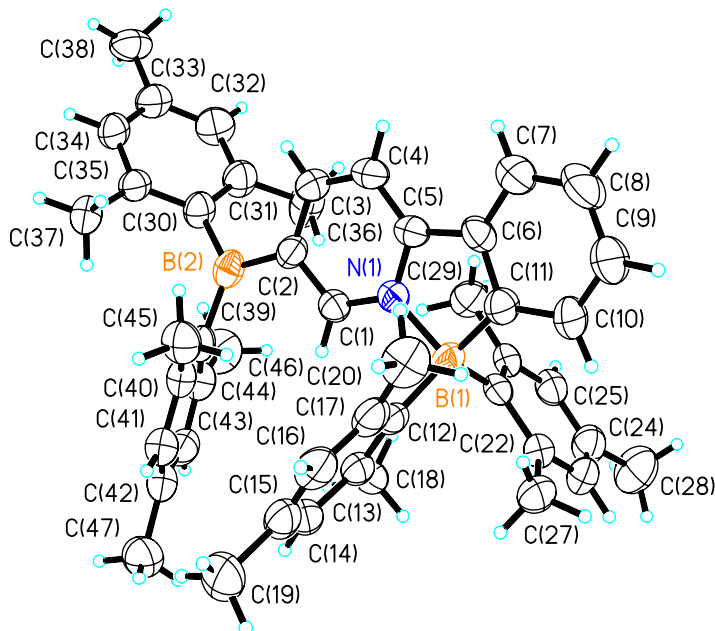
Figure 3.4 The structure of **3.1** with 50% thermal ellipsoids and labeling schemes.

3.3.3 Electrochemical properties

Compound **3.1** displays a reversible reduction peak, characteristic of triarylboron, at - 1.88 V (vs. $FeCp_2^{+/0}$ in DMF), as shown in Figure 3.5. This value is more positive than compound **2.2** from Chapter 2 (- 2.12 V (vs. $FeCp_2^{0/+}$ in DMF)), supporting that the hybrid diboron molecule **3.1** is indeed better than the monoboron **2.2** in terms of electron accepting ability, due to the second tetrahedral boron center that can further lower the LUMO energy of the whole molecule.
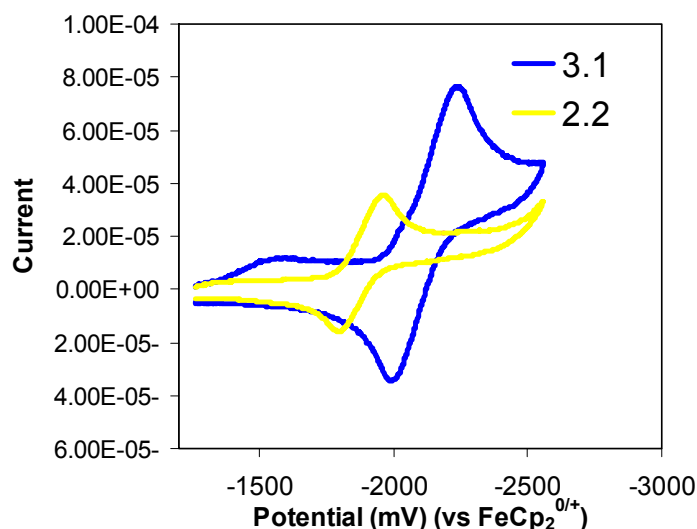
Figure 3.5 The CV diagrams for the molecules **2.2** and **3.1** recorded in DMF.

3.3.4 Absorption and luminescence properties

As shown in Figure 3.6 and Figure 3.7, **3.1** has an intense absorption band in the 200-480 nm region (λ_{max} = 351 nm, ε =1.9 $\times$ 10^4 M^{-1} cm^{-1}) and distinct luminescence with λ_{max} = 525 nm, $\Phi \approx$ 0.33 in toluene. The emission spectra shows a solvent-dependent property, as indicated in Figure 3.7. The emission maximum shifts from 497 nm in hexane to 554 nm in DMF, which indicates a polarized excited state resulting from intramolecular charge transfer. As a comparison, in the absorption spectra (Figure 3.6), the π to p_{π}-π^* maximum absorption band shifts only slightly from 351 nm (in hexane) to 340 nm (in DMF), with the increase of solvent polarity, which indicates the ground state is much less polarized than excited state.
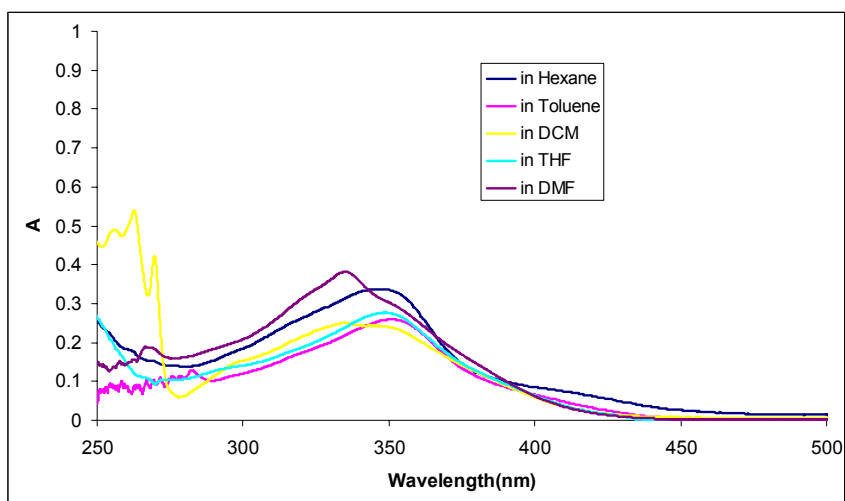
Figure 3.6 UV-Vis absorption spectra of **3.1** in various solvents (concentration = 2×10^{-5} M).
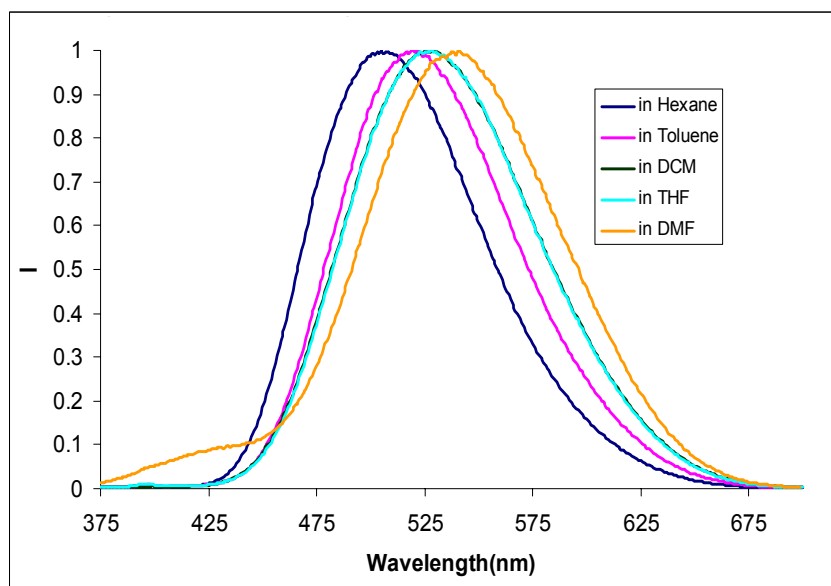
Figure 3.7 Normalized emission spectra of **3.1** in various solvents (concentration = $\sim 10^{-5}$ M), with λ_{max} = 350 nm.

Compared to that of **2.2**, the absorption and emission energy of **3.1** is clearly red-shifted (Figure 3.8, Figure 3.9), and with greater emission efficiency, owing to the presence of the second tetrahedral boron group in **3.1** that promotes π-conjugation of the py-ph unit, thus lowering the HOMO-LUMO energy gap.
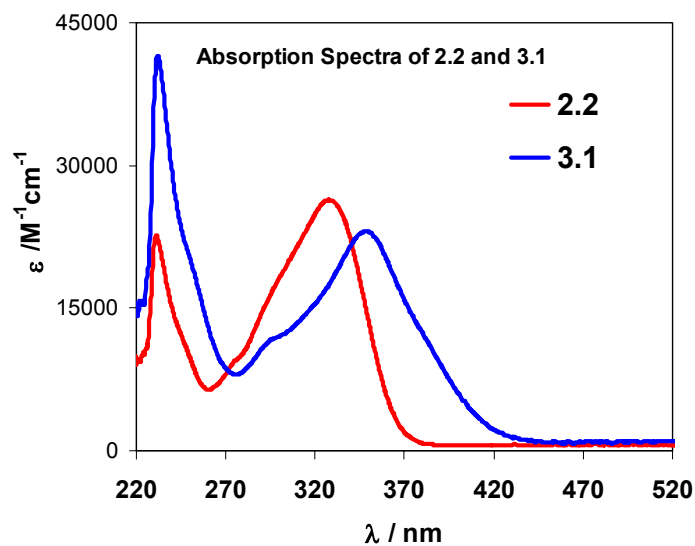
Figure 3.8 The UV-Vis absorption spectra for the molecules **2.2** and **3.1** recorded in CH_2Cl_2.
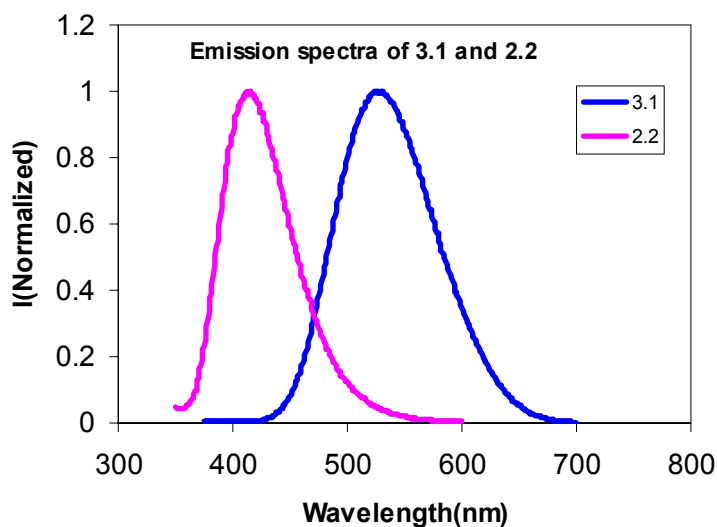
Figure 3.9 The normalized emission absorption spectra for the molecules **2.2** and **3.1** recorded in CH_2Cl_2 with $\lambda_{max} = 350$ nm.

3.3.5 Molecular orbital calculations

To better understand the origin of the electronic transitions in **3.1**, DFT calculations were performed. As shown in Figure 3.10, the HOMO is a π orbital delocalized on the mesityls of the tetrahedral boron center, while the LUMO is a π^* orbital spreading all over the Mes_2B-py-ph moiety, with a great contribution from the three-coordinate boron center. The intramolecular charge transfer process is therefore likely from the mesityls of the tetrahedral boron to the Mes_2B-py-ph moiety.

HOMO   **LUMO**

3.1
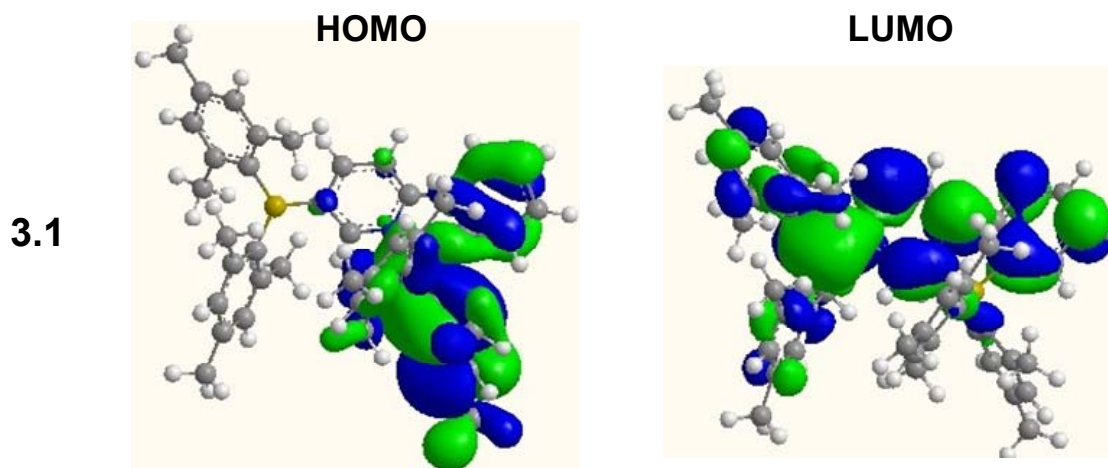
Figure 3.10 Molecular orbitals for **3.1.**

3.4 Decomposition of 3.1 to 3.1b.

As we discussed before, compound **3.1** has moderate absorption in the visible region (Figure 3.8), due to the synergetic effect of two boron moieties that can lower the HOMO-LUMO energy gap, leading to the low-energy absorption band in the visible region. Interestingly, under ambient light and air, compound **3.1** decomposed to **3.1b** gradually, as shown in Figure 3.11.
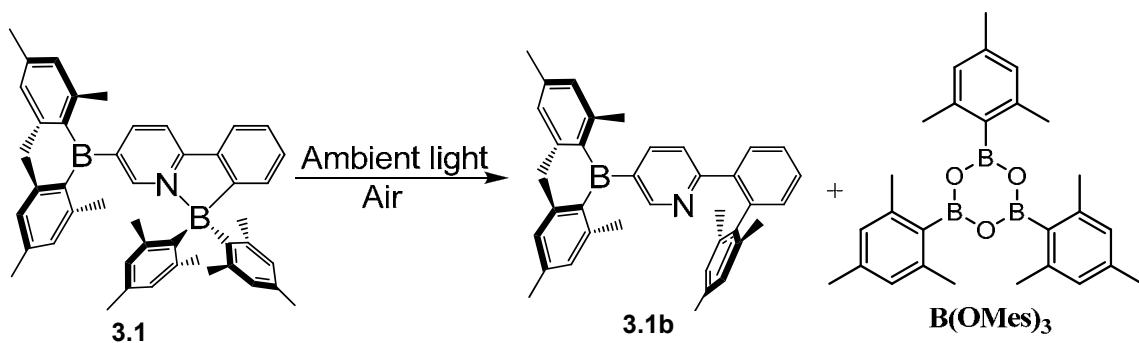
Figure 3.11 Decomposition of **3.1** to **3.1b**.

The structure of **3.1b** was confirmed by X-ray diffraction, and fully characterized by ^{1}H and ^{13}C NMR spectroscopy and elemental anaylsis. The crystal structure of **3.1b** is shown in Figure 3.12. The three-coordinate boron center in **3.1b** is still intact while the four-coordinate boron center disappeared. The structure of **3.1b** confirms that the trigonal BMes$_2$ group in **3.1** can survive the photo-oxidation process and the tetrahedral boron center no longer existed, which was eliminated as (MesBO)$_3$, based on NMR data and mass spectral evidence.
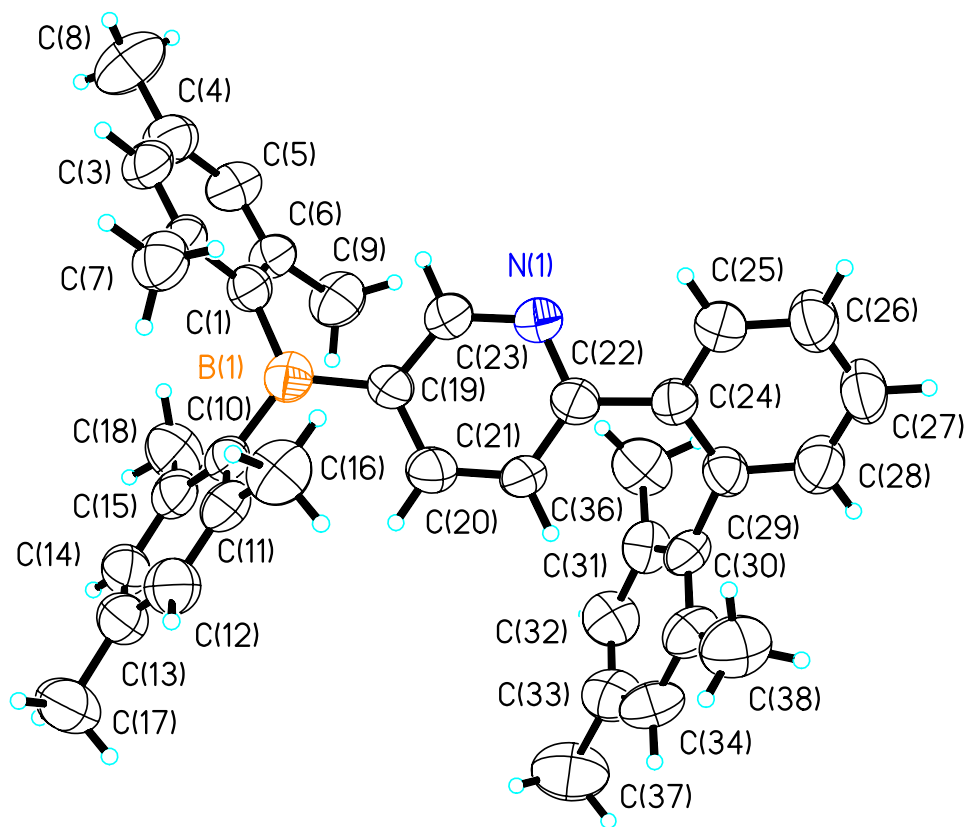
Figure 3.12 The structure of **3.1b** with 50% thermal ellipsoids and labeling schemes**.**

Upon UV irradiation (365 nm) and under oxygen, **3.1** decomposed to **3.1b** in a much faster rate than under ambient light, which can be attributed to the fact that **3.1** has a stronger absorption at wavelength 365 nm than that in the visible region.

At a concentration of ~0.03M in C_6D_6, n= ~1 x 10^{-5}mol, n_{oxygen} =~1.5x10^{-4} mol, the **3.1** to **3.1b** conversion under irradiation at 365 nm was monitored by ^{1}H NMR, as shown in Figure 3.13.
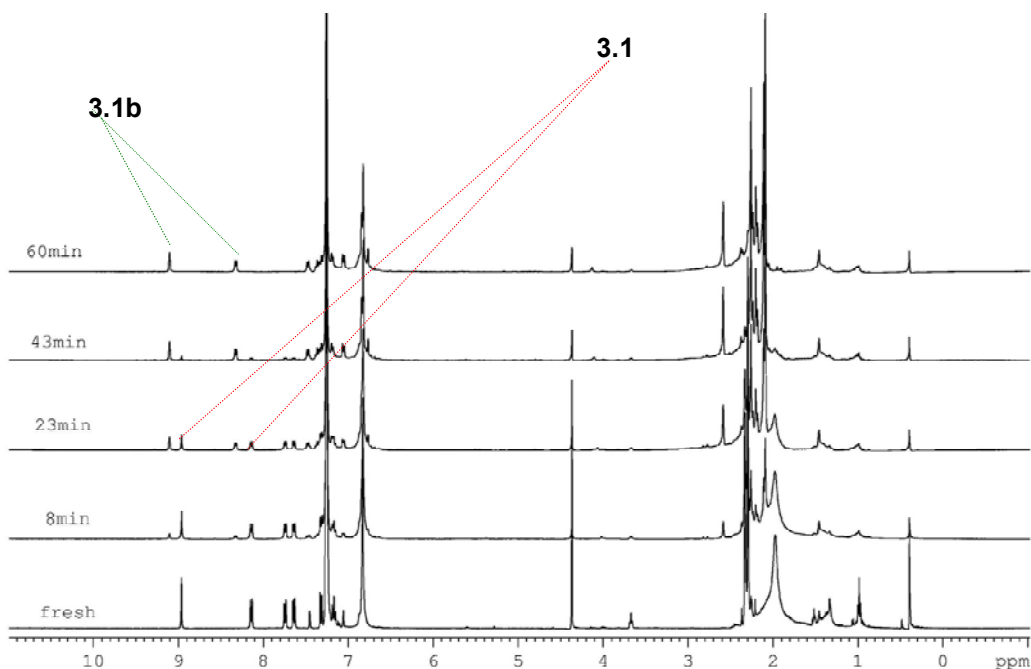
Figure 3.13 Stacked ^{1}H NMR spectra showing the conversion of **3.1** to **3.1b** under oxygen in C$_6$D$_6$ under UV (365 nm).

3.5 Discovery of the photochromic behavior of 3.1

3.5.1 Conversion of 3.1 → 3.1a under N$_2$, UV irradiation

To understand the decomposition mechanism of **3.1→ 3.1b**, monitorating of compound **3.1** upon irradiation at 365 nm under N$_2$ in toluene was conducted. **3.1** gradually became dark olive green accompanied by the rapid loss of fluorescent intensity. As shown in Figure 3.14, upon irradiation, a new broad band covering the entire 400-900 nm region (the instrument cut-off is 900 nm) with λ_{max} at 431 nm, 523 nm, and 714 nm (ε = 6190 M$^-$^{1}cm^{-1}, 2860 M^{-1}cm^{-1} , 3030 M^{-1}cm^{-1}) appears in the UV-Vis spectrum of **3.1** and gains

intensity with the exposure time. The spectra were obtained with 1.25×10^{-4} M of **3.1** in toluene upon ~ 10 s intervals of light exposure (365 nm).
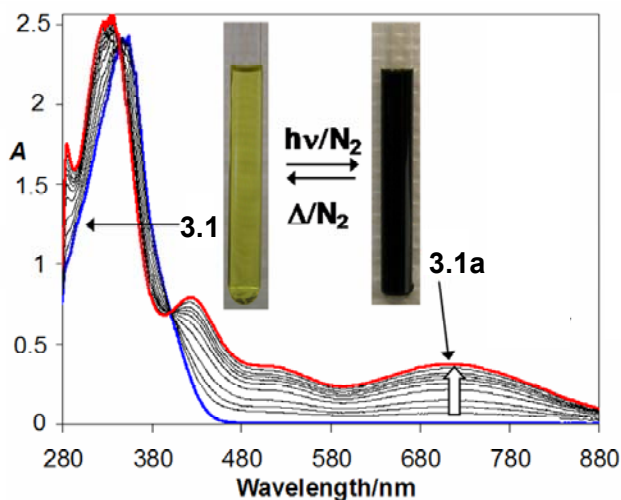
Figure 3.14 UV-Vis spectra change of **3.1** under N_2 in toluene upon UV irradiation at 365 nm. Inset, photographs of **3.1** showing the color switch before and after irradiation.

3.5.2 Proposal of structure of 3.1a

To determine the structural origin of this drastic color change, we monitored the photolysis process by ESR, ^{1}H NMR and 2D NMR experiments. Upon irradiation at 365 nm and with exposure time, **3.1** becomes dark olive green. The new species with dark olive green color was denoted as **3.1a**. The irradiated dark olive color compound is ESR silent, thus ruling out the possibility of radical species.

3.5.2.1 Proposed structure of 3.1a based on ^{1}H and ^{11}B NMR data

Upon UV irradiation, the ^{1}H NMR spectrum of compound **3.1** displays a new set of peaks belonging to a single entity **3.1a** while the original peaks diminish, as shown in Figure 3.15. All methyls and all H atoms of mesityl group on the 4-coordinate boron part have distinctive chemical shift change, which indicate that the free rotation of mesityl groups around B-C bond in the tetrahedral boron center is inhibited.[25] Stacked ^{1}H NMR spectra of **3.1** to **3.1a** with the increase of UV exposure time is show in Figure 3.16. The ^{1}H NMR spectra of **3.1→3.1a** conversion were obtained under nitrogen in C_6D_6, under UV (365 nm), concentration = ~0.03M, at room temperature, at various time intervals.
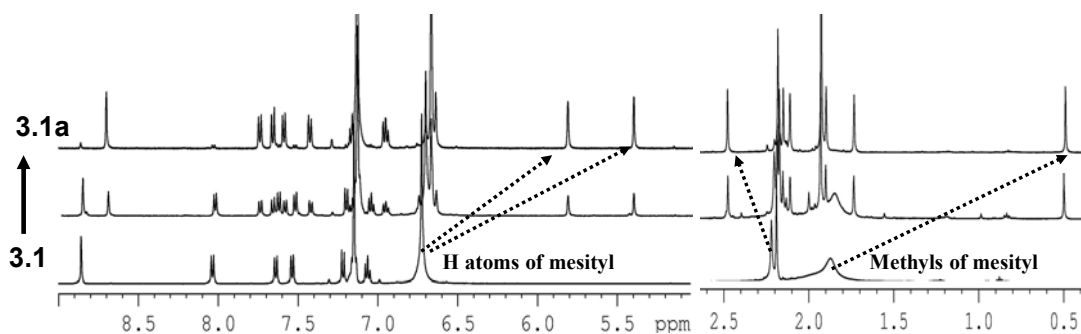
Figure 3.15 ^{1}H NMR spectra showing the conversion of **3.1** (bottom trace) to **3.1a** (top trace) in C_6D_6 after irradiation at 365 nm.
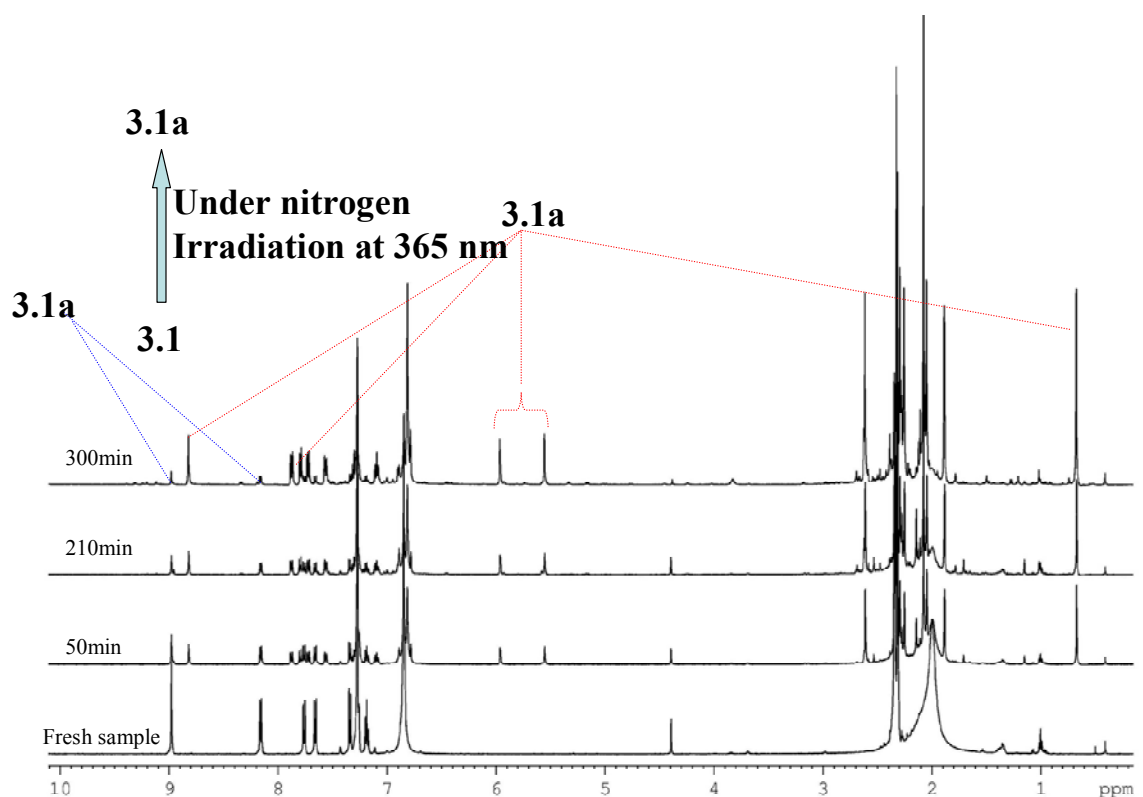
Figure 3.16 Stacked ^{1}H NMR spectra of **3.1** to **3.1a** with the increase of UV exposure time.

The ^{11}B NMR spectra of **3.1→3.1a** conversion were obtained under nitrogen in C$_6$D$_6$, under UV (365 nm), concentration = ~0.03M, at room temperature, at various time intervals. Along with UV exposure, the ^{11}B chemical shift from 4.90 ppm shifts to -9.65 ppm, as shown in Figure 3.17.
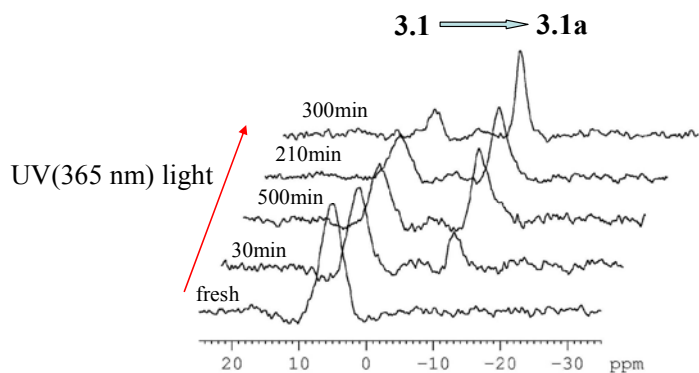
Figure 3.17 Stacked ^{11}B NMR spectra showing the four-coordinate boron chemical shift change of **3.1** to **3.1a**.
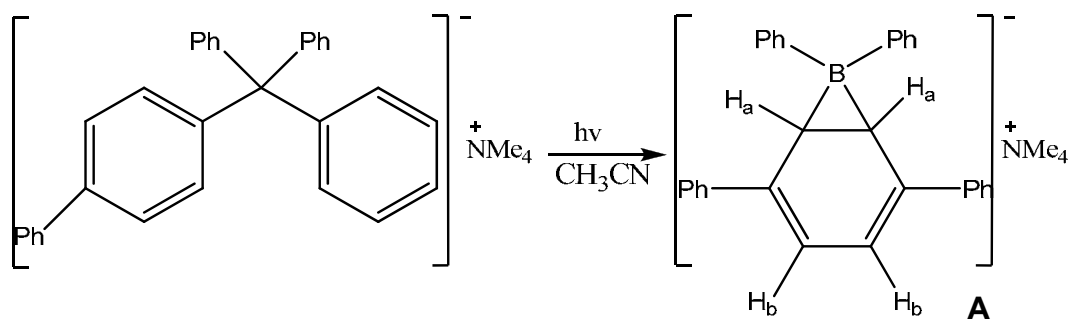
Figure 3.18 Photocylisation of {B(*p*-biphenyl)Ph$_3$}$^-$ in oxygen-free acetonitrile.

Based on these NMR data of **3.1a** and considering the previously reported anion {B(*p*-biphenyl)Ph$_3$}$^-$ from Schuster,[26, 27] which forms a dark red borate species (Figure 3.18) with two characteristic ^{1}H signals (H$_a$ at 1.39 ppm and H$_b$ at 5.55 ppm) in the NMR

spectrum upon irradiation at 254 nm, we have the confidence to propose the structure of **3.1a**, as shown in Figure 3.19.
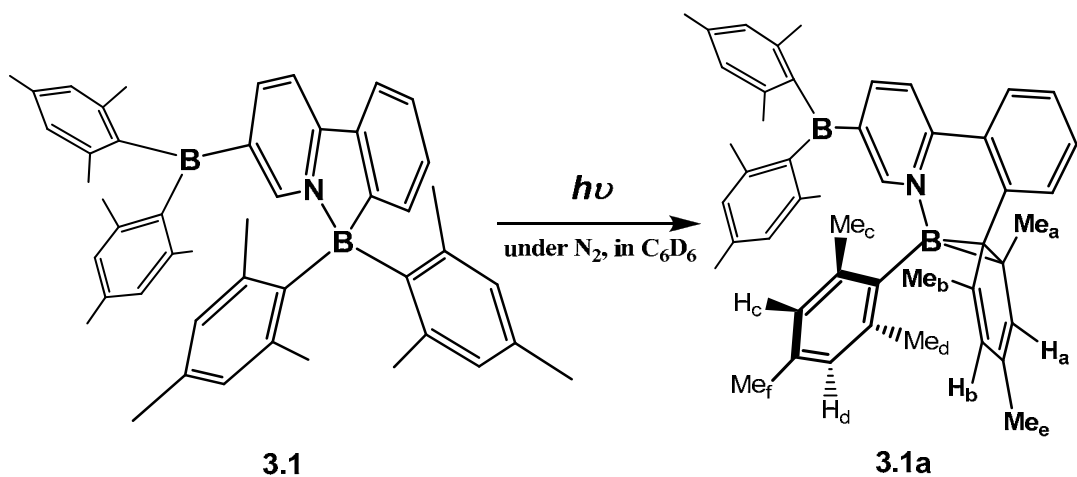
Figure 3.19 Photolysis of **3.1** to **3.1a**.

The original mesityl group attached to tetrahedral boron center is not aromatic any more, as evidenced by the distinct chemical shift change of Me_a, H_a and H_b. The absence of the A analogue in our system is clearly caused by the internal py group that prevents the B center to migrate to the *meta*-carbon. The complete assignments of ^{1}H NMR spectra of **3.1a** after nearly complete conversion from **3.1** are provided in Figure 3.20, Figure 3.21 and Figure 3.22. (*: trace of starting material compound **3.1**, due to the thermal reversal ability of **3.1a** to **3.1**, it is very hard to get a fully conversion spectra).
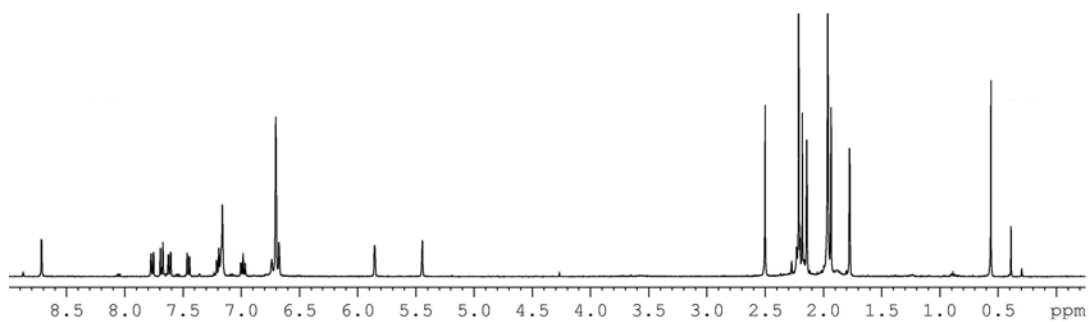
Figure 3.20 ^{1}H NMR spectral of **3.1a** in C$_6$D$_6$ at 298K .
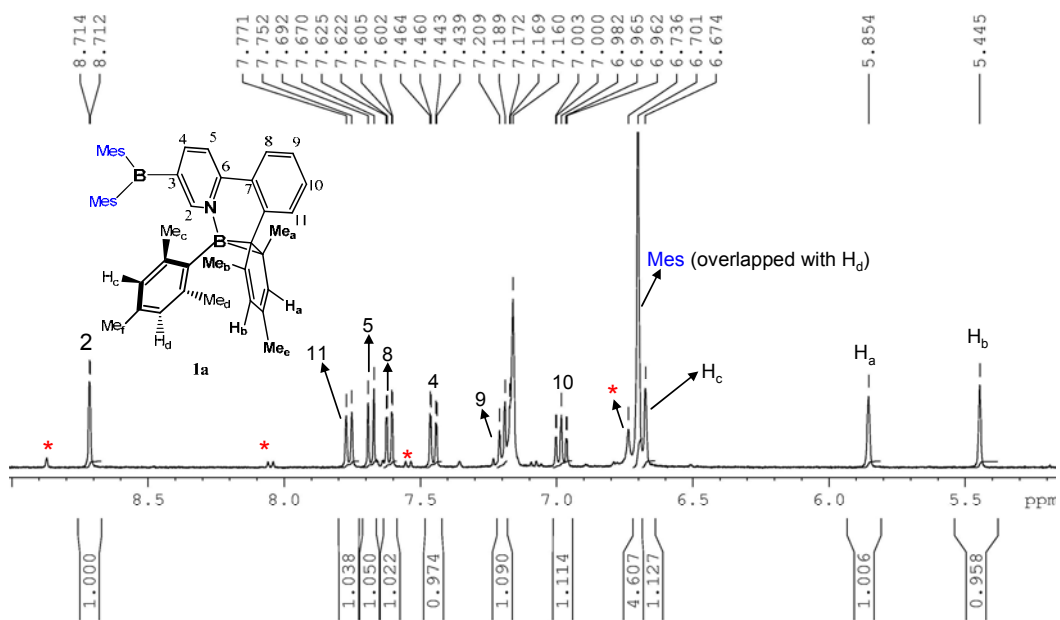
Figure 3.21 Enlargement of olefinic region of **3.1a** ^{1}H NMR spectral with assignments, in C$_6$D$_6$ at 298K.
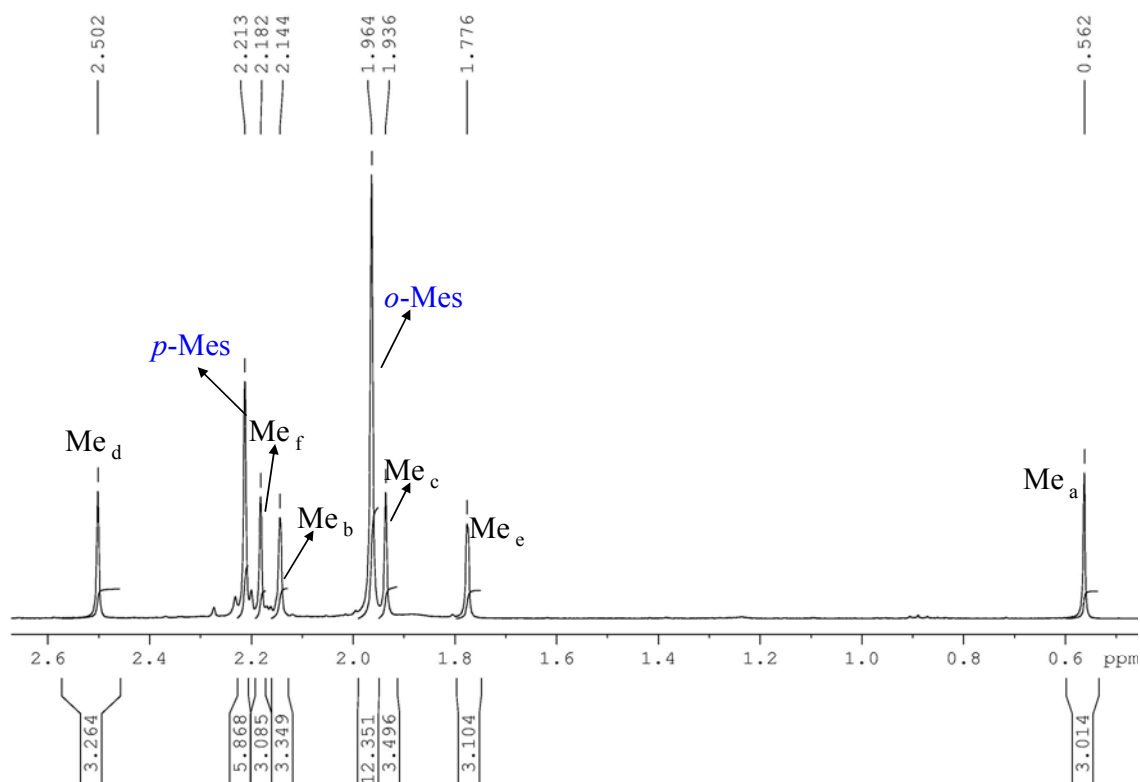
Figure 3.22 Enlargement of aliphatic region of **3.1a** ^{1}H NMR spectral with assignments in C_6D_6 at 298K.

3.5.2.2 HMBC NMR data supporting the structure of 3.1a

The HMBC NMR spectra of **3.1a** were performed at 283 K after nearly complete conversion from **3.1** under nitrogen in C_6D_6, under UV (365 nm) irradiation, concentration = ~0.03M, r.t. The HMBC NMR spectra were shown in Figure 3.23 and Figure 3.24. In Figure 3.24, the three-bond C-H coupling between C_x (46.562 ppm) and the following protons H_{11}, H_a, Me_b and Me_a was observed. Similarly, the two-bond C-H

coupling between C_y (29.236 ppm) and protons from Me_a is a clear evidence of the existence of two aliphatic carbon in **3.1a**.
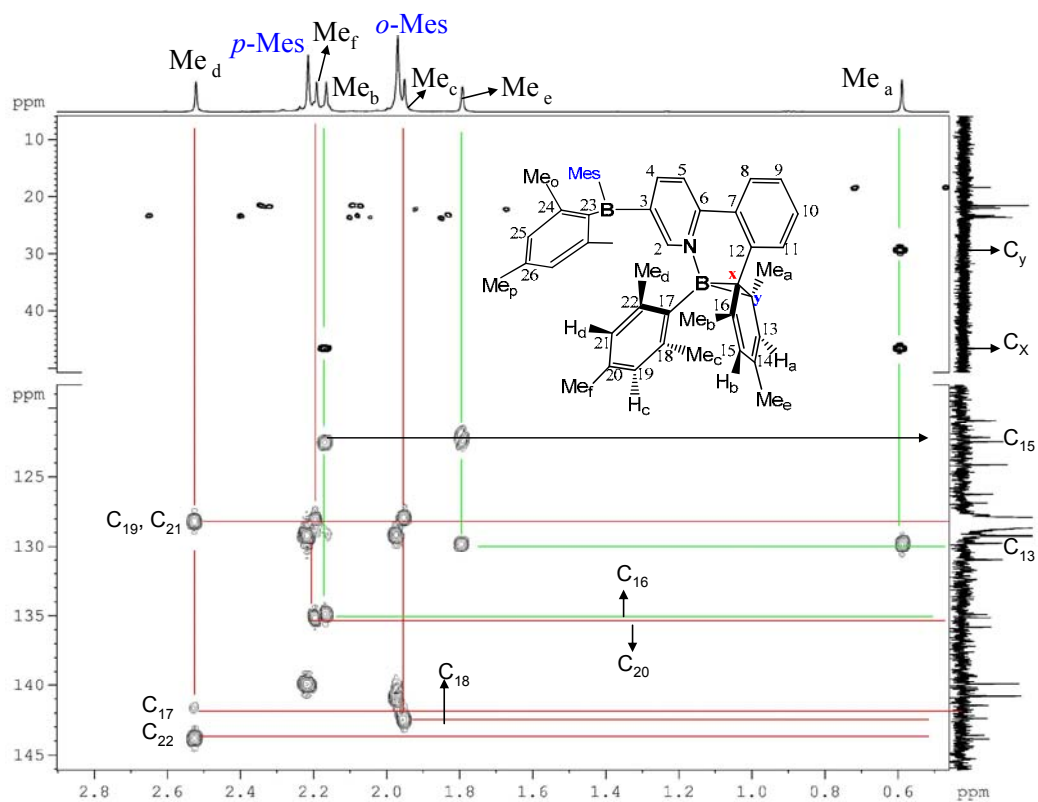
Figure 3.23 The crosspeaks of **3.1a** [1]H aliphatic region with ^{13}C in HMBC spectra in C_6D_6 recorded under nitrogen at 283K.
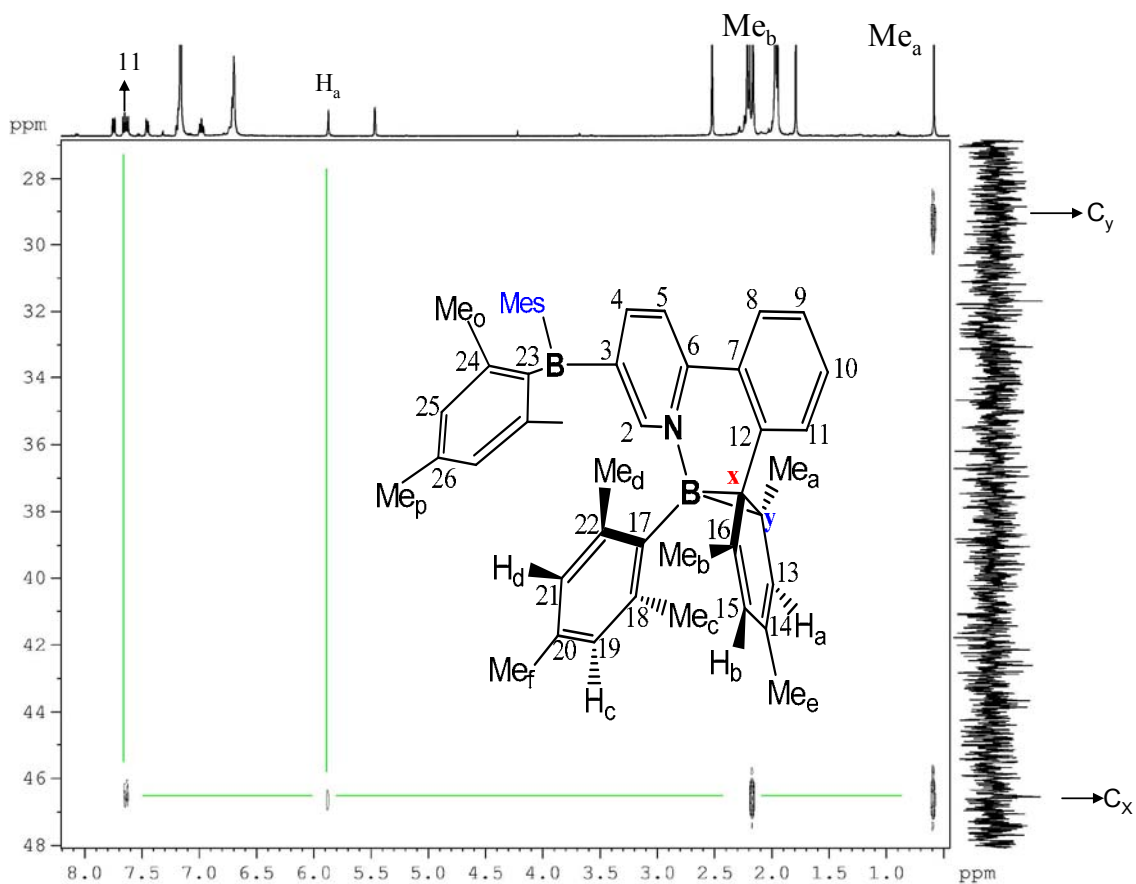
Figure 3.24 The crosspeaks of ^{13}C 20-50 ppm with ^{1}H of **3.1a** in HMBC spectra in C_6D_6 recorded under nitrogen at 283K.

3.5.2.3 NOESY NMR data supporting the structure of 3.1a

The NOESY NMR spectra of **3.1a** were performed at 283K after nearly complete conversion from **3.1** under nitrogen in C_6D_6, under UV (365 nm) irradiation, concentration = ~0.03M, r.t. The NOSEY NMR spectra of **3.1a** are presented in Figure

3.25 and Figure 3.26 with that the exchange cross-peaks are shown in red color while their NOE cross-peaks in black color.
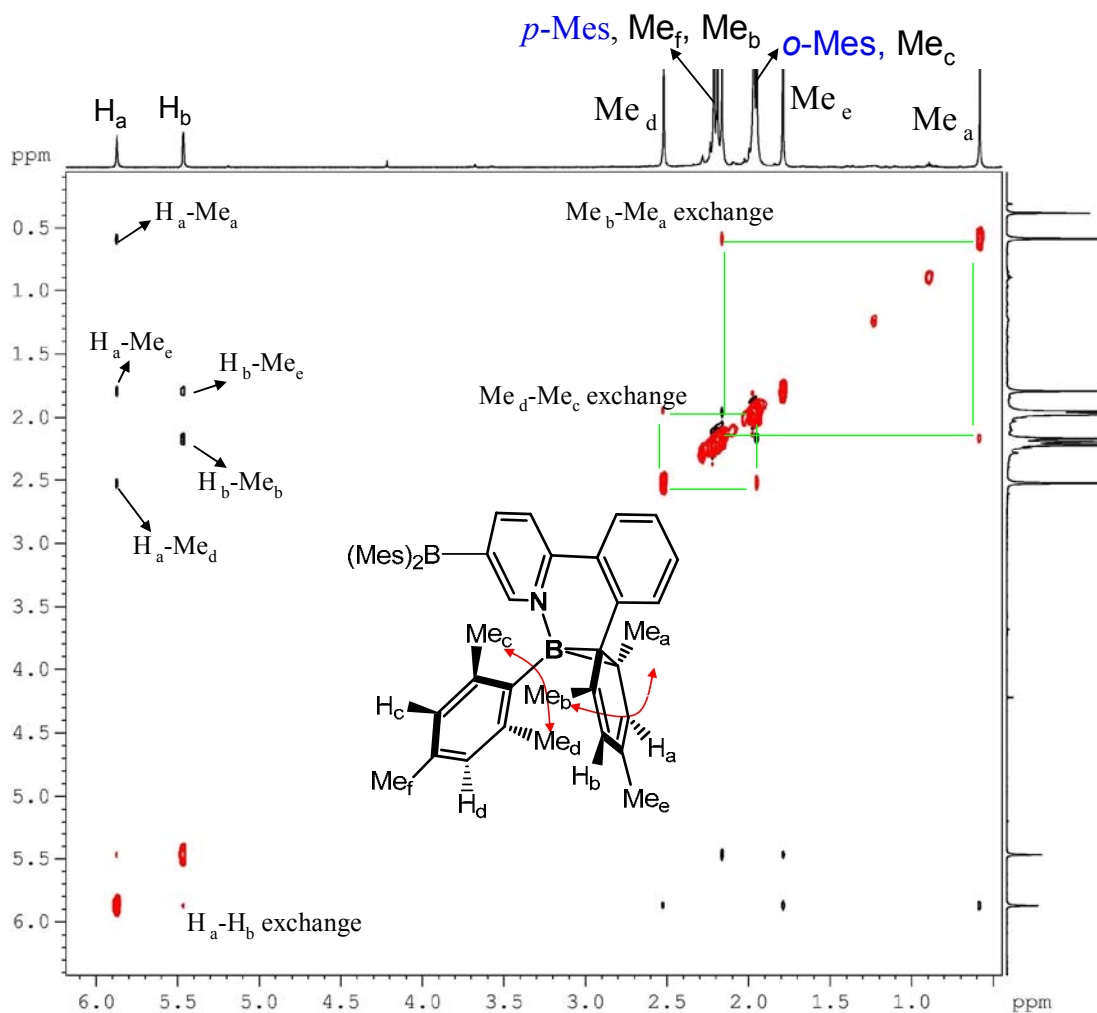
Figure 3.25 The 0.5-6.0 ppm region of NOESY spectrum of the **3.1a** recorded under nitrogen in C_6D_6 at 283K.
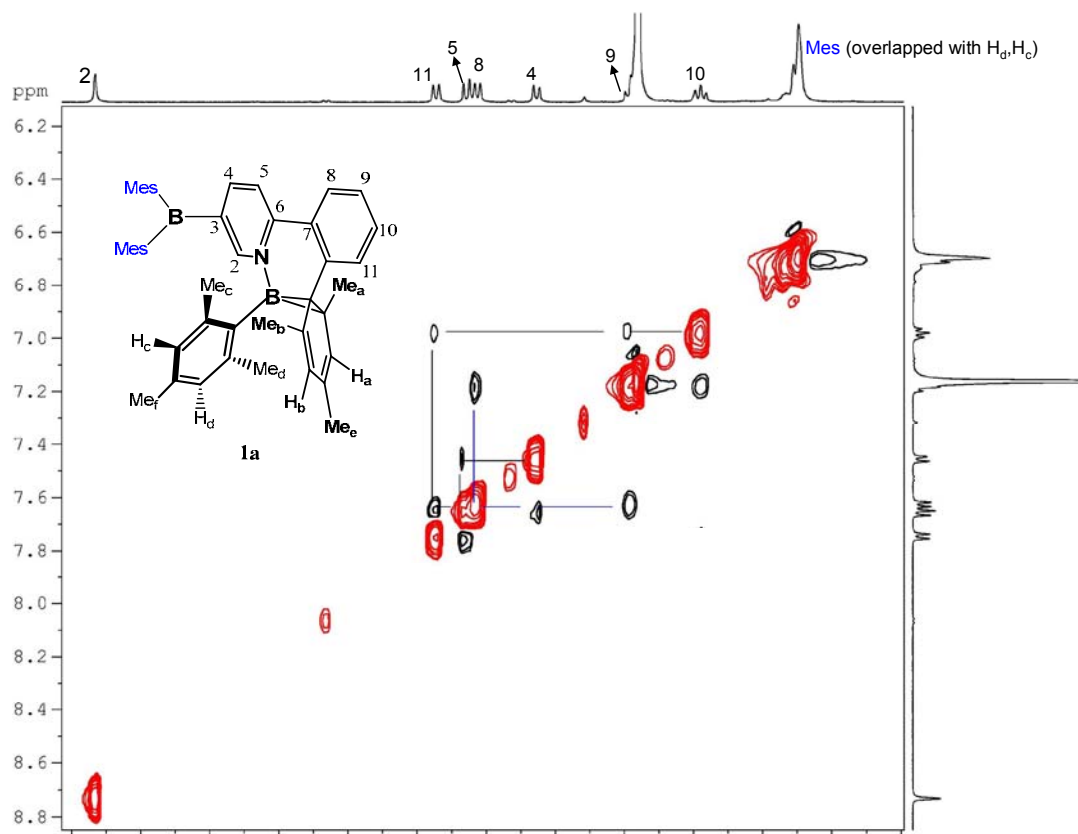
Figure 3.26 The aromatic region of NOESY spectrum of the **3.1a** recorded under nitrogen in C_6D_6 at 283K.

Strong chemical exchange cross peaks of between H_a and H_b, Me_a and Me_b on the cyclohexadienyl ring, and H_c and H_d, Me_c and Me_d on the mesityl for **3.1a** from NOESY spectra, indicating the presence of enantiomer inter-conversion in solution via B – C σ migration, as depicted in Figure 3.27.
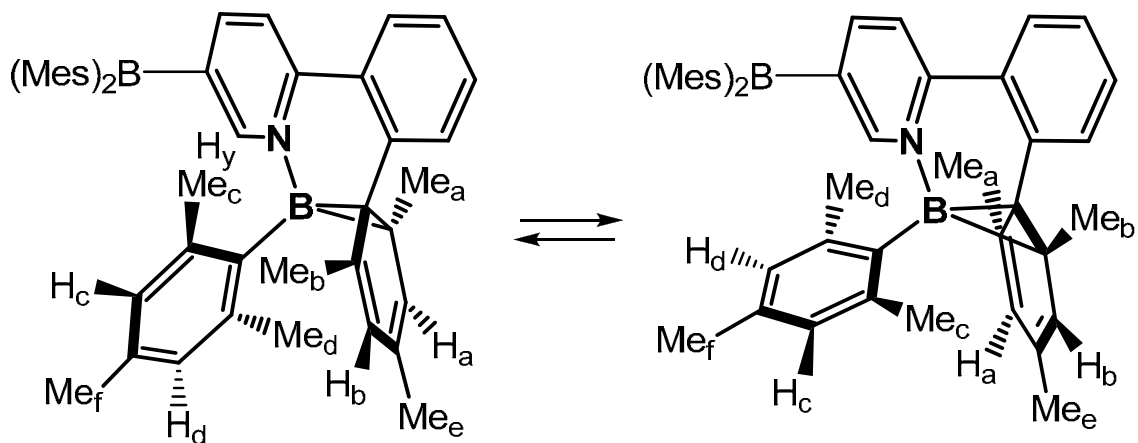
Figure 3.27 A scheme showing the racemization of **3.1a**.

3.5.2.4 COSY NMR data supporting the structure of 3.1a

The COSY NMR spectra of **3.1a** were performed at 298 K after nearly complete conversion from **3.1** under nitrogen in C_6D_6, under UV (365 nm) irradiation, concentration = ~0.03M, r.t. The COSY NMR spectra are presented in Figure 3.28 and Figure 3.29.
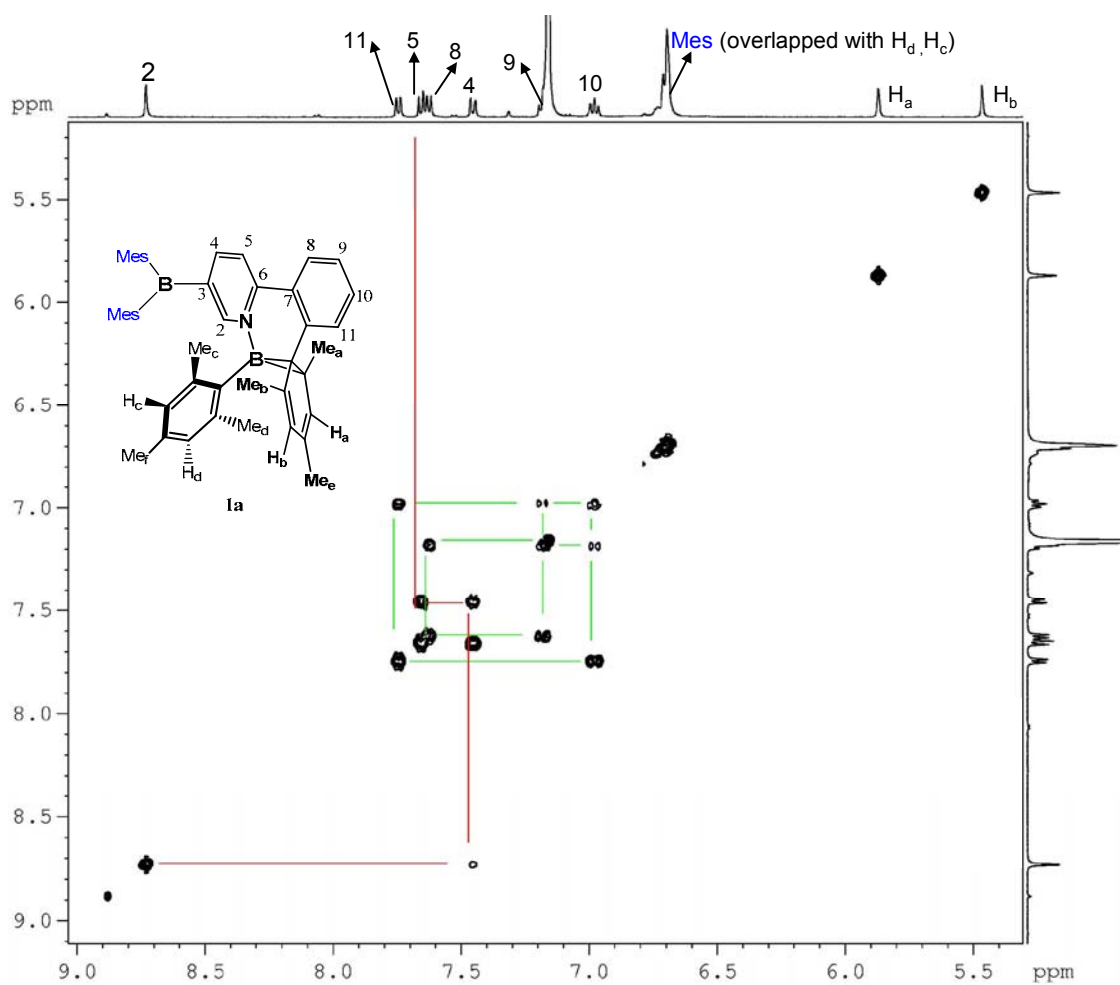
Figure 3.28 The aromatic region of the COSY spectrum of **3.1a** under nitrogen in C_6D_6, at 283K with the 1D spectral assignments.
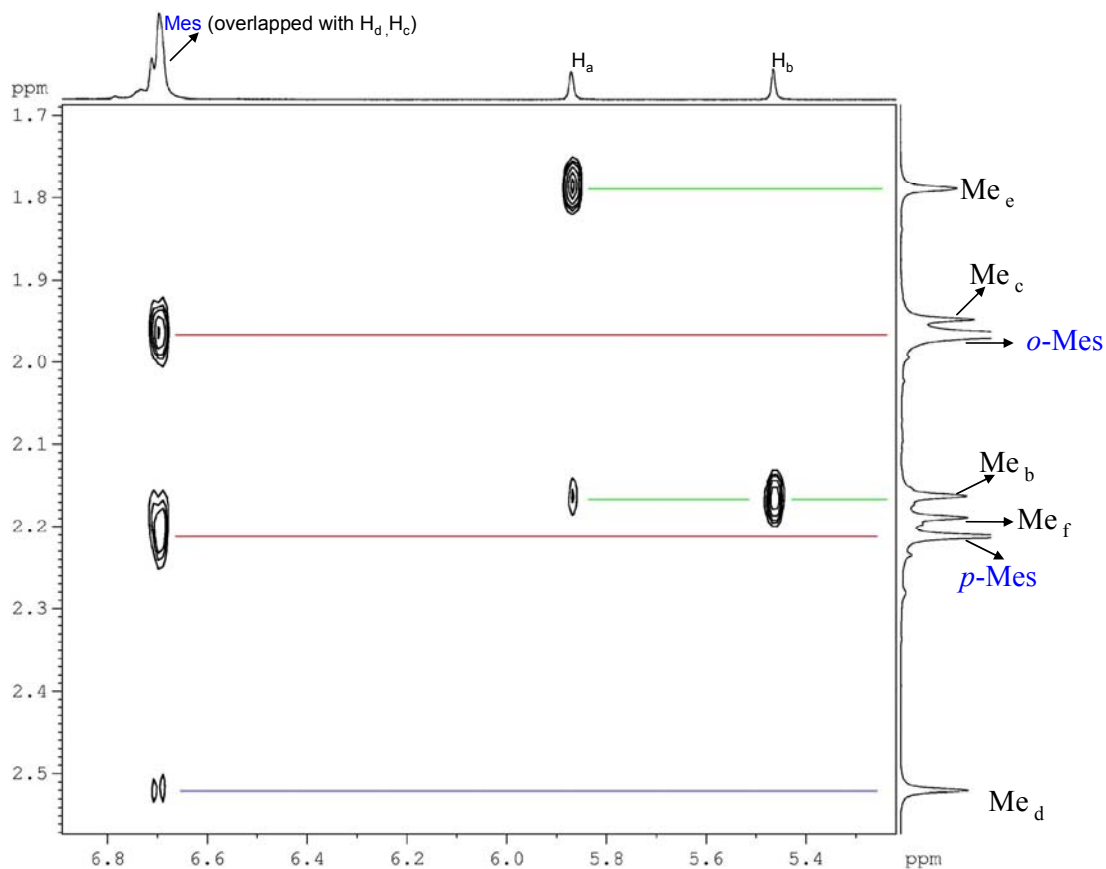
Figure 3.29 The enlargement of the COSY spectrum of **3.1a** (with trace of **3.1**) under nitrogen in C_6D_6 at 283K.

3.5.2.5 ^{13}C NMR assignment of 3.1a

The ^{13}C NMR spectra are shown in Figure 3.30 and Figure 3.31. The complete assignment of **3.1a** is based on the 1H NMR data, 2D HSQC, HMBC, NOESY, COSY NMR data.
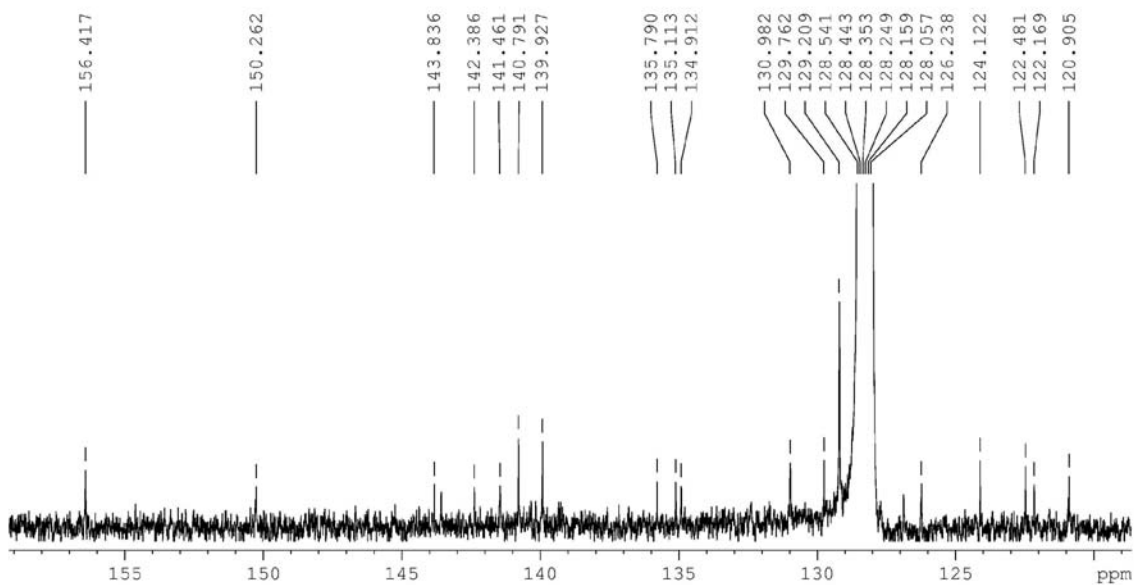
Figure 3.30 Enlargement of olefinic region of **3.1a** ^{13}C NMR spectrum.
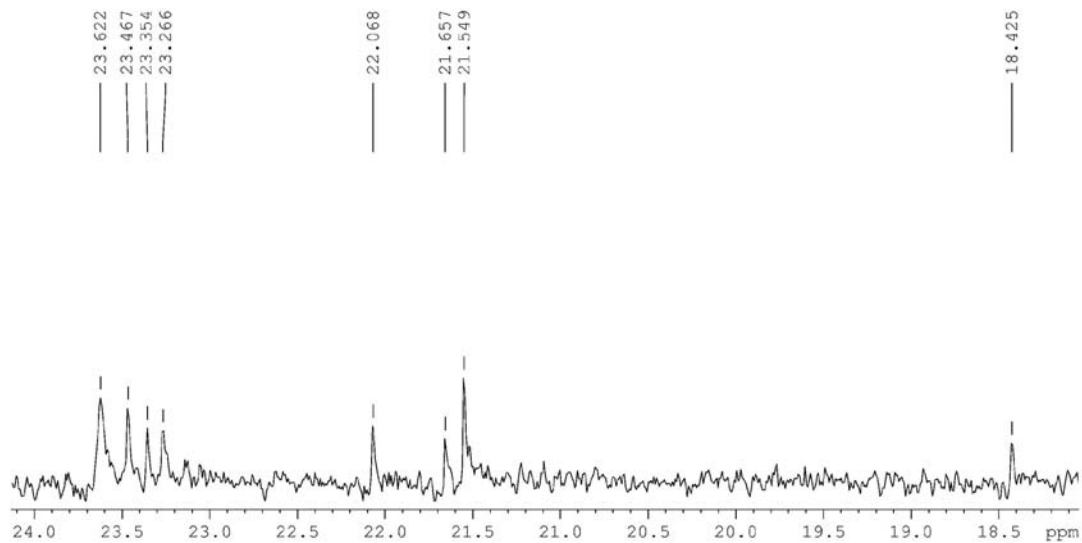
Figure 3.31 Enlargement of aliphatic region of **3.1a** ^{1}H NMR spectrum.
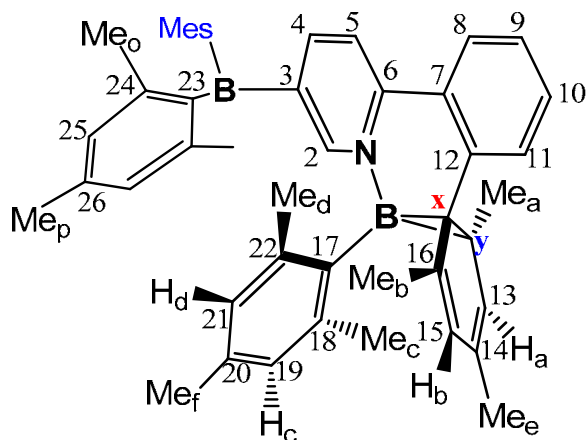
156.4 C_2;   150.2 C_6;   143.8 C_{22};   142.3 C_{18}; 141.4 C_4;   140.7 C_{24};

139.9 C_{26};   135.7 C_8;   135.1 C_{20};   134.9 C_{16}; 130.9 C_{10}; 129.7 C_{13};

129.2 C_{25};   126.2 C_{11}; 124.1 C_9;   122.4 C_{15}; 122.1 C_{14}; 120.9 C_5;

143.6 C_{12} (confirmed by HMBC NMR experiment);

128.0-128.5 C_{19}, C_{21} (overlapped with benzene-D6, confirmed by HMBC and HMQC NMR experiment);

46.5 C_x;   29.6 C_y (confirmed by HMBC and HMQC NMR experiment);

23.6 o-methyl; 23.4 methyl b; 23.3 methyl d; 23.2 methyl c;

22.0 methyl e; 21.6 methyl f; 21.5 p-methyl; 18.4 methyl a.

3.5.2.6 Structure of 3.1a optimized through DFT calculation

The attempt to crystallize the proposed intermediate **3.1a** was not successful. With the proposed structure in mind, through DFT calculations we build the structure model **3.2a** (Figure 3.32), which has simpler structure than **3.1a** and thus can save the calculation

145

time. Since three-coordinate boron center is stable towards light, we believe that the structural change in the tetrahedral center of **3.1a** is similar to that of molecular model **3.2a**.
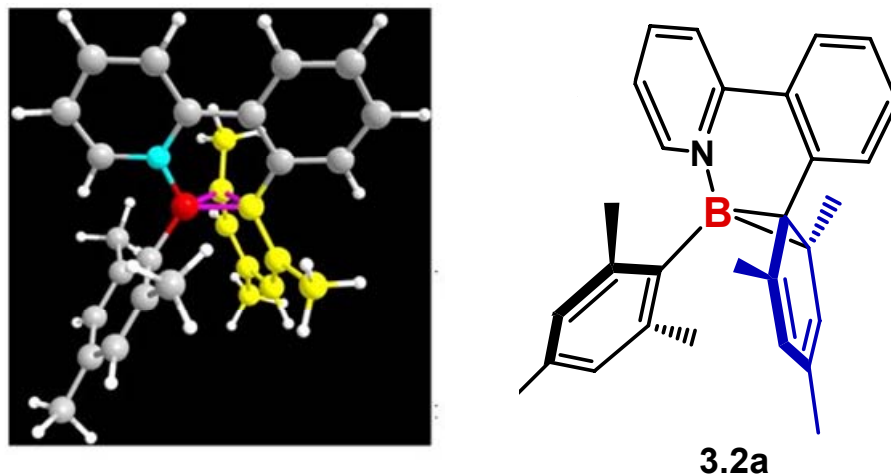
Figure 3.32 The optimized structure of **3.2a** by DFT.

All ^1H, ^{13}C, COSY, HMBC and NOESY NMR data around tetrahedral boron center of **3.1a** are consistent with that of the proposed structure model **3.2a** obtained by DFT calculations. The structure of **3.2a** shows that the 6-membered chelate ring is planar and nearly perpendicular to the BCC ring. The calculated C (ph) – C (Mes) distance is 1.48 Å, while the bond lengths within the BCC triangle are 1.66, 1.63 Å (B – C), 1.56 Å (C – C), respectively. The structure also shows that **3.1a** is sterically more congested than **3.1**, as evident by the short separation distances between the mesityl and the cyclohexadienyl, consistent with the restricted rotation of the mesityl around the B-C bond in **3.1a**, as revealed by ^1H NMR. The short spatial separation distance between H_a

and H atoms of Me$_d$ (~2.6 Å) is in good agreement with a strong NOE cross peak in the NOESY spectrum.

As shown in Figure 3.33, the HOMO of **3.2a** is mainly localized on the B-cyclohexadienyl with partly contribution from the π orbital of ph-py moiety. The LUMO of **3.2a** is dominated by the π* orbital of ph-py moiety. The HOMO and LUMO orbital of **3.1a** is believed to be similar to those of **3.2a**. The intense and dark color of **3.1a** can be explained by a low energy charge transfer transition from B-cyclohexadienyl to the B(Mes)$_2$-Ph-py moiety.

HOMO **LUMO**
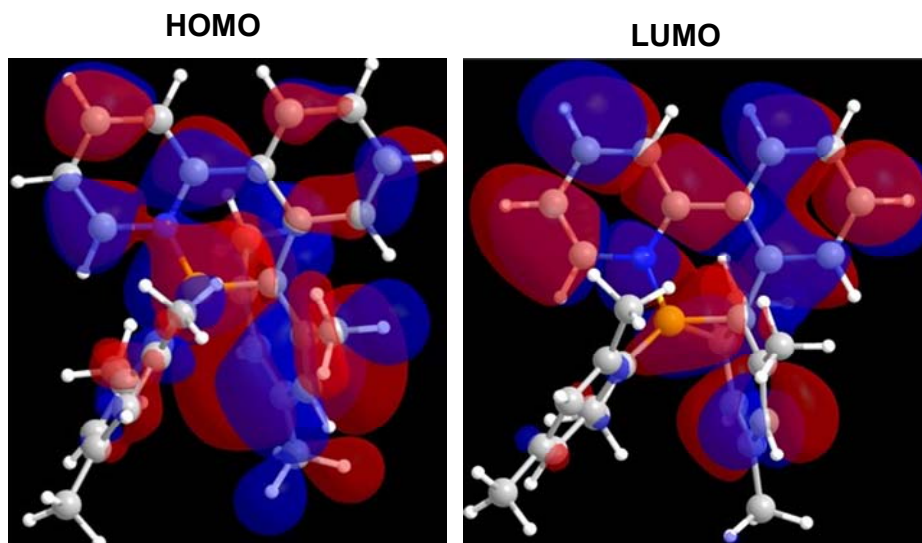
Figure 3.33 HOMO and LUMO orbital of intermediate **3.2a**.

And since the lowest electronic transition in **3.1** (Chapter 3.3.5) is charge transfer from the mesityls of tetrahedral B to the N, C-chelate, the photoisomerization is most likely initialized by a photoinduced internal electron transfer.

3.5.3 Thermal conversion of 3.1a back to 3.1 under N_2

Most remarkable is the reversibility of the **3.1a** to **3.1** transformations under nitrogen in C_6D_6. We have observed that while the dark olive green **3.1a** reverses back to the light yellow **3.1** in less than 1 h at 60°C. ^{1}H NMR experiments confirmed that the thermal reversal of **3.1a** back to **3.1** is quantitative. At 323 K, the $t_{1/2}$ is ~84 min for **3.1a**. The activation energy for the thermal reversal of **3.1a** was determined to be 106.7 kJ/mol. The stacked ^{1}H NMR spectra showing thermal reversal reaction of **3.1a** to **3.1** at 333K is presented in Figure 3.34. Spectra recorded at other temperatures are not shown. The activation energy of **3.1a** to **3.1** can be determined through different rate constant at variable temperature. The kinetic data and the activation energy of the thermal reversal of **3.1a** back to **3.1** were shown in Table 3.1 and Figure 3.35.
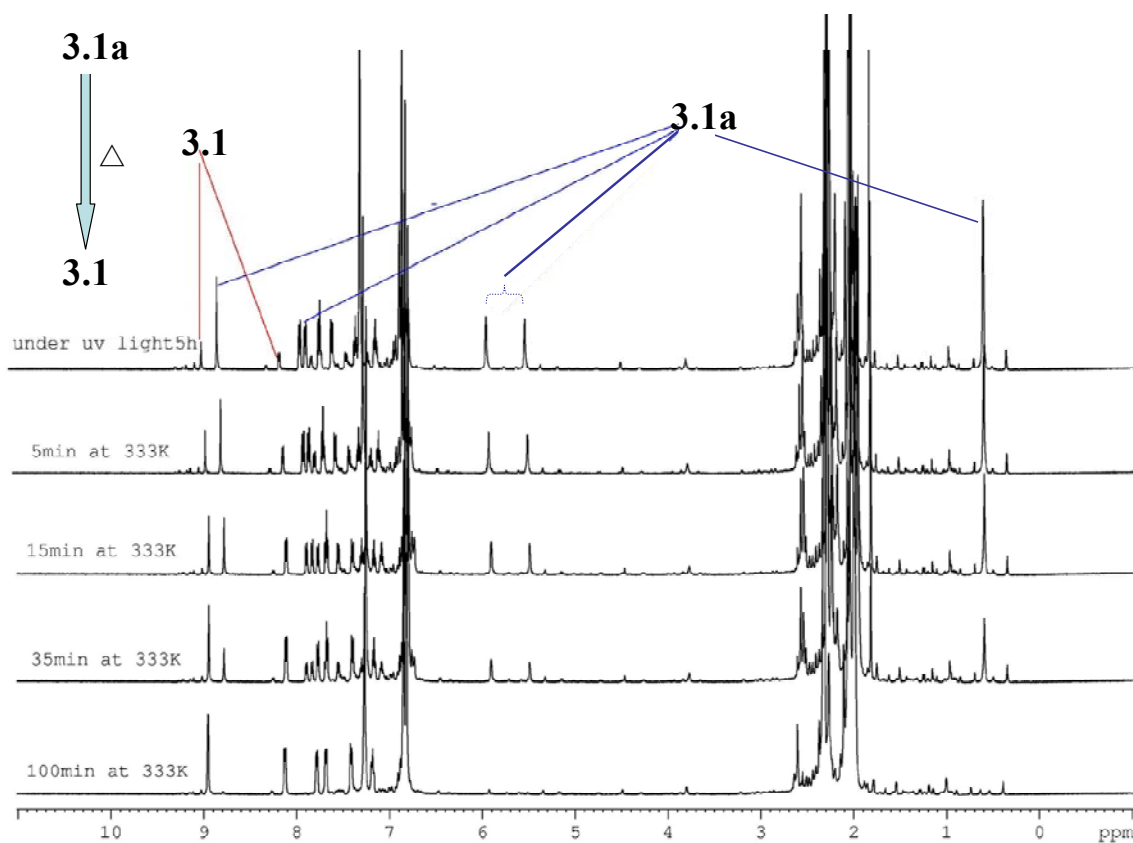
Figure 3.34 Thermal conversion of **3.1a** back to **3.1** under nitrogen in C_6D_6 at 333K at various time intervals.

T(K)	1/T	k (min^{-1})	ln(k)
298	0.003356	0.0003	-8.11173
313	0.003195	0.0029	-5.84304
318	0.003145	0.0064	-5.05146
323	0.003096	0.0082	-4.80362
333	0.003003	0.029	-3.54046
338	0.003049	0.0167	-4.09235

Table 3.1 The kinetic data of the thermal reversal of **3.1a** back to **3.1** at different temperatures.
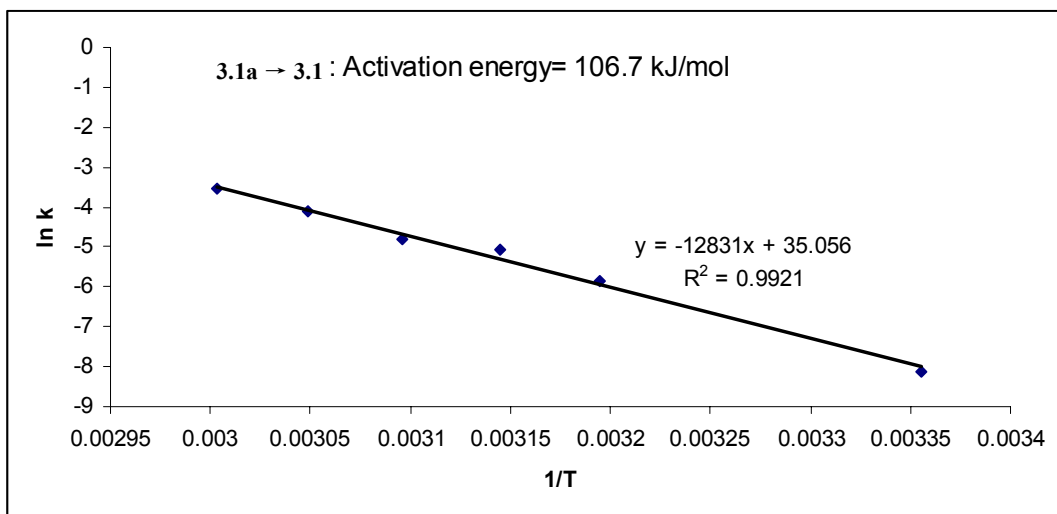
Figure 3.35 The graph showing the calculation of activation energy for the thermal reversal of **3.1a** back to **3.1**.

The coalesence temperature for any of the exchange pairs in the 1D NMR spectra could not be determined due to the rapid reversal of **3.1a** back to **3.1** at high temperatures. Nonetheless, the lower limit of the activation barrier for the racemization process was estimated by using the 1D spectra to be > 67 kJ/mol.[28]

3.5.4 Conversion of 3.1a to 3.1b under oxygen

Upon exposure to oxygen, the deep colored **3.1a** is converted to the colorless species **3.1b** instantaneously and quantitatively as established by NMR. This reactivity of **3.1a** is reminiscent of the formation of a *p*-diphenylbenzene from the O_2 oxidation of **A** (Figure 3.18). **3.1b** no longer contains the tetrahedral B center, which was eliminated as $(MesBO)_3$, based on NMR and MS evidence.

150

In summary, the photoisomerization of N, C-chelate organboron compounds is shown in Figure 3.36.
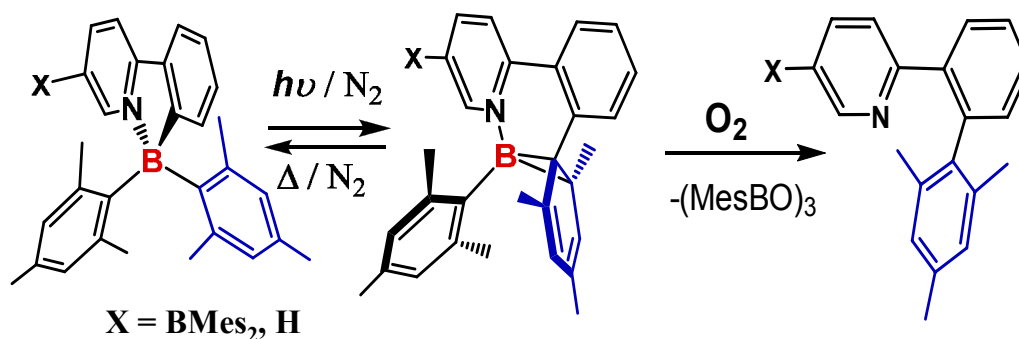
Figure 3.36 Scheme representing the photoisomerization of N, C-chelate organboron compounds.

3.6 Impact of the triarylboron center on the photochromic behavior of 3.1

To study the impact of the triarylboron center on the photochromic four-coordinate boron moiety, the monoboron compound (py-2-phenyl)BMes$_2$ (**3.2**) in Figure 3.37 was synthesized by my lab mate Hazem Amarne. Under UV irradiation, the ^{1}H, ^{11}B NMR and 2D NMR spectra of (py-2-phenyl)BMes$_2$ behaved in similar way as **3.1**, which proved again that the tetrahedral N, C-chelate mesitylboron moiety is unstable to UV light irradiation.
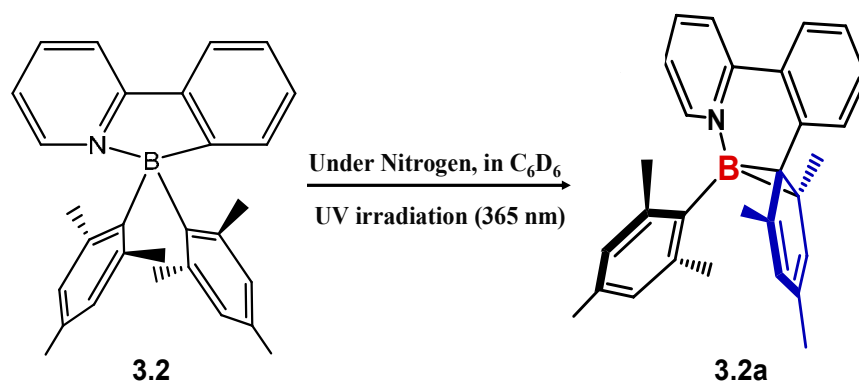
Figure 3.37 Photolysis of monoboron compound (py-2-phenyl)BMes₂.

Under same concentration and same 365 nm irradiation, the photolysis rate of **3.2** is much faster than **3.1**, even though **3.1** has larger molar extinction coefficient than that of **3.2** at 365 nm. The bulky trigonal BMes₂ group in **3.1** most likely destabilizes the transition state, hence resulting in the slower conversion of **3.1** to **3.1a**, compared to that of **3.2** to **3.2a**. Under same concentration and fluorescent light irradiation, the photolysis rate of **3.1** is faster than **3.2**, due to the fact that **3.2** has nearly no absorption in the visible region. The UV-Vis absorption spectra of **3.1** and **3.2** in toluene are show in Figure 3.38. The much faster thermal reversal by **3.1a**, relative to **3.2a**, is consistent with the greater steric congestion in **3.1a** that destabilizes the molecule.

UV-Vis Abs spectra of 3.1 and 3.2, c = 2× 10⁻⁵ M in toluene
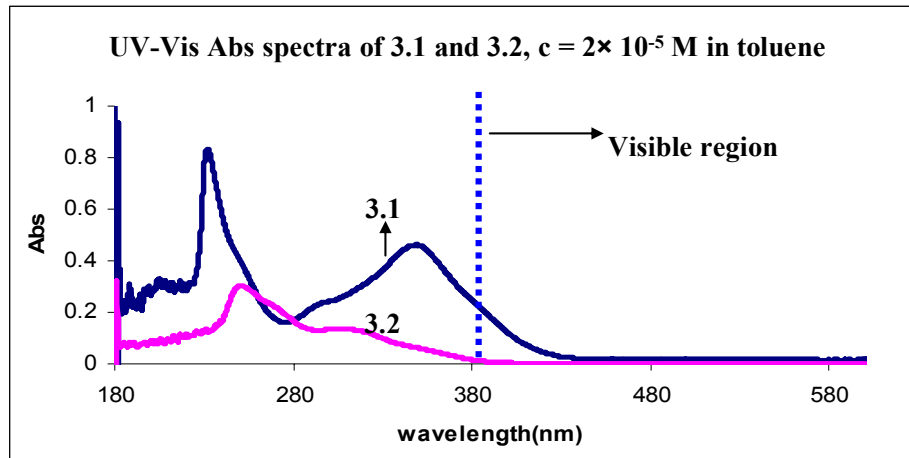
Figure 3.38 UV-Vis absorption spectra of **3.1** and **3.2** in toluene**.**

3.7 Conclusion

Incorporation of a second tetrahedral boron center into triaryboron system can greatly lower the LUMO energy level and enhance the electron affinity. A reversible isomerization process involving a tetrahedral boron center and the formation/breaking of a C – C bond has been established. Although many organic photochromic systems were known previously,[29] compounds **3.1** and **3.2** are the first examples of organoboron compounds that display a reversible photo-thermal color switching. The N,C-chelate groups in both compounds play a key role in mediating the isomerization process. The high susceptibility of **3.1a** and **3.2a** toward oxygen upon exposure to light will clearly limit the use of this class of materials in certain optoelectronic devices. However, the new C-C bond formation breaking reaction provides new opportunities in the orgonoboron photochemical research area.

3.8 References

(1) Noda, T.; Shirota, Y. *J. Am. Chem. Soc.* **1998**, *120*, 9714.

(2) Shirota, Y. *J. Mater. Chem.* **2005**, *15*, 75.

(3) Noda, T.; Ogawa, H.; Shirota, Y. *Adv. Mater.* **1999**, *11*, 283.

(4) Shirota, Y.; Kinoshita, M.; Noda, T.; Okumoto, K.; Ohara, T. *J. Am. Chem. Soc.* **2000**, *122*, 1102.

(5) Jia, W. L.; Bai, D. R.; McCormick, T.; Liu, Q. D.; Motala, M.; Wang, R.; Seward, C.; Tao, Y.; Wang, S. *Chem. Eur. J.* **2004,** *10*, 994.

(6) Jia, W. L.; Moran, M. J.; Yuan, Y. Y.; Lu, Z. H.; Wang, S. *J. Mater. Chem.* **2005**, *15*, 3326.

(7) Wakamiya, A.; Mori, K.; Yamaguchi, S. *Angew. Chem. Int. Ed.* **2007**, *46*, 4273.

(8) Sundararaman, A.; Venkatasubbaiah, K.; Victor, M.; Zakharov, L. N.; Rheingold, A. L.; Jäkle, F. *J. Am. Chem. Soc.* **2006**, *128*, 16554.

(9) Jia, W. L.; Feng, X. D.; Bai, D. R.; Lu, Z. H.; Wang, S. *Chem. Mater.* **2005**, *17*, 164.

(10) Elbing, M.; Bazan, G. C. *Angew. Chem. Int. Ed.* **2008**, *47*, 834 and references therein.

(11) Wakamiya, A.; Taniguchi, T.; Yamaguchi, S. *Angew. Chem. Int. Ed.* **2008**, 47, 834.

(12) Liu, Q. D.; Mudadu, M. S.; Thummel, R.; Tao, Y.; Wang, S. *Adv. Funct. Mater.* **2005**, *15*, 143.

(13) Liu, S. F.; Wu, Q.; Schmider, H. L.; Aziz, H.; Hu, N. X.; Popović, Z.; Wang, S., J. *Am. Chem. Soc.*, **2000**, *122*, 3671.

(14) Wu, Q.; Esteghamatian, M.; Hu, N. X.; Popovic, Z.; Enright, G.; Wang, S.; Tao, Y.; D'Iorio, M., *Chem. Mater.*, **2000**, *12*, 79.

(15) Wu, Q.; Esteghamatian, M.; Hu, N. X.; Popovic, Z.; Enright, G.; Breeze, S. Wang, S., *Angew. Chem. Int. Ed*. **1999**, *38*, 985.

(16) Chen, H. Y.; Chi, Y.; Liu, C. S.; Yu, J. K.; Cheng, Y. M.; Chen, K. S.; Chou, P. T.; Peng, S. M.; Lee, G. H.; Carty, A. J.; Yeh, S. J.; Chen, C. T, *Adv. Funct. Mater*. **2005**, *15*, 567.

(17) Hoefelmeyer, J. D.; Schulte, M.; Tschinkl, M.; Gabbai, F. P., *Coord. Chem. Rev*. **2002**, *235*, 93.

(18) Wakamiya, A.; Mori, K.; Yamaguchi, S. *Angew. Chem. Int. Ed*. **2007**, *46*, 4273.

(19) Jia, W.; Song, D.; Wang, S. *J. Org. Chem.* **2003**, *68*, 701.

(20) Zhao, S.; McCormick, T.; Wang, S. *Inorg. Chem.* **2007**, *46*, 10965.

(21) Gaussian 03, Revision C.02, Frisch, M. J.; Trucks, G. W.; Schlegel, H. B.; Scuseria, G. E.; Robb, M. A.; Cheeseman, J. R.; Montgomery, Jr., J. A.; Vreven, T.; Kudin, K. N.; Burant, J. C.; Millam, J. M.; Iyengar, S. S.; Tomasi, J.; Barone, V.; Mennucci, B.; Cossi, M.; Scalmani, G.; Rega, N.; Petersson, G. A.; Nakatsuji, H.; Hada, M.; Ehara, M.; Toyota, K.; Fukuda, R.; Hasegawa, J.; Ishida, M.; Nakajima, T.; Honda, Y.; Kitao, O.; Nakai, H.; Klene, M.; Li, X.; Knox, J. E.; Hratchian, H. P.; Cross, J. B.; Bakken, V.; Adamo, C.; Jaramillo, J.; Gomperts, R.; Stratmann, R. E.; Yazyev, O.; Austin, A. J.; Cammi, R.; Pomelli, C.; Ochterski, J. W.; Ayala, P. Y.; Morokuma, K.; Voth, G. A.; Salvador, P.; Dannenberg, J. J.; Zakrzewski, V. G.; Dapprich, S.; Daniels, A. D.; Strain, M. C.; Farkas, O.; Malick, D. K.; Rabuck, A. D.;

Raghavachari, K.; Foresman, J. B.; Ortiz, J. V.; Cui, Q.; Baboul, A. G.; Clifford, S.; Cioslowski, J.; Stefanov, B. B.; Liu, G.; Liashenko, A.; Piskorz, P.; Komaromi, I.; Martin, R. L.; Fox, D. J.; Keith, T.; Al-Laham, M. A.; Peng, C. Y.; Nanayakkara, A.; Challacombe, M.; Gill, P. M. W.; Johnson, B.; Chen, W.; Wong, M. W.; Gonzalez, C.; and Pople, J. A.; Gaussian, Inc., Wallingford CT, 2004.

(22) (a)Becke, A. D. J. Chem. Phys. 1993, 98, 5648. (b) Lee, C.; Yang, W.; Parr, R. G. *Phys. Rev.* B. **1988**, 37, 785. (c) Miehlich, B.; Savin, A.; Stoll, H.; Preuss, H. *Chem. Phys. Lett.* **1989**, 157, 200. (d)Hariharan, P. C.; Pople, J. A. *Theor. Chim. Acta* **1973**, 28, 213.

(23) *SHELXTL*, version 6.14; Bruker AXS: Madison, WI, 2003.

(24) Cole, S. C.; Coles, M. P.; Hitchcock, P. B. *Dalton Trans.* **2003**, 3663.

(25) Wrackmeyer, B. "NMR spectroscopy of Boron Compounds Containing two-, three- and Four-Coordinate Boron", In *Annu. Rep. NMR Spectrosc.* **1988**, *20*, 61.

(26) Wilkey, J. D.; Schuster, G. B., *J. Org. Chem.* **1987**, *52*, 2117.

(27) Wilkey, J. D.; Schuster, G. B., *J. Am. Chem. Soc.* **1988**, *110*, 7569.

(28) Williams, D. H.; Fleming, I., Spectroscopic Methods in Organic Chemistry, 4th ed., McGraw-Hill Book Company, London, **1987**.

(29) Dürr, H.; Bouas-Laurent, H. ed., In *Photochromism: Molecules and Systems*, 2nd edition, Elsevier, **2003** and references therein.

Chapter 4

Photochemical Reactivity of N, C-Chelate Tetrahedral Organoboron Derivative {[(2-py-phenyl)-4-py]-2-phenyl}BMes$_2$ and Its-Coupled Pt(II) Complex

4.1 Introduction

The newly discovered N, C-chelate tetrahedral organoboron compounds are a new class of photochromic compounds, with potential applications as promising materials for data storage, optoelectronics and molecular switching devices. For the well-known photochromic compounds, like diarylethene derivatives, the combination of them with metal complexes is envisioned to give rise to novel properties, such as the regulation of the lifetime of metal-ligand's excited state,[1] energy transfer between the metal center and ligand[2, 3] and fluorescence modulation.[4, 5] Further investigations into the exploration of N, C-chelate tetrahedral organoboron compounds as ligands to form metal complexes are attractive.

A Pt(II) center with intramolecular C-H bond activation can also constrain the N, C-chelating ligands in a planar fashion. Pt(II) complexes have unique electronic transitions and interesting photophysical properties different from organic molecules. To study the impact of a Pt(II) center on the tetrahedral boron moiety, molecules containing both a Pt(II) center and a tetrahedral organoboron moiety were designed and studied. As shown in Figure 4.1, free ligand {[(2-py-phenyl)-4-py]-2-phenyl}BMes$_2$ (**4.1**, B-ppy-ppy) and its Pt(II) complex {[(2-py-phenyl)Pt(4-t-Bu-py)ph-4-py]-2-phenyl}BMes$_2$ (**4.2**,

(B-ppy-ppy)-PtPh-t-Bu-py)) were synthesized. Pt(II) complex (2-py-phenyl)Pt(4-t-Bu-py)ph (**4.3**) without the tetrahedral boron moiety was also synthesized and studied for comparison.
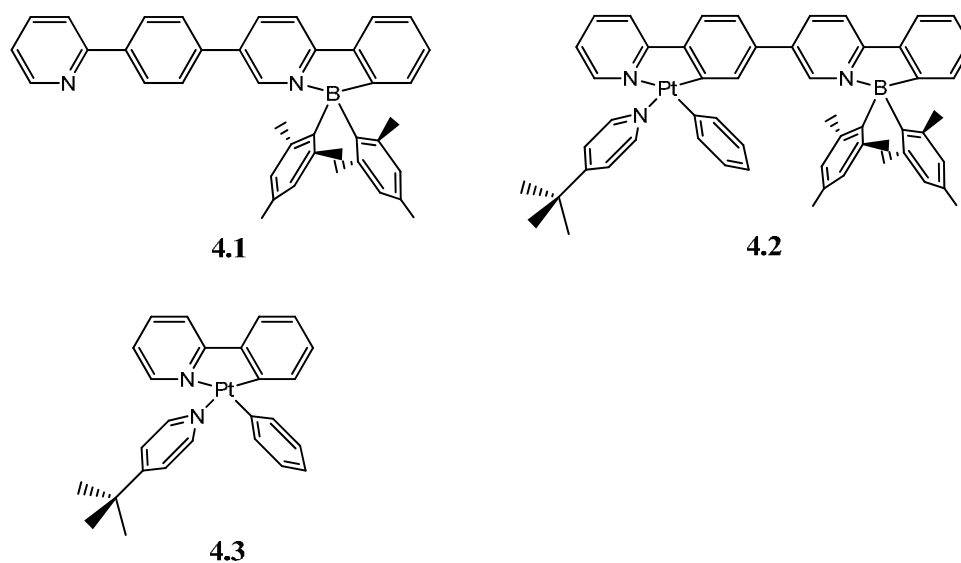
Figure 4.1 Molecular structures of **4.1**, **4.2** and **4.3**.

4.2 Experimental

4.2.1 General considerations

All reactions were performed under N_2 with standard Schlenk techniques unless otherwise noted. All starting materials were purchased from Aldrich Chemical Co. and used without further purification. DMF, THF, Et$_2$O, and hexanes were purified using an Innovation Technology Co. solvent purification system. CH$_2$Cl$_2$ was freshly distilled over

P_2O_5 prior to use. Deuterated solvents were purchased from Cambridge Isotopes and were used as received without further drying. NMR spectra were recorded on Bruker Avance 400 or 500 MHz spectrometers. High-resolution mass spectra were obtained from a Waters/Micromass GC-TOF EI-MS spectrometer, which was internally calibrated before use. UV-Vis spectra were recorded on an Ocean Optics UV-visible spectrometer. Excitation and emission spectra were recorded on a Photon Technologies International QuantaMaster model C-60 spectrometer. Emission lifetimes were measured on a Photon Technologies International Phosphorescent spectrometer (Time-Master C-631F) equipped with an Xenon flash lamp and digital emission photon multiplier tube using a band pathway of 5 nm for excitation and 2 nm for emission. $[PtPh_2(DMSO)_2]$ was synthesized according to a previous report.[6]

4.2.2 Synthesis of 4.1

Synthesis of 2-(2-bromophenyl)-5-iodinepyridine. This novel compound was synthesized using a modified Suzuki coupling procedure.[7] A mixture of toluene (30 mL), ethanol (10 mL), and water (100 mL) was stirred and purged by nitrogen for 1h. 2-Bromophenyl boronic acid (0.4 g, 2 mmol), 2,5-diiodinepyridine (0.66 g, 2 mmol), $Pd(PPh_3)_4$ (0.0625 g, 0.05 mmol), and NaOH (0.5 g, 1.25 mmol) were added to the mixed solvents. The mixture was stirred at 60 °C for 12 h. The water layer was separated and extracted with CH_2Cl_2 (3 x 15 mL). The combined organic layers were dried over Na_2SO_4, and the solvents were evaporated under reduced pressure. Purification of the crude product by column chromatography (CH_2Cl_2/hexane, 1/1) afforded the product as a

white solid in 30% yield (0.25 g). ^{1}H NMR (400 MHz, CDCl$_3$, 25°C, δ, ppm): 8.95 (d, J = 1.6 Hz; 1H), 8.10 (dd, J = 6.8 Hz, J = 2.0 Hz; 1H), 7.69 (dd, J = 6.4 Hz, J = 2.0 Hz; 1H), 7.54 (dd, J = 6.0 Hz, J = 1.2 Hz; 1H), 7.45 (m, 2H), 7.30 (td, J = 6.4 Hz, J = 1.2 Hz; 1H).

Synthesis of 2-(4-bromophenyl)pyridine. This compound is a previously known compound.[7] The procedure described here for this molecule is different from the previously reported one. A mixture of THF (50 mL) and H$_2$O (50 mL) was stirred and purged by nitrogen for 1 h. The solvent was then canulated into solid mixture of 4-Bromophenyl boronic acid (1.0 g, 5 mmol), 2-bromopyridine (0.79 g, 0.48 mL, 5 mmol), Pd(PPh$_3$)$_4$ (0.156 g, 0.125 mmol), and K$_2$CO$_3$ (3.5 g, 25 mmol) under nitrogen. The mixture was stirred at 60 °C for 12h. The water layer was separated and extracted with acetyl acetate (3 x 20 mL). The combined organic layers were dried over Na$_2$SO$_4$, and the solvents were evaporated under reduced pressure. Purification of the crude product by column chromatography flushing with CH$_2$Cl$_2$, afforded the product as a white solid in 90% yield (1.1 g).

Synthesis of 4-(pyridin-2-yl)phenylboronic acid. To a stirred THF solution of 2-(4-bromophenyl)pyridine (0.94 g, 4.0 mmol) at -78°C was added dropwise via a syringe an n-BuLi solution (1.60 M) (3.1 mL, 5.0 mmol) over 5 min. The resulting solution was stirred for 1 h at -78°C, then a solution of trimethylborane (1.5 mL, 15.0 mmol) was quickly added. The reaction mixture was kept at -78°C for another 1 h and then allowed to reach ambient temperature and stirred overnight. After the removal of the solvent,

purification of the crude product by column chromatography (flushing with CH_2Cl_2 first, then THF) afforded the product as a brownish solid in 70% yield (0.6 g).

Synthesis of 2-(2-bromophenyl)-5-(4-(pyridin-2-yl)phenyl)pyridine. This compound was also synthesized using a modified Suzuki coupling procedure.[2] 10 mL dry toluene was added to solid mixture of 4-(pyridin-2-yl)phenylboronic acid (0.8 g, 4.0 mmol), 2-(2-bromophenyl)-5-iodinepyridine (1.1 g, 3.0 mmol), $Pd(OAc)_2$ (13.0 mg, 0.06 mmol), 2-dicylohexylphosphino-2',6'-dimethoxybiphenyl (50.0 mg, 0.012 mmol) and K_3PO_4 (1.2 g, 6mmol)under nitrogen. The mixture was stirred at 60 °C for 48 h. 20 mL H_2O was added to the reaction mixture and then the water layer was separated and extracted with CH_2Cl_2 (3 x 10 mL). The combined organic layers were dried over Na_2SO_4, and the solvents were evaporated under reduced pressure. Purification of the crude product by column chromatography (hexane: THF = 4: 1), afforded the product as a white solid in 20% yield (0.23 g). ^1H NMR (400 MHz, $CDCl_3$, 25°C, δ, ppm): 9.02 (d, J = 1.2Hz; 1H), 8.73 (d, J = 4.8 Hz; 1H), 8.14 (d, J = 8.0 Hz; 2H), 8.01 (dd, J = 8.0 Hz, J = 2.0 Hz; 1H), 7.77 (m, 4H), 7.71 (m; 2H), 7.61(d, J = 6.4 Hz; 1H), 7.43 (t, J = 8.0 Hz; 1H), 7.25 (m, 2H).

Synthesis of B-ppy-ppy (4.1). To a stirred solution (diethylether/THF: 40/80ml) of 2-(2-bromophenyl)-5-(4-(pyridin-2-yl)phenyl)pyridine (0.23 g, 0.6 mmol) at -78°C was added dropwise via a syringe an n-BuLi solution (1.60 M) (0.6 mL, 1.0 mmol) over 1 min. The resulting solution was stirred for 1 h at -78°C, then a solution of dimesitylboron fluoride (0.36 g, 1.2 mmol) in Et_2O was quickly added. The reaction mixture was kept at -78°C for another 1 h and then allowed to reach ambient temperature and stirred overnight.

After the removal of the solvent, purification of the crude product by column chromatography (CH$_2$Cl$_2$/Hexane, 1/1) afforded the product as a yellow solid in 25% yield (0.08 g). The resulting yellow solid was recrystallized avoiding light from CH$_2$Cl$_2$/hexane to give yellow crystals of **4.1**. ^{1}H NMR (400 MHz, CD$_2$Cl$_2$, 25°C, δ, ppm): 8.93 (d, J =1.2 Hz; 1H), 8.71 (d, J = 4.8Hz; 1H), 8.32 (dd, J = 8.0 Hz, J = 2.0 Hz; 1H), 8.17 (d, J = 8.0 Hz; 2H), 8.10 (d, J = 8.0 Hz; 1H), 7.95 (d, J = 6.4 Hz; 1H), 7.80 (t; 2H), 7.78 (d, J = 6.4 Hz; 1H), 7.63 (d, J = 8.0 Hz; 2H), 7.32 (m; 3H), 6.68 (s; 4H), 2.18 (s, 6H), 1.87 (s, 12H). ^{13}C{^{1}H}NMR (100 MHz, C$_6$D$_6$, δ, ppm): 158.16, 156.46, 150.24, 144.55, 140.10, 138.45, 136.50, 136.33, 135.07, 134.38, 134.21, 132.16, 131.62, 130.82, 129.14, 127.08, 125.64, 122.49, 121.75, 120.12, 119.56, 117.50, 114.45, 113.18, 25.70, 20.99. Anal. calcd for C$_{37}$H$_{40}$BNOPtS: C 86.32, H 6.70, N 5.03; found: C 86.28, H 6.87, N 5.01.

4.2.3 Synthesis of 4.2

Synthesis of (B-ppy-ppy)-PtPhDMSO). To a stirred THF (20 mL) solution of [PtPh$_2$(DMSO)$_2$] (51.0 mg, 0.10 mmol) was added **4.1** (50 mg, 0.09 mmol). The mixture was stirred at 50°C for 6 h and the solvent was removed under reduced pressure. Pure {[(2-py-phenyl)Pt(DMSO)ph-4-py]-2-phenyl}BMes$_2$ was obtained after the residue solid was washed with hexane and ether, with 70% yield. ^{1}H NMR (400 MHz, CD$_2$Cl$_2$, 25°C, δ, ppm): 9.70 (d, J = 4.8 Hz; 1H), 8.55 (s; 1H), 7.96 (m; 2H), 7.84 (m; 3H), 7.71 (d, J = 8.0 Hz; 2H), 7.47 (d, satellites, J_{Pt-H} = 60.0 Hz, J = 8.0 Hz; 2H), 7.73 (m; 3H), 7.18 (dd, J

= 8.0 Hz, J = 1.6 Hz; 1H), 6.98 (t, J = 7.2 Hz; 2H), 6.87 (d; J = 6.8 Hz; 1H), 6.81 (d, J =

2.0 Hz; 1H), 6.64(s; 4H), 2.94 (s, satellites; 6H), 2.18 (s, 6H), 1.76 (s, 12H). This

compound was used in next step as a precursor for **4.2** without further characterization.

Synthesis of (B-ppy-ppy)-PtPh-t-Bu-py (4.2). To a CH_2Cl_2 (20 mL) solution of {[(2-

py-phenyl)Pt(DMSO)ph-4-py]-2-phenyl}BMes$_2$ (45 mg, 0.05 mmol) was added excess

t-Bu-4-pyridine (0.2 mL).   The mixture was kept standing for several hours. After the

remove of solvent and washing with hexanes, the yellow powder of **3.3** was obtained in

90% yield (40 mg). ^{1}H NMR (400 MHz, C_6D_6, 25°C, δ, ppm): 9.35 (s; 1H), 8.57 (dd, J =

5.2 Hz, J = 1.6 Hz; 2H), 8.18 (d, J = 8.0 Hz, 2H), 8.14 (d, J = 2.0 Hz; 1H), 7.67 (m; 2H),

7.60 (d, J = 8.0 Hz; 1H), 7.40 (m; 3H), 7.34 (d, J = 8.0 Hz; 1H), 7.12 (m; 1H), 7.05 (m;

2H), 6.94 (s; 4H), 6.65 (dd, J = 4.8 Hz, J = 1.6 Hz; 2H), 6.43 (t, J = 4.8 Hz; 1H), 2.27 (s;

12H), 2.21 (s; 6H), 0.87 (s; 9H). Due to the poor solubility of **4.2** the ^{13}C NMR spectrum

was not obtained. Anal. calcd for $C_{55}H_{54}N_3BPt$ • 1.2 DMSO: C 65.24, H 5.84, N 3.98,

found: C 64.56, H 5.48, N 4.04.

4.2.4 General procedure for photo-conversion of 4.1 and 4.2

For NMR under N$_2$: The photoisomerizations of **4.1** and **4.2** were carried out by

preparing a C_6D_6 (dried over NaH) solution (~0.03 M) in a NMR tube inside an inert

atmosphere dry box. The solution was placed under in a photochemical reactor at room

temperature and the exposure time was recorded. After each exposure period, the NMR

spectrum was recorded.

For NMR under N₂ (4.1a → 4.1): The solution of **4.1a** in C_6D_6 in NMR tube was prepared in the same manner as described above. After the temperature inside the NMR probe was increased to the desired temperature and the ^{1}H NMR spectra showing conversion of **4.1a → 4.1** were recorded with time.

For UV-Vis experiments: The solution was prepared in the same manner as for NMR experiments except that the NMR tube was replaced by a UV cuvette that has a screw-on cap and the solution concentration is ~1.25×10^{-4} M. The solvent used is toluene, freshly distilled.

4.2.5 Synthesis of 4.1b

Compound 4.1 (B-ppy-ppy) (0.027 g, 0.05mmol) in toluene (15 mL) was reacted with oxygen at r.t. under UV (365 nm) for 3 hrs. After the removal of the solvent, purification of the crude product by preparative TLC plates (CH_2Cl_2/hexane, 1/1) afforded the product as a white solid (yield ~92%, based on NMR). ^{1}H NMR (400 MHz, C_6D_6, 25°C, δ, ppm): 9.08 (d, $J = 2.4$ Hz; 1H), 8.68 (dd, $J = 4.8$Hz, $J = 2.0$Hz; 1H), 8.42 (dd, $J = 7.6$ Hz, $J = 1.2$ Hz; 1H), 8.18 (d, $J = 8.0$ Hz; 2H), 7.43 (td, $J = 7.2$ Hz; $J = 1.2$ Hz; 1H), 7.38 (d, $J = 6.8$ Hz; 1H), 7.34 (m; 3H), 7.21 (m, overlapped with C_6D_6; 2H), 7.11 (d, $J = 8.0$ Hz; 1H), 6.75 (m; 2H), (d, $J = 6.4$ Hz; 1H), 7.63 (d, $J = 8.0$ Hz; 2H), 7.32 (m; 3H), 6.93 (s; 2H), 6.68 (s; 4H), 2.27 (s; 6H). HRMS, calcd. for $C_{31}H_{26}N_2$: m/z 426.2096; found 426.2100.

4.2.6 Quantum yield measurement

Quantum yields of the boron compound **4.1** was determined in CH_2Cl_2 using 9,10-diphenylanthracene as the standard at 298 K ($\Phi_r = 0.90$). The absorbance of all the samples and the standard at the excitation wavelength is approximately 0.096-0.109. The quantum yields were calculated using previously known procedures in Chapter 1. For the Pt(II) complex **4.2**, the quantum efficiency was measured under N_2 using $Ir(ppy)_3$ as the standard ($\Phi = 0.40$) in CH_2Cl_2.[8] The decay lifetime at r.t. for **4.2** was measured under N_2.

4.2.7 Molecular orbital calculations

DFT molecular orbital calculations were performed for **4.1**, and metal complex **4.2**. The geometrical parameters obtained for **4.1** from X-ray diffraction experiments were used as the starting point for their individual geometry optimization. The energy calculations were performed using Gaussian03 package with the B3LYP/6-311G(d) basis set for all atoms except Pt, for which LAN2LDZ basis set was used.[9-10]

4.2.8 X-ray crystallographic analysis

A single crystal of **4.1** was mounted on glass fibers for data collection. Data were collected on a Bruker Apex II single-crystal X-ray diffractometer with graphite-monochromated M_o K_α radiation, operating at 50 kV and 30 mA and at 180 K. Data were processed on a PC with the aid of the Bruker SHELXTL software package (version 5.10)[11] and corrected for absorption effects.

4.3 Results and discussion

4.3.1 Synthesis

As shown in Figure 4.2, the synthesis of the free ligand 2-(2-bromophenyl)-5-(4-(pyridin-2-yl)phenyl)pyridine was achieved by Suzuki-Miyaura coupling of 4-(2-py)-phenylboronic acid with 2-(2-bromophenyl)-5-iodine-pyridine. The precursor 2-(2-bromophenyl)-5-iodine-pyridine was also obtained through the Suzuki coupling reaction between 2,5-diiodinepyridine with 2-bromophenyl boronic acid. In both coupling reactions, the boronic acid coupled selectively with the iodine on the pyridine, due to the better reactivity of iodine than bromine. However, the side reaction of coupling with bromide is inevitable under the conditions described in Figure 4.2, and the coupling reactions with iodine in steps a and d are all low yield.
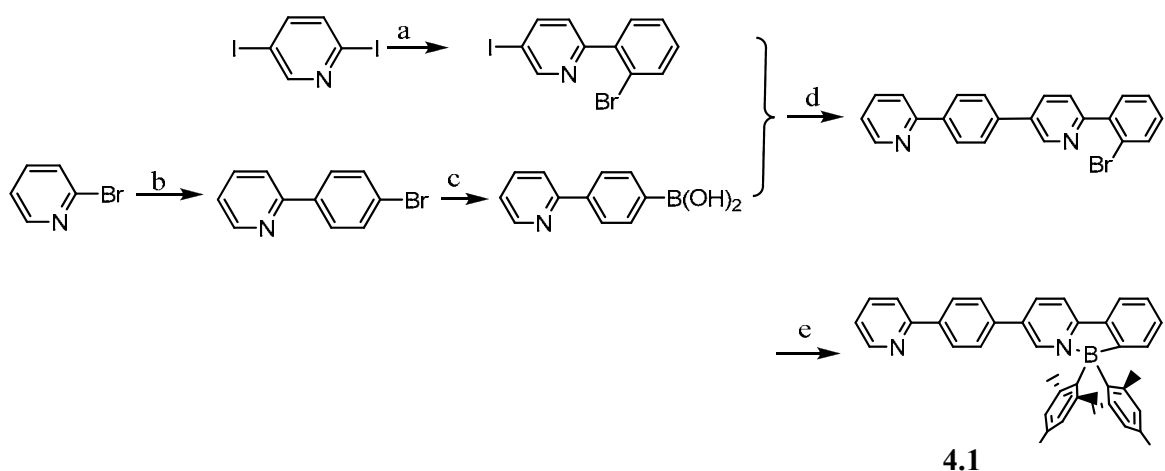
aReagents and conditions: a) toluene, ethanol, and water (3:1:1), 2-bromophenyl boronic acid, Pd(PPh$_3$)$_4$, and NaOH, 60°C. 12 h; b) THF/H$_2$O (1:1), 4-bromophenyl boronic acid, Pd(PPh$_3$)$_4$, K$_2$CO$_3$, 60°C. 12 h; c) (i) n-BuLi, THF, -78 °C; (ii) B(OMes)$_3$, rt, overnight. d) Toluene, Pd(OAC)$_2$, 2-dicyclohexylphosphino-2',6'-dimethoxybiphenyl, K$_3$PO$_4$, 60°C. 12 h; e) (i) n-BuLi, THF, -78 °C; (ii) BMes$_2$F, rt, overnight

Figure 4.2 Synthetic scheme for **4.1**.

The DMSO complex {[(2-py-phenyl)Pt(DMSO)ph-4-py]-2-phenyl}BMes$_2$ was obtained readily by cyclometalation reactions of [PtPh$_2$(DMSO)$_2$] with ligand **4.1**, in THF at 50°C. Due to the poor solubility of this Pt(II) complex with the DMSO ancillary ligand in most organic solvents, the ligand DMSO was replaced with 4-*t*-Bu-pyridine to increase the solubility. As shown in Figure 4.3, the 4-*t*-Bu-pyridine complex **4.2** was obtained by the reaction of excess 4-*t*-Bu-pyridine with {[(2-py-phenyl)Pt(DMSO)ph-4-py]-2-phenyl}BMes$_2$, through a ligand substitution reaction.
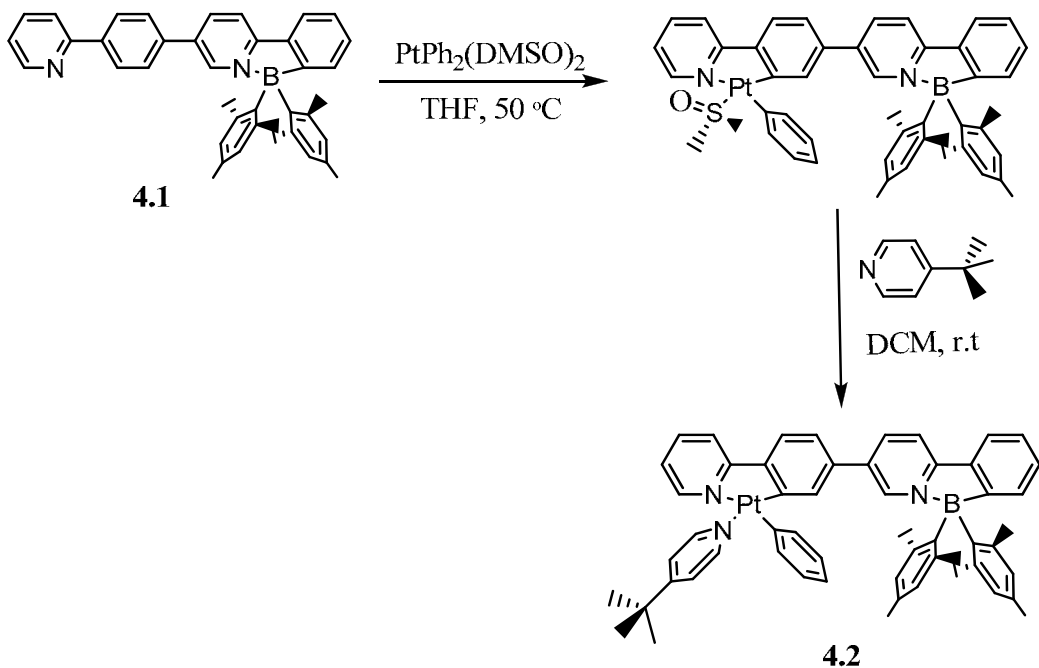
Figure 4.3 Synthetic scheme for **4.2**.

4.3.2 Crystal structrue of 4.1

The crystal structure of **4.1** determined by X-ray diffraction analysis is shown in Figure 4.4. The four-coordinate boron adopts a tetrahedral geometry. With the intramolecular N(1) to B(1) coordination, the phenyl and the pyridyl planes are constrained in a nearly coplanarity, with a distortion angle of 6.70°. The B-C bond lengths around the tetragonal B(1) center are around 1.633(2) – 1.645(7) Å. The B-N bond length in **4.1** (1.645(5) Å) is within the normal B-N bond length range in a tetrahedral environment.[18] The other phenyl and the pyridyl planes without the tetrahedral boron center are also in a coplanar geometry, due to the constrain from intramolecular N-H(34) hydrogen bonding. These two different phenylpyridine rings are in a distortion angle of 35.68°.
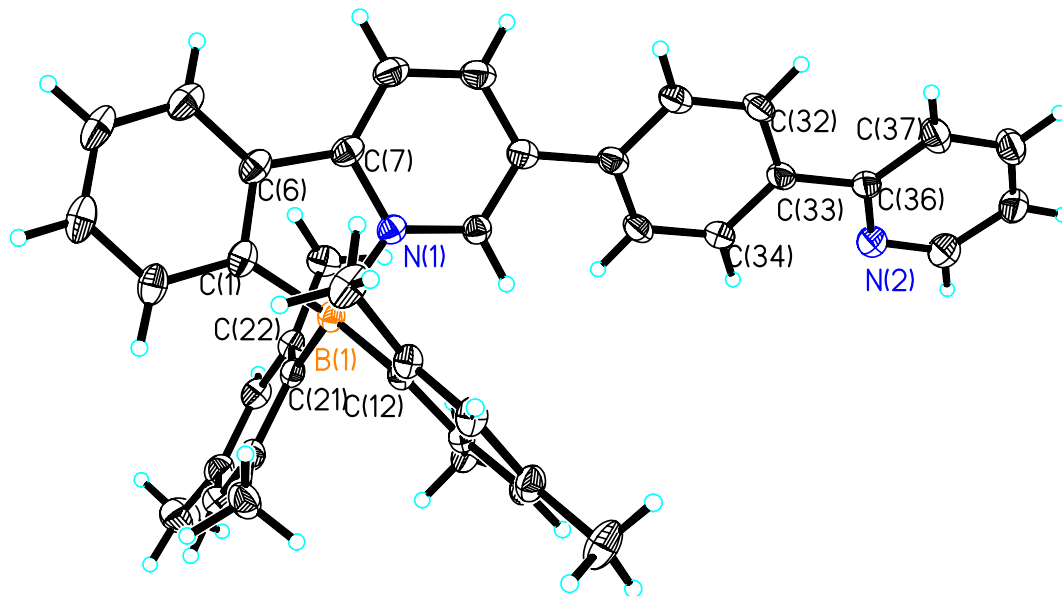
Figure 4.4 The structure of **4.1** with 50% thermal ellipsoids and labeling schemes.

4.3.3 Absorption and luminescence properties

The absorption spectra of the free ligand **4.1** and Pt(II) complexes **4.2** and **4.3** are shown in Figure 4.5. The Pt(II) complex **4.2** displayed absorption bands similar as the corresponding free ligand **4.1** and a new well resolved MLCT band with a moderate intensity in the 400-450 nm region. The enhancement of π conjugation through metal chelation leads to the red-shift of the π to p_π-π^* absorption band in **4.2**. The well resolved MLCT band is lower in energy than the π to p_π-π^* band. The red shift of MLCT band in **4.2** compared to **4.3** can be attributed to the tetrahedral boron center can lower the molecular LUMO energy level. The Pt(II) complex **4.3** has no distinct absorption around 330 nm region which is characteristic of the tetrahedral boron moiety.

169
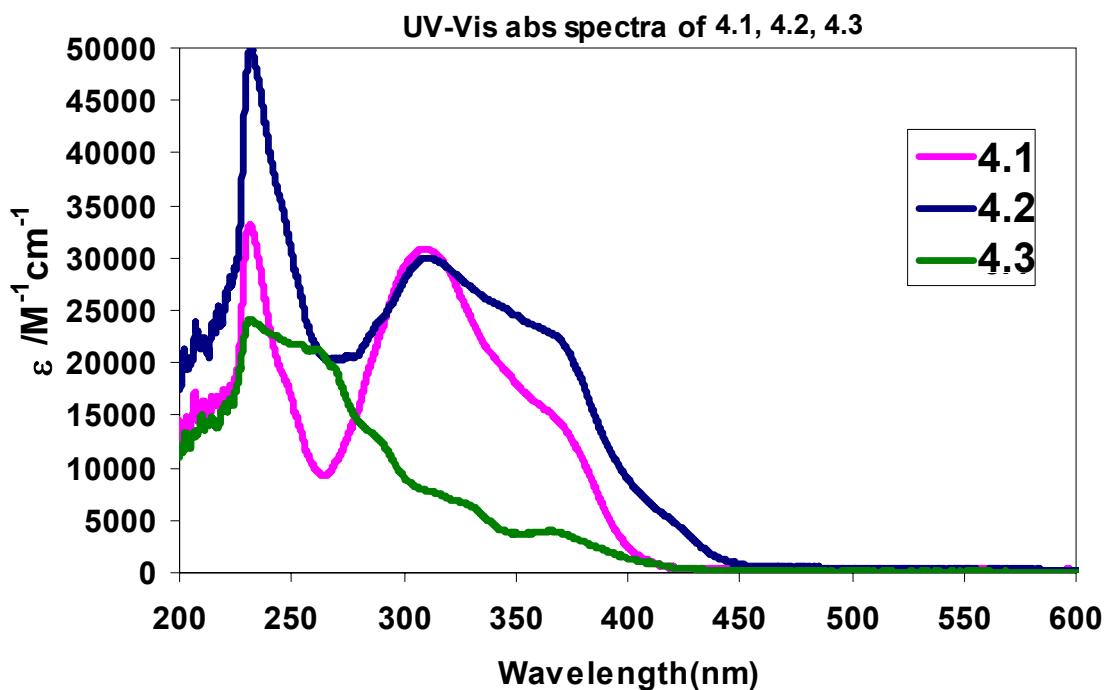
Figure 4.5 The UV-Vis absorption spectra for the **4.1**, **4.2** and **4.3**, recorded in CH_2Cl_2.

The luminescent properties of the free ligand **4.1** were examined by fluorescence spectroscopy. Under UV irradiation, **4.1** displayed bluish green luminescence in solution (toluene) at ambient temperature with λ_{max} = 480 nm (Φ = 0.18). The Pt(II) complex **4.2** exhibits a strong phosphorescence at r.t in the range of 400-650 nm with λ_{max} at 553 nm (τ = 10.2 μs) and an emission quantum yield Φ of 0.03, based on Ir(ppy)$_3$ in degassed toluene as the reference (Φ = 0.40). The emission band of **4.2** is red-shifted compared to that of **4.1**, in consistent with the lower energy the π to p_π-π* and MLCT absorption band in **4.2**. The emission spectra of **4.1** and **4.2** at ambient temperature in CH_2Cl_2 are shown in Figure 4.6.

Emission Spectra of 4.1, 4.2 in toluene, r.t
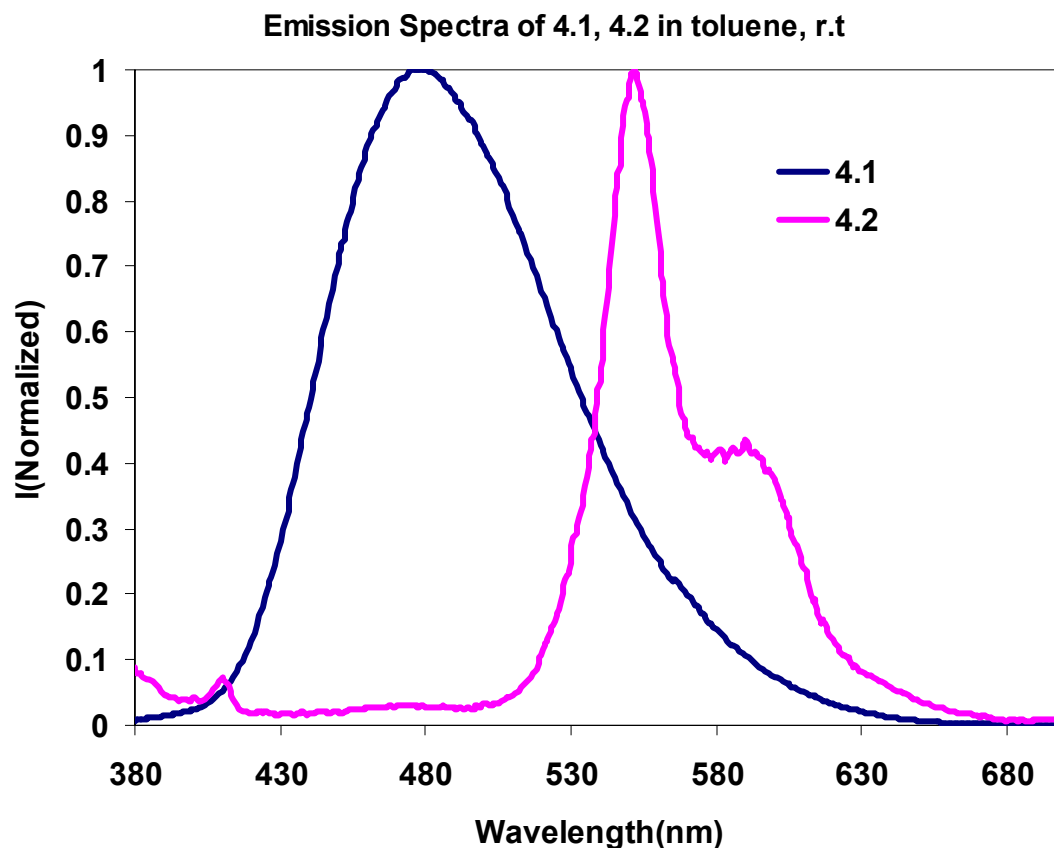
Figure 4.6 The normalized emission absorption spectra for **4.1** and **4.2** recorded in CH_2Cl_2 at r.t.

As shown in Figure 4.7, at 77 K in frozen CH_2Cl_2 solution, upon irradiation, the emission maximum of **4.1** is blue-shifted to 446 nm (480 nm at r.t), with a shoulder emission peak around 530 nm. The blue shift of emission energy at 77K in glass state compared to the solution state is due to the rigidity in glass state in which the solvent cannot reorient themselves to stabilize the excited state of molecules, leading to an increase of excited state energy.
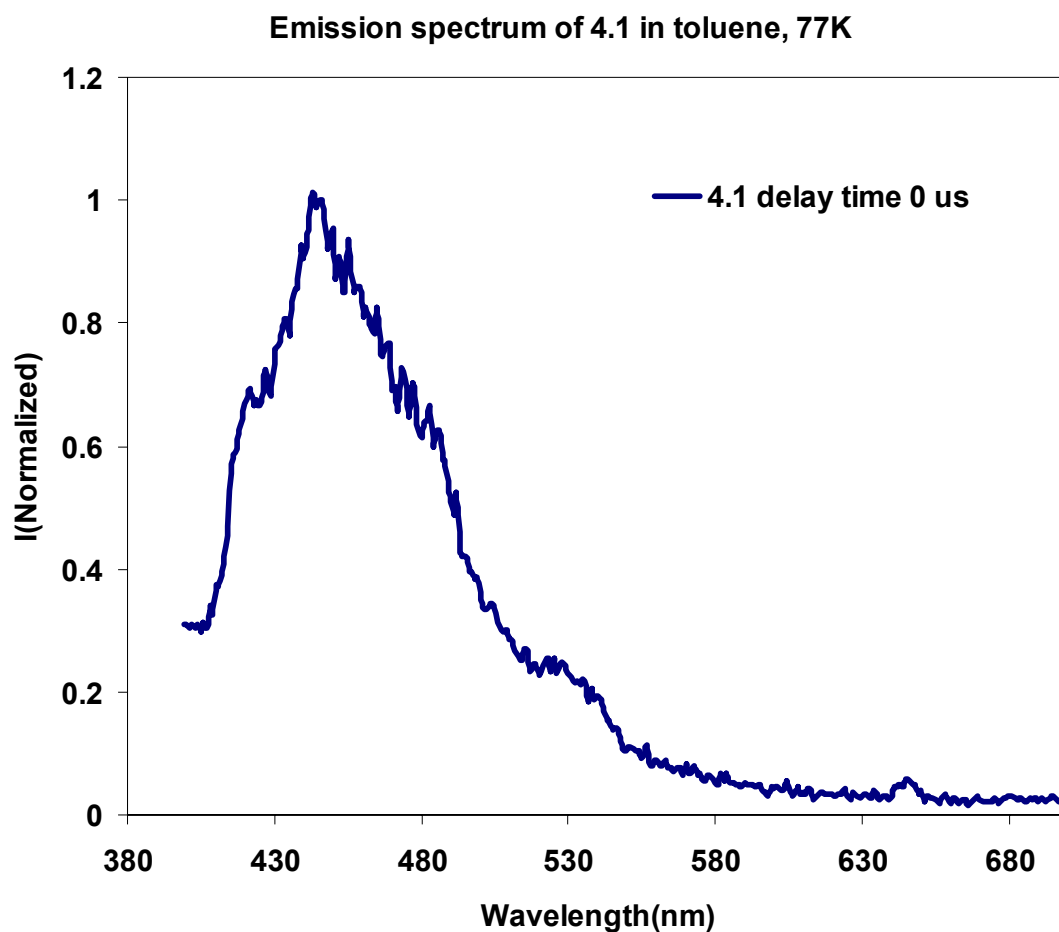
Figure 4.7 The emission spectrum of **4.1** in toluene at 77 K.

The phosphorescent spectra of **4.1** and **4.2** at 77 K obtained on a time-resolved phosphorimeter are show in Figure 4.8. At 77 K, the emission maximum of **4.2** shifts from 553 nm (r.t) to 515 nm ($\tau = 80.8(3)$ μs). The overlap of the time-resolved emission spectra of **4.1** and **4.2** proved that the LC (Ligand-Centered) character dominates the emission of **4.2**.
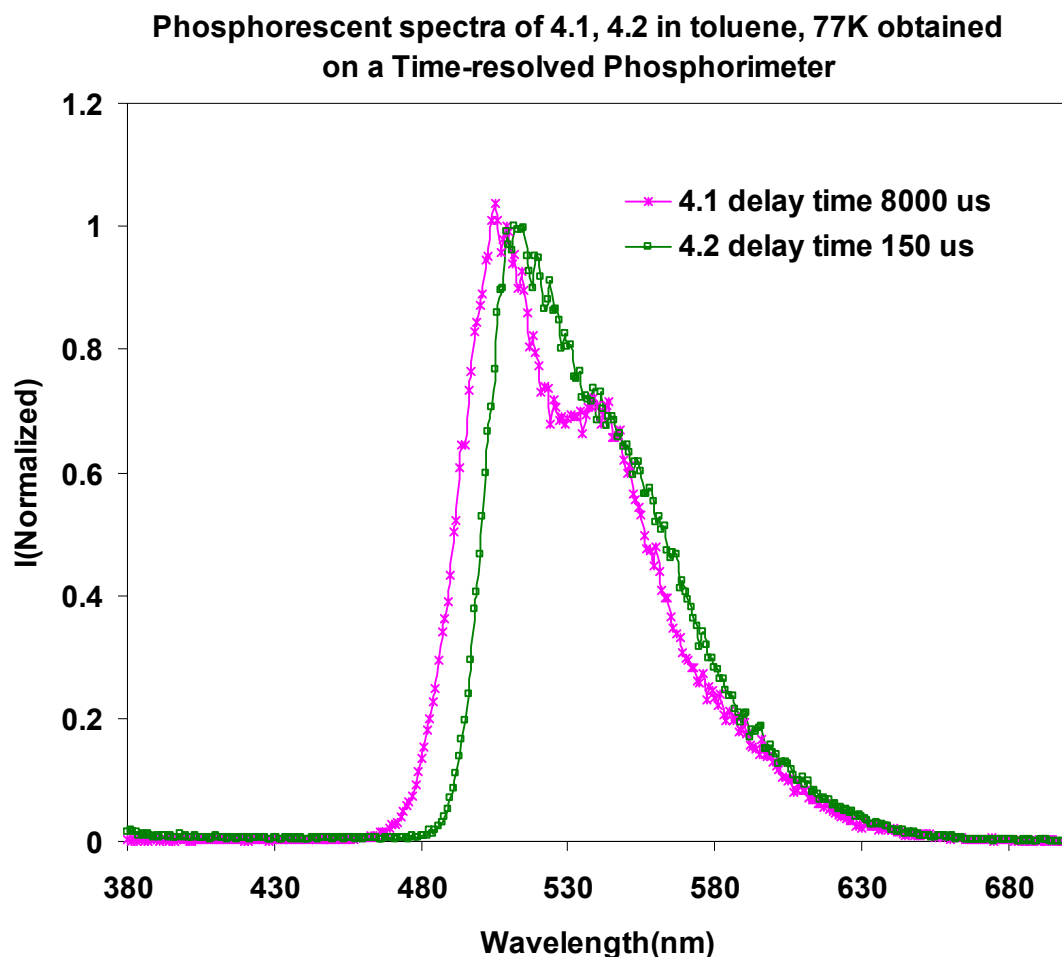
Figure 4.8 The normalized phophorescent spectra for **4.1** and **4.2** recorded in toluene obtained on a time-resolved phosphorimeter at 77 K.

4.3.4 Molecular orbital calculations

To better understand the origin of the electronic transitions in **4.1** and **4.2**, DFT calculations were performed. The HOMO and LUMO diagrams are shown in Figure 4.9. The HOMO of **4.1** is dominated by the mesityl group of boron center, while the LUMO is dominated by the π* orbital of py-ph-py-ph conjugated aromatic area. The lowest

electronic transition in this compound is therefore from the mesityls of the tetrahedral boron to the py-ph-py-ph moiety similar to compound **3.1**. In metal complex **4.2**, the HOMO and LUMO are similar to those of **4.1**, except that in LUMO has small contribution from the Pt(II) center and the ancillary ligand 4-*t*-Bu-pyridine. Even though different functional groups (triayrlboron in **3.1**, phenylpyridine in **4.1**, Pt(II) complex in **4.2**) were utilized to modify the tetrahedral boron moiety, DFT (Gaussian03) calculations established that the lowest electronic transitions in these three individual compounds are almost the same: the HOMO is localized on the mesityls of the tetrahedral boron, the LUMO is spreaded out at the other part of molecules, Mes$_2$B-py-ph in **3.1** or the py-ph-py-ph moiety in **4.1**, **4.2**.

HOMO   **LUMO**

4.1

HOMO   **LUMO**

4.2
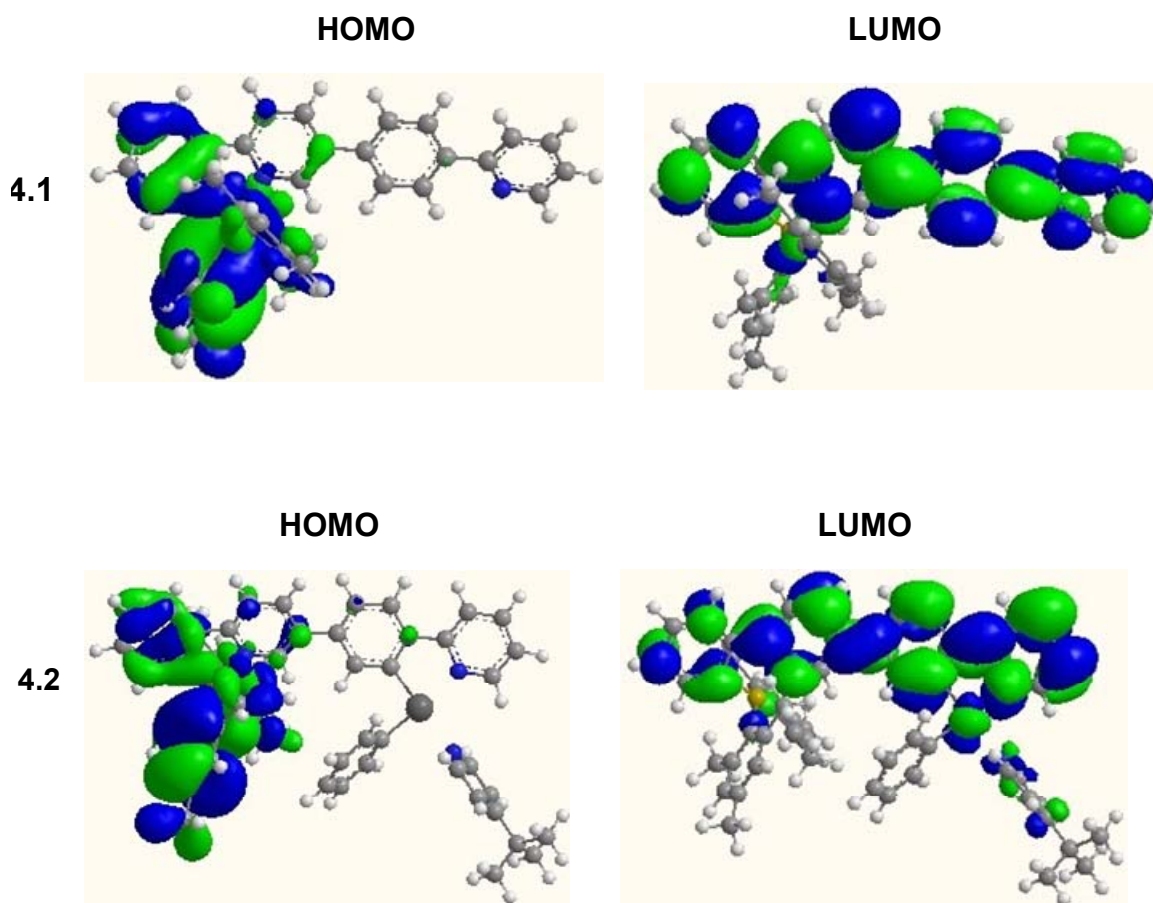
Figure 4.9 Molecular orbitals for **4.1** and **4.2**.

4.3.5 Photochemical reactivity of 4.1

Upon irradiation at 365 nm, under N_2, in C_6D_6, the tetrahedral boron center in the free ligand **4.1** undergoes isomeration in the same way as **3.1**, as depicted in Figure 4.10. The colorless solution of **4.1** changed to dark blue upon irradiation.
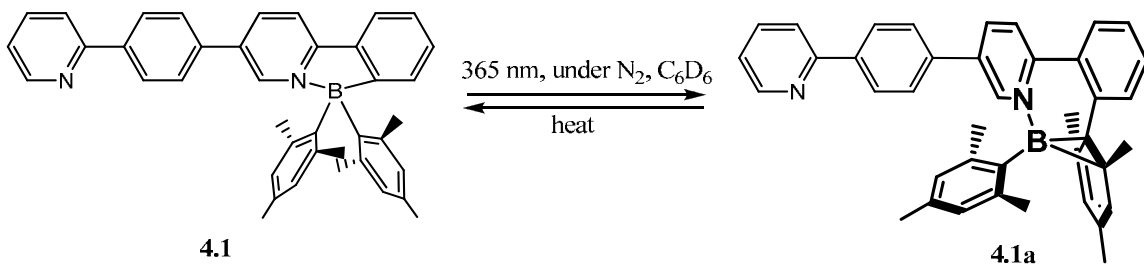
Figure 4.10 Photoisomeration of **4.1**.

From the UV-Vis absorption spectra changes from Figure 4.11, upon irradiation, a new broad band covering the entire 400-780 nm region appears in the UV-Vis spectrum of **4.1** and gains intensity with the exposure time. The spectra were obtained when **4.1** at concentration of 1.25 x 10^{-4} M in freshly distilled toluene, with ~ 10 s intervals of light exposure (365 nm) at the beginning, and ~ 2 min intervals later on.
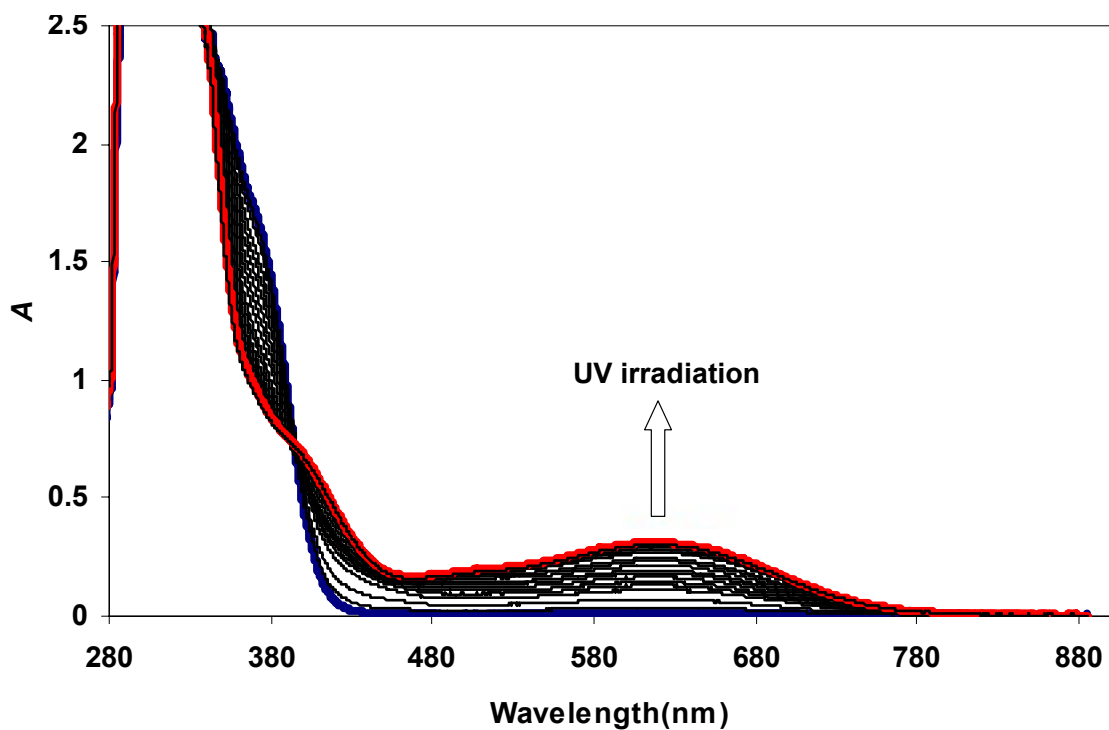
Figure 4.11 UV-Vis spectra of **4.1** under N_2 in toluene along with UV irradiation.

As shown in the stacked ^{1}H NMR spectra in Figure 4.12 and Figure 4.13, along with the increase time of UV exposure, distinct ^{1}H signals belonging to the intermediate **4.1a** showed up with growing intensity. The ^{1}H NMR spectral pattern of **4.1a** is similar to that of **3.1a**, thus, confirming the formation of the same isomeration species.
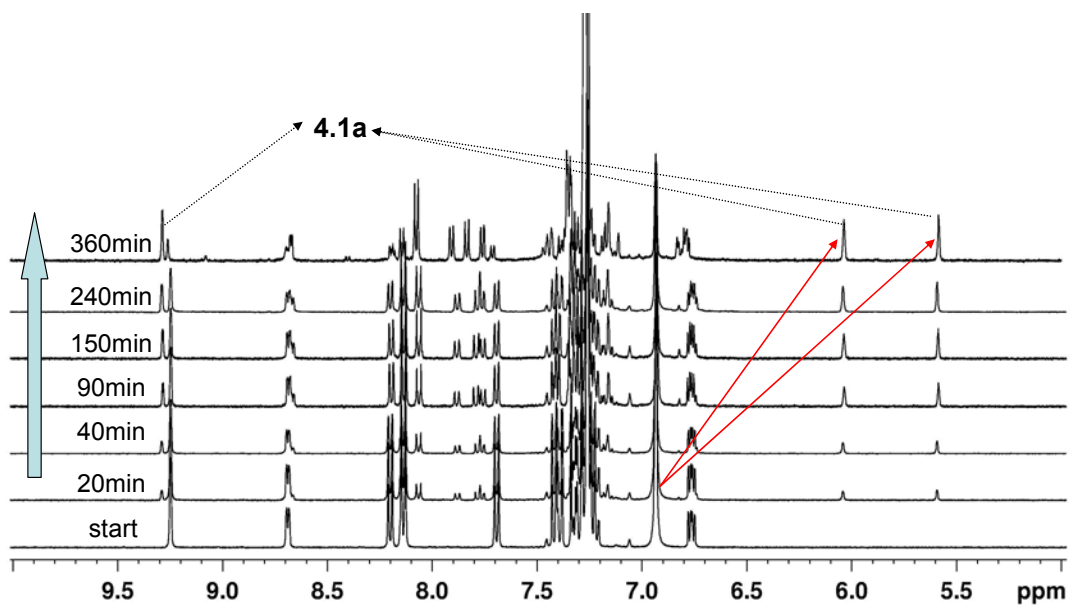
Figure 4.12 Stacked ^{1}H NMR spectra of **4.1** upon UV irradiation, under N_2, in C_6D_6 (aromatic region).
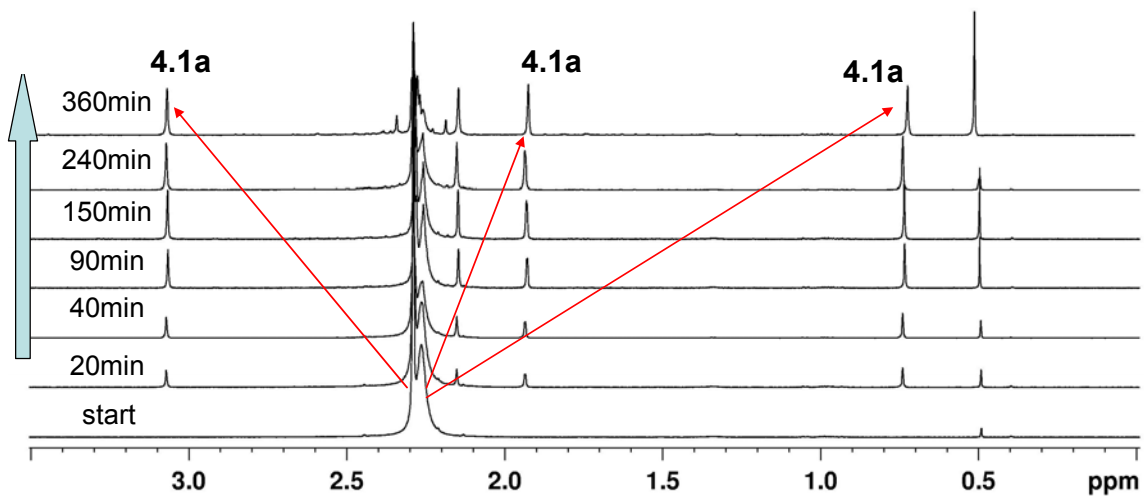
Figure 4.13 Stacked ^{1}H NMR spectra of **4.1** upon UV irradiation, under N_2, in C_6D_6 (aliphatic region).

Interestingly, the photoismoerization of **4.1** is much slower relative to that of **3.1** and **3.2**. As shown in Figure 4.14, at 365 nm, compound **4.1** has similar molar extinction coefficient with that of **3.1** at 365 nm, larger than that of **3.2**. The slower photoisomerization is possibly due to the extended py-ph-py-ph moiety with conjugated π* orbital can stabilize the excited state and slow down the photochromic switching process. This demonstrates that the extention of the π-conjugation of the ph-py chelate does have a significant impact on the photochromic behavior of the boron compound.
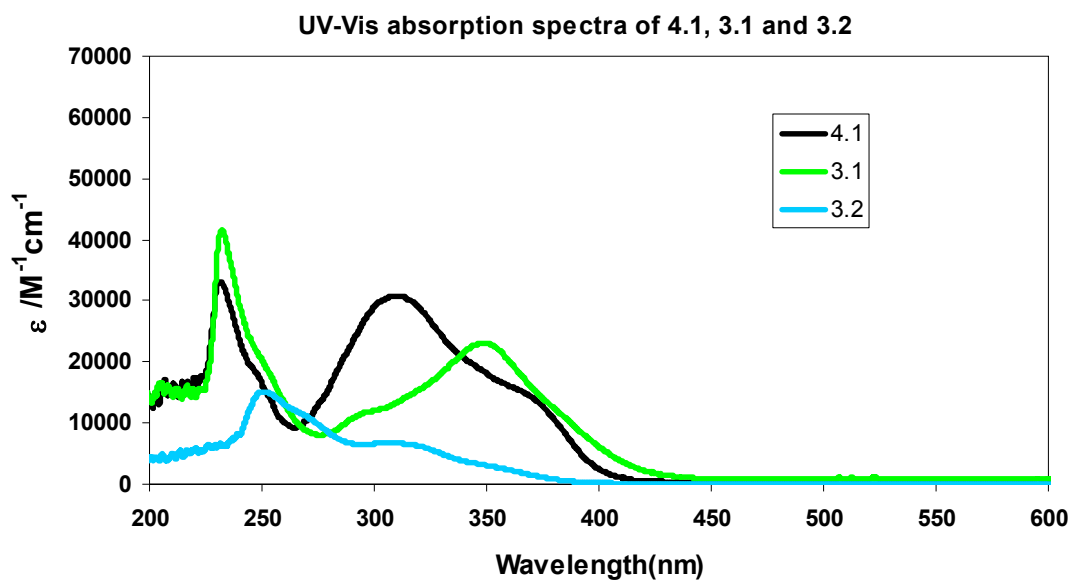
Figure 4.14 UV-Vis absorption spectra of **4.1**, **3.1** and **3.2** in toluene.

When exposed to oxygen, **4.1a** was converted to the C-C coupled product **4.1b** (Figure 4.15) in a similar manner as **3.1a**, while the original tetrahedral boron moiety was

eliminated as B(OMe)$_3$. Product **4.1b** and B(OMes)$_3$ were identified through ^{1}H NMR spectra and high resolution mass spectra.
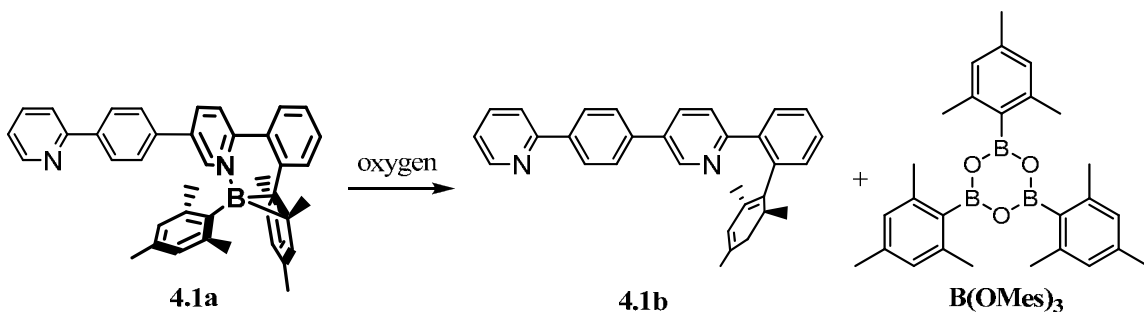
Figure 4.15 Conversion of **4.1a** to **4.1b** under oxygen.

The ^{1}H spectra and mass spectra of B(OMes)$_3$ are the same as reported in Section 3.42.

4.4 Photochemical reactivity of 4.2

Upon irradiation at 365 nm, under N$_2$, in C$_6$D$_6$, the tetrahedral boron center in metal complex **4.2** is fairly stable compared to that of **4.1**. The proposed photoisomerization of **4.2** is shown in Figure 4.16. With UV exposure time up to 12 h, the ^{1}H NMR spectra of **4.2** has less than a 5% change, which can be assigned as the isomerized product **4.2a**, as shown in Figure 4.17 and Figure 4.17. These data support that the Pt(II) center stabilizes the B-ppy-ppy chromophore towards photoisomerization.
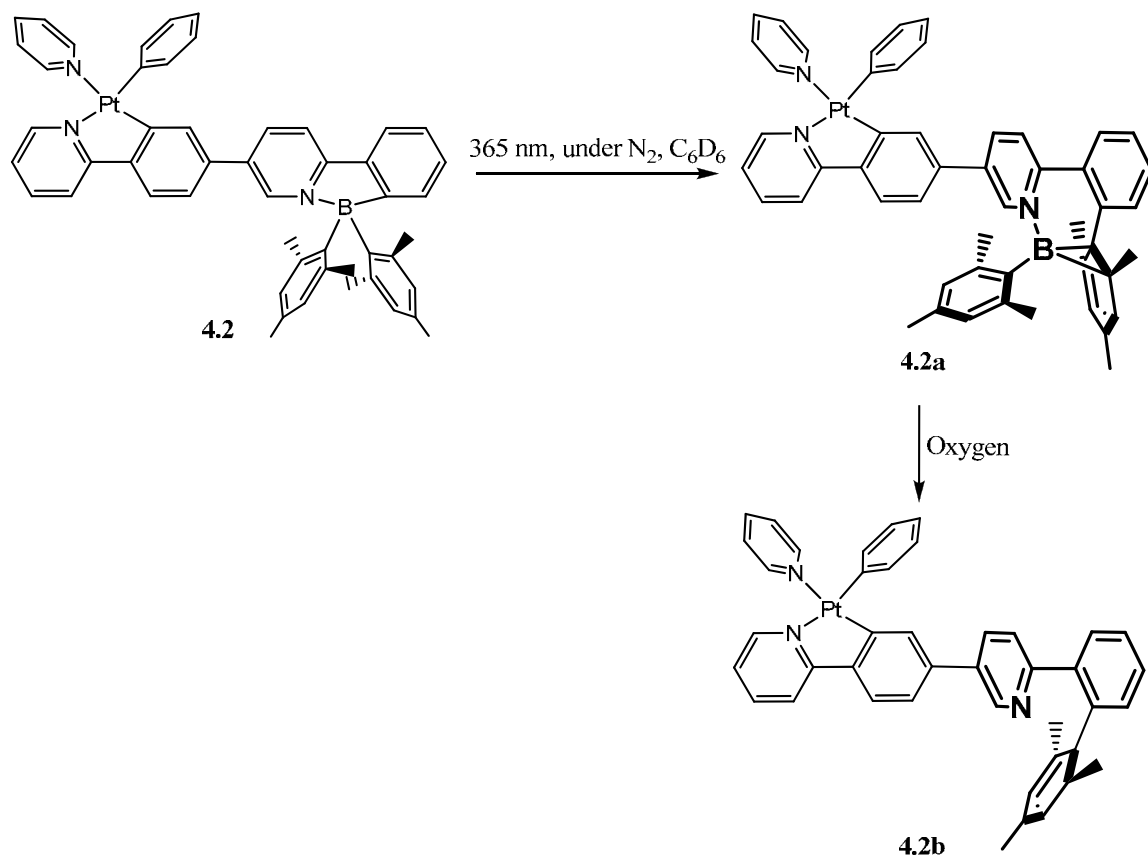
Figure 4.16 Proposed isomerization scheme of **4.2**.
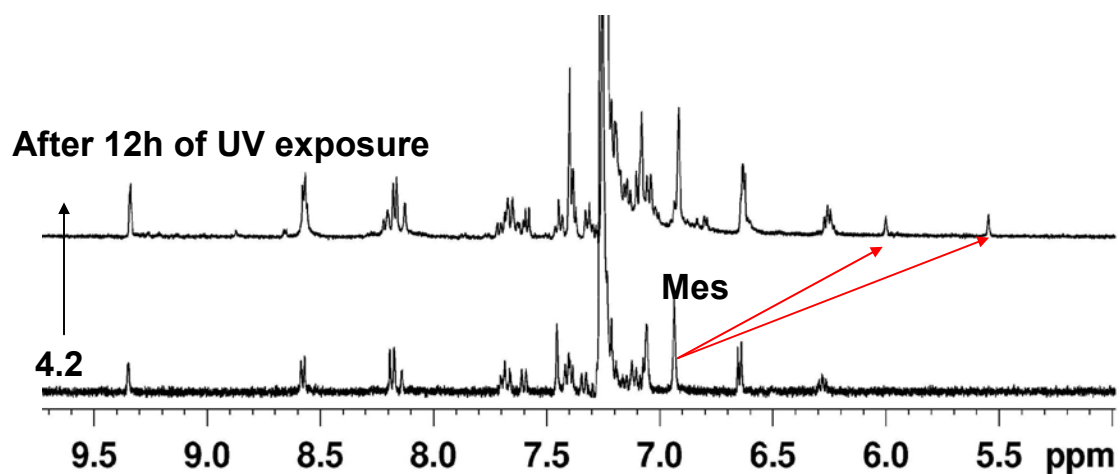
Figure 4.17 ^{1}H NMR spectra of pure **4.2** (bottom) and the solution after 12 h irradiation (top) under N_2, in C_6D_6 (aromatic region).
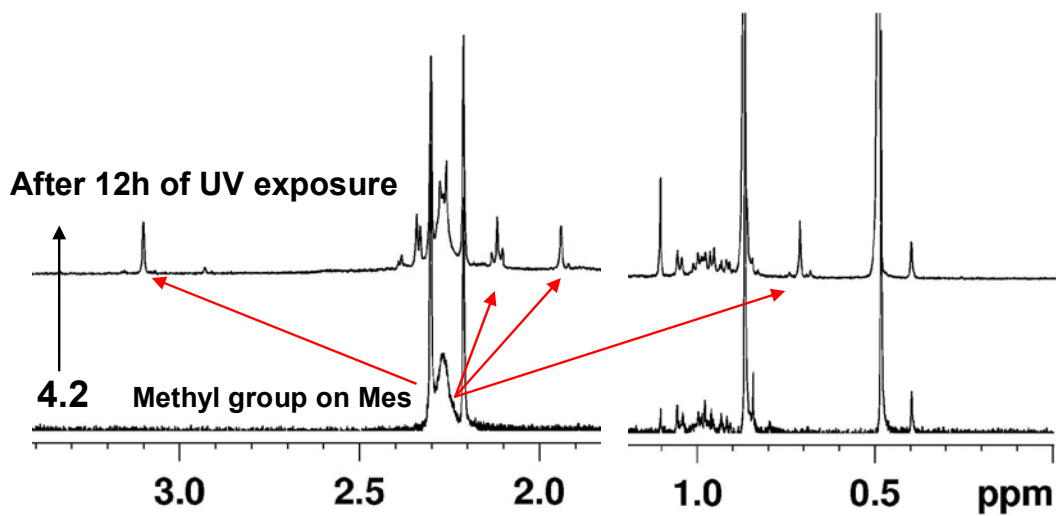
Figure 4.18 ^{1}H NMR spectra of pure **4.2** (bottom) and the solution after 12 h irradiation (top) under N_2, in C_6D_6 (aliphatic region).

Attempts to convert compound **4.2** to the C-C coupled product **4.2b** under oxygen upon UV irradiation failed, due to the decomposition of the N, C-chelate Pt(II) center into some unidentied spieces under such conditions. The instability of the N, C-chelate Pt(II) center toward UV light and oxygen can be proved by the behavior of the Pt(II) in compound **4.3** which does not contain a tetrahedral boron center. The Pt(II) complex **4.3** also decomposed in a similar way as **4.2** under UV light and oxygen. Further work is needed to characterize the Pt(II) center reactivity under UV light and oxygen.

Over all, the photochromic switching pathway of the tetrahedral N, C-chelate boron moiety in metal complex **4.2** is deactivated. This may be due to the presence of a low-lying MLCT state. The electron in the excited state for the photochromic pathway returns to the lowest ^{3}MLCT excited state and then the excess energy dissipated as phosphorescence, as shown in Figure 4.19. It is also possible that the Pt(II) chelation greatly enhances the π conjugation of the conjugated backbone, thus stabilizing the excited state.
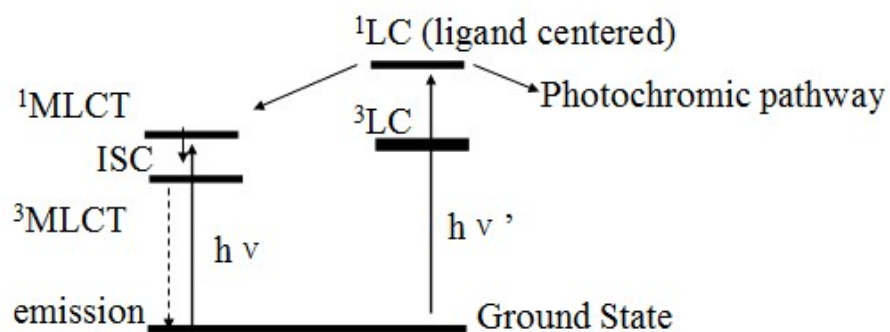
Figure 4.19 Energy diagram for the metal complex **4.2**.

4.5 Conclusion

N, C-chelate four-coordinate organoboron derivatives B-ppy-ppy (**4.1**) and Pt(II) complex (**4.2**) were successfully synthesized and fully characterized. The photoisomeration of the four-coordinate boron center in ligand **4.1** behaved in the same way as **3.1**. The relatively slow photoisomeration rate of **4.1** compared to **3.1** is likely caused by the stabilization of the extended π conjugation of py-ph-py-ph moiety. The photoisomeration of tetrahedral boron center in Pt(II) complex **4.2** is nearly completely deactivated, which may be attributed to either the low-lying ^{3}MLCT excited state in **4.2** through which the excess energy in excited state was dissipated as phosphorescence or the greater π conjugation which can stabilize the excited state.

4.6 References

(1) Robert, M. N.; Nagle, J. K.; Finden, J. G.; Branda, N. R.; Wolf, M. O. *Inorg. Chem.* **2009**, *48*, 19.

(2) Ko, C-C.; Kwok, W-M.; Yam, V. W.; Phillips, D. L. *Chem. Eur. J.* **2006**, *12*, 5840.

(3) Murguly, E.; Norsten, T. B.; Branda, N. R. *Angew. Chem. Int. Ed.* **2001**, *40*, 1752.

(4) Fraysse, S.; Coudret, C.; Launay, J. P. *Eur. J. Inorg. Chem.* **2000**, 1581.

(5) Chen, B. Z.; Wang, M. Z.; Wu, Y. Q.; Tian, H. *Chem. Commun.* **2002**, 1060.

(6) Klein, A.; Schurr, T.; Knodler, A.; Gudat, D.; Klinkhammer, K. W. K.; Jain, V.; Zalis, S.; Kaim, W. *Organometallics*. **2005**, *17*, 4125.

(7) Jia, W.; Song, D.; Wang, S. *J. Org. Chem.* **2003**, *68*, 701.

(8) Brooks, J.; Babayan, Y.; Lamansky, S.; Djurovich, P.; Tsyba, I.; Bau, R.; Tompson, M. E. *Inrog. Chem.* **2002**, *41*, 3055.

(9) Gaussian 03, Revision C.02, Frisch, M. J.; Trucks, G. W.; Schlegel, H. B.; Scuseria, G. E.; Robb, M. A.; Cheeseman, J. R.; Montgomery, Jr., J. A.; Vreven, T.; Kudin, K. N.; Burant, J. C.; Millam, J. M.; Iyengar, S. S.; Tomasi, J.; Barone, V.; Mennucci, B.; Cossi, M.; Scalmani, G.; Rega, N.; Petersson, G. A.; Nakatsuji, H.; Hada, M.; Ehara, M.; Toyota, K.; Fukuda, R.; Hasegawa, J.; Ishida, M.; Nakajima, T.; Honda, Y.; Kitao, O.; Nakai, H.; Klene, M.; Li, X.; Knox, J. E.; Hratchian, H. P.; Cross, J. B.; Bakken, V.; Adamo, C.; Jaramillo, J.; Gomperts, R.; Stratmann, R. E.; Yazyev, O.; Austin, A. J.; Cammi, R.; Pomelli, C.; Ochterski, J. W.; Ayala, P. Y.; Morokuma, K.; Voth, G. A.; Salvador, P.; Dannenberg, J. J.; Zakrzewski, V. G.; Dapprich, S.; Daniels, A. D.; Strain, M. C.; Farkas, O.; Malick, D. K.; Rabuck, A. D.;

Raghavachari, K.; Foresman, J. B.; Ortiz, J. V.; Cui, Q.; Baboul, A. G.; Clifford, S.;

Cioslowski, J.; Stefanov, B. B.; Liu, G.; Liashenko, A.; Piskorz, P.; Komaromi, I.;

Martin, R. L.; Fox, D. J.; Keith, T.; Al-Laham, M. A.; Peng, C. Y.; Nanayakkara, A.;

Challacombe, M.; Gill, P. M. W.; Johnson, B.; Chen, W.; Wong, M. W.; Gonzalez,

C.; and Pople, J. A.; Gaussian, Inc., Wallingford CT, 2004.

(10) (a) Becke, A. D. J. Chem. Phys. 1993, 98, 5648. (b) Lee, C.; Yang, W.; Parr, R. G.

Phys. Rev. B. **1988**, *37*, 785. (c) Miehlich, B.; Savin, A.; Stoll, H.; Preuss, H. *Chem.

Phys. Lett.* **1989**, *157,* 200. (d)Hariharan, P. C.; Pople, J. A. *Theor. Chim. Acta*

1973, *28*, 213.

(11) *SHELXTL*, version 6.14; Bruker AXS: Madison, WI, 2003.

Chapter 5
Summary and Perspectives

5.1 Summary and conclusions

This work started with the investigation of the impact of a Pt(II) complex on the photophysical properties of triarylboron compounds. Phenylpyridine with an N, C chelate site is chosen as the molecular skeleton. For the free ligands, the Lewis acidity of the boron center of *p*-ppy-B can be further enhanced with a boron moiety on the pyridine ring, due to the electron-withdrawing property of nitrogen in pyridine ring. Two constitutional isomers with either BMes$_2$ on the phenyl ring (*p*-B-ppy) or on the pyridine ring (*p*-ppy-B) have a distinct impact on the structure, stability, electronic and photophysical properties of the Pt(II) complexes.

The phosphorescent decay lifetimes of the Pt(II) complexes *p*-B-ppy and *p*-ppy-B are all much longer than those of Pt(ppy)(acac) and its derivatives, which may be due to the stabilization of the excited state by the BMes$_2$ group or the influence of the phenyl ligand and the auxiliary ligand.

Pt(II) chelation can enhance the electron accepting ability of ppy-B rather than that of B-ppy. This is due to the fact that upon Pt(II) chelation, a neutral ppy molecule is changed to an anionic ligand. For B-ppy, the direct conjugation of the B center with the negatively charged phenyl ring weakens the electron accepting ability of the boron center. Due to the steric constraint upon Pt(II) chelation, the Pt(II) complexes of ppy-B and B-ppy do not have significant changes in their Lewis acidity with fluoride compared to their corresponding free ligands. Therefore, for N,C-chelate ligands, it is most effective

187

with the boron moiety being directly conjugated with the nitrogen heterocycle in order to enhance the electron accepting ability and Lewis acidity. Furthermore, metal chelation often introduces a greater steric constraint on the BMes$_2$ group, thus may have a negative impact on its binding ability with anions such as fluoride.

The impact of different ancillary ligands, DMSO, pyridine, 4,4'-bipyridine, on the Pt(II) complexes were also examined. The electron accepting ability of boron center can be further enhanced with the ancillary ligand DMSO which is a relatively weaker electron donor. In the dinuclear Pt(II) complexes with a 4,4'-bipyridine ancillary ligand, electronic communication between the two boron centers is possible in a sterically less congested system (B-ppy) that allows extended conjugation through the entire molecule.

Different from the N, C-chelate Pt(II) center, incorporation of a second tetrahedral boron center into the triaryboron system can greatly lower the LUMO energy level and enhance the electron affinity. A reversible isomerization process involving a tetrahedral boron center and the formation/breaking of a C–C bond has been established. Compounds **3.1** and **3.2** are the first examples of organoboron compounds that display a reversible photo-thermal color switching. The N,C-chelate group plays a key role in mediating the isomerization process.

The relatively slow photo-isomeration process of the N, C-chelate four-coordinate organoboron derivative B-ppy-ppy (**4.1**) demonstrates that the extention of the π-conjugation of the ph-py chelate dose have a significant impact on the photochromic behavior of the boron compound. The relatively slow photoisomerization rate of **4.1**

compared to **3.1** is likely due to the stabilization of the extended π conjugation of py-ph-py-ph moiety.

Direct conjugation of Pt(II) center to the four-coordinate organoboron compounds has a profound impact on the photoisomerization process of boron center. The deactivation of the photoisomerization process in the photochrome-coupled Pt(II) complex **4.2** is due to either the low-lying ^{3}MLCT excited state in **4.2** through which the excess energy in excited state was dissipated as phosphorescence, or the greater π conjugation which can stabilize the excited state.

5.2 Future directions

N, C-chelate Pt(II) complexes with acac ancillary ligands have higher luminescent efficiency. For practical use as an emitter in OLEDs, it is necessary to synthesize Pt(*p*-B-ppy)(acac) and Pt(*p*-ppy-B)(acac) complexes.

To further study the photochromic behavior of N, C-chelate four-coordinate organoboron compounds, two photochromic centers connected together through a conjugated chain, such as a phenyl group, or an acetylene group (as shown in Figure 5.1) are worth exploring. With phenyl ring (**5.1a**, **5.2a**) or pyridine ring (**5.1b**, **5.2b**) close to the conjugated site, the lowest electronic transitions in these compounds are intriguing and might be different. However, the synthetic route to **5.1a** and **5.2a** is challenging.
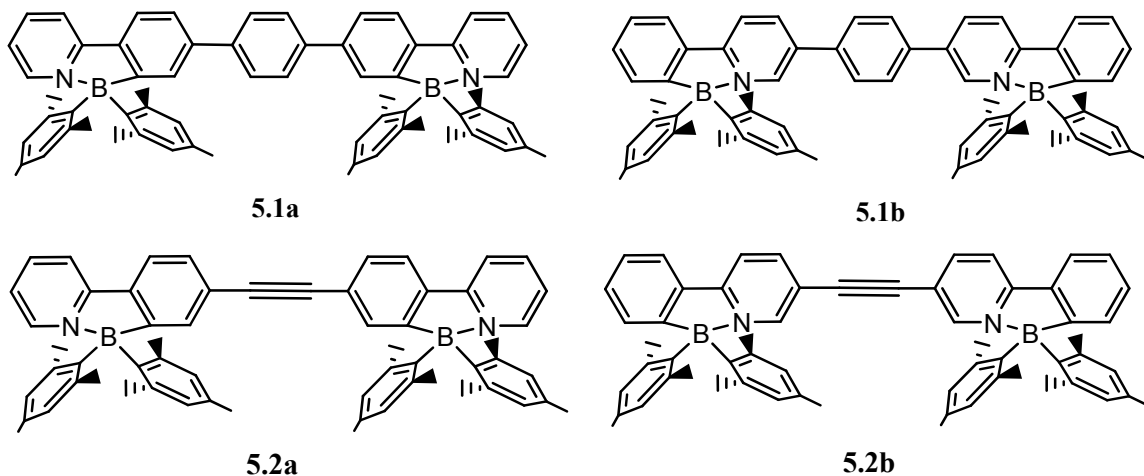
Figure 5.1 Molecular structures of conjugated N, C-chelate four-coordinate boron compounds.

For the photochromic-metal coupled complexes, N, C-chelate transition metal Pt(II) with a low-lying MLCT band deactivates the photochromic process. Incorporation of a d^{10} transition metal without a MLCT band, such as Zn, into the photochromic organboron system may enhance the π conjugation backbone, without inhibiting the photochemical property.